

THESE

En vue de l'obtention du : **DOCTORAT**

Centre de Recherche : Sciences des Matériaux

**Structure de Recherche : Matériaux, Nanotechnologies et Environnement / Optique,
Photonique et Nanotechnologie**

Discipline : Chimie physique

Spécialité : Photonique et Nanotechnologie

Présentée et Soutenue le : 05/11/2020 par :

Yahya BOUGDID

3D Laser Nanofabrication in Photoresist by Two-Photon Absorption

JURY

Abdelilah BENYOUSSEF	PES	Académie Hassan II des Sciences et Techniques - Rabat - Maroc	Président
Zouheir SEKKAT	PES	Faculté des Sciences, Université Mohammed V de Rabat - Maroc	Directeur de Thèse
Abdallah GUENBOUR	PES	Faculté des Sciences, Université Mohammed V de Rabat - Maroc	Rapporteur / Examineur
Hamid EZ-ZAHRAOUY	PES	Faculté des Sciences, Université Mohammed V de Rabat - Maroc	Rapporteur / Examineur
Abdelmajid AINANE	PES	Faculté des Sciences, Université Moulay Ismail de Meknès - Maroc	Rapporteur / Examineur
Abdelkbir BELLAOUCHOU	PES	Faculté des Sciences, Université Mohammed V de Rabat - Maroc	Examineur
Mohammed ABD-LEFDIL	PES	Faculté des Sciences, Université Mohammed V de Rabat - Maroc	Examineur

Année Universitaire: 2019/2020

*It is never too late to get started on a new path
of success ...*

I dedicate this thesis:

To my Mother ... & my Father ... & my Sister ...

& to my Friends ...

Acknowledgments

This thesis is part of the requirements for my Ph.D. degree at Faculty of Sciences, Mohammed V University in Rabat. The work carried out in this thesis has been conducted under the supervision of Professor Zouheir SEKKAT in the laboratory of Materials, Nanotechnology and Environment / Optics, Photonics and Nanotechnology at the Faculty of Sciences of Rabat in collaboration with Optics and Photonics center in MAScIR (Moroccan Foundation for Advanced Science, Innovation and Research).

My deepest gratitude and acknowledgments are firstly expressed to my research supervisor and thesis director, Pr. Zouheir SEKKAT, who recommended me an interesting research topic and continually supported my work. Without his patience, guidance, uncountable advices, and help, this thesis project would not have been possible. His advice on both research as well as career has been invaluable, and I take this opportunity to thank him sincerely for his guidance, criticisms, gentilities, availability, and human qualities.

Besides my dear advisor, my special thanks go to Pr. Abdelilah BENYOUSSEF, PES, Faculty of Sciences, Mohammed V University in Rabat, for accepting to preside the honored jury of this thesis defense, and for his insightful comments, guidance and feedback, which have been absolutely invaluable. Warm thanks to him for his interest in my research and for being an integral part of the dissertation committee.

I would like to thank Pr. Abdallah GUENBOUR, PES, Faculty of Sciences, Mohammed V University in Rabat, for having accepted to review this work and for his guidance, encouragement, availability and understanding during my thesis.

A special thanks is owed to Pr. Hamid EZ-ZAHRAOUI, PES, Faculty of Sciences, Mohammed V University in Rabat, for taking time to review this work and for having their advice through this process, which provided me positive encouragement.

For Pr. Abdelmajid AINANE, PES, Faculty of Sciences, Moulay Ismail University in Meknes, I would like him to accept my warm thankfulness, respect and gratitude for accepting to review my thesis. And I took this opportunity to thank him sincerely for his gentilities, availability and human qualities.

I would like to thank Pr. Abdelkbir BELLAOUCHOU, PES, Faculty of Sciences, Mohammed V University in Rabat, for having accepted to examine this work and for their invaluable guidance.

I also graciously acknowledge Pr. Mohammed ABD-LEFDIL, PES, Faculty of Sciences, Mohammed V University in Rabat, for having accepted to examine this work and for their invaluable guidance.

I am writing this note of gratitude as a finishing touch of my thesis. It has been a period of intense learning for me, not only in the academic aspect, but also in the aspect of personality. I would like to express my gratitude to the people who have helped me throughout my Ph.D. thesis.

I would like to acknowledge financial support from the Handai Project, financed by Osaka University, and from PPR RE/10/2016 project (Next Generation Optical Media Recordable via Nanophotonics) which is supported by the Moroccan Ministry of Higher Education and Training and Scientific Research (Ministère de l'Enseignement Supérieur, de la Recherche Scientifique et de la Formation des cadres).

I would like to thank MAScIR foundation for providing a good working environment and the access to the platform with cutting edge equipment and leadership to make it a success. A very warm thanks to MAScIR platform staff for their help and guidance during my stay at MAScIR. My deep appreciation goes out to the MAScIR administration who have offer at me infinite support (from Handai and PPR RE/10/2016 projects; as one of Pr. Zouheir SEKKAT projects) to my Ph.D. project.

Also, a great thanks to all members from Optics and Photonics center, MAScIR foundation, and all my labmates: Dr. Imad MAOULI, Sara MOUJDI, Dr. Siham REFKI, Nada BENHADDOU, Dr. Zakaria LAGHFOUR, Ibrahim BOUDENE, Dr. Safae AAZOU, Najat ANDAM, Ismail BENNANI, Sanaa ELHANI, Youssef EL-IDRISSI, Ikram ANEFNAF, Abdeljalil ER-RAFYG, Naoufal ENNOUHI, and Dr. Kentaro MOCHIZUKI from Osaka university. Thank you for everyone with whom I shared great moments both in the lab and outside the lab.

Last but not least, I would like to thank my friends for always being there for me. Words cannot express how grateful I am to my parents, my grandfather, my grandmother, and my sister, who helped me so much that I could pursue my educational career and fulfilling my personal dreams.

Sincerely

Abstract

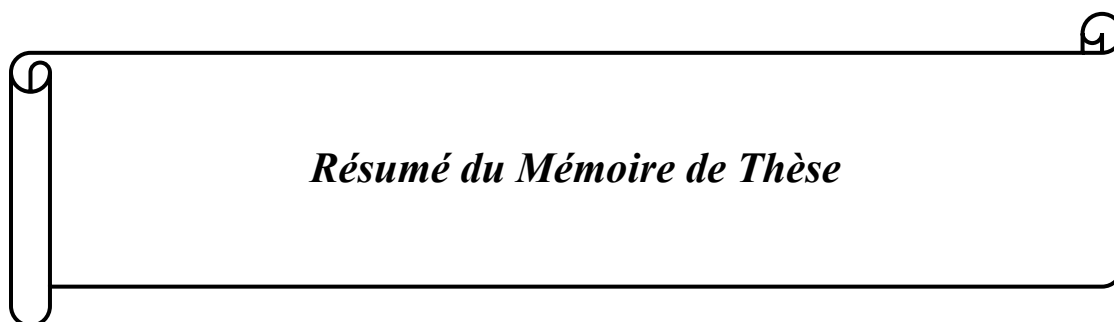
This PhD work aims to investigate the spatial resolution of 3D micro/nano-fabrication by two-photon absorption using a systematic nanofabrication process which we developed. Therefore, to perform 3D micro-nano-fabrication based on two-photon polymerization, we developed a home-made optical setup (inverted-microscope) by utilizing a femtosecond (ultrashort) laser as excitation source. The optimization of voxels (3D equivalent of 2D pixels) obtained by individual shot of exposure; meaning the building blocks of the printed 3D micro-nano-objects, is important in determining the resolution of 3D nanofabrication. Thus, we discuss the factors influencing the resolution, including the laser intensity, exposure time and scanning speed by fabricating polymerized -voxels, nanolines, and suspended nanofibers. Also, we revisit, and present a systematic study of voxels nanofabrication by varying the position of the laser's focal spot (laser focus), with respect to the cover glass/resin interface; *i.e.* in the longitudinal direction (z-direction). We show that the voxels can be optimized and their spatial arrangement; *e.g.* orientation, manipulated when the laser focus is moved in the z-direction from the substrate into the resin. Such a study clearly demonstrates the impact of the z-position of the laser focus on the precision of nanofabrication; a feature which is of primary importance in 3D laser nanoprinting. Lastly, we have fabricated stable 3D microstructures with sub-diffraction-limit accuracy; *e.g.* with $\sim 100\text{ nm}$ of resolution.

Keywords: Femtosecond laser, Nonlinear optical effect, Photoresin, Two-photon absorption, Two-photon polymerization, Voxels, Spatial resolution, 3D micro-nano-objects.

Résumé

Le travail effectué dans le cadre de cette thèse porte sur une étude approfondie de la résolution spatiale de la micro-nano-fabrication 3D par l'absorption à deux photons en utilisant un processus de nanofabrication systématique. Pour réaliser la nanofabrication 3D par laser, nous avons développé un montage optique avancé (microscope inversé) en utilisant un laser femtoseconde (laser-pulsé) comme source d'excitation. L'optimisation des voxels (l'équivalent 3D des pixels 2D) ; c'est-à-dire les éléments de base des micro/nano-objets 3D, est importante pour déterminer la résolution de la nanofabrication 3D laser. De ce fait, les facteurs influençant la taille et les dimensions des voxels et les micro-lignes, y compris l'intensité du laser d'irradiation, le temps d'exposition et la vitesse de nano-impression laser ont été discutés. De plus, une étude systématique de nanofabrication des voxels a été faite en faisant varier la position du point-focal du laser, par rapport à l'interface entre le substrat du verre et la photorésine ; c'est-à-dire dans la direction longitudinale (direction z). Et, il a été démontré que les voxels peuvent être optimisés ainsi que leur disposition spatiale ; par exemple l'orientation, manipulée lorsque le point-focal du laser est déplacé dans la direction z. Cette étude a démontré clairement l'impact de la position z sur la précision et la stabilité de la nanofabrication par l'absorption à deux photons ; une caractéristique qui est de première importance dans la nanoimpression laser 3D. Enfin, nous avons fabriqué des micro/nano-objets 3D avec une précision inférieure à la limite de diffraction de la lumière ; *p. ex.* avec une résolution de $\sim 100 \text{ nm}$.

Mots-clés : Laser femtoseconde, Effet optique nonlinéaire, Photorésine, Absorption à deux photons, Polymérisation à deux photons, Voxels, Résolution spatiale, Micro/nano-objets 3D.



Résumé du Mémoire de Thèse

Résumé du Mémoire de Thèse

Au cours des deux dernières décennies, la micro/nano-fabrication 3D basée sur la polymérisation à deux photons (c-à-d ; la polymerization induite par l'absorption à deux photons) a été établie comme un outil optique de nano-fabrication efficace afin de résoudre les problèmes de résolution, précision, et coût, et qui ne sont pas possibles autrement dans les différents domaines scientifiques et industriels. En raison de sa capacité de fabriquer des structures/objets 3D avec une précision de dizaines de nanomètres (par exemple avec $\sim 100\text{ nm}$ de résolution), la nanofabrication 3D par l'absorption à deux photons est considérée comme une technologie unique et puissante pour produire des micro-dispositifs fonctionnels ; par exemple les microrobots mobile et médicale.

Reposant sur le phénomène non linéaire de l'absorption à deux photons, la technologie de la nanofabrication 3D par laser permet de créer/fabriquer des micro-nano-objets 3D à partir d'un matériau photo-polymérisable (par exemple, les résines photoréticulables). Une large gamme de polymères peut être aussi utilisée, comme des photopolymères, des matériaux bio-compatibles, voire même des protéines et d'autres biomatériaux. Dans le processus de nanofabrication 3D par la polymérisation à deux photons, deux photons peuvent simultanément être absorbés par la résine dans le très petit volume appelé "voxel : l'équivalent 3D des pixels 2D " au point focal du laser pulsé (laser femtoseconde utilisé pour l'excitation). Après l'excitation, une photoréaction chimique (photo- polymérisation) est déclenchée ; en conséquence, la résine liquide polymérise et devient solide autour du point focal du laser. Ici, le diamètre (la taille latérale) du voxel polymérisé peut être inférieur à 100 nm . De ce fait, l'optimisation des voxels ; c-à-d les éléments de base des micro/nano-objets 3D, est importante pour déterminer la résolution de la nanofabrication 3D par laser.

Dans ce contexte, le travail effectué dans le cadre de cette thèse porte sur une étude approfondie de la résolution spatiale de la micro-nano-fabrication 3D par l'absorption à deux photons en utilisant une étude systématique de nanofabrication. Pour cela, nous avons développé un montage optique avancé de nanofabrication 3D en utilisant un laser femtoseconde comme source d'excitation. Guidée par notre stage-piézo de nano-mouvement (couplé avec la conception assistée par ordinateur ou CAO ; *en anglais* Computer-Aided Design or CAD), notre system optique (microscope inversé) déplace le point focal du laser à l'intérieur de la résine photo-polymérisable pour polymériser/fabriquer les microstructures 3D. Au cours du processus de nanofabrication, le

point focal du laser peut également traverser les parties déjà polymérisées ; de ce fait, le voxel est déplacé librement dans toute la résine (en 3-dimensions) sans absorption à la surface ; ceci permet de fabriquer toute forme de micro et nano-structure 3D avec une précision au-delà de la limite de diffraction de la lumière ; par exemple avec $\sim 100\text{ nm}$ de résolution. Voilà pourquoi la technologie de nanofabrication 3D par laser est parfaitement adaptée à la nano-impresion 3D avec une très haute résolution ($\sim 100\text{ nm}$). La Figure ci-dessous présente notre montage optique (photo réelle) de nanofabrication 3D par l'utilisation d'un laser femtoseconde.



Fig. Système optique de la micro/nanofabrication 3D par l'absorption à deux photons.

L'objectif de cette thèse consiste à étudier la nanofabrication laser 3D dans les résines photoréticulables par la polymérisation à deux photons. Ce mémoire de thèse intitulé « Nanofabrication laser 3D dans les résines photoréticulables par l'absorption à deux photons » en vue de l'obtention du grade de Docteur en Chimie-physique ; Spécialité : Photonique et Nanotechnologie, comporte quatre chapitres structurés en trois parties (bibliographie, matériaux/méthodes, et résultats/discussions), et totalise 168 pages. Le manuscrit de cette thèse inclut à la fin une liste de références bibliographiques.

Après un résumé en français et en anglais et une introduction générale, cette thèse se compose de quatre chapitres. Le chapitre I « State of the Art : Two-Photon Polymerization-Based 3D Micro & Nano Fabrication Using Femtosecond Laser » est consacré à l'étude bibliographique où le contexte général de cette recherche a été présenté. Ce chapitre expose les connaissances de base liées à cette

thèse telle que le principe du processus de l'absorption à deux photons, l'effet optique non linéaire, les caractéristiques de la résine photoréticulable utilisée dans la nanofabrication 3D par laser, la nanofabrication 3D basée sur la polymérisation à deux photons, la résolution de cette technologie de nanofabrication 3D, et quelques exemples d'applications réalisées à travers la nanofabrication 3D par l'absorption à deux photons. Il souligne également l'état actuel de la recherche sur la stéréolithographie basée sur la polymérisation à deux photons.

Le chapitre II de cette thèse « Material for Two-Photon Absorption & 3D Nanoprinting Optical Setup & Microfabrication Controller-Software » présente les matériaux et les méthodes expérimentales utilisées pour réaliser ce travail de nanofabrication 3D par laser. La première partie de ce chapitre détaille les propriétés optiques non linéaire du matériau photosensible (photorésine) employé pour fabriquer les micro/nanostructures avec une résolution au-delà de la limite de diffraction de la lumière. La deuxième partie décrit le système optique développé (microscope inversé) pour effectuer la micro/nanofabrication 3D. la dernière section de ce chapitre présente la conception assistée par ordinateur (CAO) qui comprend un ensemble de logiciels et de techniques de modélisation géométrique à l'aide d'un ordinateur et des techniques de simulation numérique pour produire les designs 3D des micro-nano-structures.

Le chapitre III « Systematic $\lambda/21$ Sub-wavelength Resolution by Two-Photon Absorption Induced Polymerization », suivant la suite chronologique du travail, rédigé sous forme de discussion des résultats expérimentaux, présente les facteurs influençant la taille et les dimensions des voxels (où la résolution de la nanofabrication 3D par laser), y compris l'intensité du laser, le temps d'exposition et la vitesse de nano-impression laser. Dans cette étude systématique, une nouvelle approche a été discutée pour améliorer la résolution du nanofabrication 3D; c'est-à-dire $\sim 36 \text{ nm}$ de résolution spatiale.

Le dernier chapitre de ce manuscrit « Voxels Optimization in 3D Laser Nanoprinting » porte sur une étude systématique de nanofabrication des voxels qui a été faite à travers la variation de la position du point-focal du laser, par rapport à l'interface entre le substrat du verre et la photorésine ; c'est-à-dire dans la direction longitudinale (direction z). Et, il a été démontré que les voxels peuvent être optimisés ainsi que leur disposition spatiale ; par exemple l'orientation, manipulée lorsque le point-focal du laser est déplacé dans la direction z. Cette étude a démontré clairement l'impact de la position z sur la précision de la nanofabrication laser des micro/nano-objets 3D.

Au final, nous avons fabriqué des micro/nano-objets 3D avec une résolution inférieure à la limite de diffraction de la lumière en utilisant notre montage optique de nanofabrication 3D par laser.

La conclusion générale synthétise les principaux apports de la thèse ainsi que quelques perspectives.

Mots-clés :

Laser femtoseconde, Effet optique nonlinéaire, Photorésine, Absorption à deux photons, Polymérisation à deux photons, Voxels, Résolution spatiale, Micro/nano-objets 3D.

Table of Contents

Acknowledgments.....	3
Abstract.....	5
Résumé.....	6
Résumé du Mémoire de Thèse.....	8
List of Abbreviations and Symbols.....	16
General Introduction	18
 CHAPTER I State of the Art: Two-Photon Polymerization-Based 3D Micro & Nano Fabrication Using Femtosecond Laser	
I.1. Introduction.....	22
I.2. Two-Photon Absorption (TPA)	23
I.2.1. Mechanism of TPA	23
I.2.2. Theory of Two-Photon Absorption Process.....	24
I.3. Two-Photon Polymerization (TPP)	26
I.3.1. Polymerization Reaction Mechanism.....	26
I.3.2. Polymerization Kinetics.....	27
I.3.3. Application of TPP in 3D Nanoprinting	30
I.3.4. Non-Linear Nature of TPA Polymerization	31
I.4. Stereolithography Using Two-Photon Polymerization.....	33
I.4.1. TPA Materials: Photoresist.....	33
I.4.2. Optical System For 3D Micro and Nanofabrication	35
I.4.3. Two-Photon Polymerization Threshold	36
I.4.4. Submicrometric Polymerized Voxel.....	38
I.4.5. The Diffraction Limit	41
I.4.6. Realization of Sub-Diffraction-Limit Features	43
I.5. Applications via TPA-based 3D Laser Nanoprinting.....	46
I.5.1. Functional Micro-Optical Devices.....	46

I.5.2. Multifunctional Electrical MicroDevices	49
I.5.3. 3D Printed Enzymatically Microswimmers: Micromachine.....	53
I.6. Conclusion	57
CHAPTER II Material for Two-Photon Absorption & 3D Nanoprinting Optical Setup & Microfabrication Controller-Software	
II.1. Introduction	60
II.2. Two-Photon Absorption Material (Photo-resist)	60
II.2.1. Introduction	60
II.2.2. Photopolymerizable Resin For 3D Nanoprinting	61
II.2.2.1. Methyl Methacrylate Monomer, MMA-M.....	63
II.2.2.2. Photoinitiator (PI)	66
II.2.2.3. Photosensitizer (PS).....	67
II.2.2.4. Cross-Linker: DPE-6A.....	68
II.2.2.5. Raman Spectroscopy: Analysis of TPA material.....	69
II.3. Experimental: TPP Optical Setup	71
II.3.1. Introduction	71
II.3.2. Femtosecond (Fs) Laser System	72
II.3.2.1. Fs Control Software: The Main Menu	74
II.3.2.2. Femtosecond (Fs) Laser Specification	77
II.3.2.3. Typical Tuning Curve	78
II.3.3. Tight Light Focusing: Focusing Lens	79
II.3.4. Nano-Positioning Translation System: Piezostage (PZT).....	81
II.4. 3D Micro- Nanofabrication Software: CAD model	83
II.4.1. Influence of TPP-Scanning Mode	83
II.4.2. Creation of 3D Microstructures Design Model.....	84
II.4.3. Generation of G-Code Data Using . <i>stl</i> File	86
II.5. Laser Beam and Intensity Control	87
II.6. 3D Nanoprinting by TPP	88
II.7. Conclusion.....	89

CHAPTER III Systematic $\lambda/21$ Sub-wavelength Resolution by Two-Photon Absorption Induced Polymerization

III.1. Introduction.....	92
III.2. Realization of Sub-Diffraction-Limit Features	92
III.2.1. Voxel Dimensions in 3D Nanoprinting.....	92
III.2.2. Laser Intensity Dependency on Resolution	94
III.2.2.1. Voxel Diameter Dependency: Lateral Resolution.....	94
III.2.2.2. Line-Width Dependency.....	98
III.2.2.3. Focal Spot Evolution (Duplication)	100
III.2.3. Exposure Time Dependency	102
III.2.3.1. Dependence of Voxel Diameter	102
III.2.3.2. Microline Diameter Dependency	104
III.2.3.3. Radical diffusion (Re): Voxel Growth.....	105
III.2.4. Focal Spots Related to TPE.....	107
III.3. Realization of $\lambda/21$ Sub-Wavelength Resolution	111
III.3.1. SDL Resolution in 3D Nanoprinting	111
III.3.2. Achievement of $\lambda/21$ Sub-Wavelength Resolution	113
III.4. Achievement of SDL 3D Microstructures	116
III.5. Conclusion	118

CHAPTER IV Voxels Optimization in 3D Laser Nanoprinting

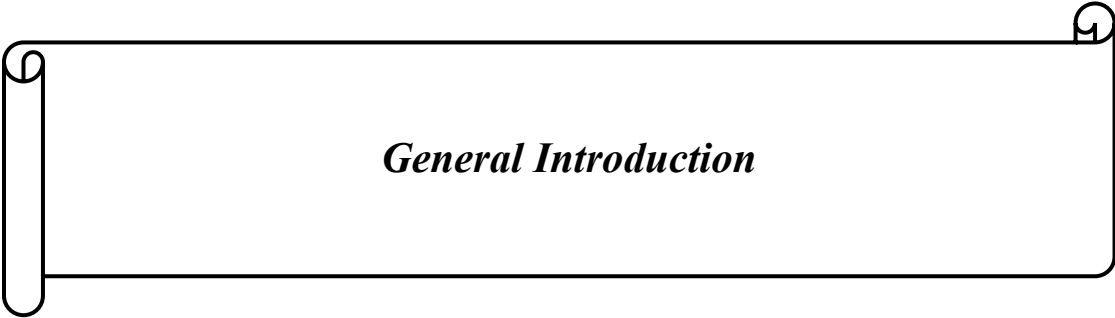
IV.1. Introduction.....	121
IV.2. TPA Recording Medium and Developed Optical Set-up	122
IV.3. Laser Nanofabrication of Voxels Using TPP.....	124
IV.3.1. Scaling Laws of Voxels in 3D Nanoprinting	124
IV.3.2. Achievement of SDL Resolution	126
IV.4. Analysis of Voxel Dimensions	128
IV.4.1. Experimental Results: Evolution of Δx and Δz	128
IV.4.2. Gaussian Profile of the SLI Distribution	129

IV.4.3. Theoretical Analysis.....	130
IV.4.3.1. Voxel Dimensions Dependency on Laser Dose	130
IV.4.3.1. Voxel Dimensions Dependency on z-Position	132
IV.5. Truncation Issue in TPP NanoPrinting	134
IV.6. Effect of z-Position on 3D Nanofabrication	135
IV.7. Spatial Arrangement of Voxel in 3D Nanofabrication	137
IV.8. Voxel Dimensions Dependence on Z-position of LFS.....	141
IV.8.1. Lateral Size Dependency	141
IV.8.2. Longitudinal Size Dependency.....	143
IV.9. Effect of TPA-Threshold and z-Position on 3D Printing	145
IV.10. Effect of Z-position on the Aspect Ratio (AR).....	147
IV.11. Linewidth Dependence Z-position of LFS	149
IV.12. Achievement of SDL Resolution of Voxels	150
IV.13. 3D Laser Nanoprinting at SDL Resolution	152
IV.14. Conclusion	153
General Conclusions.....	155
Areas of Future Research	156
References List.....	157
Scientific Production	166
1. Publications & Conference Proceedings.....	166
1.1. Peer-Reviewed Publications.....	166
1.2. Conference Proceedings	166
1.3. Upcoming Publications	166
2. Oral & Poster Presentation.....	166
3. Participation: Summer School - Laval University, Canada	167
4. Research Training - Osaka University, Japan.....	168
5. Awards.....	168

List of Abbreviations and Symbols

<i>2D</i>	Two-Dimensional
<i>3D</i>	Three-Dimensional
<i>Fs Laser</i>	Femtosecond Laser
<i>CAD</i>	Computer-Aided Design
<i>CCD</i>	Charge Coupled Device
<i>CW</i>	Continuous Wavelength
<i>SDL</i>	Sub-diffraction Limit
<i>MMA</i>	Methyl Methacrylate
<i>MW</i>	Molecular Weight
<i>PMMA</i>	Poly (methyl methacrylate)
<i>NA</i>	Numerical Aperture
<i>FWHM</i>	Full Width at Half Maximum
<i>STED</i>	Stimulated Emission Depletion
<i>OL</i>	Objective Lens
<i>PI</i>	Photoinitiator
<i>PS</i>	Photosensitizer
<i>DPE-6A</i>	Dipentaerythritol Penta-/Hexa-Acrylate
<i>UV</i>	Ultra-Violet
<i>NIR</i>	Near Infra-Red
<i>MPA</i>	Multi-Photon Absorption
<i>TPA</i>	Two-Photon Absorption
<i>TPP</i>	Two-Photon Polymerization
<i>NLO</i>	Non-Linear Optical
<i>SLI</i>	Squared Light Intensity
Δ_{xy}	Lateral size of voxel
Δ_z	Longitudinal size of voxel
<i>AR</i>	Aspect Ratio

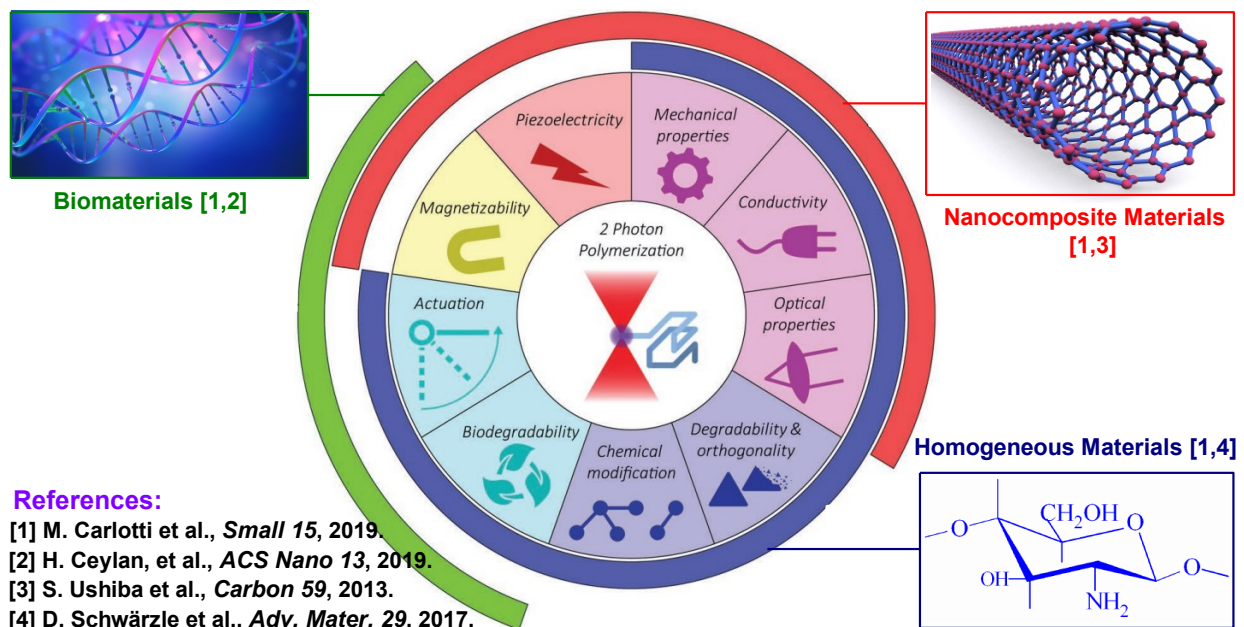
<i>I</i>	Intensity
<i>P</i>	Power
<i>T</i>	Exposure time
<i>SEM</i>	Scanning Electron Microscopy
<i>PZT</i>	PieZsoTage
λ	Laser wavelength
<i>FsLDW</i>	Femtosecond Laser Direct Writing
<i>LSF</i>	Laser Focal Spot
d_{xy}	Lateral Size of Microline



General Introduction

General Introduction

Three-dimensional (3D) lithography; universally considered to be the backbone of nano-technology, has been consistently undergoing several developments to produce functional microdevices with subdiffraction limit (SDL) resolution [1-3]. Research in this field has allowed the development of a set of techniques; e.g. four-wave mixing [4], generation harmonics [5], and multiphoton absorption (MPA) [6], that are based on the nonlinear optical (NLO) effect [3]. Among the MPA processes which interest us, one distinguishes in particular, the polymerization induced by two-photon absorption (TPA); meaning two-photon polymerization (TPP) [3]. TPP-based 3D nanoprining has attracted significant interest due to its advantages in creating advanced 3D microdevices from computer-aided design (CAD) patterns by adding and exposing transparent photopolymerizable resins point-by-point and layer-by-layer in 3D [7-11]. Shown in Fig.0 are the functional applications that can be achieved by the use of TPP-based 3D laser nanoprining.



Scheme. 0. Summary of the functionalities achievable in TPP-based 3D nanoprining by the use of different classes of material; e.g. biological (green), nanocomposites (red), and homogeneous materials (blue) [1].

TPP-based 3D nanoprining is the process by which one can create micro/nano-objects by tracing the laser's focal spot (LFS) of a femtosecond (Fs) laser beam in a liquid photoresin through an objective lens (OL) [11]. The work of this thesis falls within this background with the main objective of studying TPP lithography as nano-processing tool for printing 3D micro-sized structures/objects [12,13]. The development of TPP technology is driven by the need to increase the stability and performance of the printed components, and also to lower their cost [3]. New

technologies will certainly evolve to further develop 3D nanoprinting that will have new applications beyond information processing and storage [14] in areas such as optics [15], biomedicine [16], and materials science [17].

Many of the true advances in TPP nanoprinting have resulted from a more profound understanding of the interaction of matter with light. Light-matter interaction is of fundamental importance in nanotechnology, due to the possibility to manipulate matter by light and of light by matter [3]. Fs laser interaction with matter essentially differs from those with continuous lasers in its significant nonlinearity, which means that the excitation; *e.g.* two-photon excitation, is confined to a volume very close to the focus where the intensity is highest; giving rise to pinpoint 3D resolution [18,19].

The research presented in this thesis focuses on characterizing and improving the efficiency of 3D nanoprinting and its resolution. This thesis consists of four chapters. Chapter I introduces the background knowledge related to this thesis such as the principle of the TPA process, NLO effect related to TPP, TPA material (photoresin), TPP resolutions, and some examples of applications realized by the use of TPP. It also points out the current research status of TPP stereolithography.

In chapter II, we will detail the experimental apparatus and methods used in this work. We describe our TPP optical system, and we characterize its performances. Also, we detaily discuss the recording media; *i.e.* resin, used to 3D print structures [3]. In the 3rd section of this chapter, we will present the software used to create the CAD models, and G-code data of the printed 3D structures.

In chapter III, we report on the resolution of TPP printing using a systematic nanofabrication process which we developed. Here, we discuss the factors influencing the resolution; including the laser intensity, exposure time, and scanning speed by printing voxels; *i.e.* the smallest polymerized unit, and nano- lines, and nanofibers. Also, we introduce a novel approach to 3D printing to improve the resolution; *i.e.* $\sim 36\text{ nm}$, by combining high intensity and fast writing speed [12].

In the last chapter, we revisit and present a systematic study of voxels nanofabrication using TPP by varying the position of the LFS; *i.e.* in the longitudinal z-direction, with respect to the glass/resin interface. In this study, by controlling the z-position of focus, we demonstrate that the spatial arrangement; *i.e.* orientation, of voxels in 3D can be accurately changed and manipulated. Also, we investigate the effect of the laser dose and the z-position of focus on the width (Δ_{xy}), height (Δ_z), aspect ratio (AR) ($AR = \Delta_z/\Delta_{xy}$), and stability of the printed voxels [20].

***CHAPTER I:* State of the Art**

**Two-Photon Polymerization-Based 3D Micro & Nano-
Fabrication Using Femtosecond Laser**

1.1. Introduction

Recent years have witnessed an increasing trend in 3D laser nanoprinting induced by two-photon polymerization (TPP) [2,9] in diversified fields, such as nanophotonics [21,22], micro- and nano-optics [23,24], plasmonics [25], and biomedicine [26,16]. Moreover, with its intrinsic sub-diffraction limited (SDL) machining resolution [9] and its 3D laser-direct-writing (3D-LDW) capability [6,20], TPP stereolithography has been used to fabricate a wide assortment of advanced 3D microdevices; *e.g.* micromechanical systems [27], and photonic crystals [22], and movable micromachines [8,9], and micro-optical components [23,24]. TPP-based 3D nanoprinting started since 1997; when Maruo et al. [10] fabricated a 3D microsized spiral with a diameter of $\sim 7 \mu\text{m}$ and $\sim 50 \mu\text{m}$ long spiral-coil with a line cross-section of $\sim 1.3\text{-}2.2 \mu\text{m}$. Then in 2001 [9], a 3D microbull with near-diffraction-limit features of $\sim 120 \text{nm}$; *i.e.* $\lambda/6.5$ resolution, was fabricated. After that, Kawata's group developed the technology of TPP nanoprinting, as reported in a series of works [11,28,29].

3D nanoprinting induced by TPP is performed by scanning a tightly focused femtosecond (Fs) laser beam into a transparent photopolymerizable resin through a high numerical aperture (NA) objective lens (OL) [20]. TPP reaction is induced by the two-photon absorption (TPA) process. TPP; *i.e.* an irreversible photochemical reaction, occurs only in a tiny nanometric volume; *i.e.* voxel $\sim \lambda^3$; around the laser's focal spot (LSF), because of the quadratic dependence of TPA probability on the photon fluence density; *i.e.* the squared light intensity (SLI); this meaning the nonlinear optical (NLO) effect of TPA process. The SLI distribution related to TPA reduces the volume of light-matter interaction; thus, improving the resolution of TPP printing. Generally, the printed voxel via one-shot of exposure is considered as a feature key to determine the TPP resolution [9,30].

In this chapter which is considered as a literature review, we introduce the background knowledge related to this dissertation; *e.g.* the principle of TPA induced TPP, fundamental of NLO effect, analysis of voxel dimensions, TPP resolutions, TPP-nanoprinting of sub-micrometric features, etc. It also points out the current research status of 3D nanoprinting. Finally, we will discuss how the optical methods based on the nonlinear absorption; meaning TPP lithography, are implemented for the fabrication of functional microdevices and micromachines; *i.e.* functional applications realized for different fields through the TPP technology.

I.2. Two-Photon Absorption (TPA)

I.2.1. Mechanism of TPA

Multiphoton absorption (MPA); e.g. TPA process, was predicted as early as 1931 [31], and it was experimentally observed immediately after the invention of lasers [32]. Experimentally, TPA is considered as a nonlinear phenomenon, and it can be conceptualized as follows: photosensitive molecules exposed to high light intensity can undergo near-simultaneous TPA mediated by a virtual state. Thus, the combined energy of two photons accesses an excited state of the molecule, as shown in Fig.I.1(a). TPA involves the interaction of both photons that combine their energies to produce an electronic excitation analogous to that conventionally caused by a single photon of a correspondingly shorter laser wavelength (Fig.I.1(a)) [3].

When the energy of each photon is the same, the process is said to be a degenerate state; otherwise, it is called a non-degenerate state [33]. Most of the applications use the degenerate state of the TPA-process; because of its simplicity of the experimental setup; e.g. TPA-based 3D nanoprinting [3,9]. Shown in Fig.I.1(b) is the excitations of a photoactive material; e.g. photoinitiator (PI) system, achieved by the use of one-photon absorption (OPA) (bottom) and TPA (top) [34].

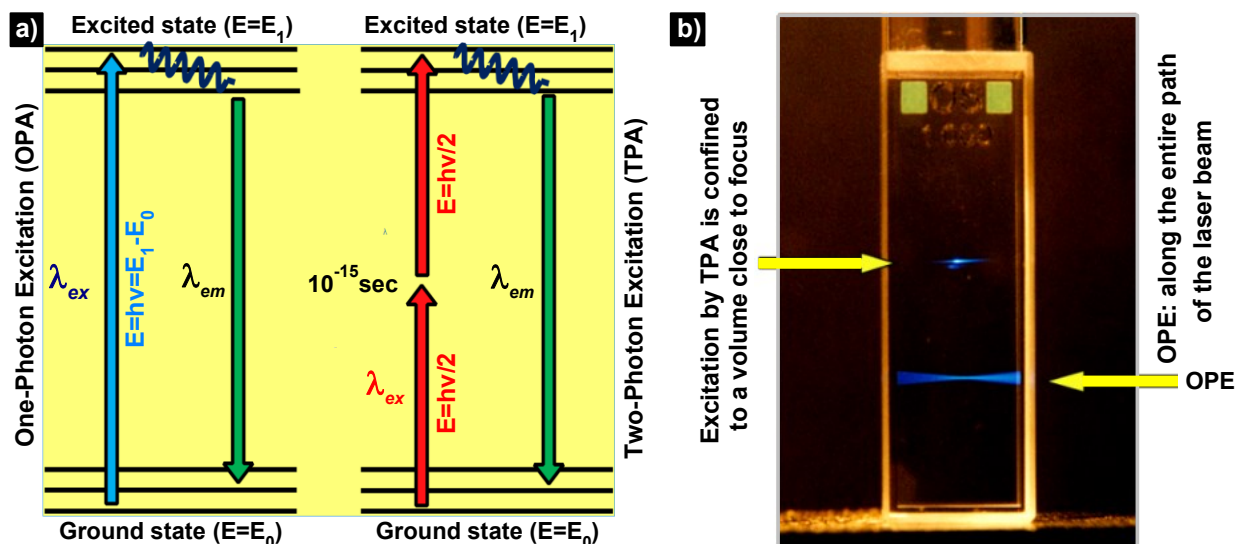


Figure I.1. Mechanism of TPA and OPA when simultaneous excitation occurs. (a) Schematic presentation of the excitation of a photoactive molecule from the ground to excited state by OPA (left) and TPA (right). (b) Comparison of excitation profiles of two-photon (top) and one-photon (bottom) absorption. TPA was realized by the use of an infrared (IR) *Fs* laser (1 femtosecond = 10^{-15} s). The blue light visible in the photograph is the fluorescence emitted by the photosensitive molecules after excitation [34].

Fig.I.1(a) shows a simple Jablonski diagram of the OPA and TPA process. In the OPA process, single-photon of an energy $h\nu_1$ mediates the optical transition from the ground state S_0 into an

electronically excited state S_1 . In the TPA process, two photons with an energy $h\nu_2$ are simultaneously absorbed by the molecule in a very short time; *i.e.* in a range of ~ 1 fs, thus, the molecule gets excited to the electronically excited state S_1 . Each individual-photon doesn't carry enough energy corresponding to the S_1 state, but their combination does carry enough energy to excite; *i.e.* λ_{ex} , the molecule to the S_1 state. This is followed by a non-radiative relaxation and consequently by spontaneous emission; *i.e.* fluorescence λ_{em} [3,34].

Recently, the TPA process was considered as a very useful tool in the field of micro- and spectroscopy; since the selection rule for two-photon excitation (TPE) is different from that of OPA excitation. Unlike OPA, whose the probability is linearly proportional to the intensity of the irradiation light; TPA depends on both a spatial and temporal overlap of the incident photons and takes on a quadratic dependence on the irradiation intensity; *i.e.* NLO effect, resulting in highly localized excitation; *i.e.* TPE, at the LFS (Fig.I.1(b)) [35]. In the early 1990s, some potential applications with this technique were demonstrated, such as two-photon fluorescence (TPF) 3D data storage [36], and TPF microscopy [37].

TPA process has at least two advantages compared to OPA used in conventional rapid prototyping. First, common pre-polymers have negligible linear absorption in the near IR region; so, the LFS can deeply penetrate into the transparent resin and directly induces TPE in the inside without contaminating outside of the LFS (Fig.I.1(b)). Secondly, the quadratic dependence of polymerization rate on the irradiation laser-intensity provides the ability to confine photo-chemical and physical events around the LFS; thus, a near-diffraction-limit resolution can be achieved [3,6,30].

I.2.2. Theory of Two-Photon Absorption Process

A photopolymer that can be used as a TPA material; *e.g.* photoresin, should be carefully selected considering their TPA cross-section in order to get efficient and stable 3D nanoprinting [18]. Recently, much effort and money are being poured into manufacturing and preparing a noble PI system with a high TPA-cross-section [3]. Evidence of the occurrence of NLO absorption; *i.e.* TPA, can be obtained when using an ultrashort laser as a light source. Fig.I.2(a-b) illustrates the advantage of using a NIR light for achieving TPE, meaning that the incident light can be only absorbed in the vicinity of the LFS; *i.e.* 3D nanoprinting of voxels, as shown in Fig.I.2(b) [6]. Oppositely in OPA process, when the resin was irradiated by the use of a continuous wavelength

(CW) laser; *e.g.* around $\sim 400\text{ nm}$, the polymerization was occurred from the top side where the irradiation started (Fig.I.2(b)); *i.e.* linear absorption [33].

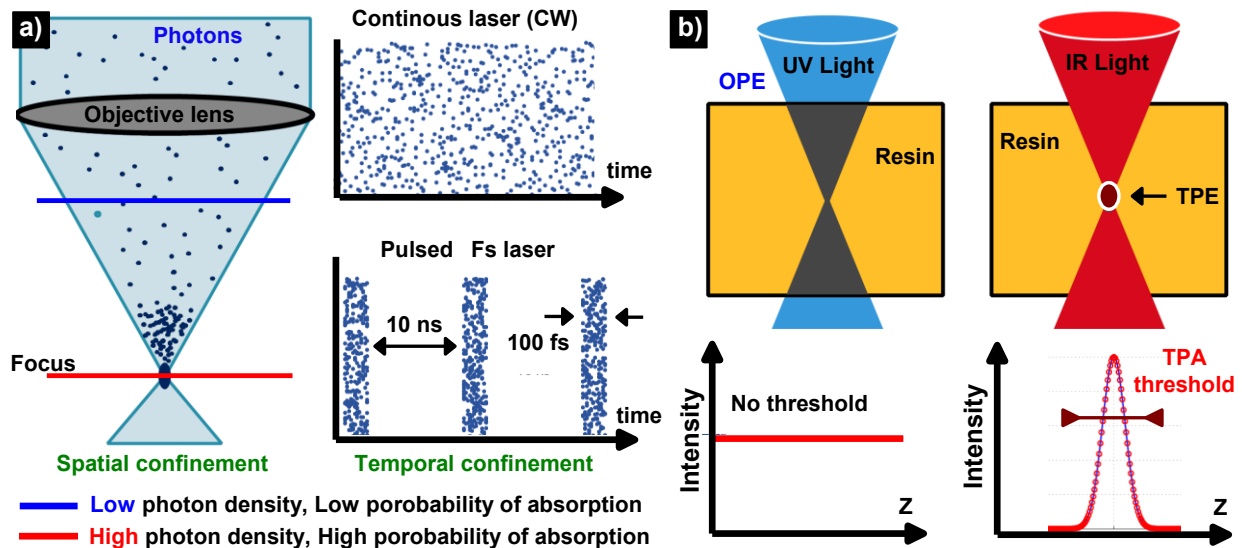


Figure I.2. Theory of TPA process. (a) Presentation of the two methods for increasing the absorption probability; (left) density of photons is increased by spatial compression using high NA-OL, (right) temporal confinement using ultrafast Fs and CW laser. (b) Photons with sufficient energy are linearly absorbed throughout the beam path (left), and photons with insufficient energy are only absorbed in the focal point through the NLO effect (right) [13,34].

Linear absorption is governed by photon flux; *i.e.* ($\text{Photon}/\text{s}\cdot\text{cm}^2$), which is proportional to the incident intensity of irradiation (Watt/cm^2). The adequate energy dose needed to trigger the absorption; *i.e.* TPA process, is reachable either by a feeble intensity of irradiation for a long time or intense irradiation for a short time; *e.g.* Fs laser, (Fig.I.2(a)) [3,34]. To date, there is no experimental report on photopolymerization observed when IR laser works in CW mode; where the output power is uniformly delivered over time. Oppositely, polymerization occurs with the same irradiation dose under a pulsed mode (Fs laser). By the use of a Fs laser operated at 82 MHz repetition rate, 100 fs pulse width, and 1 mW as the power of exposure, a diffraction-limited LFS has a photon flux density of $\sim 10^{29}\text{ Photons}/\text{s}\cdot\text{cm}^2$ in the pulse duration, which is 1.2×10^5 times larger than when the incident laser is operating in CW mode; this expected phenomenon is explained by the reason that the polymerization; *e.g.* TPP, is induced by the nonlinear effect [3].

The efficiency of the TPA transition depends on the PI cross-section and photon energy [15,18]. It's an effective area provided by the PI system for the interaction of the incoming photon in order to achieve TPE; this quantity is measured in GM units, where $1\text{GM} = 10^{-50}\text{cm}^4\text{ s}/\text{photon}$ [11,30]. The molecular TPA cross-section is usually quoted in the units of Goeppert-Mayer (GM).

Hence, large photon flux is required to achieve efficient TPP. The laser-dose used to induce the TPP reaction is fairly reduced for a large PI cross-section. Consequently, it's thought possible to use a low-cost microlaser for realizing TPP by using photosensitive media with a larger TPP cross-section [38].

The measured cross-section (σ) of a TPA material; *i.e.* involved in the preparation of the resin, is proportionally related to the intensity of irradiation (I), and is expressed as follows [39-41].

$$\sigma = \sigma^{(2)}I \quad (I.1)$$

Where $\sigma^{(2)}$ symbolizes the coefficient, which describes the strength of the TPA process; consequently, the atomic transition rate (R) for the TPA scaling was defined as follow:

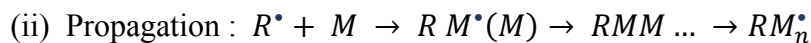
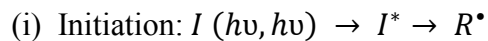
$$A = \frac{\sigma I}{\hbar \omega} = \frac{\sigma^{(2)} I^2}{\hbar \omega} \quad (I.2)$$

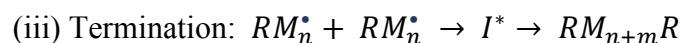
Where \hbar , and ω are the reduced Planck constant, and the photon angular frequency; respectively. Thus, TPA is proportional to SLI distribution at the focal region; this is due to the NLO effect of the TPA process (Eq.I.2). The main interest of TPA compared to OPA is that the excitation is localized within the LFS; *i.e.* $\sim \lambda^3$ [41].

I.3. Two-Photon Polymerization (TPP)

I.3.1. Polymerization Reaction Mechanism

Photopolymerization is an important area of investigation due to its wide industrial micro-applications and enormous potential in the simple and fast manufacture of polymeric devices with special properties; *e.g.* spatial resolution, 3D design, and stability [6,40]. Polymerization (or-Crosslinking) is a photoreaction that converts a liquid or gel monomer into a solid polymer. This reaction requires the use of a photosensitive molecule; *e.g.* PI and photosensitizer (PS) systems, that produces an active species upon light irradiation. The coming photons from light irradiation excite the PI; thus, creating free radicals that initiate the polymerization; that arises as a reaction chain by successive accumulation of monomers; *e.g.* MMA, to an active center. Generally, the polymerization chain consists of three steps: (i) initiation, (ii) propagation, and (iii) termination, as processed as follows [13,40].





The symbol $(h\nu, h\nu)$ denotes the simultaneous TPA; here $I, I^*, M,$ and R^{\bullet} denote a PI system, an intermediate state of PI after excitation, a monomer, and a radical; respectively. The first reaction of polymerization is the initiation during which the free PI-radical is decomposed with light; *i.e.* UV or IR light, in order to induce an active specie; *e.g.* active radical (R^{\bullet}). In the next reaction, known as propagation, R^{\bullet} reacts with monomer molecules to form the first active body that is capable of being polymerized. Monomers continue to add in the same manner resulting in the formation of macroradicals that are end-active polymers. The last reaction is the termination, during which the growth center is deactivated and the final polymer molecules are formed; *e.g.* solid-state of the resin. Photopolymerization of multifunctional (meth)acrylates monomers is a very effective process for the generation of highly cross-linked polymers chain [3,12].

I.3.2. Polymerization Kinetics

Photopolymerization reactions involve a polymerizable radical and more; or less, complex photoinitiating system [10,42]. The photoinduced radical polymerization occurs according to the typical radical mechanism and involves initiation, propagation (including chain transfer), and termination, where the transfer and termination steps can occur by several mechanisms. The radical mechanisms limit the range of applicable monomers to those with olefinic double bonds; *i.e.* acrylates and methacrylates group. Shown in Fig.I.3 are the chemical structures of acrylates in (Fig.I.3(a)) and methacrylates monomer in (Fig.I.3(b)) [42,43].

L. J. Jiang's group [44] investigated the degree of conversion (DC) of the acrylic-based resin in TPP nanoprinting through the raman spectroscopy. A comprehensive representation of how the TPP manufacturing parameters; *e.g.* laser powers and scanning speeds, affect the evolution of DC is demonstrated in Fig.I.3(c). In acrylic-based resins, the DC is considered as a measure to quantify the amount of the consumed carbon-carbon double bonds ($C=C$) during the TPP process. At a constant writing speed, the DC values monotonically increase with the increase of the irradiation power. At $20 \mu m/s$ as writing speed, a nonlinear increase in DC from 26% to 42% is observed with the increase of power (Fig.I.3(c)). Based on the TPA model, it was demonstrated that the expected DC would be proportional to the reciprocal of the writing speed and square of the average power. Thus, the measured DC of the resin shows more dependence on laser power than scanning speed.

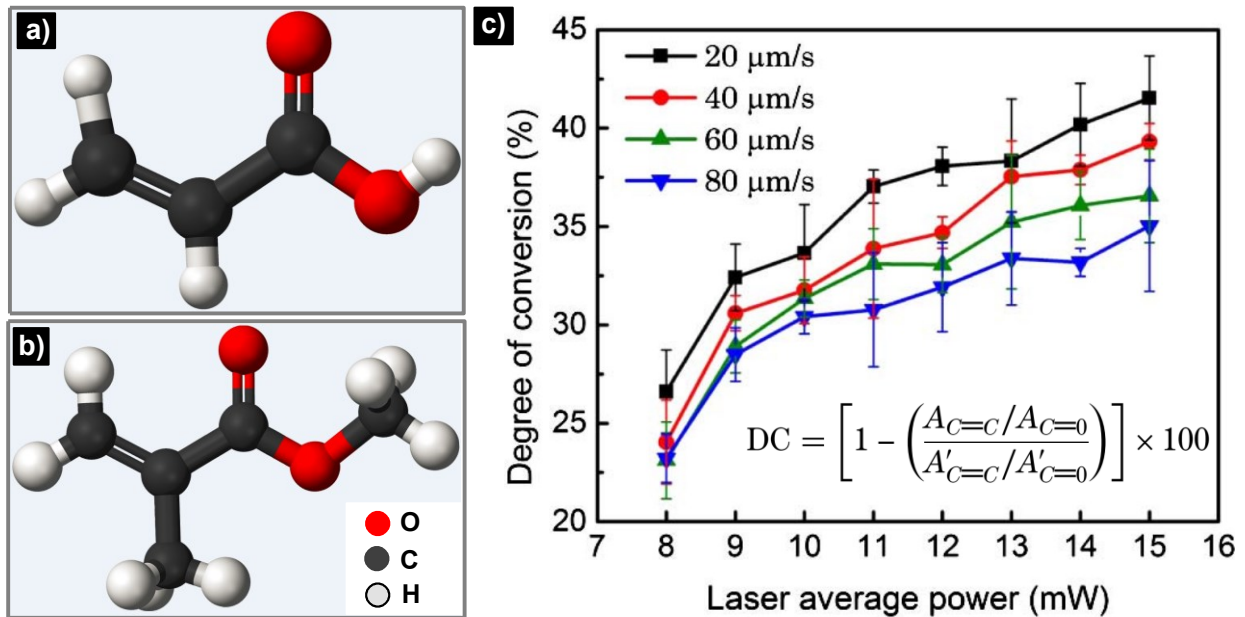
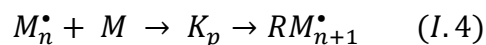


Figure 1.3. Polymerization Kinetics. Schematic presentation of the half-developed chemical structures of the (a) acrylate and (b) methacrylate functionality. (c) DC of the acrylate resin polymerized as a function of different powers and scanning speeds; $A_{C=C}$, $A_{C=O}$, $A'_{C=C}$ and $A'_{C=O}$ denote the integrated peak intensities of raman spectroscopy related to C=C and C=O bonds in the polymerized and the unpolymerized resin, respectively [44].

Owing to their optical-absorption properties, monomers; *e.g.* acrylate groups, are usually not sensitive to available lights; *e.g.* UV or IR. By exception, a few cases involving specifically designed light-absorbing structures. The addition of a PI (~1%wt) is at least necessary to achieve an efficient polymerization of monomers; *e.g.* TPP reaction. The amount of local cross-linking of the resin depends on the accumulated absorbed laser-dose [45]. Through the initiation-step of polymerization, primary radicals ($In^{\bullet} = PI^{\bullet}$) are formed with a rate constant K_d and the concentration of PI depends on the efficiency of the formation of In^{\bullet} (reaction (3.a)). In the next step of initiation, they add to monomer with a rate coefficient K_i (reaction (3.b)). The rate of the addition of primary radicals to monomers; *i.e.* K_i , is usually very higher than K_d ; *i.e.* excitation of In^{\bullet} [46]. Thus, radical formation is the rate-determining step for the initiation ($2h\nu$).



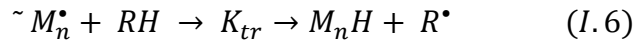
The propagation-step mechanism consists of successive additions of monomer to an active radical center M_1^{\bullet} . Reaction (4) shows the addition of monomer to M_1^{\bullet} .



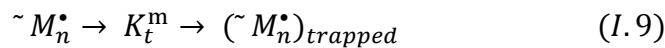
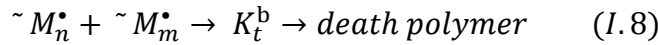
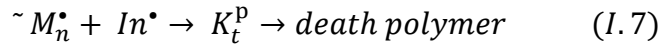
The rate of this reaction is expressed by the following Eq., where $[M]$ and $[P^\bullet]$ symbolize monomer and total reactive radical concentration, respectively [46].

$$R_p = K_p [M] [P^\bullet] \quad (I.5)$$

The photo- propagation reaction is accompanied by a side reaction; *i.e.* chain transfer, which can occur to a small chain transfer agent; *i.e.* monomer, initiator, or to polymer molecule. If the radical R^\bullet is reactive, this reaction leads to branching in the case of transfer to the polymer or a decrease of their molecular weight.



In the duration of the termination step, the growth of the polymer chain is stopped, which means that the radical centers are destroyed or eliminated from further reaction; *e.g.* as expressed by the reactions (7), (8) and (9);



The termination reaction can be occurred by a bimolecular reaction (reaction (7)) of macroradicals with primary radicals. This reaction becomes important at too high PI radical production; *i.e.* at high concentration of PI molecules and intensity of irradiation. Also, it's occurred by a bimolecular reaction between two macroradicals (reaction (8)). The last reaction, generally named bimolecular termination, is the dominant termination process in polymerization in the absence of added transfer agents. The termination reaction rate R_t^b is described by the second-order Eq., which is described as following [46]:

$$R_t^b = -\frac{dP^\bullet}{dt} = 2 K_t^b [P^\bullet]^2 \quad (I.10)$$

The monomolecular termination rate coefficient K_t^b represents a fraction of radicals immobilized in the polymer network per unit of time [47]. The overall reaction rate of the loss of reactive radicals is the sum of K_t^b and K_t^m . The general expression for the polymerization rate derived under assumptions of the steady-state and exclusively bimolecular termination, as shown in the following Eq. [46]:

$$R_p = K_p [M] \left(\frac{R_i}{2 K_t^b} \right)^{0.5} \quad (I. 11)$$

Where, R_i symbolizes the initiation rate.

For a long time, the polymerization kinetics of free radicals has been studied in detail; see *e.g.* the refs. [47-48]. The kinetics of polymerization can be treated by a simplified analytical method based on the steady-state approximation which equates the initiation and termination rates.

I.3.3. Application of TPP in 3D Nanoprinting

3D nanoprinting based on TPP is performed by scanning a tightly focused Fs-laser beam through a high NA OL; *i.e.* LFS, into a transparent photopolymerizable resin from the bottom to top surface in-order-to fabricate entire 3D micro-nano-objects [6,13]. In parallel, by using a computer-aided design (CAD) which generated 3D models of structures, any kind of 3D design can be produced via the TPP process (Fig.I.4(a-d)). After TPP nanoprinting, the non-irradiated liquid resin; *i.e.* unscanned area, can be washed out by the use of an organic solvent; *e.g.* ethanol, in the so-called rinsing step (Fig.I.4(e)) [45]. Shown in Fig.I.4(e) is the experimental procedure used for 3D laser nanoprinting which provides rapid and simple 3D nanofabrication procedures and proves much better structural quality and resolution; *e.g.* less than $\sim 100 \text{ nm}$ [27,28].

Fig.I.4(b) and Fig.I.4(d) show the scanning electron micrographs (SEM) of the 3D microsized bulls sculpture fabricated by the use of the two-photon process. This $10 \mu\text{m}$ -long, $7 \mu\text{m}$ -high 3D bulls are considered as the smallest model animals ever made artificially (Fig.I.4(d)), and are about the size of a red human blood-cell. The 3D printed bulls shown by the SEM images in Fig.I.4 consist of rough and smooth curvatures and sharp horns; *i.e.* with near-diffraction-limit features of $\sim 120 \text{ nm}$ [9]. From refs. [1,6], the spatial resolution which can be achieved via the TPP-fabrication is almost $\sim 100 \text{ nm}$; here, the diffraction limit is exceeded by the nonlinear nature of the TPA process. Thanks to TPP nanoprinting, the tiny volume attainable for such printed micromachines would allow them to be transported to locations inside the human body through even the smallest blood vessels; *e.g.* movable micromachines to deliver clinical treatments (drug delivery). Shown in Fig.I.4(a-d) are the two scanning modes used to fabricate the 3D microsized bull; for more detail, refer to refs. [40].

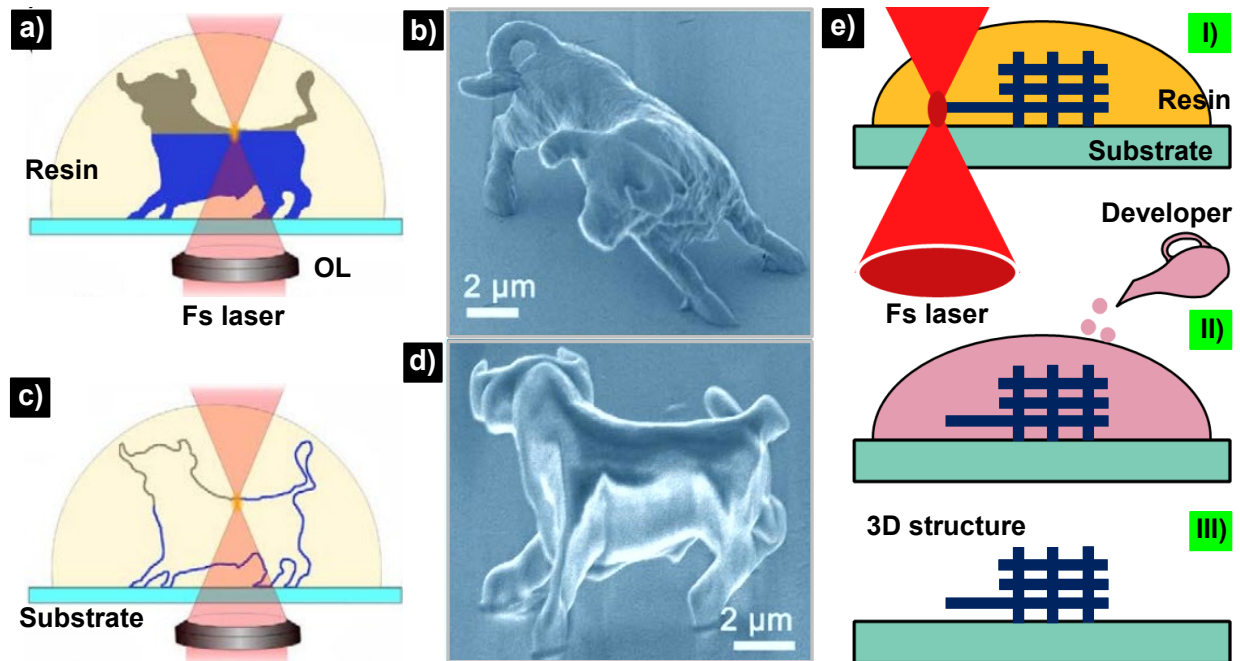


Figure I.4. Micro- and nanofabrication at SDL resolution. TPP fabrication of a microbull sculpture produced by (a) raster scanning and by (c) surface profile scanning mode. For the latter, only the bull crust was printed by TPP, the inside liquid was polymerized by illumination under a UV light. In this particular structure, TPP scanning time was reduced by 90% due to the scan only contour; this nanofabrication took 13 min. (b) SEM image of the fabricated 3D bull showed in (a); the process took 180 min. (d) SEM image of the 3D bull illustrated in (c). (e) Experimental set-up of 3D nanoprinting [9].

Compared with other manufacturing techniques, TPP nanoprinting has unique merits [13,38]; (i) it has intrinsic nanomachining ability to 3D print structures. Additionally, the long-wavelength of irradiation chosen for TPP-printing has less absorption; *i.e.* almost $\sim 0\%$, and less scattering, which gives rise to the deep penetration of the LFS inside the transparent resin. (ii) The TPP optical setup resembles a laser scanning inverted microscope, which doesn't need vacuum conditions during the processing. (iii) No mask, mold, or stamp was needed for TPP nanostructuring. In the work realized by Kawata's group [9,40]; *i.e.* corresponds to Fig.I.4(a-d), a 780 nm Ti: sapphire Fs laser operating in mode-locked at 76 MHz as repetition rate, and 150 fs pulse width, was used as a light source and it was deeply focused through an OL of $NA \sim 1.4$. Nonlinear absorption has occurred in the focal voxel which is considered much smaller than $\sim \lambda^3$; a feature that is considered as a key to high TPP resolution, *e.g.* $\lambda/6.5$ nm.

I.3.4. Non-Linear Nature of TPA Polymerization

The virtue of TPP-based FsLDW as a nanoprocessing tool for making functional microdevices lies to its 3D fabrication capability and SDL machining resolution. Here, we show that the diffraction limit can be exceeded; *e.g.* SDL resolution, by the use of NLO effect-based TPP nanoprinting

[1,20]. For a linear exposure, the photosensitive media (photo-resin) responds to light excitation to the first-order effect (1st); while for the TPA process, the response is restricted to high orders (3rd effect). The quadratic intensity dependence of TPA leads to higher flexibility compared to the OPA process [38-40].

Generally, the degenerate TPA, where the two photons are simultaneously absorbed with the same energy is employed for the process of 3D nanoprinting. TPA is an NLO property related to the imaginary part of the 3rd order susceptibility in the photoactive material polarization. Thus, under an applied electric field E , the polarization of the material is described by the following Eq. [39]:

$$P = P_0 + \chi^{(1)}E + \chi^{(2)}EE + \chi^{(3)}EEE + \dots; \quad (I.12)$$

Where, $\chi^{(i)}$ symbolizes the susceptibility of the i th tensor, $\chi^{(2)}$ and $\chi^{(3)}$ are the 2nd order and 3rd order susceptibilities, respectively. The 3rd order susceptibility, $\chi^{(3)}$, is the sum of the NLO refraction, χ_{real}^3 , and the nonlinear absorption, χ_{imag}^3 . The imaginary part of the 3rd order susceptibility is related to the TPA of the materials. For the centrosymmetric molecule systems absorbing two photons with the same frequency, the even tensors, $\chi^{(2)}$, $\chi^{(4)}$, etc. do not contribute to the resonant process. The TPA rate of energy is proportional to SLI, i.e. I^2 , which can be expressed as follows [42]:

$$\frac{dW}{dt} = \frac{8\pi^2\omega}{n^2c^2} I^2 I_m(\chi^{(3)}); \quad (I.13)$$

Where ω symbolizes the optical frequency of the incident light, I is the used laser intensity, c is the speed of light in vacuum, n is the medium refractive index, and $I_m(\chi^{(3)})$ is the imaginary part of the 3rd order susceptibility.

The measure of TPA effectiveness of material; i.e. TPA cross-section (σ_2) is governed by:

$$\frac{dn_{photon}}{dt} = \sigma_2 NF^2; \quad (I.14)$$

Where, $dn_{photon}/dt = \sigma_2 NF^2$ denotes the number of the coming photons absorbed per unit of time, N is the density of the absorbing TPA molecules, and F is the flux of the incident laser-beam; F can be written as a function of the intensity as follow; $F = h\nu$. From: $dn_{photon}/dt = dw/dt$, and Eq. (I.14), The TPA cross-section σ_2' (cm^2/GW) can be expressed as follow:

$$\sigma_2 = \frac{8\pi^2 h\nu^2}{n^2 c^2} I_m (\chi^{(3)}); \quad (I.15)$$

Following the measure of the effectiveness of the used TPA material in 3D nanoprinting, the molecular TPA coefficient; *i.e.* β (cm/GW), and TPA cross-section σ_2 can be expressed as follows:

$$\beta = \sigma'_2 N_0 = \sigma_2 N_A d_0 \times 10^{-3}; \quad (I.16)$$

Where, N_0 is the molecule density (cm^3) of the photosensitive media, N_A denotes the Avogadro number, and d_0 symbolizes the concentration in a mole (mol). Also, for σ_2 value, it can be expressed as follow: σ_2 (*Goppert-Meyer, GM* = $10^{-50} cm^4/$ photon.molecule); this expression is obtained by multiplying the energy of the coming photon $h\nu$ to σ'_2 . This is the wide method used as a scale to compare the TPA activity of a photoresin. Currently, several techniques can be used to measure σ_2 ; *e.g.* TPF emission [39]. For more detail, refer to ref. [49]. Both the optical nonlinearity and threshold peculiarity contribute to the resolution of 3D laser nanoprinting. However, due to the existence of the quencher effect; *e.g.* the dissolved oxygen in the resin; TPP can be only induced around the LFS, and thus a threshold effect is formed. This shows that the TPP resolution is influenced by the NLO effect of the TPA process [39,49,50].

I.4. Stereolithography Using Two-Photon Polymerization

As discussed in the previous axes, 3D nanoprinting (by the use of TPP) provides an effective technology for manufacturing complex 3D microdevices that cannot be achieved with other fabrication processes [45]. The two most important components used to perform TPP-based 3D nanoprinting are an ultrashort; *i.e.* Fs, laser, and a photosensitive resin. The nanoprinted structures are produced by the use of a 3D scan of the laser-focus inside the photoresin following the trajectory of a predefined CAD pattern; *e.g.* pre-programmed 3D design [6,20].

I.4.1. TPA Materials: Photoresist

Usually, TPP-based 3D nanofabrication is performed in a viscous pre-polymer resin which is dropped on a cover glass. Thus, the most common materials involved in the preparation of the resin are; a PI that is used for the generation of radicals after the TPE, and a monomer or oligomer; *e.g.* acrylate monomer, that acts as the main skeleton of the nanoprinted structures [13,27].

Some special resins contained other compounds for adding different functionality and performance to the polymerized structures; for example, the crosslinkers that ensure the stability of the

nanoprinted structures. Also, an additional requirement for effective initiation of TPP is the PS that is capable of absorbing light and transferring its excitation energy to the PI system [2,12]. The efficient initiation of TPP in the acrylate resin under TPE demonstrates that it has a significant TPA cross-section at $\sim 800\text{ nm}$ wavelength of excitation. Shown in Fig.I.5(a) is the absorption spectrum of our prepared acrylate resin used in the work described in this thesis [20]. Furthermore, a wide variety of acrylate monomers is available for TPP nanoprinting; making it possible to tailor the chemical and physical properties of resins to its intended applications (Fig.I.5(b)) [12].

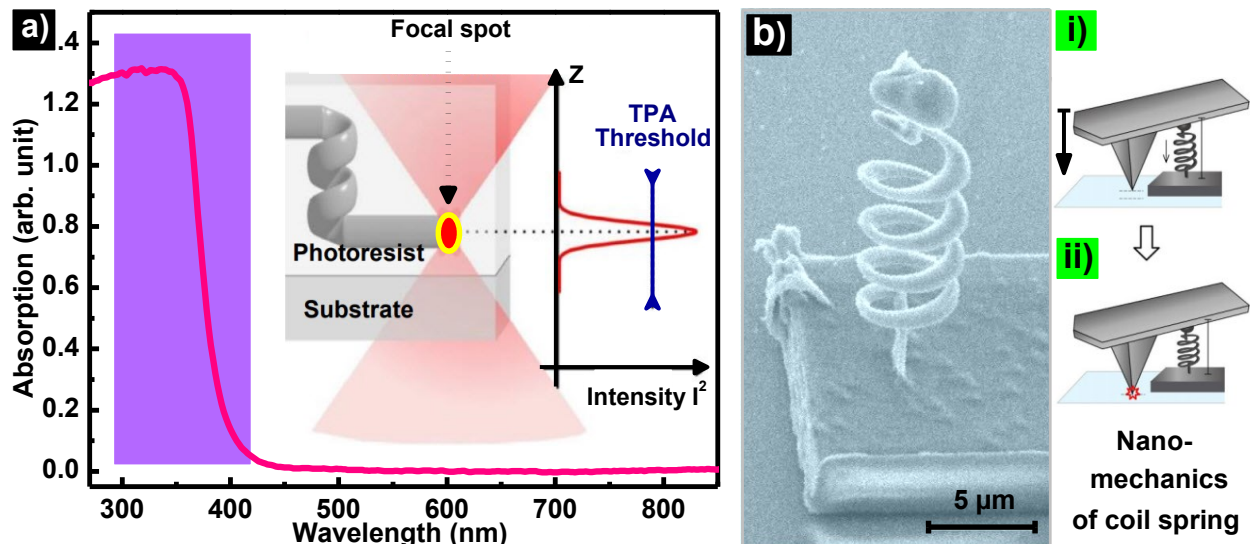


Figure I.5. (a) Absorption spectrum of MMA-based resin; the presentation of the TPP principle is shown as an inset; TPP occurred only around the focal spot (voxel). (b) SEM image of a vertically free-standing polymer nanocoil spring fabricated on this resin; (i-ii) procedure showing a compression test using AFM (as an application via TPP technique) [27]. AFM symbolizes atomic force microscopy.

As shown in Fig.I.5(a), this resin presents a strong optical absorption in the UV range; this is due to π - π bond of PI-benzil. Oppositely, no absorption can be observed in the near IR region; e.g. at 780 nm , this suggests that the simultaneous TPA initiates polymerization at the focal region, as shown by the schematic presentation in the inset of Fig.I.5(a) [12]. Fig.I.5(b) shows a functional microdevice (as an application) printed by the use of TPP lithography. As shown in Fig.I.5(b), the coil spring shaped polymer nanowire was printed on the acrylate resin. In this work, S. Ushiba's group [27] investigated the mechanics of the cross-linked PMMA nanowires formed into coil springs; here, PMMA means polymethyl methacrylate.

In 3D nanoprinting induced by TPP, the used wavelength of irradiation is localized in the IR region; e.g. 780 nm ; a range of which most of the photopolymerizable resins are transparent [40]. When

the PI absorbs suitable photon energy; *e.g.* TPE, it is transformed into a reactive initiating species like free radicals or cation radicals. Cationic PIs are photoacid generators that yield cations upon light excitation. Cationic PIs are used for the polymerization of epoxides or vinyl ethers via a cationic mechanism of photopolymerization [3]. The photolysis of cationic initiator has been shown to result in the generation of free radicals allowing the combination of monomer molecules to be polymerized; *e.g.* chain-end of polymerization. The most commonly used free-radical PI is benzophenone and its derivatives [51]; *e.g.* we use benzil as a PI system in our resin mixture. It is beyond the scope of this axis to present an exhaustive review of the TPA materials (resin), a recent comprehensive summary of this topic can be found elsewhere (chapter II).

I.4.2. Optical System For 3D Micro and Nanofabrication

Recently, the exploration of novel optical technologies to satisfy the increasing demand for the functional microdevices constitutes an important driving force for the progress of TPP-based 3D nanoprinting. Significant progress for the technology of 3D nanoprinting has been achieved with the efforts made by experts all over the world in recent years [7,52-54]. The optical systems that are used for 3D nanoprinting vary according to different applications, but the basic components are shared in common (Fig.I.6).

The optical system used to perform TPP-based 3D nanoprinting functionally consists of three parts; fulfilling functions of (i) Fs laser source output and beam control, (ii) two-photon focusing (OL), and *in-situ* monitoring, and (iii) computer graphic generation; *i.e.* CAD, and scanning control [3,6]. First, (i) the laser beam comes from a Fs laser system, where the peak intensity is high enough; in terms of power, to promote the TPP reaction. Then, the laser beam was expanded through a beam expander in-order-to reduce the divergence angle. For the focusing system, (ii) the laser beam was tightly focused within the sample through an OL of high NA; *i.e.* ~1.4. The focusing of light is of primary importance to perform the TPA polymerization, and also to get a nanomachining fabrication capability; *i.e.* with near-diffraction-limit resolution. This is an expression related to the maximum angle that the coming light rays are collected from the object plane; *i.e.* for imaging, or the maximum angle that a laser beam is converged onto the focal region; *i.e.* for focusing [20,40]. At the focal region, the size of volume where TPE was triggered depends on $1/(NA)^4$ [55,56]. Therefore, choosing a large NA focusing-optic is essential for obtaining a high accuracy of TPP printing; *e.g.* ~100 nm resolution.

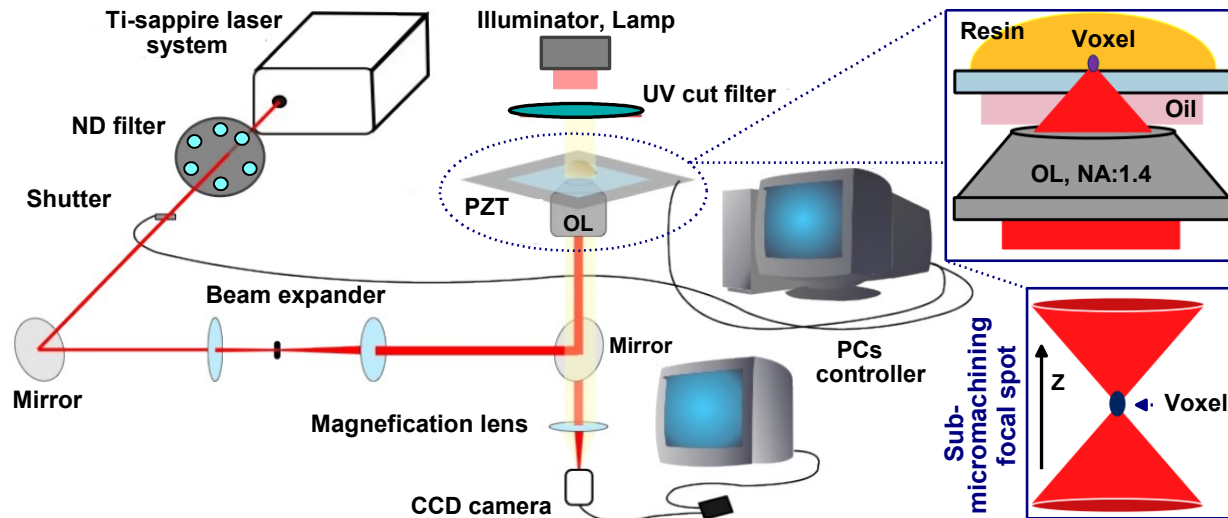


Figure I.6. A typical experimental set-up for TPP-based 3D nanoprinting; microstructures are printed through a voxel-by-voxel stacking process. The use of a high NA lens (~ 1.4) is critical to launching SDL resolution; the localization of the LFS inside the resin is shown as an inset.

To 3D print structures, (iii) the TPP scanning relative to the sample is realized by a piezostage (PZT) that is displaced with high resolution; e.g. ~ 1 nm step. TPP scan method will have a crucial impact on the throughput of the fabrication process; e.g. accuracy. This is accomplished through two possible means: the first possibility is to use galvanomirror (for horizontal scanning) coupled with a 2D stage (for vertical scanning); this system presents the advantage to scan with high speed. However, the total horizontal range accessible by this strategy is limited to a few tens of micrometers due to spherical aberration when using high NA. Secondly, the most popular solution consists to scan in x , y , and z directions by using a 3D PZT, while the scan speed is low; i.e. few ~ 100 μm [40,45]. For monitoring, a charged coupled device (CCD) camera is used to adjust the z -position of the laser's focal spot and *in-situ* fabrication [12].

I.4.3. Two-Photon Polymerization Threshold

Before discussing the overall process of 3D laser nanoprinting in more detail; we will first shortly introduce and discuss the commonly used threshold effect. For simplicity, it is often assumed that the polymerization induced by TPA is a threshold photoreaction. The TPA threshold is closely related to the radical quenching effect, meaning that the existence of dissolved oxygen in the mixture of the resin is considered as a detrimental factor to control the TPP threshold; meaning the laser threshold intensity (I_{th}). However, due to the existence of radical quenchers; i.e. dissolved oxygen, radicals survive and initiate TPP only around the LFS at the region where highest laser density is localized; i.e. \propto SLI, and thus a threshold behavior is formed, as schematically illustrated

in Fig.I.7(a) [3,40]. As shown in Fig.I.7(a), the SLI distribution at the submicron machining LFS is assumed to be a Gaussian beam and it can be expressed with the following Eq. [20,57]:

$$I(r_0, 0) = I_0 \exp(-2r_0^2/w_0^2); \quad (I.17)$$

Where r_0 denotes the radius of the laser beam, and I_0 is the laser intensity at the center axis in the focus plane, and w_0 is the radius of the focus; *i.e.* the beam waist.

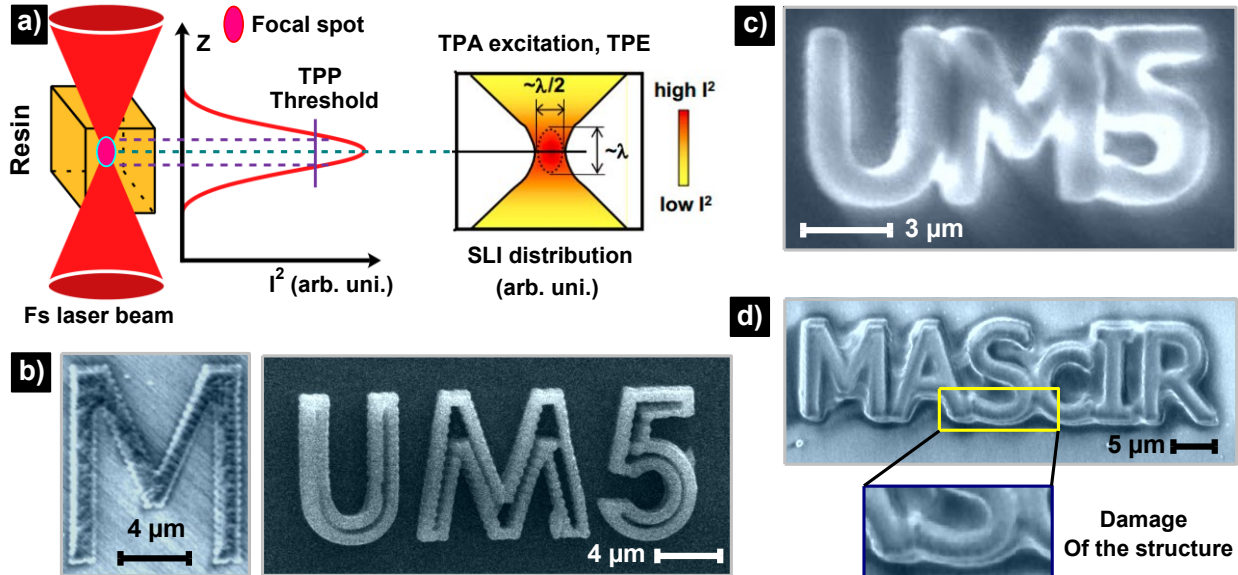


Figure I.7. TPA threshold effect on the accuracy of 3D nanoprinting. (a) Total TPA per transversal plane; *i.e.* calculated by integrating the SLI over the plan (Gaussian profile); the distribution of the SLI at the center of the focal region is shown as an inset. (b) SEM images of M character and UM5 patterns that are exactly polymerized at I_{th} . (c-d) SEM image of structures printed above I_{th} ; the structures are damaged (zoom image). In this work the I_{th} was fixed at $\sim 820 \text{ kW/cm}^2$, and the exposure time was 1 ms.

For a polymeric structure, to withstand the solvent employed for the washing phase; a certain degree of cross-linking; *i.e.* 100% of polymerization, is required; thus, the degree of cross-linking was determined by the threshold effect [40]. The laser intensity relative to TPP threshold; *i.e.* I_{th} , is continuously adjustable by reducing the irradiation intensity (I_{irr}) and exposure time. According to the thresholding effect, the size of the nanoprinted voxels which defines the TPP resolution can be tuned to be much smaller than that defined by the diffraction limit [9,12]. Shown in Fig.I.7(b) are the SEM micrographs of the nanoprinted structures that were exactly polymerized at I_{th} .

Experimentally, TPA threshold is well-defined as the minimum intensity fluence required for the initiation of an irreversible photochemical reaction; *i.e.* TPP, in a short timeframe (Fig.I.7(a-b)) [3,13]. When $I_{irr} > I_{th}$, the overall form of the printed structures can be damaged; meaning that

the smallest patterns of these structures may be deformed (Fig.I.7(c-d)). Here, UM5 pattern symbolizes -université Mohammed V (en français)- and MASCIR abbreviation denotes -moroccan foundation for advanced science, innovation, and research-. It is known from the literature [6,40] that the threshold of TPP can be precisely determined and controlled by optimizing the irradiation intensity, the number of pulses, the NA focusing, and the exposure time. This allows resolution up to $\sim 100\text{ nm}$; *e.g.* as shown in Fig.I.7(b).

I.4.4. Submicrometric Polymerized Voxel

Understanding the performance of individual voxels is critical to establish the TPP process as a 3D nanoprocessing tool. A voxel is well-defined as the smallest unit of patterns produced by the use of one exposure-shot. Due to the NLO and thresholding effect of TPP, the printed voxel can be smaller than the LFS size [20,58]. Moreover, photogenerated radicals in the focal volume were subject to scavenging by the dissolved oxygen; so, TPP wasn't triggered when I_{irr} was less than I_{th} , as shown in Fig.I.8(b). This property defines the TPA threshold and excluded the low-intensity lobe; *e.g.* the zero-order edge and the subsidiary maxima of the airy pattern, from polymerization and thus further reduces the size of the nanoprinted voxel (Fig.I.8(c)) [9].

In 3D nanoprinting, TPP-resolution is the most important issue that needs addressing. The achieved SDL resolution of TPP nanoprinting was found possible in a threshold system; *e.g.* TPA materials, that responded to the nonlinear excitation with a pronounced threshold behavior; *i.e.* materials nonlinearity (Fig.I.8(c)) [3,11]. Hence, a lateral resolution (Δ_{xy}) down to $\sim 120\text{ nm}$ can be achieved (Fig.I.8(a)) by the use of high $NA\sim 1.4$ focusing optic. Fig.I.8(a) shows a SEM image of voxels that were two-photon printed under different optimized pulse energies and exposure times [9]. To apply the achieved SDL voxel in 3D nanoprinting, the LFS was three-dimensionally moved from voxel to voxel (Fig.I.8(e)) in-order-to nanoprint desired microsized objects; *e.g.* 3D microbull shown in Fig.I.8(e) [9,58].

Based on the NLO behavior of TPP, SDL resolution of printed nanofibers connecting two boxes was achieved (Fig.I.8(d)); thus, the fiber width can be further reduced; *i.e.* $\sim 65\text{ nm}$, corresponding to $\lambda/12$ of resolution [59], and in some occasions $\sim 25\text{ nm}$; *i.e.* $\lambda/31$ resolution [60]. From Fig.I.8(d), a fast scanning speed was applied when the LFS moving from the first box to the next, thus, the time of exposure of voxels was reduced. This effect is called materials nonlinearity. The combinative action of the chemical, and optical, and material nonlinearity makes it possible to

achieve reproducible SDL resolution; *i.e.* at a level of $\sim \lambda/10$ to $\sim \lambda/50$ [59]. Thus, the voxel size is strongly influenced by the laser dose, materials nonlinearity, and processing accuracy.

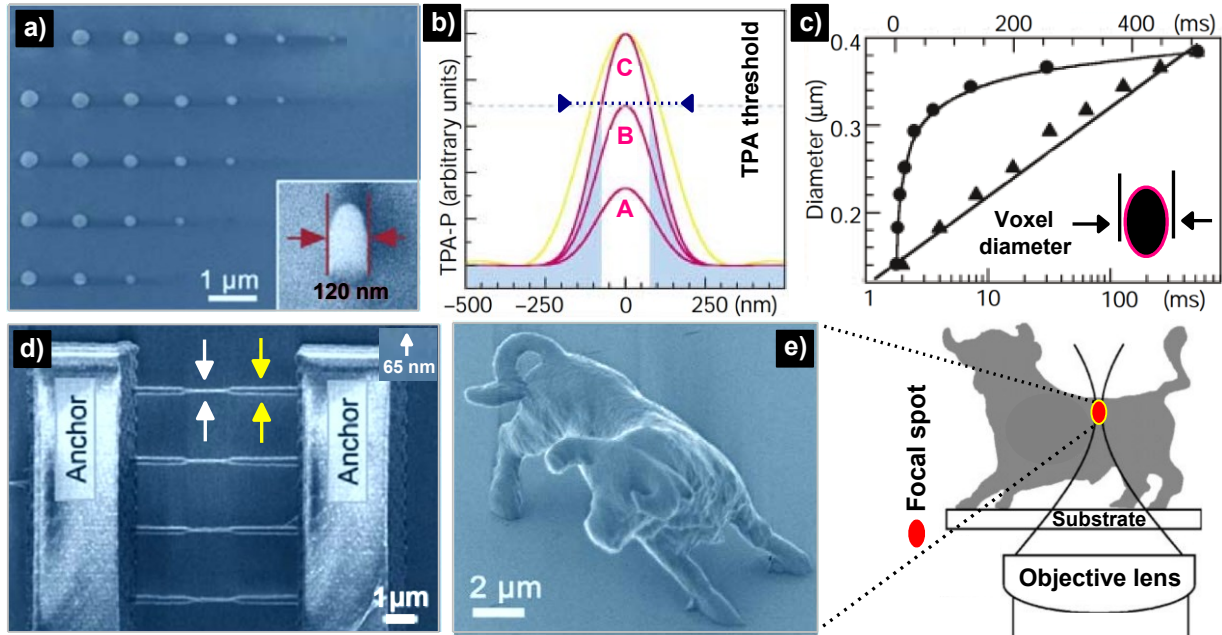


Figure I.8. 3D laser nanoprinting at SDL resolution. **(a)** SEM image of voxels polymerized at different exposure conditions. **(b)** Achievement of SDL resolution, where A, B, and C denote the laser-pulse energy below, at, and above TPP threshold (dashed blue line), respectively; the yellow line represents the range of OPA; TPA-P means TPA-probability. **(c)** Dependence of Δ_{xy} on exposure time; the same data are presented using both logarithmic (triangles; bottom axis) and linear (circles; top axis) coordinates, to show the logarithmic dependence and TPA threshold. **(d)** SEM image of the suspended array of nanowires, the exposure time of the ended (yellow arrow) and the central (white arrow) segments were fixed at 8 ms and 2 ms, respectively, under a laser pulse energy of 75 pJ. **(e)** SEM image of a bull sculpture produced via voxel-by-voxel accumulation that is based on raster scanning mode (inset) [9,59].

Fig.I.9(a.1) and Fig.I.9(a.2) show SEM images of voxels formed at moderate laser power (P) and exposure time (T); *e.g.* $(P * T)_{th}$. Since it is already known that a near-threshold exposure gives the highest resolution and accuracy of 3D laser nanoprinting. At near-threshold, the dimensions of printed voxel scaling abide by two laws; *i.e.* approaches (models), which means P-approach and T-approach [11,28]. Fig.I.9(a.3) and Fig.I.9(a.4) show the voxel size evolution following these two exposure approaches; thus, the lateral (Δ_{xy}) and longitudinal (Δ_z) sizes of the printed voxels were investigated. It is observed that it is no difference in the evolution of voxel sizes with varied P and T, as shown in Fig.I.9(a.3) and Fig.I.9(a.4). It is seen from these Figs. that the voxel expansion in both P and T scheme is well fitted with the following formula [28]:

$$S = l_{diff} \alpha \sqrt{\ln(E_{re}/E_{th}) / 4n \ln 2}$$

Where, S symbolizes the voxel size, l_{diff} is the diffraction limit of LFS, and α is a constant reflecting the characteristic of TPA materials and exposure schemes and therefore describing the fact that the l_{diff} is not the only factor that determines the size of a printed voxel. E_{re} and E_{th} , represent real and threshold power (P_{re}, P_{th}) at a given exposure time; *i.e.* real and threshold (T_{re}, T_{th}). $n = 2$ means the number of photons that were simultaneously absorbed; *i.e.* TPA [40].

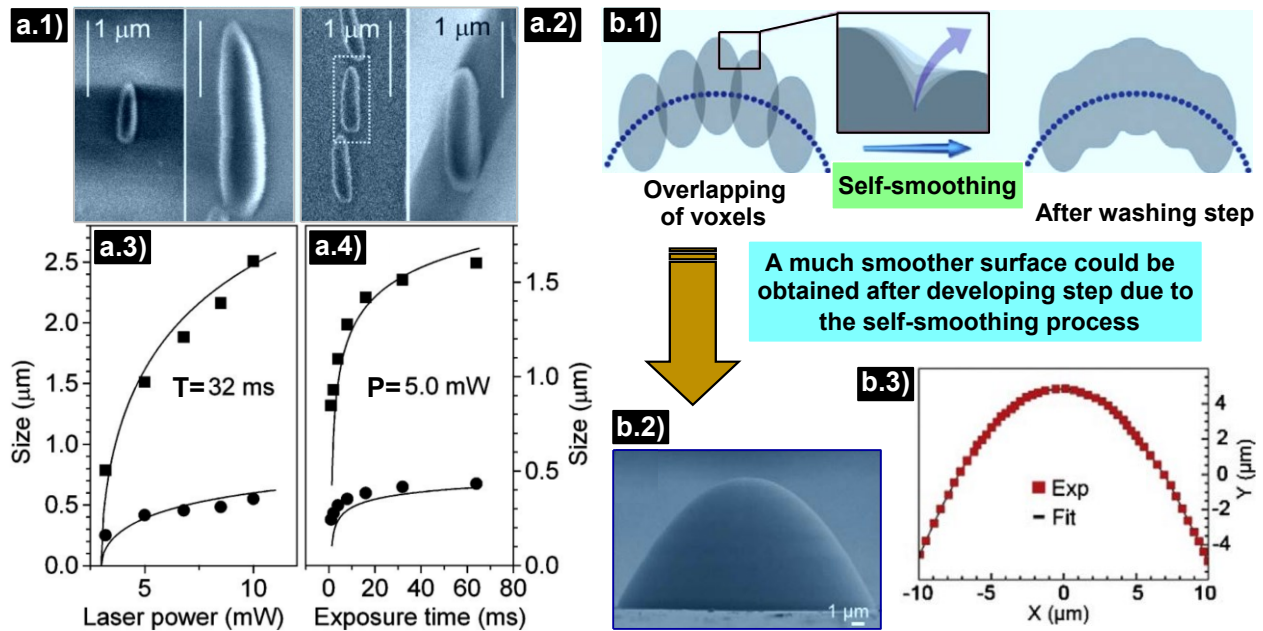


Figure I.9. Achievement of SDL resolution. (a) Exposure time (T) and power (P) dependent voxels sizes; (a.1) SEM images of voxels obtained under (3.2 mW, 32 ms) and (10 mW, 32 ms); (a.2) voxels produced with varied exposure time (5 mW, 1ms) and (5 mW, 64ms); (a.3) P dependence and (a.4) T dependence; the dark circles denote the experimental Δ_{xy} , and Δ_z is denoted by the dark square; the solid curves present the fit. (b.1) An illustrative model shows the voxels overlapping during TPP printing which induce high resolution. (b.2) SEM image of a parabolic polymerized microlens. (b.3) the measured profile (square symbol) and the theoretical curves (solid line).

Generally, the TPP resolution is determined by controlling the voxels shape and size, but higher processing accuracy has been achieved in the practical prototyping model (programmed pattern), as was ascribed to the unique merits of TPP printing [61]. Primary, unlike self-assembling of colloidal nanoparticles, which turns to a close package of rigid spheres, nanofabricated 3D objects are built from polymerized voxels that can overlap with each other, as shown in Fig.I.9(b). Thus, the desired center-to-center distance of voxels is carefully chosen, meaning the possibility of dimension definition to any value larger than voxel itself with an accuracy much beyond the restriction of polymerized-voxels size [6]. The higher accuracy of 3D nanoprinting was technically controlled by the following systematic factors: (i) high positioning accuracy of focus; due to the

usage of PZT moving with a motion accuracy better than $\sim 1 \text{ nm}$ step; and (ii) high reproducibility of the shape and size of printed voxels. As well, the laser pulse energy instability; *i.e.* generally less than $\sim 5\%$, leads to a fluctuation of voxels size less than $\sim 5 \text{ nm}$ [40,58].

Another important factor that may affect the stability and functions of nanofabricated structures is the surface quality (Fig.I.9(b)). Better surface quality can be achieved when the scanning pitch of the PZT is reduced to around $\sim 100 \text{ nm}$ (for $\Delta_{xy} \sim 100 \text{ nm}$). Shown in Fig.I.9(b.2) is a side view SEM image of a polymerized curved surface; here, the surface roughness is estimated at $\sim 2.5 \text{ nm}$, and the overall deviation of the surface from design was measured to be $\sim 17.3 \text{ nm}$ [61]. High surface smoothness of structures cannot be only achieved by the overlapping of voxels, by the reason that the corner formed at the boundary of two adjacent voxels is quite sharp (Fig.I.9(b.1)), where the surface Gibbs free energy is expected to be much smaller than that at the voxel tip end; *e.g.* tip of an iceberg [6]. The unpolymerized liquid resin localized there is thus difficult to remove by rinsing. So, the locally rugged surface tends to be straightened when the surface starts to expose to air, due to surface tension; *i.e.* self-smoothing effect. The local surface reforming due to the self-smoothing effect can significantly improve the surface quality; *e.g.* smoothness [61].

I.4.5. The Diffraction Limit

In nonlinear optic, the diffraction of light plays an essential role in the resolving power of the focusing light through an objective microscope. In 1873, E. Abbe [62] proved that the resolution of the optical imaging instruments is fundamentally limited by the diffraction limit. E. Abbe's research [62] revealed that the resolution of a microscope is related to the wavelength of the used light and aperture of the focusing optic. Diffraction limit means that an imaging lens could not resolve two adjacent objects located closer than $\sim \lambda/2NA$. Shown in Fig.I.10 is the principle which describes the diffraction limit phenomenon. The diffraction-limited phenomenon hindered the performance of optical microscopy for over a century and was considered as a fundamental unbreakable rule.

Recently, several new exciting optical approaches in imaging microscopy have emerged that can possibly break this rule under certain circumstances. His insight introduced optical imaging approaches; *e.g.* electron and scanning tip microscope [63,64]. In these approaches, spatial resolutions were improved either by decreasing the wavelengths of the probe laser-beam by using electron, atom, ion waves or by using a sharp tip-end to reduce the light and specimen interaction

area as done in STMs; *i.e.* scanning tunneling microscopes, near-field scanning optical microscopes (NSOMs) and AFMs [62,64]. The resolution informed from these optical complexes systems ranges from $\sim 100\text{ nm}$ down to a remarkable value of less than $\sim 1\text{ nm}$.

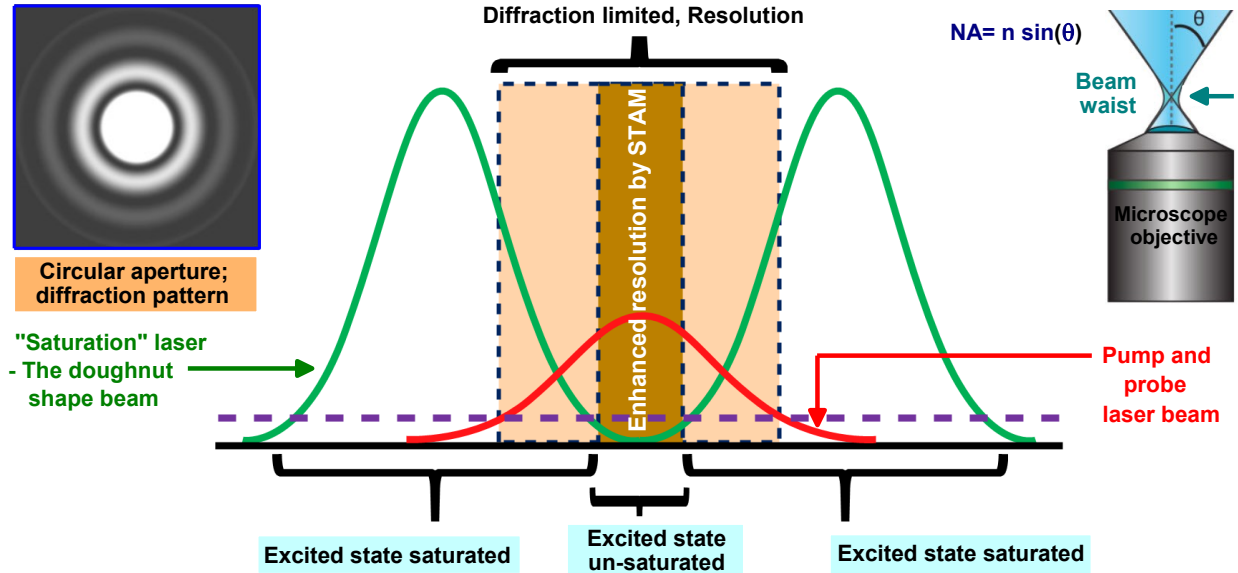


Figure I.10. Scheme presentation of the diffraction limit. (Inset) optical microscopes still must overcome a critical limit in optical resolution caused by the diffraction of light wavefronts when they pass through a focusing lens (right-inset). The circular aperture-diffraction pattern is shown as a left-inset [40,62].

3D nanoprinting induced by NLO effect (TPP-nanofabrication) presents one of the most techniques where the diffraction limit rule is broken; *e.g.* SDL size of voxels [3,6]. In this technique and by the use of an OL ($NA \sim 1.4$ which focuses light), the light distribution at the focal plane essentially arises from Fraunhofer diffraction (inset of Fig.I.10), and the size of the active zone (where TPE was localized) can be smaller than the diffraction limit. Thus, the light intensity distribution at the focal region was assumed to follow a formula due to Airy [40,52].

$$I(x) = (2J_1(x)/x)^2 I_0$$

Where $I = E D / \lambda^2 R^2$ denotes the focused intensity at the pattern center (inset of Fig.10), E is the total incident energy upon the aperture, and $D = a \pi^2$ is the area of the aperture with an effective radius a , and $x = 2\pi a \omega / \lambda$, ω is the coordinate in the diffraction pattern. For imaging formation, the resolving power was limited by Rayleigh's criterion; *i.e.* $\delta_r = K_1 \lambda / NA$, which is due to the signal overlapping from adjacent object points, where $K_1 = 0.4 \sim 0.6$ is a constant depending on the laser linewidth and projection geometry [40].

Next, we will show the advantage of the use of the NLO effect of TPA to overcome the diffraction limit issue in 3D nanoprining. Fig.I.11(a) shows the excitation efficiency of OPA polymerization ($\lambda_{ex} \sim 375 \text{ nm}$) and TPP ($\lambda_{ex} \sim 780 \text{ nm}$). The NA of the lens which focuses light is the same for both cases [30]. The “magic” of TPA, as opposed to OPA, lies in the tails of a tight laser-focus; *i.e.* LFS. As seen in Fig.I.11(a) the Full width at half maximum (FWHM) is bigger for TPP than OPP; this is due to the smallest excitation wavelength (λ_{ex}) in the case of the OPP process [45,52].

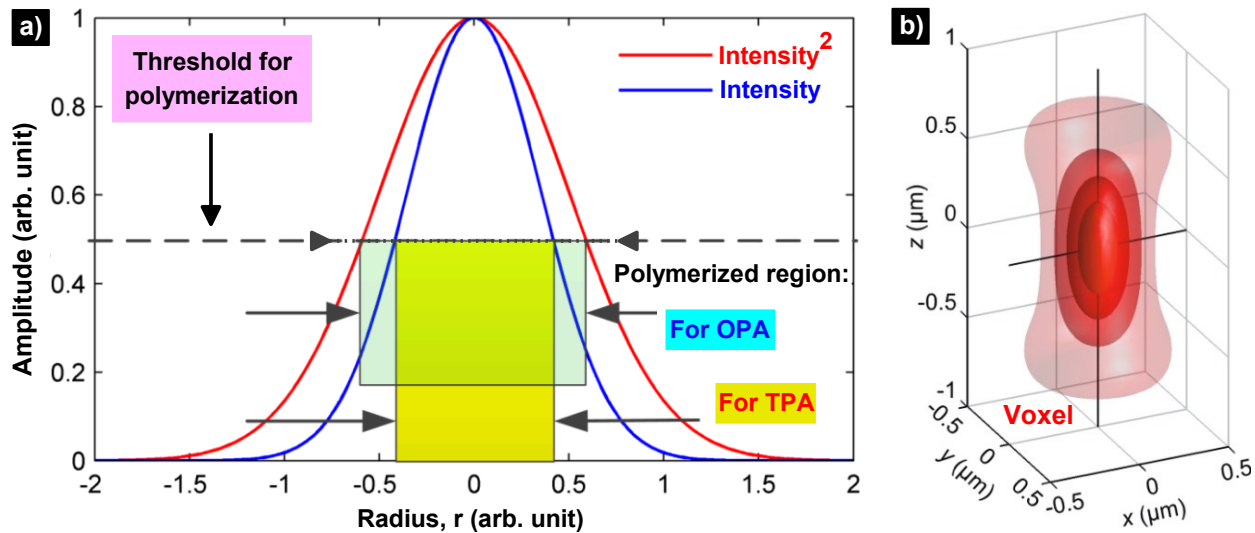


Figure I.11. Light intensity analysis for achieving SDL resolution. (a) Distribution of light intensity at the focus of a gaussian beam: $I(r) = I_0 \exp(-2r^2/\omega_0^2)$; where $\omega_0=1$ and the intensity is $I_0 = 1$. The focal intensity (solid-blue line) and SLI (solid-red line) distribution are associated with OPE and TPE processes, respectively. (b) The focal intensity distribution of a typical writing spot (dimensionless for clarity) [52].

The excitation (TPE) rate quadratically decreases as a function of the distance from the focal plan increases in the case of TPP. This is not the case with OPP, where the excitation rate decreases linearly as the distance from the focal plan increases. TPP takes place at the region where the light intensity reaches the critical threshold; *i.e.* I_{th} [30]. In 3D nanoprining, the resolution is provided by the λ of irradiation and NA of the focusing OL, and it’s not limited by the diffraction of light. Thus, we conclude that the diffraction limit of light can be circumvented by the use of the NLO effect of TPA [65].

I.4.6. Realization of Sub-Diffraction-Limit Features

Recently, the research into TPP nanoprining is increasingly driven by the demand to produce smaller features and complex functional microdevices (Fig.I.12) [8,29,45]. Compared with light or electron-beam lithography (EBL), the virtue of TPP-based 3D printing as a tool for fabricating microdevices lies to its 3D fabrication capability; *e.g.* with SDL resolution of nanofabrication (inset

of Fig.I.12(a)) [3,9]. As an example of the SDL 3D-fabrication capability of the TPP process, Kawata et al. [9] fabricated a movable microsized oscillator which must be the smallest functional machine that can be produced (Fig.I.12).

Shown in Fig.I.12(a-b) is a microspring that has a diameter of only $D \sim 300 \text{ nm}$ (Fig.I.12(c)). Thanks to TPP, it is possible to print devices with nanoscale features; e.g. $\sim 120 \text{ nm}$ resolution (Fig.I.12(a-b)). Besides, high TPP resolution can be achieved (e.g. less than $\sim 100 \text{ nm}$), but it is difficult for voxels to appear in the same SEM characterization used in this work, so, in this nanofabrication trick (Fig.I.12) [9], the obtained resolution may be better than $\sim 120 \text{ nm}$.

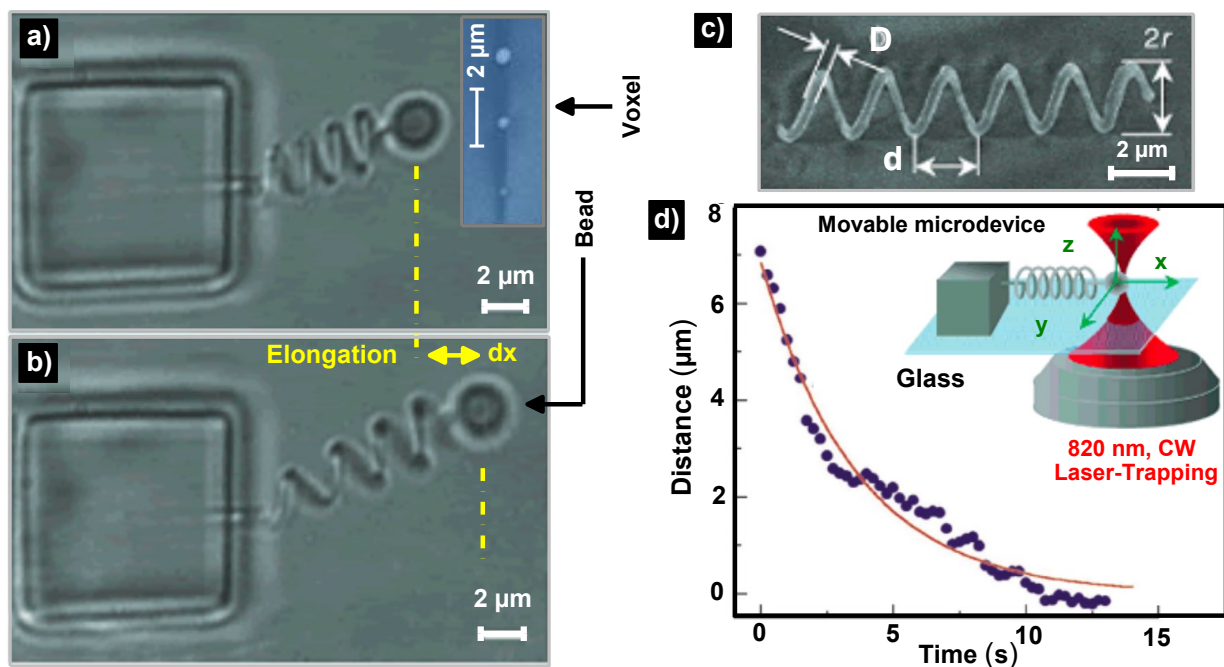


Figure I.12. Finer features for the functional oscillator system. (a) SEM image of spring fixed at a microbox (original state). (b) Polymerized microsized spring prolonged. (c) SEM image of a micro spring with different dimensions; e.g. $D = 300 \text{ nm}$. (d) Restoring curve of the damping oscillation; inset, a diagram showing driving of the oscillator by the process of the optical trapping in which a CW laser; i.e. $\lambda = 820 \text{ nm}$, was used.

To functionalize the printed spring as movable micromachine, a microsphere (bead) was fabricated at its one end and fixed it at the other end to a polymerized anchor that was attached to the cover glass (Fig.I.12(a-b)). For this application, an optical trapping technique was applied; meaning an optical laser-trapping force was utilized to capture the bead which pulled the spring (inset of Fig.I.12(d)), and then released its displacement to set the vibration in motion (Fig.I.12(d)) [9,40]. When the focal spot ($\lambda = 820 \text{ nm}$ trapping) was carefully adjusted, the bead could be three-dimensionally trapped and freely manipulated (inset Fig.I.12(d)); an oscillation was thus initiated.

For more detail see ref. [9]. According to these results, we believe that the TPP-based 3D nanoprinting would be a powerful tool for fabricating functional microdevices.

Next, we reviewed the work realized by S. Ushiba et al. [27] in which the TPP was used to 3D print movable nanocoil springs on a cross-linked PMMA. For more detail, see the supplementary information related to this work in the ref. [27]. The nano-spring presented in Fig.I.13(b); *i.e.* consists of smooth and rough surfaces, has a spiral width of ~ 300 nm; *i.e.* $\lambda/2.6$ resolution. Shown in Fig.I.13(a) is the spring dimensions (represented by the CAD model).

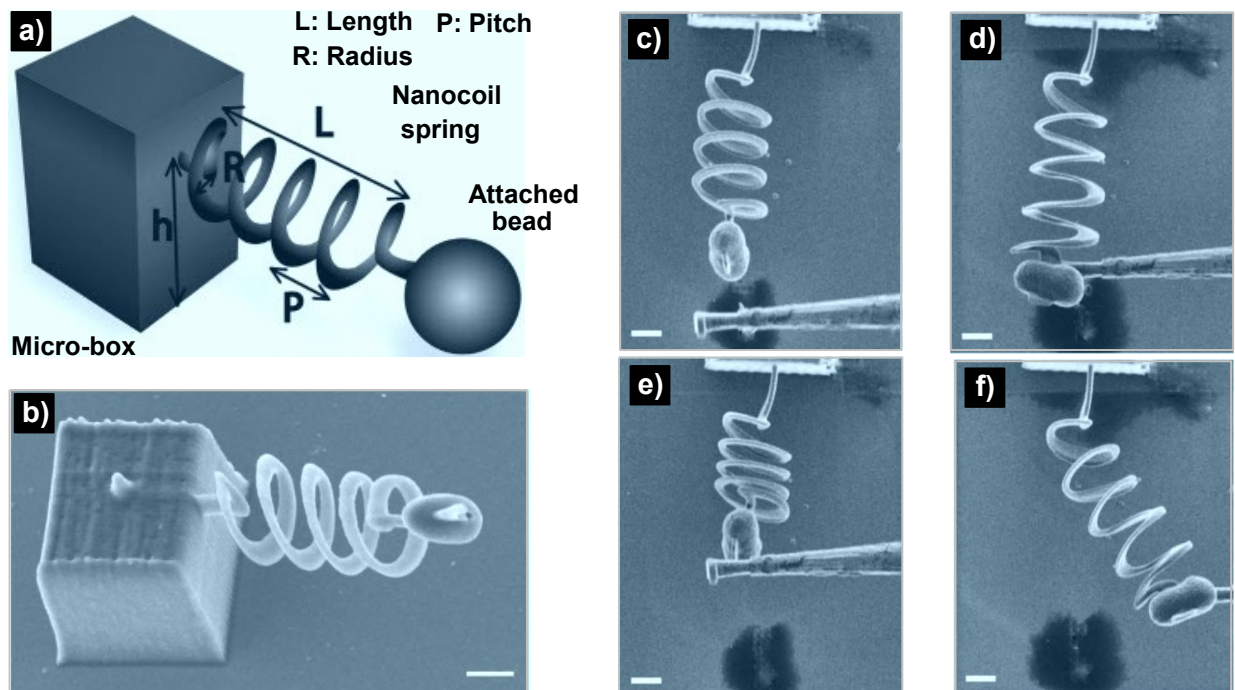


Figure I.13. 3D laser nanoprinting of coil spring shaped polymer nanowires. (a) CAD model showing the dimensions of a nanocoil spring; the coil R , P , L and the number of turns N , are $2.5 \mu\text{m}$, $2 \mu\text{m}$, $13 \mu\text{m}$, and $4 \mu\text{m}$, respectively. (b) A perspective view SEM image of a 3D nanocoil spring. (c-f) FIB images of spring before loaded (c), stretched (d), compressed (e), and bent (f). All scale bars shown in this figure are $2 \mu\text{m}$ [27].

Thanks to TPP, it is found that the nanoprinted coil springs can be moved (nanomachine) against an applied force following Hooke's law; *i.e.* linear-response against applied force, as revealed by compression and elongation tests realized by AFM as shown in Fig.I.13(c-f). Thus, the nanoprinted polymeric oscillator ($R \sim 400$ nm) exhibited the properties of stretch (Fig.I.13(d)), compress (Fig.I.13(e)), and bend (Fig.I.13(f)), against AFM manipulation forces; clearly indicating that the spring behaves as a conventional spring. Further, the elasticity of the nanocoil springs is found to become significantly greater as the wire radius is decreased from ~ 550 nm to ~ 350 nm. The

$\sim 13 \mu\text{m}$ long and $\sim 2 \mu\text{m}$ pitch coil is considered as small as a human red-blood-cell [3]. Their submicrometric volume and movable capability allow us to send them to any location inside the human body through blood micro-vessels to make clinical treatments [6].

I.5. Applications via TPA-based 3D Laser Nanoprinting

In 1997-2001, the emergence of TPA enabled 3D nanoprinting capability in a sub $\sim 100 \text{ nm}$ scale [9,10]. Since then, increasing demand in functional microdevices lead to the fast development of 3D laser nanoprinting; thus, this technology has found applications in different fields, such as photonic crystals [17,21], micro-optical elements [23,24], and metamaterials fabrications [66], as well as in biomedical; including biodegradable materials and protein microstructuring [8]. In the following sections, we do not intend to review all the literature in these kinds of applications; rather, we will highlight some important achievements on the application of TPA nanofabrication.

I.5.1. Functional Micro-Optical Devices

Potential of micro-optics as enabling technology for multidisciplinary science; attracting great attention in the industry, providing new methods for the TPA fabrication of novel functional microdevices [7,27]. Here, we discuss how the FsLDW based on TPA is implemented for making optical devices; *i.e.* microlens arrays (MLA), to control light's flow at increasingly reduced space and size [67]. MLA with multifocal planes and wide-angle of view are required for future technologies (*i.e.* applications); *e.g.* smart surveillance, monitoring, and self-driving vehicles [68]. The small geometric footprint and unique optical performances of MLA have made them essential elements in a wide range of applications; *e.g.* integrated micro-optics [69], 3D laser nanoprinting [70], and photoelectric devices [71].

H-B. Sun et al. [67] proposed a novel approach that combines TPA-based FsLDW with ion beam etching (IBE) for a simple and versatile fabrication of nanosmooth MLA on hard and ultra-hard materials; *e.g.* fused silica (Fig.I.14(a)). Owing to the SDL resolution of FsLDW; *i.e.* induced by the NLO effect, and IBE, high surface roughness of smooth MLAs was achieved. To fabricate MLA (Fig.I.14(a)), a 800 nm Fs laser, with 120 fs pulse width, and 1 kHz as repetition rate, was focused onto the hard material through an OL of 0.85 NA . Due to the NLO effect of TPA, Fs laser modifies the material when the pulse energy was larger than the TPA threshold; laser energy $En_{irr} > En_{th}$. After TPA modification; *i.e.* Fs laser ablation, a modified region was shaped around

the micropits with the formation of nanocracks (Fig.I.14(a.i)) [72,73]. Then, the modified region was etched by argon (Ag^+) physical sputtering in the IBE system (Fig.I.14(a.ii)).

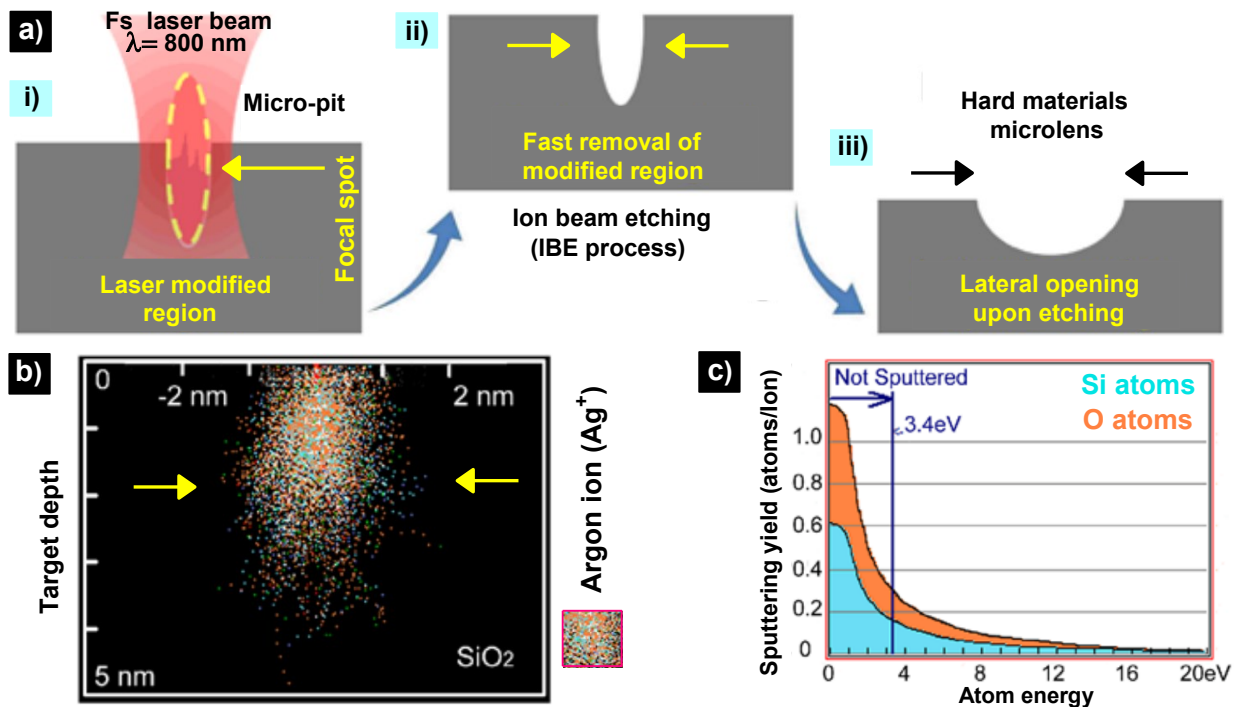


Figure I.14. TPA nanofabrication of optical MLAs. **(a)** Fabrication of MLA on hard materials by TPA followed by the IBE process. **(b)** The x - y distribution of the argon ions (Ag^+) and atom collision at normal incidence in the fused silica. **(c)** Dependence of the sputtering yields of the target atoms versus the Ag^+ energy [67].

To understand how the fabricated MLAs are laterally expanded during the IBE process, the argon sputtering process was simulated by the Monte Carlo method. Fig.I.14(b) shows the x - y distribution of the Ar^+ and atomic collisions at normal incidence to the fused silica. Fig.I.14(c) displays the simulated sputtering yield under the conditions employed for the IBE process. Refer to ref. [67] for more detail concerning the experimental setup used in this work.

Fig.I.15(a-b) presents the fabricated MLAs; *i.e.* optical devices (focusing lenses), and their optical characteristics. The SEM image taken at a 60° -tilted view (Fig.I.15(b)) reveals a high surface quality and concave geometry character of MLAs. Also, the MLAs show the same height and diameter (Fig.I.15(c)) [67]. The fill factor of the arrays of microlens can reach to $\approx 100\%$ for both the closely packed square and hexagonal patterns. The uniform MLAs exhibit excellent imaging (Fig.I.15(d)) and focusing (Fig.I.15(e)) performances which commensurate with their high smoothness quality of the surface. The FWHM of the light intensity passed through these MLAs

was $\sim 2.5 \mu\text{m}$; *i.e.* measured at the focal plan. With the unique advantages; *i.e.* nanometric size, lightweight, and low cost, MLAs has been widely used in light field manipulation [68,69].

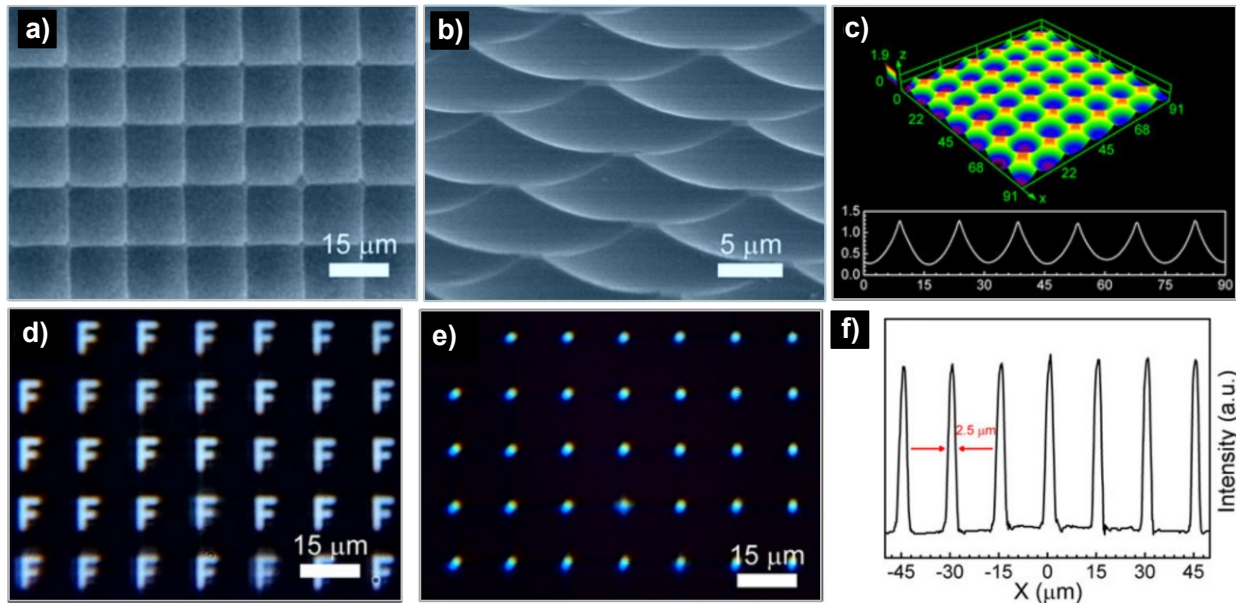


Figure I.15. Achievement of functional MLAs. (a) Top-view and (b) 60°-tilted views of SEM images of MLAs. (c) 3D morphology of MLAs obtained by laser scanning confocal microscope (LSCM); the cross-section profile of the array is shown as an inset. (d, e) Photos show the imaging and focusing performance of MLAs, respectively. (f) Light intensity distribution at the focal plane of MLA; *i.e.* used as a focusing lens.

TPA modification induced by Fs laser; *i.e.* Fs laser ablation, followed by IBE process; *i.e.* Ar^+ beam dry-etching, were used to construct uniform MLAs on different hard or ultrahard materials, as shown in Fig.I.16. Hexagonal concave MLAs on fused silica (Fig.I.16(a)), and SiC (Fig.I.16(b)), and diamond (Fig.I.16(c)) surfaces were fabricated. Based on the Monte Carlo method, the calculated sputtering yields of fused silica, SiC, and diamond are ~ 0.15 , ~ 0.15 , and $\sim 0.1/1\text{Ag}^+$, respectively. For more details refer to ref. [67].

Consequently, due to the high surface quality; *e.g.* smoothness, of the concave MLAs, excellent and uniform imaging and focusing properties can be achieved. The dimensions of nanosmooth MLAs, as well as their focal length, can be controlled by TPA exposure conditions; *e.g.* laser intensity, and pulses number, and also by etching time. Lastly, this method which coupled TPA nanofabrication and IBE strategy serves as a versatile and novel approach to 3D nanofabricate concave optical MLAs on hard and ultrahard materials; *e.g.* refractive or diffractive micro-optical components [67]. Shown in Fig.I.16 is the obtained MLAs on different materials by the use of TPA fabrication and IBE process.

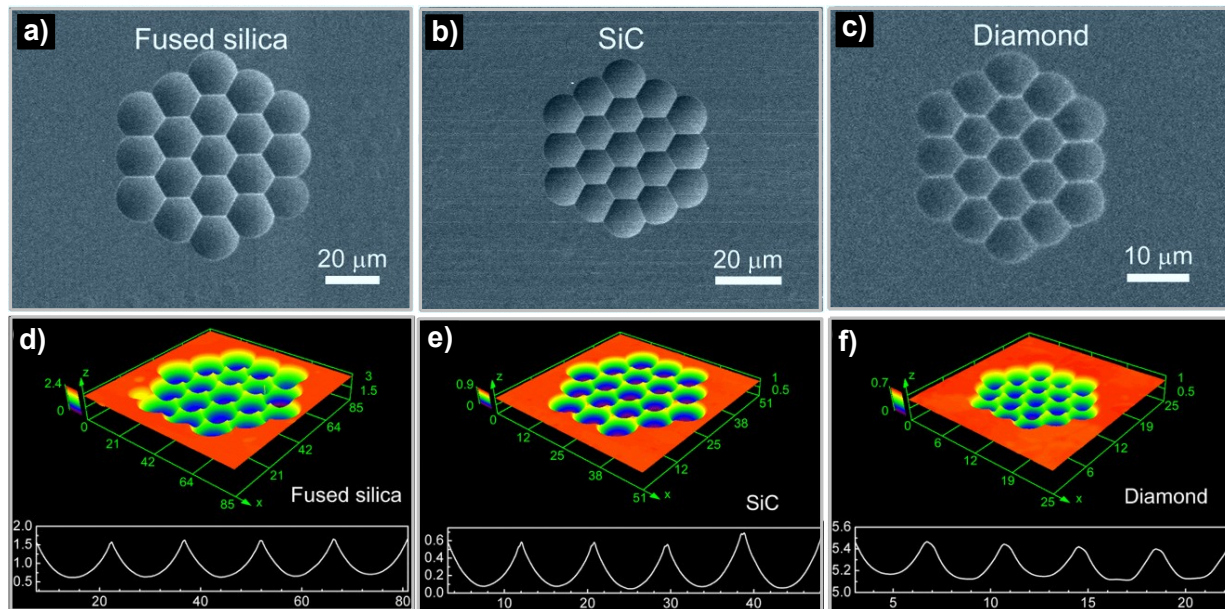


Figure I.16. Top-view SEM images of MLAs fabricated on different materials. (a) Fused silica. (b) SiC. (c) Diamond, respectively. 3D morphology obtained by LSCM of MLAs fabricated on (d) fused silica, (e) SiC, and (f) diamond surface; the cross-section profile of MLAs is shown as an inset. Height and width cross-sections of MLAs are scaled in micrometers (μm) [67].

The finish fabricated MLA allowed that the FsLDW based on the TPA process is considered as a true 3D nanoprocessing tool which can be used for the production of functional microdevices for future applications [65,66].

I.5.2. Multifunctional Electrical MicroDevices

Advanced TPP nanoprinting of functional microsized devices presents a key research topic in modern nanotechnology [3,74], and it is critically important in numerous emerging fields; e.g. nanoelectronics [75], nanophotonics [21,22], and biomedicine [8,65]. TPP-based 3D nanoprinting was found to be an ideal nanoprocessing tool for developing functional microdevices on composite resins doped with various functional materials, including semiconductor carbon nanotubes (CNTs) [29], metallic nanoparticles (Nps) [76], photoisomerizable dyes [77], and magnetic NPs [8].

In the present section, we report the TPP-based 3D nanoprinting on nanocomposite resin embedded with CNTs [75]. CNTs exhibit remarkable mechanical, electrical, thermal, and optical properties, which leads to enhance the performances of the printed functional microdevices [78]. W. Xiong et al. [75] make use of TPP to produce 3D microarchitectures based on CNTs-polymer. To make performance microdevices via TPP, it is strategically important to develop a compatible resin with maximum CNTs amount; for more detail, referee to ref. [75]. Shown in Fig.I.17 is the experimental

procedure involved in the preparation of MWNT-thiol-acrylate (MTA) resin (*i.e.* with 0.1 wt% CNTs) and also the TPP experimental setup used for 3D nanoprining. Here, the thiol grafting method was used in functionalizing MWNTs.

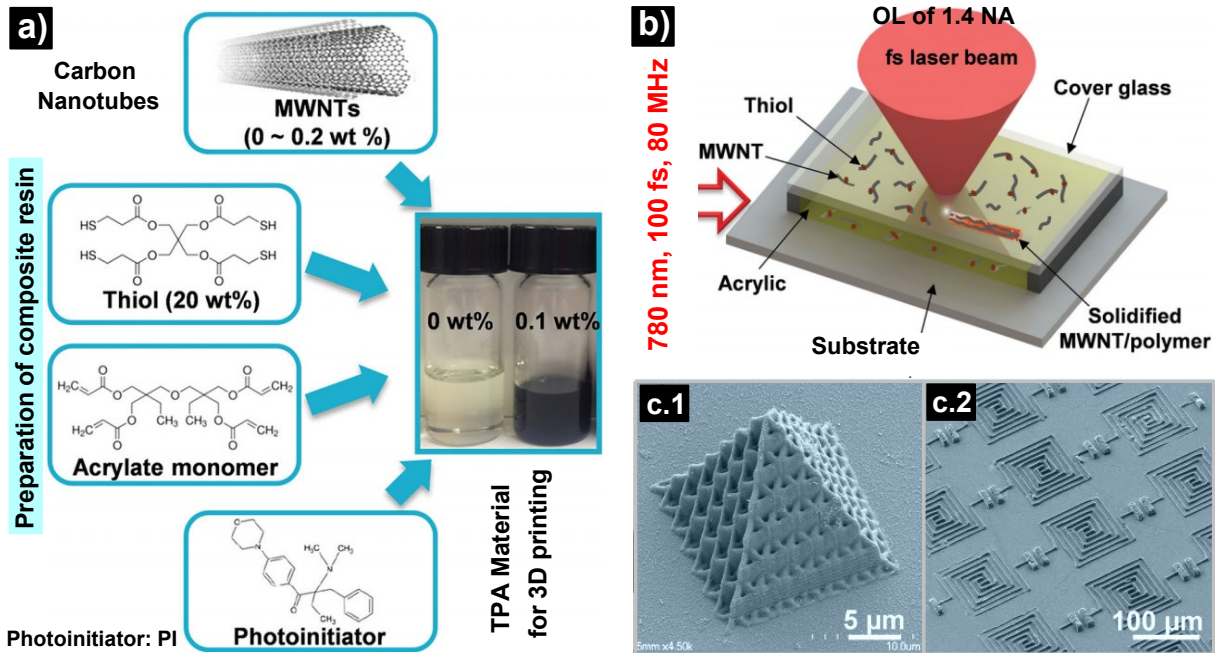


Figure 1.17. TPP-based 3D micro and nanofabrication on MTA resin. **(a)** Experimental procedure for MTA preparation. **(b)** Schematic presentation of the TPP FsLDW setup. **(c)** SEM micrographs of some microsized structures that were two-photon printed on MTA; **(c.1)** a micro pyramid, **(c.2)** arrays of micro capacitors. The laser power and scanning speed used were 15 mW and 0.5 mm s^{-1} , respectively [75].

Fig.I.17(c) shows some microsized structures that are fabricated by the use of TPP (on MTA resin); *e.g.* microsized pyramid and resistors. A raman spectroscopy (Fig.I.18(a)) was conducted to confirm that the CNTs were indeed incorporated inside the printed patterns; thus, the observation of characteristic G-band and D-band proved the existence of MWNTs.

The strong attachment of CNTs with polymerized resin induce the observed blue shift of CNTs G-band (Fig.I.18(a)), due to the increase in the elastic constant of the harmonic oscillators of the resin-doped MWNTs [79]. Shown in Fig.I.18(b) is a “TPP” pattern fabricated on MTA resin. Fig.I.18(c) visualizes the spatial distribution of MWNTs inside the polymerized “TPP” pattern via raman mapping. The uniform mapping image of the “TPP” structure was obtained via G-band intensity at each pixel. The raman image matched the SEM image indicating that the CNTs were uniformly distributed throughout the whole printed structure (Fig.I.18(c)) [29].

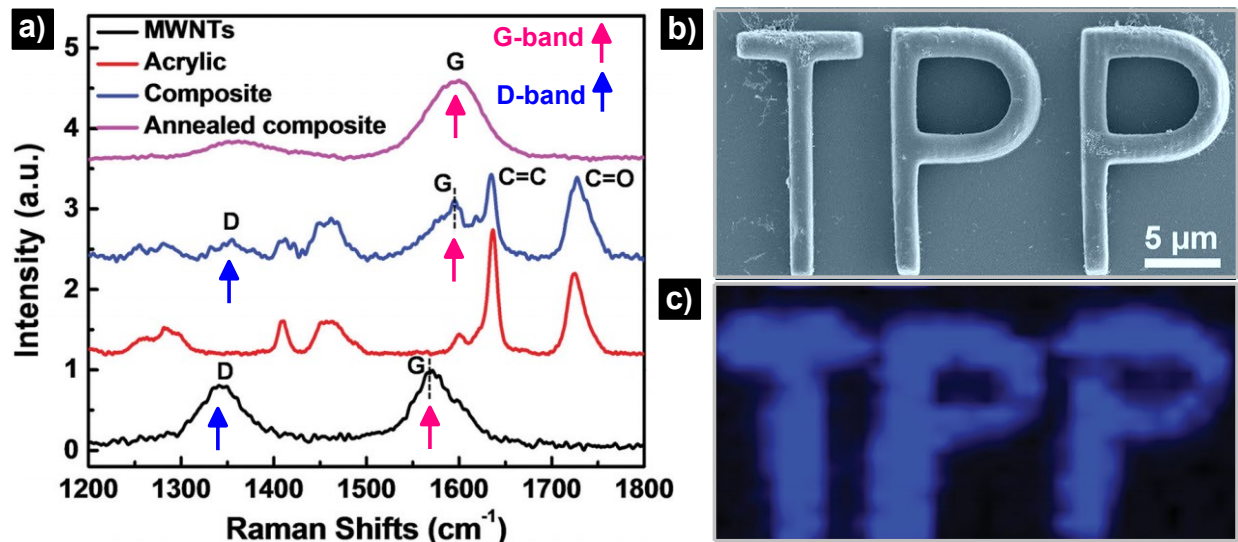


Figure I.18. Distribution of CNTs. (a) Raman spectrum of MWCNTs (black), acrylate monomer (red), MWNT-acrylate composite (blue), and MWNT-acrylate composite annealed at 500 °C for 5 min (violet). (b) SEM image of a “TPP” pattern that was two-photon printed on the composite resin. (c) Raman mapping image of the “TPP” pattern via G-band of MWNTs.

To investigate the electrical conductivity of the microprinted devices, two $5 \times 5 \times 75 \mu\text{m}^3$ ($W \times H \times L$) bar-shaped channels connecting two pairs of Au electrodes were printed. Both channels are fabricated with the same geometry; *e.g.* longer axis of bars, but with two directions of TPP scanning (laser nanowriting); either parallel or perpendicular, as shown in Fig.I.19(a) [75].

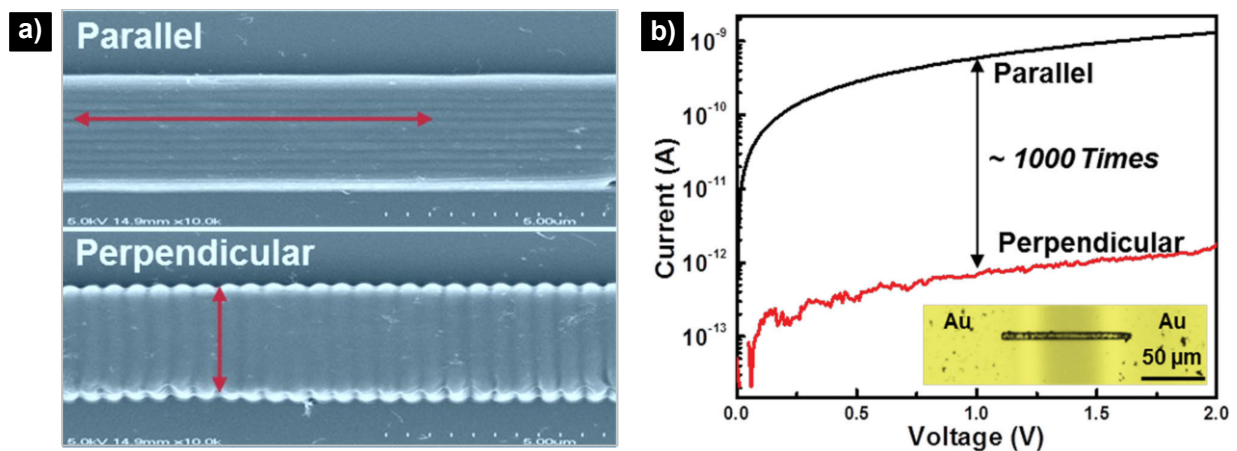


Figure I.19. Electrical properties of CNTs-polymers. (a) SEM image of assembled microwires between two Au electrodes that were two-photon printed by either (top) parallel and (bottom) perpendicular TPP scanning modes. (b) The $I = f(V)$ curve of both corresponding bars between Au electrodes; the optical micrograph of the bridge bar is shown as an inset.

The current-voltage curves; *i.e.* $I = f(V)$ in Fig.I.19(b), shows that the bar-shaped channel fabricated by parallel scanning was 10^3 times more conductive than that with perpendicular mode.

This 10^3 of magnitude difference matched with the high anisotropy in electrical conductivity of MWNTs in parallel directions, which further confirms the strong alignment; *i.e.* orientation, of MWNTs inside the nanoprinted wires [75].

To demonstrate the potential of 3D laser nanoprinting on MTA resin; *i.e.* with 0.1 wt% MWNT, a series of electronic microdevices; *i.e.* arrays of micro-capacitors (Fig.I.20(a)), and microresistors (Fig.I.21(a)), were printed. The electrical performance of these electronic devices was measured by an Agilent semiconductor parameter analyzer 4155C and an impedance analyzer 4192A. Fig.I.20(b) shows a typical hysteresis loop of the capacitor arrays; *i.e.* containing ten capacitors in parallel. The capacitance was measured to be ~ 50 pF. Refer to ref. [75] for more detail.

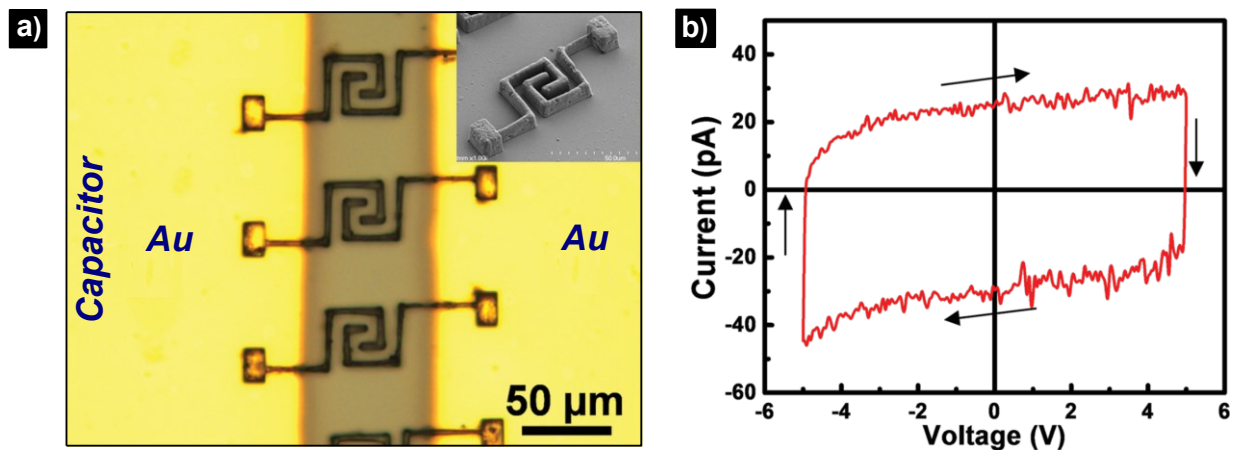


Figure I.20. Application via TPP nanoprinting; *e.g.* functional capacitor. (a) Optical micrograph of a capacitor array between two Au electrodes; the SEM image of a single capacitor is shown as an inset. (b) Hysteresis loop of 10 micro capacitors connected in parallel; scanning frequency is fixed at 0.025 Hz.

In addition, the authors reported on the frequency responses of transmission lines (Fig.I.21(b)) which is containing 20 zigzag microresistors (Fig.I.21(a)) in parallel and copper micro-ribbon; *e.g.* length \times width \times thickness: $1\text{ cm} \times 5\ \mu\text{m} \times 50\ \text{nm}$, produced by Cu sputtering with a shadow mask.

From Fig.I.21(b), in the low-frequency range, from 0 to 100 KHz, both MTA polymer and Cu transmission lines relatively exhibited stable impedances of $\sim 90\ \text{K}\Omega$ and $\sim 900\ \Omega$, respectively. However, in the high-frequency range, which is above 100 KHz, the two transmission lines showed different frequency responses. However, for Cu transmission line, it's due to increasing skin effect at high frequency, thus the impedance of transmission line increased from $\sim 900\ \Omega$ (100 kHz) to $\sim 1356\ \Omega$ (10 MHz), as shown in Fig.I.21(b). For more detail refer to ref. [75].

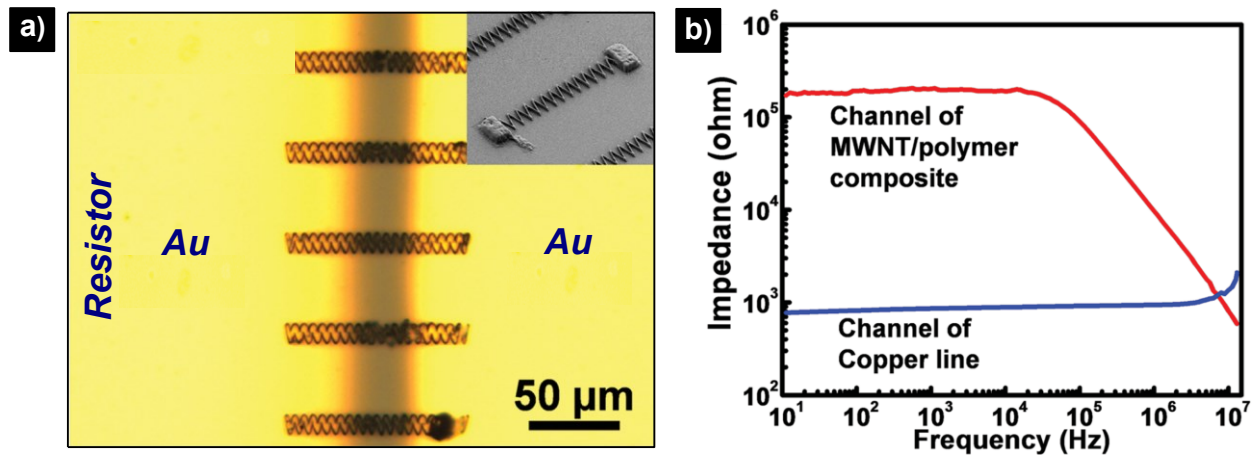


Figure I.21. Functional micro-resistor. (a) Optical micrograph of an array of zigzag resistors; the SEM micrograph of a single zigzag resistor is shown as an inset. (b) Frequency responses of transmission lines made of MTA composite (0.1 wt% MWNT), and copper; i.e. as a reference.

W. Xiong's group [75] have developed a method to incorporate a large-amount of well-aligned CNTs into functional microdevices. 3D nanoprinting of electronic microdevices; including micro-capacitors and resistors were demonstrated (Fig.I.21). The combination of high electrical conductivity and anisotropic properties of the realized microdevices is promising for a broad range of optoelectronic applications; e.g. light-emitting diodes, solar cells, and integrated optics.

I.5.3. 3D Printed Enzymatically Microswimmers: Micromachine

Imagine a world where the functional microrobots which taken the size of human cells operate inside the human body. Thanks to TPP nanoprinting, this application might sound like a science fiction story. Therefore, different types of small-scale robots; e.g. microswimmers (MSs), have been evaluated *in vivo*, especially to investigate their motion capabilities as nanomachines [80,81]. The printed soft helical MSs with non-cytotoxic biodegradable components will allow for enhanced device assimilation, optimal tissue interaction, and minimized immune reactions [82,83].

TPP nanoprinting of biodegradable MSs on a non-toxic photocrosslinkable gelatin methacryloyl (GelMA) hydrogel is reviewed. GelMA has been widely used for various biomedical applications due to their tunable physical characteristics and suitable biological properties [83]. MSs are capable to transform different categories of energy into locomotion, have proved great potential in microsurgery [84], sensing and diagnosis [85], and targeted drug delivery [86].

Here, we review the TPP printing parameters that are used to 3D print helical MSs on protein-based GelMA. We also assess the biocompatibility, biodegradability, and locomotion behavior of 3D

magnetically MSs in a biologically relevant environment; *e.g.* like human body settings [87-89]. Shown in Fig.I.22 is the experimental procedure including for 3D laser printing of soft MSs. The MSs fabrication was carried out in two steps; first, MSs were two-photon printed on GelMA-based resin, as shown in Fig.I.22(a). Next, the printed MSs were magnetically rendered by Fe_2O_3 Nps ($10\text{ mg}\cdot\text{mL}^{-1}$) (Fig.I.22(b)) (swimming test). The TPP process and the enzymatic degradation mechanism of GelMA including in the fabrication of MSs are shown in Fig.I.22(c), and Fig.I.22(d); respectively.

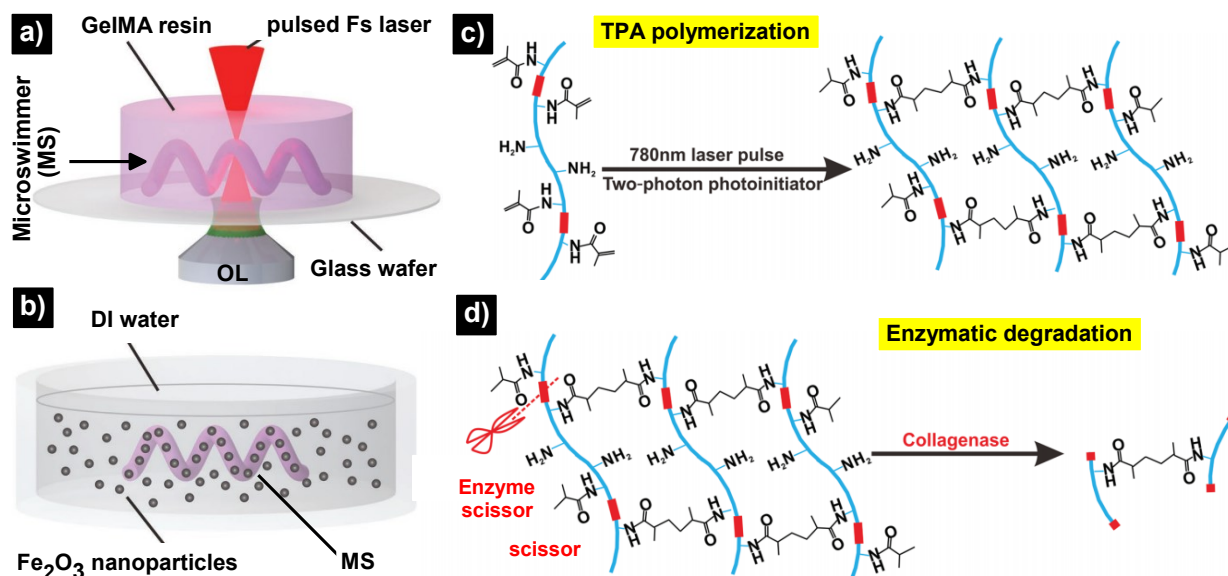


Figure I.22. Microfabrication of biodegradable GelMA helical MSs. **(a)** TPP-based FsLDW experimental setup; *i.e.* $\lambda = 780\text{ nm}$, 80 MHz repetition rate, OL of 0.63 NA . **(b)** Decoration of MSs with magnetic Nps by incubation in water suspensions of Fe_3O_4 for 1 h . Illustration of **(c)** TPP mechanism, and **(d)** Enzymatic degradation; *i.e.* enzyme scissor, of GelMA-based MSs [82].

Next, we report the application of MSs made from GelMA. Fig.I.23(a-b) displays the printed helical MSs under different laser powers and writing times, and Fig.I.23(c) shows the corresponding fluorescent image. Fig.I.23(d-e) presents the printed MSs of different sizes and cylindrical cross-sections, respectively. The size and shape of the printed MSs are tunable due to the nature of the TPP printing approach; *i.e.* pre-programmed pattern. Fig.I.23(f) presents the decorated MSs with Fe_3O_4 Nps. Note that the iron oxide Nps used in this study for the decoration of the printed MSs are coated with PVP in-order-to prevent particle agglomeration in solution [82].

Shown in Fig.I.23(g) is a cryo-SEM image (top) and the corresponding EDX mapping (bottom) of decorated MSs. The cryo-SEM and EDX mapping show that the Nps of Fe_3O_4 are uniformly distributed on the surface of the hydrated MSs. In biomedicine, the gelatin-coated iron oxide Nps

was demonstrated as a stable carrier for drug delivery [82,90]. Hence, it is hypothesized that a complex interplay of molecular interactions; *e.g.* hydrogen-bonds, are the driving forces for Fe_3O_4 adsorption on GelMA surfaces. This approach for functionalizing GelMA helical MSs is facile and can be extended to other functional particles [91]; *e.g.* sensing reagents or drugs [8].

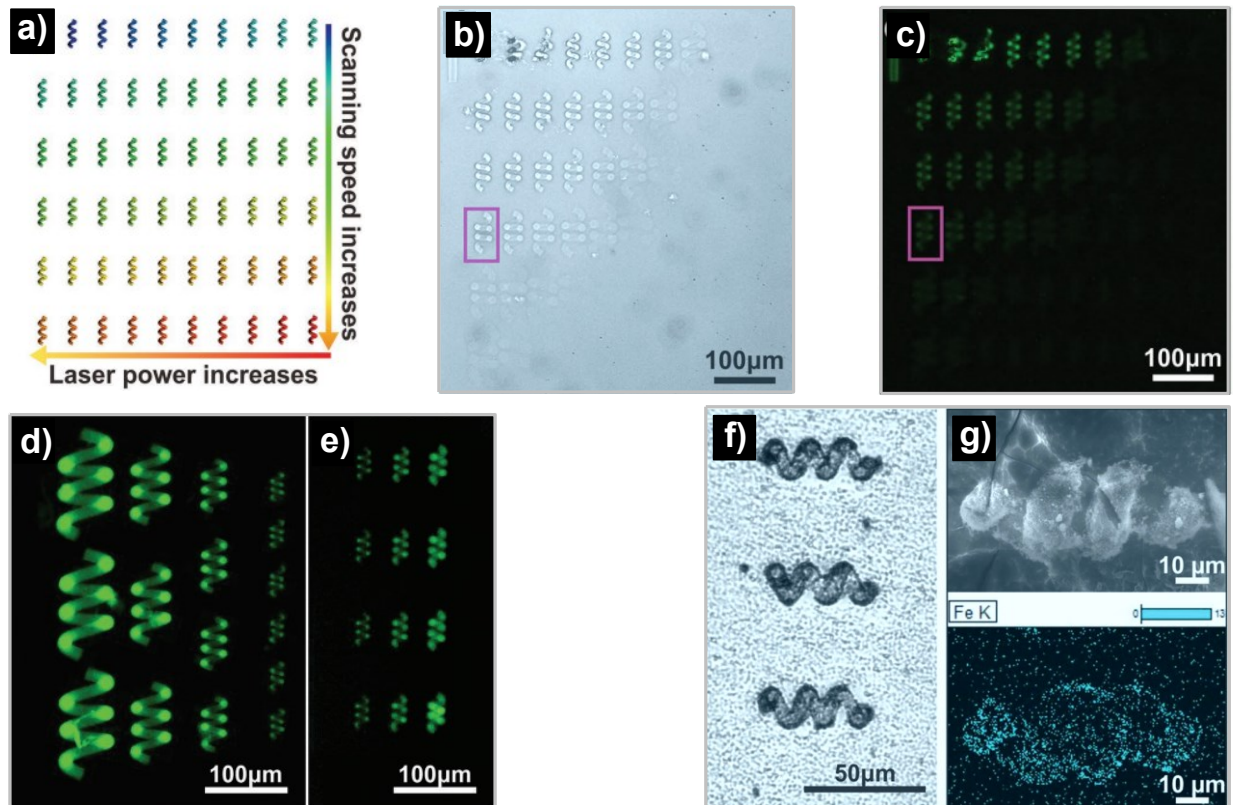


Figure I.23. Biodegradable MSs characteristics. (a) Color chart representing MSs that were printed at different exposure conditions; *i.e.* powers: 9.5 to 95 mW and writing speeds: 1, 3, 5, 10, 30, and 50 mm/s. (b) Optical image of the printed MSs in (a). (c) Corresponding fluorescent image of (a). (d-e) Fluorescent image of MSs printed with different sizes and thicknesses, respectively. (f) Optical image of MSs decorated with Fe_3O_4 . (g) Cryo-SEM (top) and EDX (bottom) mapping of iron corresponding to a hydrated MSs.

For the swimming test of the printed MSs, a rotating magnetic field of 8 mT was applied. Fig.I.24(a) shows a video screenshot showing the moving of MSs in a biological solution. Fig.I.24(b) displays the swimming velocities of MSs versus the frequency of the rotating magnetic field. At low frequency; *i.e.* < 6 Hz, produced MSs show a wobbling motion. Also, it is observed (Fig.I.24(b)) that the drift velocity was quite high and the forward one was relatively low, due to the interaction of MSs with the cover glass. As the frequency increased, the forward velocity significantly increased and the drifting effect lessened. Then, the swimming stabilized into the

corkscrew region with an increase of frequency [8]. This unique behavior is most probably caused by the soft nature of the TPP-printed MSs.

To characterize the mechanical softness of the printed MSs, the storage modulus (E') of the GelMA was measured in the duration of the photocrosslinking process, as shown in Fig.I.24(c). The E' of polymerized GelMA is in the range of 40–50 kPa, which is much lower than that of SU₈ resin (≈ 2 GPa), SU₈ is commonly used to 3D print rigid helical MSs that are needed for many applications. The low E' of GelMA-based resin indicates that the MSs are very soft and prone to tighten when they are subject to strong magnetic torques [92].

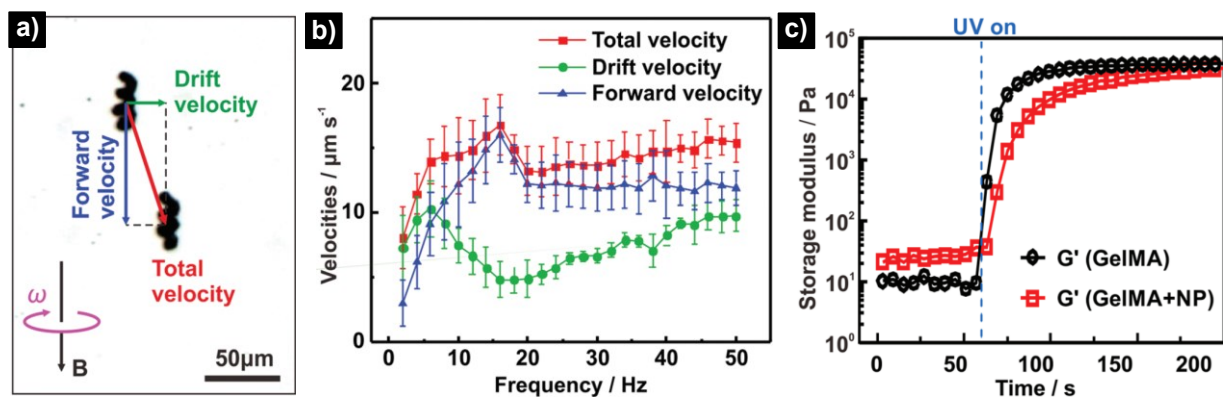


Figure I.24. Swimming performance of MSs. **(a)** Screenshots of a video showing a MSs moving in a biologically relevant solution. **(b)** Swimming velocities of MSs dependency on the rotational frequency. **(c)** Time-resolved E' of GelMA formulations during UV-induced photocrosslinking *W/O* Fe₃O₄ Nps, measured by in-situ photorheology: 20% GelMA in Irgacure 2959; the irradiation conditions were: UV laser source $\lambda \sim 365$ nm, $I_{\text{irr}} \sim 20$ mW cm⁻².

The biocompatibility (Fig.I.25(a)) and cytotoxicity (Fig.I.25(b)) of protein-based GelMA and PEGDA precursors; *i.e.* commonly used for 3D nanoprinting on hydrogels, were analyzed in solution with equal molar concentrations of terminal groups; *i.e.* acrylate and MA monomer [82]. After 24 *h* of cell incubation, the 3 tests of GelMA protein exhibited a negligible influence on cell metabolic activity. The biocompatibility and biodegradability of GelMA MSs are demonstrated (Fig.I.25(c)). Both PEGDA and GelMA are biocompatible molecules, the toxicity tests must focus on the influence of acrylates versus MA groups. C. Heller et al. [93] proved that the protein cytotoxicity caused by the high acrylate reactivity with the cell membrane proteins; *i.e.* Michael reactions.

It's known [82,93] that the acrylate has significantly higher cytotoxicity than MA groups. From Fig.I.25(a), PEGDA solutions at 30×10^{-3} and 60×10^{-3} M induced more than a ~ 90 %

decrease in cell viability. The diluted solution of PEGDA caused a lower decrease of cell viability due to the lower dosage of acrylate. Oppositely, the cytotoxicity of protein-based GelMA is negligible (Fig.I.25(b)), whereas the cytotoxicity of PEGDA is remarkably high as a function of acrylate dose. Shown in Fig.I.25(c) is the biocompatibility and degradability analysis of GelMA-based MSs.

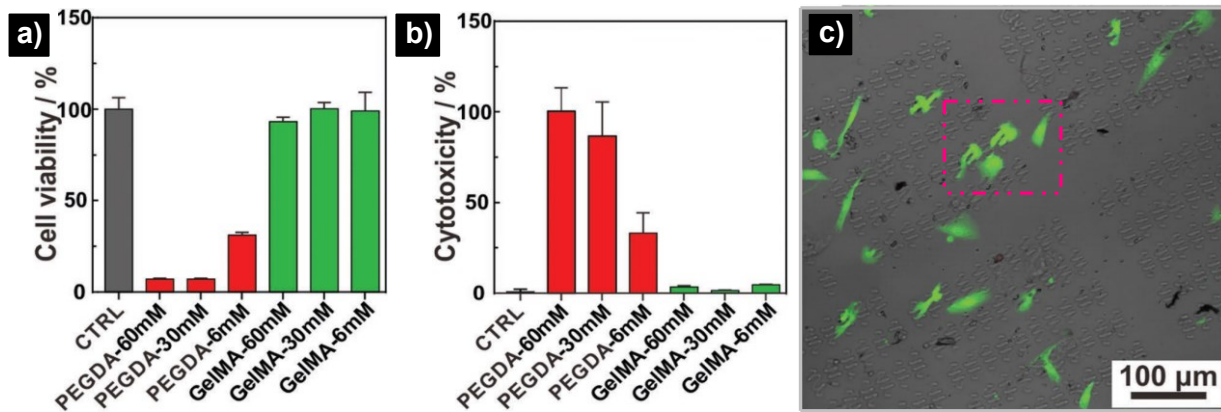


Figure I.25. Biocompatibility/degradability of GelMA-based MSs. **(a)** Cell viability after 1 day of incubation with GelMA and PEGDA solutions. **(b)** Cytotoxicity of GelMA and PEGDA solutions after 1 day of incubation; PEGDA was used as a reference. **(c)** Confocal microscopy image of live-dead stained human fibroblasts seeded on GelMA helices after half-day [82].

To confirm the compatibility of GelMA-based MSs with human cells, human skin fibroblast cells were cultured on arrays of the printed MSs (Fig.I.25(c)), and the negligible quantities of red-colored dead cells indicate excellent cell compatibility. Helical MSs powered by external magnetic fields possess significant potential in biomedical applications, due to their active locomotion, precise localization capabilities, and microscale wireless actuation [87]. Their untethered control and small size could allow deep tissue penetration and thus could revolutionize minimally invasive surgeries and therapies [8,82].

I.6. Conclusion

Nanophotonics addresses controlling, detecting, and 3D printing nano- features in a spatial sub-micron volume much smaller than that defined by the diffraction limit; *e.g.* the 3D equivalent of 2D pixels [40,45,102]. Essentially, there are two routes to access the SDL regime in optics; first is the near-field; *i.e.* based on sharp-tip induced photon tunneling of an evanescent field [94]. The second is based on the MPA technology; *e.g.* TPA, which possesses SDL resolution due to the NLO effect [95,96]. TPP-based 3D printing of functional devices with nanoscale features is an important task of nanophotonics [97]. 3D nanoprining still in its infancy and the subject of active

research has potential applications in diverse fields such as; optoelectronics [75], biology [83], micromachines [9], and so forth [7,88,98]. Thanks to TPP, the smallest features produced thirty years back were twice the irradiation wavelength; *e.g.* $\lambda_{irr} \sim 780 \text{ nm}$, but today they are twenty-time less; *e.g.* $\sim \lambda/21$ resolution [12]. Many research [26-29,99] has been done along this line, as we have reviewed and discussed in this chapter. Future research in TPP printing of functional microdevices is needed to further its use in diverse scientific research fields and industrial future applications. The innovation of TPA-based 3D nanoprinting and the birth of stimulated emission depletion (STED) microscopy has promised a lot for the reduction of the size of microdevices - nanomachines- in the future [100,101].

CHAPTER II

**Material for Two-Photon Absorption & 3D
Nanoprinting Optical Setup & Microfabrication
Controller-Software**

II.1. Introduction

Recently, photopolymerization by nonlinear absorption; *i.e.* two-photon polymerization (TPP), has been introduced to 3D nanoprinting; breaking the spatial-resolution boundaries set by the classical optics [6,9]. TPP printing is the process by which functional 3D microdevices were produced by tracing the focal spot of a pulsed; *i.e.* femtosecond (Fs), laser beam in a photopolymerizable resin [1,20]. The three most important components involved in the set-up of TPP 3D-printing are: (i) a Fs laser, (ii) a two-photon absorption (TPA) resin, and (iii) a pre-program pattern; *i.e.* the structures that need to be printed was pre-designed and programmed using a computer-aided design (CAD) model [6]. TPA provides the ability to confine photo-physical and chemical events; *e.g.* TPP, to the order of irradiation laser-wavelength in 3D (λ^3) [3,13], and the process of TPA has found applications in microscopy [102], 3D nanoprinting [18], data-storage [36], and biomedical [82,96].

Historically; in 1997, Maruo's group [10] introduced the first stereolithography (STL) machine based on the process of TPA, and they detailed it in subsequent research publications [18,21,28]. In the first segment of this chapter, we will discuss in detail the TPA material (photoresist) used in this work. In the second section, we will describe our custom-made optical system which we developed to perform the TPP nanoprinting. In the last section, we detailed the CAD program, G-cod, and .*stl* file, that are used to control the size and shape of structures hope printed through the TPP stereolithography. Structures data in .*stl* file insures the TPP-based 3D nanoprinting. We also show that the precision and stability of 3D nanoprinting depend on the positioning accuracy of the 3D stage translation and the alignment of the TPP optical setup.

II.2. Two-Photon Absorption Material (Photo-resist)

II.2.1. Introduction

A photo-resist; or -resin, is a light-sensitive chemical material. It is used in different industrials fields such as 3D lithography and photoengraving to form micro-nano-patterned structures [2,11]. The resin basically consists of a (i) monomer, *i.e.* individual unit of material, and a (ii) photoinitiator (PI), *i.e.* photoactive specie. Generally, the resin is divided into two groups, namely positive and negative [3]. The positive one means a type in which the irradiated part can be washed away by a developer [104]. Oppositely, the negative is a type in which the irradiated part remains after the washing step [12]. The developer means the solvent used for washing (rinsing) after light exposition [99]. The negative resin is further divided into groups; solid and liquid [3]; the solid one

is *e.g.* epoxy-based cationic resin; *i.e.* SU_8 [105], and the negative liquid-resins are commonly acrylate-based [27] and organically modified ceramics; *e.g.* *ORMOCER* [106,107].

II.2.2. Photopolymerizable Resin For 3D Nanoprinting

Developments in TPA material (resin) research have kept space with the commercialization of the Fs lasers [6]. The resin suitable for TPP nanoprinting must contain at least two basic components: (i) a PI system that will absorb light; *e.g.* in the IR region, and provide an active species that will cause TPP, and (ii) a pre-polymer monomer, which will become the polymeric backbone of the printed structures [12]. Due to the nonlinear optical (NLO) effect of TPA, the TPP reaction occurred only in the vicinity of the focal voxel. To achieve this event in the resin, the following conditions must be met [40,108]; (i) both the PI and monomer systems need to be transparent at the irradiation wavelength; *e.g.* $\lambda \sim 780 \text{ nm}$, (ii) the monomer needs to be transparent at $\lambda/2$, in order to overcome the thermal damage or laser ablation, and (iii) the PI needs to have a high TPA cross-section, highly-active radical species, and high radical quantum yield.

The mechanisms of light-matter interaction; *e.g.* by the use of UV or IR light, initiated photopolymerization are shown in Fig.II.1 [109]. The PI system can be excited by UV light; *e.g.* one-photon absorption (OPA), but it is transparent to longer wavelengths. Due to the NLO effect and by the use of an IR light; *e.g.* $\sim 780 \text{ nm}$, PI becomes electronically and vibrationally excited; *i.e.* TPA excitation (TPE) (Fig.II.1(a)). As shown by the initiation step in Fig.II.1(a), the PI system quickly relaxes by internal conversion on a time scale of picoseconds (*ps*); *i.e.* $1 \text{ ps} = 10^{-12} \text{ sec}$, and then undergoes intersystem crossing to a triplet state. Triplet states tend to have longer lifetimes, by the reason that their relaxation back to S_0 is quantum mechanically forbidden (Fig.II.1(a)) [40,109].

While in the triplet state, PI can α -cleave to yield radicals; *e.g.* α -cleavage generates R^* , as shown by the Jablonski diagram (Fig.II.1(a)). The R^* radical system is extremely reactive and will attack the double bond of carbon ($C=C$) to produce a new $C-C$ bond, as processed by the propagation step shown in Fig.II.2(b). Then, the new radical species continues the process of polymerization until R^* are fully consumed, as shown by the termination step (Fig.II.1(b)). Sometimes, molecular oxygen; *i.e.* $O=O$, can also act to terminate the propagation of polymerization by forming less reactive peroxy radical; this phenomenon is called quenching effect; see refs. [3,109] for more detail.

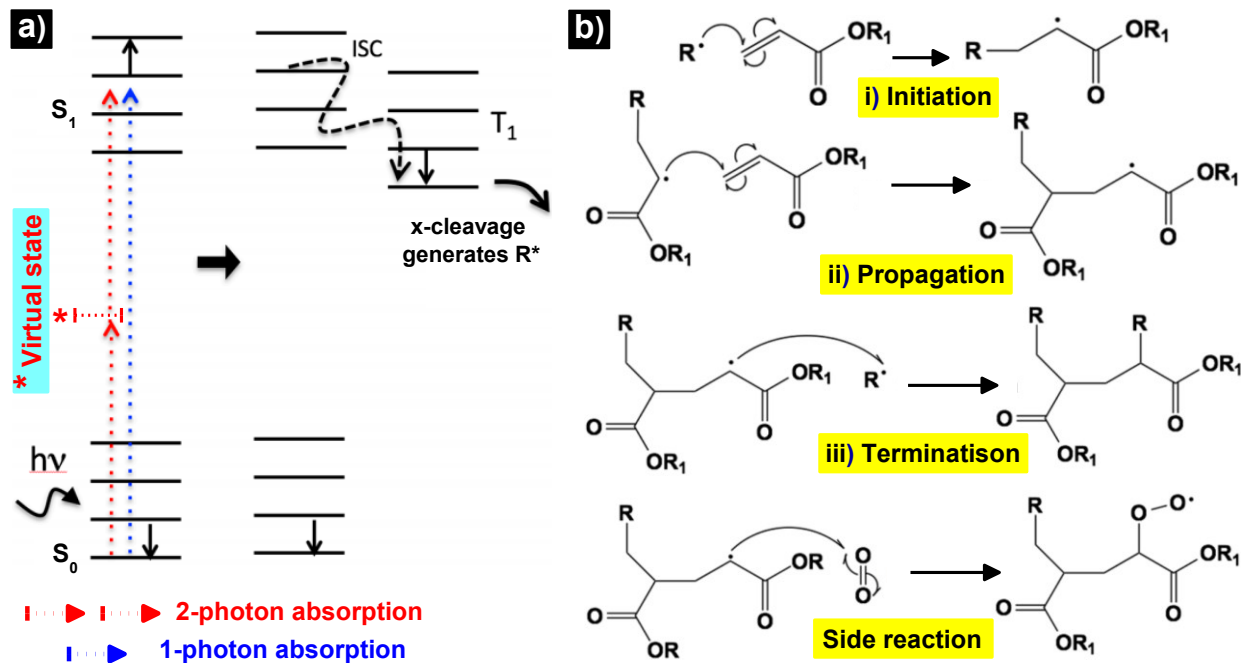


Figure II.1. Photopolymerization mechanism in resin. **(a)** Jablonski diagram where an electron in the PI become excited from the ground, S_0 , to an excited state, S_1 , either by absorbing UV light or two-photons of IR light. **(b)** Photopolymerization steps and side reaction, in which the radical-peroxy quench the propagation of polymerization; in this typical photopolymerization, an acrylate-based material is used. $h\nu$ denotes excitation energy [109].

In 3D nanoprinting, a NIR light; *i.e.* typically a Fs laser of $\sim 780\text{-}800\text{ nm}$ wavelength and $\sim 100\text{ fs}$ pulse, is used to initiate TPP [20,18]. Upon TPE, molecules can undergo near-simultaneous TPA, mediated by a virtual state (Fig.II.1(a)), and the combined energy of two-photons accesses an excited state (S_1). TPA involves the interaction of both photons that combine their energies to produce S_1 analogous to that caused by an irradiation of a correspondingly shorter wavelength; *i.e.* OPA. Unlike OPA, who's the probability is linearly proportional to the incident intensity, TPA depends on both a spatial and temporal overlap of the incident photons and takes on a quadratic dependence on the intensity (NLO effect of TPA). Thus, we can say that the photoresin used in TPP-based 3D nanoprinting shows a nonlinear response to the light excitation [3].

Shown in Fig.II.2(a) is the absorption spectrum of our methacrylate-based resin (MMA-resin) [108]. By using an UV-Vis spectrophotometer (Perkin Elmer-Lambda 1050), we show that our resin presents a strong optical absorption in the UV region; this is due to π - π bond of PI benzil. On the contrary, no absorption can be detected in the NIR region; *i.e.* nearly 100% transmittance, this suggests that the simultaneous TPA; initiates the TPP reaction (Fig.II.2(c)) [20].

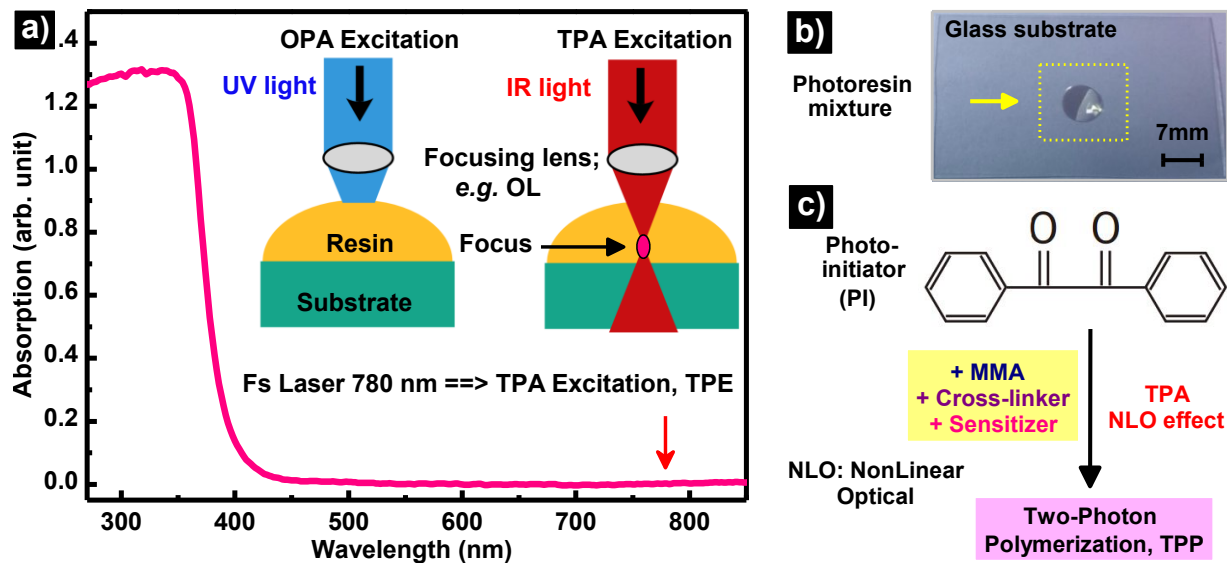


Figure II.2. (a) Absorption spectrum of the prepared resin; illustration of two typical absorption excitation: ($\hbar\nu$, OPA) and ($2\hbar\nu$, TPA) are shown as an inset; the wavelength of excitation is indicated by a red arrow on the spectrum. (b) The TPA-resin dropped on a glass substrate (used in 3D nanoprinting). (c) The chemical structure of the PI system and chemical mechanism of the TPP process.

The inset of the Fig.II.2(a) shows the difference between OPA and TPA during the interaction of light with resin. It is known that the continuous wavelength (CW) laser that is emitted at UV range; *e.g.* 405 nm, is absorbed along the path of the laser beam. The main difference between OPA and TPA is that TPA involves the simultaneous interaction of 2-photons, and so it increases with the squared light intensity (SLI) [110]. The SLI distribution related to the nonlinear absorption reduces the light-resin interaction (Fig.II.2(a)); thereby improving the resolution of 3D nanoprinting.

It is known from a long literature [3,40] that there are two critical components involved in the preparation of the resin which is used for TPP-based nanoprinting; *i.e.* a PI system and monomer. Other components; *e.g.* monomer, PI, photosensitizer, and cross-linker, can be added into resins to introduce new functions and performance to the nanoprinted structures. In the next sections, we will give a brief discussion of each compound involved in the preparation of our resin.

II.2.1.1. Methyl Methacrylate Monomer, MMA-M

Acrylates are extensively used in industry; and so are commercially available in a wide range of compositions and functionalities [6]. Recently, the majority of researches including 3D laser nanoprinting reported on the involved radical-polymerization with methacrylate monomers; *e.g.* MMA [12,27]. The monomer involved in the preparation of our resin is the MMA with an aspect ratio in weight of 49w%. The MMA act as the main skeleton of the printed structures; *i.e.* poly-

methylmethacrylate (PMMA). Fig.II.3(a) illustrates the semi-developed chemical structure of MMA-M, and Fig.II.3(b) shows the corresponding absorption spectrum [12]. From Fig.II.3(b), it is observed that the MMA-M shows negligible absorption in the UV range. Due to the mono-functionality of MMA-M, it is experimentally demonstrated that it is difficult to fabricate stable structures by only using MMA-M as a TPA-resin (recording media). Thus, it is necessary to introduce few amounts (*e.g.* $\sim 1\text{w}\%$) of PI to MMA, in order to prepare an efficient TPA resin [20].

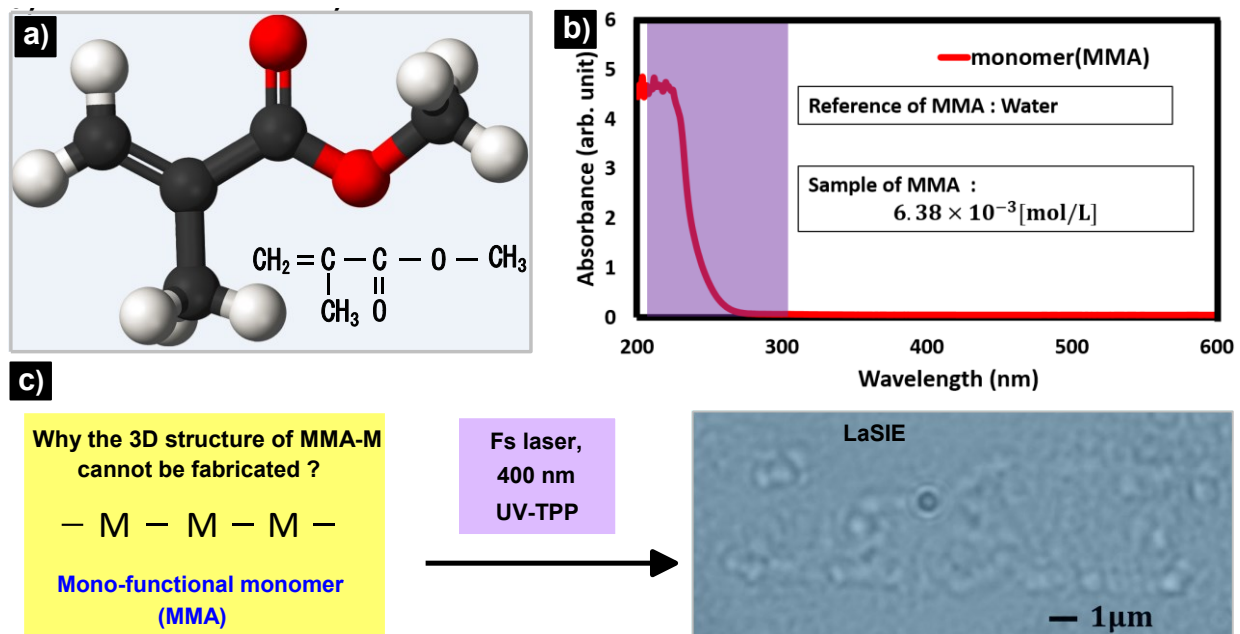


Figure II.3. Methyl methacrylate monomer. (a) Chemical structures of MMA-M. (b) The corresponding absorption spectrum. (c) TPP-based Fs UV laser writing on MMA; the inset is a bright-field image of the 3D pattern of LaSIE that was printed using TPP. We use as focusing parameters, laser source $\lambda = 400 \text{ nm}$, power: $\sim 90 \text{ mW}$, and exposure time 4 ms .

Acrylates group generally have high rates of polymerization, which makes them attractive candidates for TPP-based 3D printing. Methacrylates have favorable mechanical properties and are chemically resistant to harsh solvents used for rinsing step [20]. TPP nanofabrication on acrylate resin started in 1997, when Maruo's group [10] fabricated a 3D spiral with a diameter of $\sim 7 \mu\text{m}$ and $\sim 50 \mu\text{m}$ long spiral-coil with a line cross-section less than $\sim 2.2 \mu\text{m}$ (Fig.II.4(a)).

In our work, we characterize the nonlinear properties of the MMA-based resin in TPP printing of nanostructures using our developed TPP optical setup [110]. The SEM images of some of these structures are shown in Fig.II.4(b-c). In particular, the SEM image of MAScIR pattern presents some nanoscale features of $\sim 94 \text{ nm}$; *i.e.* $\sim \lambda/8.5$ resolution. The SEM image shown in Fig.II.4(c)

depicts the SDL fibers with a polymerized width of $\sim 121\text{ nm}$; *i.e.* $\sim \lambda/6$ resolution [12]. We found that the achieved TPP resolution with our resin is limited by the radical diffusion and growth of polymer chains that are proceed outside of the illuminated region focal (*i.e.* around the LFS) [108].

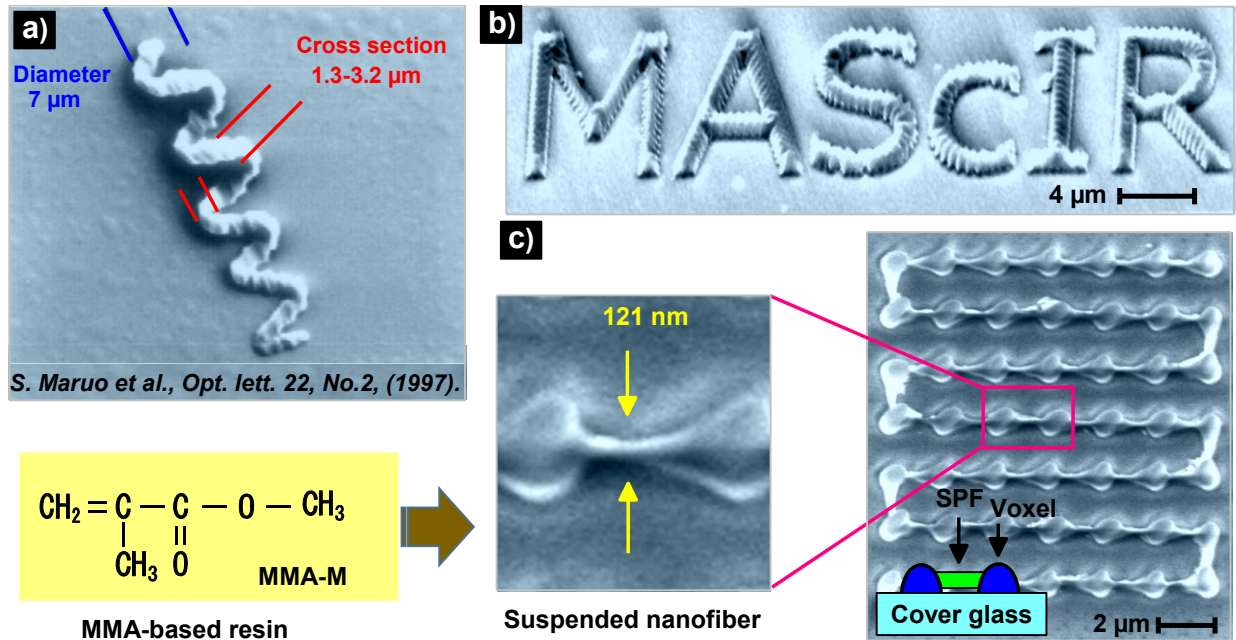


Figure II.4. TPP microfabrication on MMA-based resin. (a) The first 3D structure fabricated by TPP on acrylate-based resin; the chemical structure of MMA-M is shown as an inset. (b) 3D microstructures of MAScIR. (c) Achievement of SDL fibers that were two-photon polymerized between two adjacent-voxels. The typical laser intensities are $\sim 1.14 \times 10^9\text{ mW cm}^{-2}$ in (b) and $\sim 1.80 \times 10^9\text{ mW cm}^{-2}$ in (c) [12].

MMA-resin is considered as a fast recording media to achieve a high speed (scanning) of 3D nanoprinting; meaning that the MMA-M can be instantaneously polymerized just after interaction with excitation light. Thus, rapid and performance TPP enables high-speed of TPP nanoprinting of large-scale [111]. Upon TPE, MMA-M has a much smaller molecular weight and consists of one or several reactive groups. Reactive groups play an important role in determining the TPP efficiency; *e.g.* stability and precision of the printed structures [43,111].

Upon TPE, the monomers may be solidified by two means; (i) polymerization or (ii) crosslinking. An important feature of (i) TPA polymerization is the chain reactions; *i.e.* propagation phase, in which the polymerized macromolecules are created. While (ii) the cross-linking is more concerned with the formation of crosslinks with chemical bonds of the polymerizable species [110,112]. The difference between these two types of reaction lies in their quantum yield (Φ), which is defined as the ratio of the number of the polymerized monomer units to the number of the incident photons that are needed to induce these photoreactions. In the case of photocrosslinking, the addition of

each monomer unit requires the absorption of a photon, leading to a Φ less than 1. In contrast, polymerization is processed via many chains of reactions [40,112].

II.2.2.2. Photoinitiator (PI)

To trigger TPP, a nonlinear photoactive material is needed; *i.e.* PI system. In our work, we use as PI the benzil (Initiator, Wako) with a ratio of 1wt% relative to the resin mixture [20]. The chemical structure of the PI-benzil is shown in Fig.II.5(a). PI is employed for generating the free radical; *i.e.* an active species, after TPE (Fig.II.5(d)). An ideal PI needed for TPP printing should be easily synthesized, nontoxic, and have high stability in darkness (to avoid degradation), and high quantum yield in the generation of active moieties, and highly soluble in the resin [3]. When the PI absorbs a suitable photon's energy; *i.e.* $2h\nu$, it is transformed into a reactive initiating species; *e.g.* radicals or cation radicals, as shown by the initiation step in Fig.II.5(d). Fig.II.5(b) shows the PIs excitation profiles by the use of OPE (left) and TPE (right) process [28].

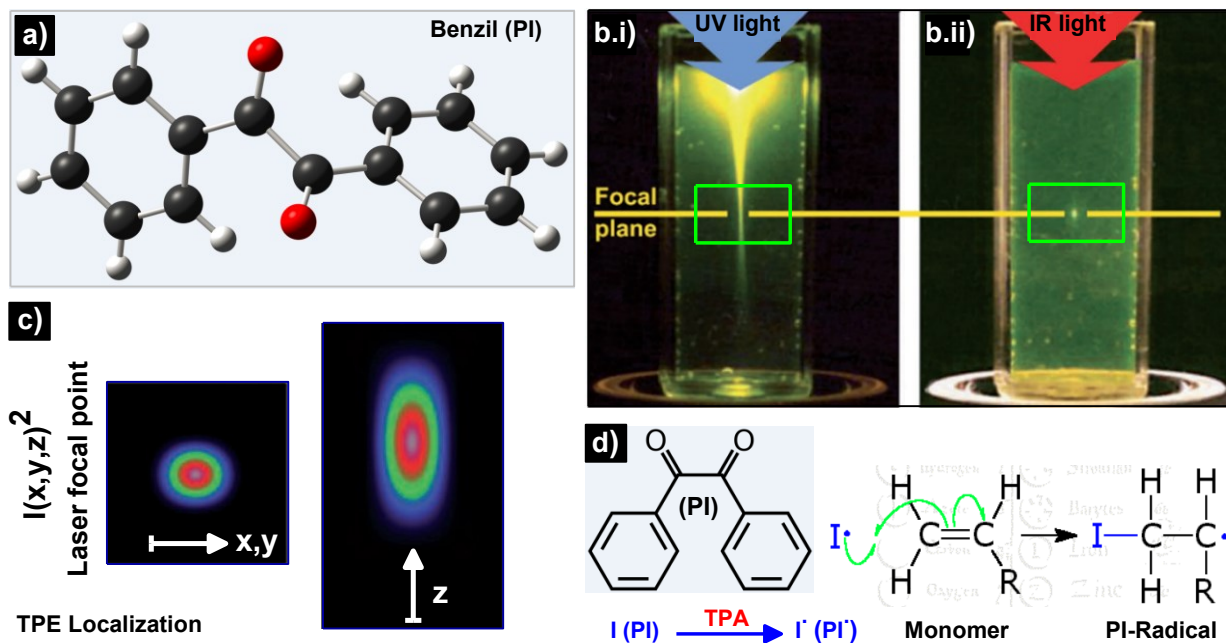


Figure II.5. TPA initiator and polymerization mechanism. (a) Chemical structures of PI-benzil. (b) TPA vs. OPA mechanism; two laser beams are focused on a photosensitive solution; *e.g.* PI; (i) the left beam is tuned at UV range at which OPA can take place, (ii) the right one at IR range that can excite the molecules by TPA. (c) Lateral and axial views of the LFS where TPE was triggered. (d) Photoinitiation mechanism of polymerization via an excited PI-benzil [52].

Cationic PIs are photoacid generators that produce cations upon TPE. Cation radicals are used for TPP of epoxides or vinyl ethers via a cationic mechanism. The photolysis of cationic PIs has been shown to result in the generation of free radicals allowing the combination of monomers to be TPA-

polymerized. Conventional PIs generate free radicals upon excitation, which initiate a free-radical polymerization process of vinyl ethers or acrylates group [40]. The most commonly used free-radical PI is benzophenone and its derivatives; *e.g.* benzil, as shown in our previous work [108].

From the Fig.II.5(b), if the laser beam is focused into the photosensitive material; *e.g.* PI, at a suitable wavelength for OPA; *i.e.* UV light, molecules are excited throughout the beam path, as evidenced by the fluorescence emission in the top part of the cuvette (Fig.II.5(b.i)). If the laser beam is tuned at a wavelength at which the material exhibits TPE ($\sim 800\text{ nm}$ Fs-laser), only the molecules located very close to the LFS are excited (Fig.II.5(b.ii)), this is related to the fact that the excitation rate depends on I^2 . At the LFS (Fig.II.5(c)), the intensity takes their maximum; *i.e.* NLO effect, and decreases approximately with the square of the distance from the focal plane along the z -direction [20].

II.2.2.3. Photosensitizer (PS)

An additional requirement for effective initiation of polymerization induced by TPA is the photosensitizer (PS); thus, we use 2-Benzyl-2-(dimethylamino)-4'-morpholino-butyrophenone (97%) (Sensitizer, Aldrich) as PS system (1wt%) [27]. The chemical structure of the used PS is presented in Fig.II.6(a), and the corresponding absorption spectrum is shown in Fig.II.6(b). The PS exhibits a strong absorption in the UV range; this is due to π - π bond of the aromatic cycle. On the contrary, it relatively shows negligible absorption in the NIR region; *e.g.* at 780 nm (Fig.II.6(b)).

After absorption of an IR light, PS is capable to absorb and transfer the excitation energy to the PI system, as shown by the photo- mechanism illustrated in Fig.II.6(c). Consequently, their emitted fluorescence in the UV-Vis region will be absorbed by the initiator with special chemical reactivity and give rise to the radical's species (Fig.II.5(d)). Then, the radicals react with the monomers; *i.e.* $-C=C-$; resulting in the generation of monomer radicals; *i.e.* $-C-C^{\bullet}$ -, which would expand in a chain reaction until two radicals meet and undergo termination of TPP [3,108].

Farsari's group [113] reported the TPP induced photocrosslinking of pre-polymer-based protein. They produced 2D and 3D microstructures on avidin, bovine serum albumin, and biotinylated bovine serum albumin. The multiphoton photocrosslinking of proteins was demonstrated with a nontoxic biomolecule flavin mononucleotide (PS-system). Microsized structures were fabricated from several different compositions of protein and sensitizer. Refer to ref. [113] for more detail.

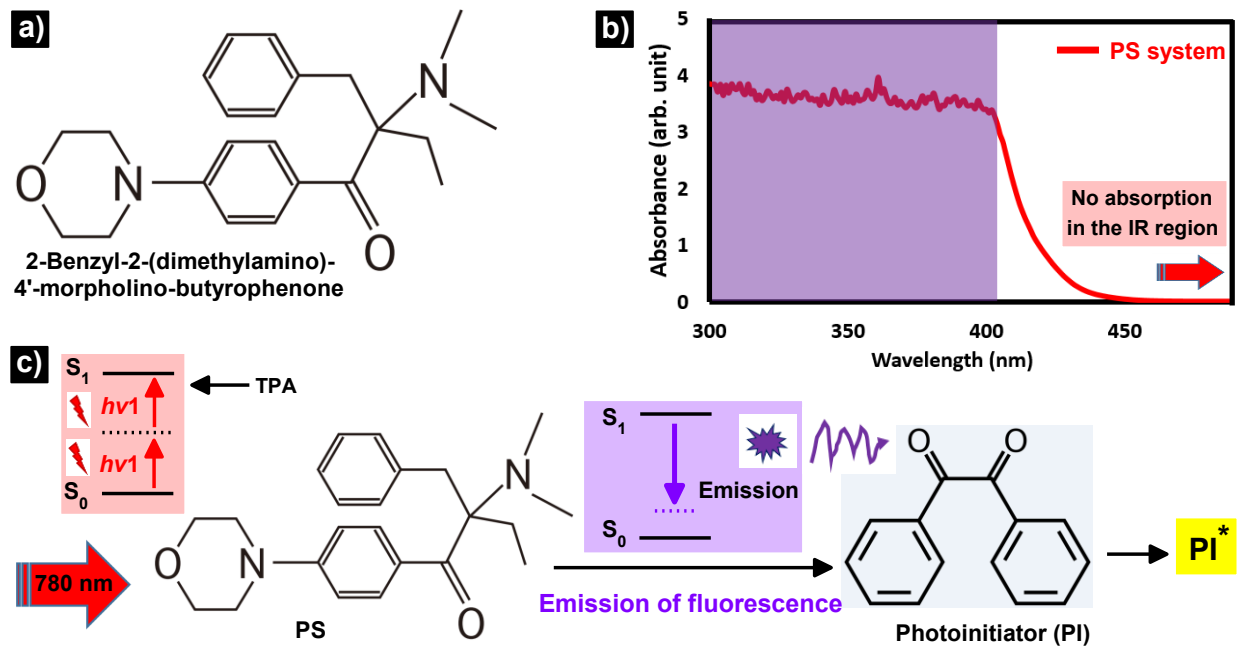


Figure II.6. Photosensitizer proprieties and functionalities. (a) Chemical structure of PS. (b) The corresponding absorption spectrum. (c) The functionality of PS including in two-photon mechanism; i.e. the fluorescence emission from the PS to PI; PI^* denotes the PI after absorbing UV emission from the PS.

Y. L. Sun et al. [114] used TPP to produce microarchitectures on a sensitizer-based protein. The protein molecules are TPA-crosslinked in the presence of the PS to form a hydrogel. As a TPA medium, they used a commercial bovine serum albumin and a PS (methylene blue) to fabricate microarchitectures; e.g. protein microlenses. Generally, the TPA cross-section is one of the most important factors that determine the potential for the application of a PS in 3D laser nanoprinting.

II.2.2.4. Cross-Linker: DPE-6A

The third compound involved in the preparation of our resin is the crosslinker DPE-6A (Kyoeisya Chemical CO., LTD) with a ratio of 49wt%, which ensures the insolubility of the resin; e.g. chemical stability, in the duration of the developing phase [108]. Fig.II.7(a) presents the semi-developed chemical structures of DPE-6A, and Fig.II.7(b) shows the corresponding absorption spectrum. It is clearly observed that DPE-6A presents a negligible absorption in the UV range. Thus, DPE-6A presents an attractive candidate for deep UV-based TPP 3D-nanoprinting (Fig.II.7(c)).

DPE-6A can be used alone as a prepolymer media for TPP 3D-printing (deep UV nanofabrication) by the use of a Fs laser emitted at $400\text{ nm} = 800\text{ nm}/2$ wavelength. Comparing to MMA monomer; DPE-6A is a poly-functional monomer; thus, it can be photo-crosslinked under appropriate manufacturing conditions; e.g. deep-UV. In polymer chemistry, the functionality of a

monomer means its number of polymerizable groups and affects the formation and degree of crosslinking of polymers [3]. A monofunctional molecule possesses one function, a difunctional means two polymerizable groups, and a trifunctional contain three groups that can be polymerized, etc. [115].

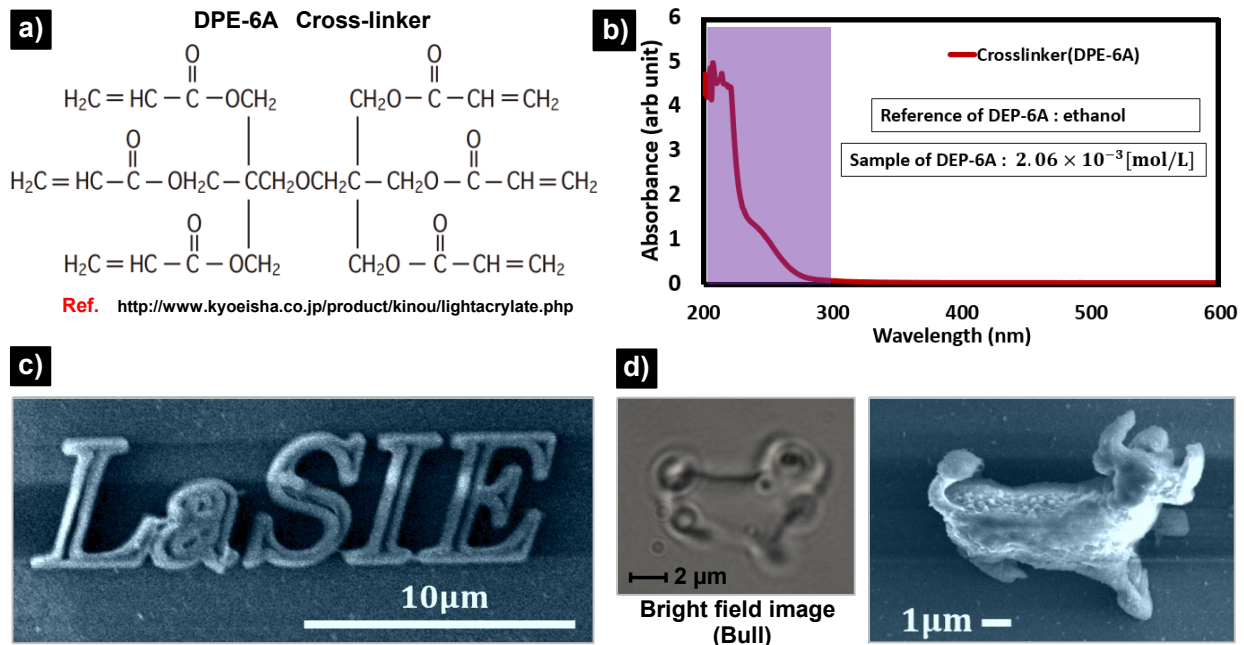


Figure II.7. DPE-6A properties and applications. (a) Chemical structures of DPE-6A cross-linker. (b) The absorption spectrum of DPE-6A. (c) Illustration of the achievement of SDL fabrication accuracy; i.e. SEM image of LaSIE pattern that was two-photon printed on DPE-6A. (d) SEM image of a 3D microbull. The fabrication conditions are: $\lambda = 400$ nm Fs laser, 4 ms exposure time, and 30 mW laser power.

Fig.II.7(c) presents the nanoprinted structures by the use of DPE-6A as a recording media for deep UV-based 3D printing. Shown in the inset of Fig.II.7(d) is the bright field image of the printed microsized bull on DPE-6A. A high spatial resolution of less than ~ 100 nm was achieved via this novel nanofabrication process. In this novel TPP-based 3D nanofabrication, a BBO crystal was used to change the pulsed laser wavelength from 800 nm to 400 nm.

II.2.2.5. Raman Spectroscopy: Analysis of TPA material

Recently, raman microspectroscopy is proved to be an effective, and rapid, and nondestructive tool for investigating the chemical properties of the pre-polymer resin, as well as the nanoprinted structures [44]. Methylmethacrylate resin cross-linked through the two-photon process, resulting in a cross-linked-PMMA. Fig.II.8(a) shows the raman spectrum of each compound involved in preparing our resin. Shown in Fig.II.8(b) is the raman data obtained from the polymerized; i.e. solidified, state of the resin (printed structures). From Fig.II.8(a) and the literature [27,116], a

raman peak of the cross-linked-PMMA at $\sim 545 \text{ cm}^{-1}$ is assigned to the carbon-carbon ($C-C-C$) skeletal mode in PMMA and cross-linker, and a peak at $\sim 1595 \text{ cm}^{-1}$ is assigned to a raman mode of benzene rings in the PI and PS systems. Shown in Fig.II.8(c) is a raman mapping of a printed structure using TPP; *e.g.* MAScIR pattern.

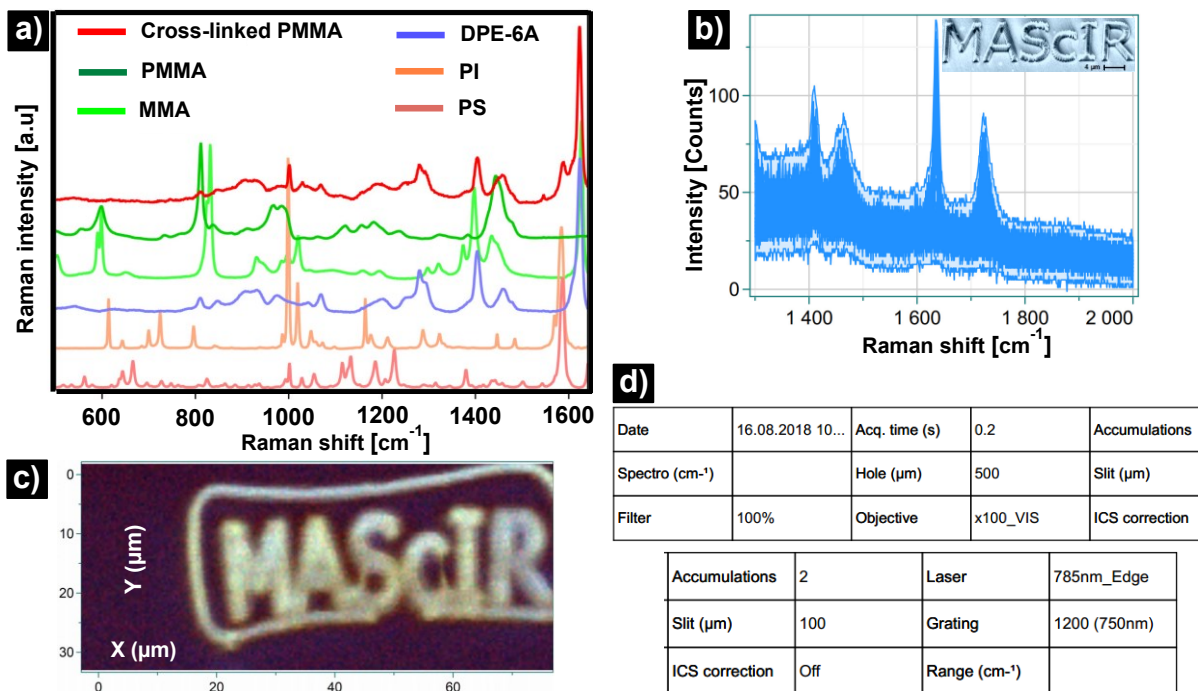


Figure II.8. Investigating chemical properties via raman spectroscopy. **(a)** Raman spectrum of: materials used for preparing our resin; *i.e.* (green) MMA-M, (blue) cross-linker, (orange) PI, and (pink) PS, and (red) cross-linked PMMA, (yellow-green) PMMA [12]. **(b)** Raman spectrum of polymerized resin; *e.g.* MAScIR structure; many spectra are shown in this data. **(c)** Raman elementary mapping; with 1400, 1595 cm^{-1} . **(d)** Parameters used for raman measurement; a laser wavelength of 785 nm is used as light source.

Upon TPE induced polymerization, the $C=C$ double bonds of the ester units in the MMA-M are consumed to form $C-C$ single bonds; *i.e.* TPP propagation, leading to a highly crosslinked polymer; *e.g.* PMMA. Raman measurements indicate that the $C=C$ bonds gradually disappear in the duration of the TPP process. L. J. Jiang et al. [44] investigated the degree of conversion (DC) of the acrylic resin upon TPA-polymerization through raman spectroscopy; the DC is used to quantify the amount of the consumed double bonds upon TPP. For acrylic monomers, chain addition takes place in the $C=C$ bonds that are presented in the molecule's ester moiety. However, the DC is related to the crosslinking of the ultimate polymers [117]. Refer to ref. [44] for more detail.

The DC of the liquid resin; *e.g.* acrylate resin, can significantly affect the final stability, precision, and mechanical properties of the nano-micro-printed polymeric structures [118]. Thus, establishing

the correlation between the TPP focusing parameters and the corresponding DC is a fundamental step to achieve a precise and stable 3D nanoprinting process. Raman spectroscopy was conducted to investigate and characterize the constituent of the resin before and after the TPP process.

II.3. Experimental: TPP Optical Setup

II.3.1. Introduction

Here, we will experimentally demonstrate the use of the technology of TPP-based 3D nanoprinting (Fig.II.9) to fabricate various polymeric structures with near-diffraction-limit features; *e.g.* $\sim 100\text{ nm}$ resolution. Our optical setup used to perform TPP 3D-nanoprinting comprises at least three key components: (i) Fs laser source, (ii) beam delivery system; *i.e.* focusing optics, and (iii) 3D positioning system [12,20]. Shown in Fig.II.9 is the setup of our developed TPP optical system.

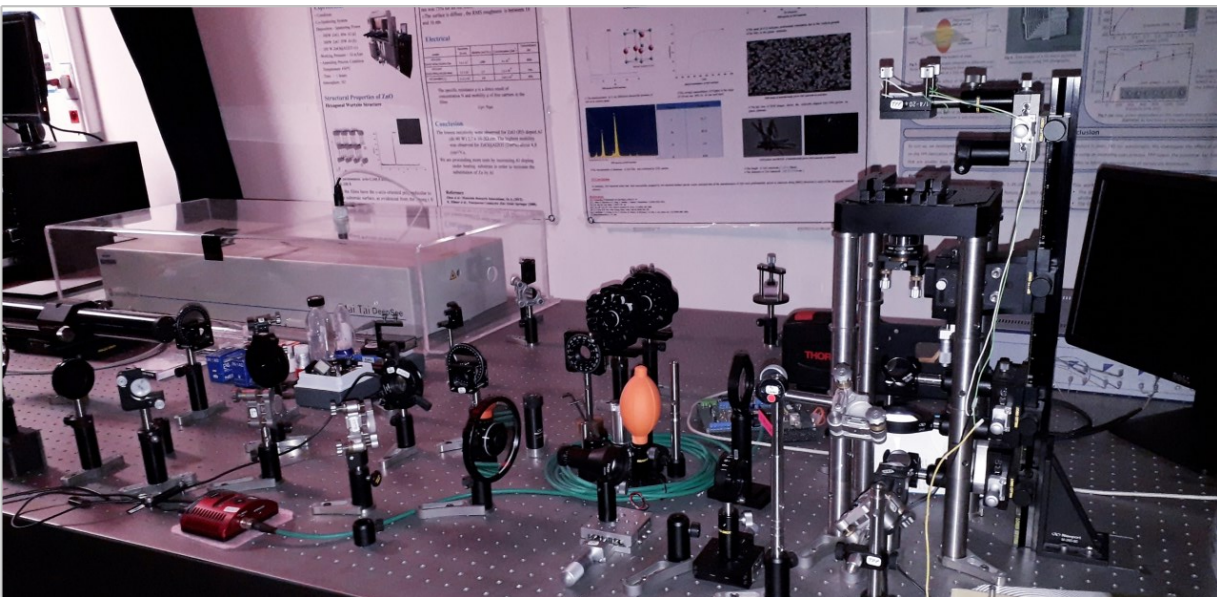


Figure. II.9. The optical set-up used for our TPP-based 3D micro and nanofabrication; in our laboratory [12]. The output stability of the pulsed-laser-power and the accuracy of laser focus/sample scanning guarantee high precision of TPP nanoprinting. An inverted microscope is used as a focusing optic.

As a light source (in our experiments), we use a Ti: sapphire Fs laser (Mai Tai: Spectra-Physics) system emitted at 780 nm wave-length, $75\text{-}140$ pulse width, and 80 MHz repetition rate. For focusing optics, an objective lens (OL) of $NA=1.4$ was employed (Fig.II.9). The choice of TPP stereolithography for achieving SDL spatial resolution depends on various adjustable parameters, including LFS size, focusing lens NA, and required laser dose [20,108]. The ultimate beam properties will be determined by the combination of Fs laser and the OL which focuses light. High

reproducibility of the peak power; *i.e.* maximum optical power of a pulse, of the Fs-laser is needed to achieve high precision of TPP nano-micro-printing.

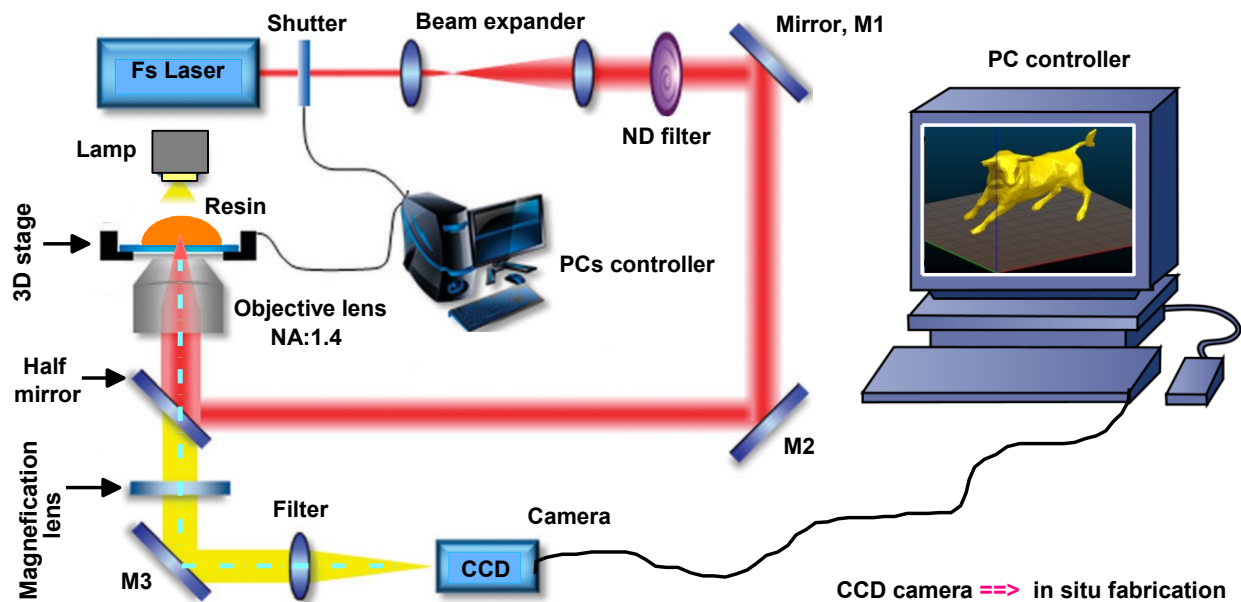


Figure II.10. A schematic drawing of our TPP nanoprinting setup; the 3D stage means a 3D piezoelectric translator. The models of the pr-programmed structures were created by a homemade software. The high NA lens is critical to launching near-diffraction-limit resolution [2,12].

For the nanopositioning system, we use a 2D piezoelectric stage (P-517.2CL, SN110024792, Multi-Axis Piezo Scanner) with 1 nm step; *i.e.* in the x- and y-direction, which allows moving the sample during TPP processing. The nano-positioning in the z-direction was assured by the motorized OL (which focuses light). In addition to these components, our TPP set-up usually includes other elements; *e.g.* illumination, real-time process observation; *i.e.* CCD camera, Filters, and lenses, as presented in Fig.II.10. Next, we will detailly discuss the light sources, focusing optics (OL), and nano-positioning systems from the viewpoints of the underlying concept, characteristics, and performance [108].

II.3.2. Femtosecond (Fs) Laser System

Ultrashort-pulse laser, include Fs laser that emits light pulses duration of 1 ps or less; that means in the range of Fs duration; *e.g.* $1fs = 10^{-15}s$ (Fig.II.11) [119,120]. The generation of such short pulses is nearly always achieved with the technique of passive mode-locking. Mode locking is a method; or actually a group of methods that are employed to obtain ultrashort pulses from lasers; *i.e.* mode-locked systems. Fig.II.11(a) shows the basic characteristics of a pulsed laser [121]. In

our TPP set-up (Fig.II.11(b)), the optical pulses generated from a mode-locked system are extremely short; *i.e.* in the range of 75-140 *fs*.

TPP induced by the Fs lasers is currently the hot topic of technical research as it offers the most promise for micromachining of complex and functional microsized architectures (3D micro-objects) [3]. Also, Fs lasers exhibit excellent capability in performing 3D processing in transparent materials; *e.g.* glasses, which makes them a powerful processing tool for manufacturing optical fibers. Optical fiber is typically made from transparent silica glass and functions as an optical waveguide; *i.e.* only slightly larger than that of a human hair; *e.g.* $\sim 100 \mu\text{m}$ [122].

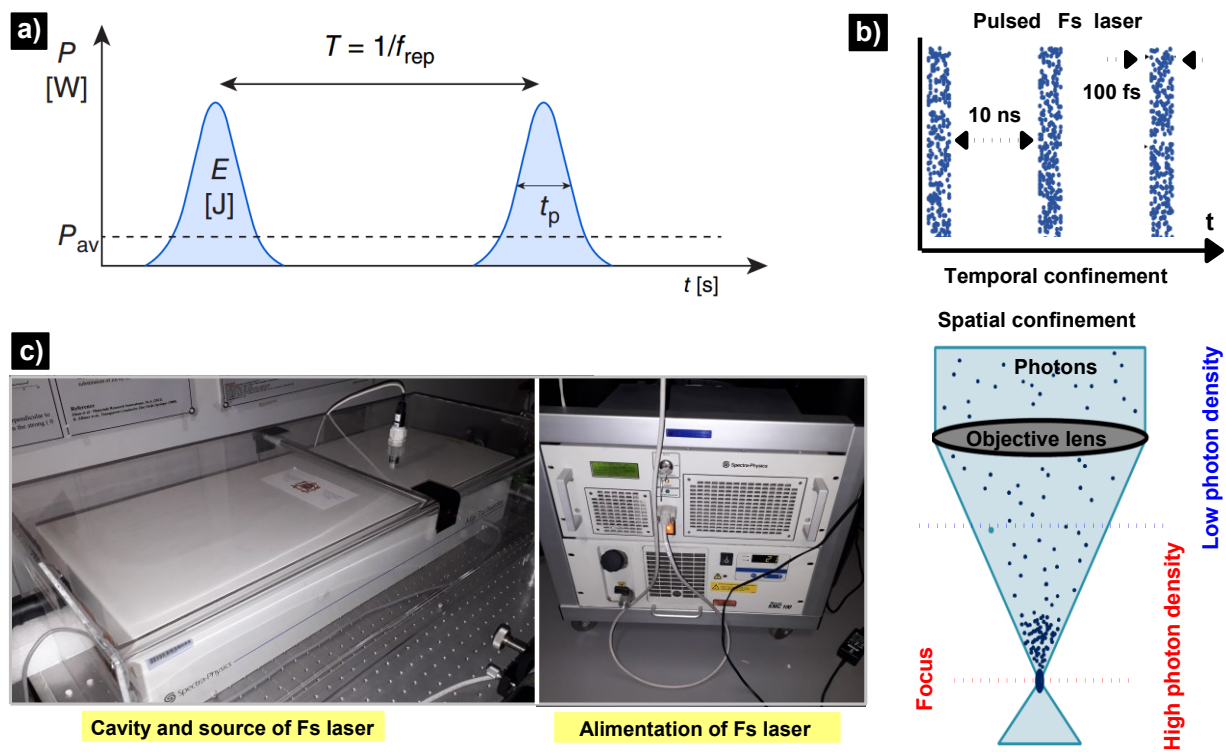


Figure II.11. *Fs* laser characteristics and proprieties. **(a)** Basic characteristics of laser pulses: P , E , $P_{av} = E * f_{rep}$, f_{rep} , and t_p denote pulse power, pulse energy, average power, repetition rate, and pulse duration, respectively. **(b)** Temporal (top) and spatial (bottom) confinement of photons that are coming from *Fs* laser system; a high NA-OL was used to focus the coming photons to a smallest possible 3D volume in space; *e.g.* voxel. **(c)** *Fs* laser system (in our laboratory); including laser- alimentation (right), cavity and source (left) [120,121].

Generally, the Ti: Sapphire oscillator lasers, Spectra-Physics Mai Tai®, are employed for a variety of applications ranging from general to multiphoton microscopy. With properly chosen optics, Ti: sapphire laser (Fig.II.11(b-c)) delivers a range of wavelengths from $\lambda=690 \text{ nm}$ to 1080 nm , and pulse duration $< 20 \text{ fs}$ [119,123,124]. The light source used for TPP nanoprinting was strongly impacted the nonlinear process by its physical properties. Relevant properties include (but are not

limited to): (i) laser wavelength; *i.e.* in the NIR region that is limited by the optical absorption of the resin, (ii) pulse energy, (iii) pulse duration, (iv) repetition rate, (v) spectral bandwidth, and (vi) beam quality and profile [124].

II.3.2.1. Fs Control Software: The Main Menu

A special version of LabWindows™ software is provided by spectra-physics for controlling the Mai Tai HP system [125]. A command-line interface allows this control through the RS-232 serial connection. As shown in Fig.II.12(a), the main menu allows the operator to monitor the Fs laser system; *e.g.* turn it ‘on’ and ‘off’, set the operation wavelength, and open and close the shutter. It monitors pulsed laser output power, and it shows the system status, including whether or not the laser is pulsing; *e.g.* mode-locked, and the shutter is open and that the computer is successfully communicating with the laser system (RS-232 Active) [125].

Inside the cavity of the Fs-laser system, several sliders control the laser parameters that serve to modify how the applet laser functions. The pulse width slider can be utilized to adjust this value between 75 and 140 *fs*, and the wavelength slider operates the tuning slit to vary output wavelengths from 690 to 1040 *nm* (Fig.II.12(a)). Shown in Fig.II.12(b) is the absorption and emission spectra of Ti: Sapphire. Here, the titanium ion Ti^{3+} is responsible for the laser action of Ti: sapphire. See more detail in the Fs laser manual [125].

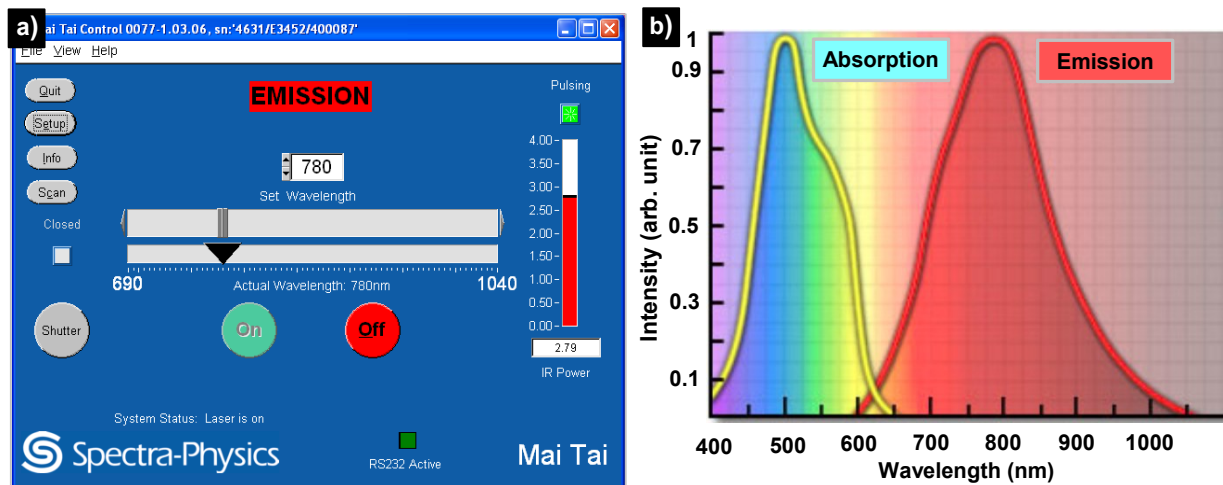


Figure II.12. Fs laser control and properties. (a) The Main menu showing the optional sub-menu buttons; The RS232 active is shown by a green color. Here, the Fs-laser is fixed at 780 nm wavelengths. (b) Absorption and emission spectra of Ti: Sapphire.

As shown in Fig.II.12(b), the absorption transitions occur over a broad range of wavelengths from 400 *nm* to 600 *nm*. Fluorescence transitions; *i.e.* induced by titanium ion Ti^{3+} , occur from the

lower vibrational levels of the excited state to the upper vibrational levels of the ground state. The resulting emission and absorption spectra are shown in Fig.II.12(b). Although the fluorescence band extends from wavelengths as short as 600 nm to wavelengths greater than 1000 nm , the lasing action is only possible at wavelengths longer than 670 nm because of the long-wavelength side of the absorption band overlaps the short-wavelength end of the fluorescence spectrum [125].

The main menu presented in Fig.II.12(a) appears when the control software of the Fs laser system starts (green button), following the com port setup menu. The five control features of the main menu include: (i) emission on/off, (ii) shutter open/close, (iii) wavelength select/monitor, (iv) IR power monitor, (v) sub-menu selection. From this menu, the operator can access three other sub-menus: setup, info, and scan [125]. To get high performance and stability of the Fs laser system, the parameters of these menus need to be accurately controlled.

II.3.2.1.1. The Setup Menu

The setup menu presented in Fig.II.13 is for use by spectra-physics service personnel only. The information shown on this display is not required for the routine operation of the Fs laser system. Therefore, these controls are not described here, but in the service manual [125].

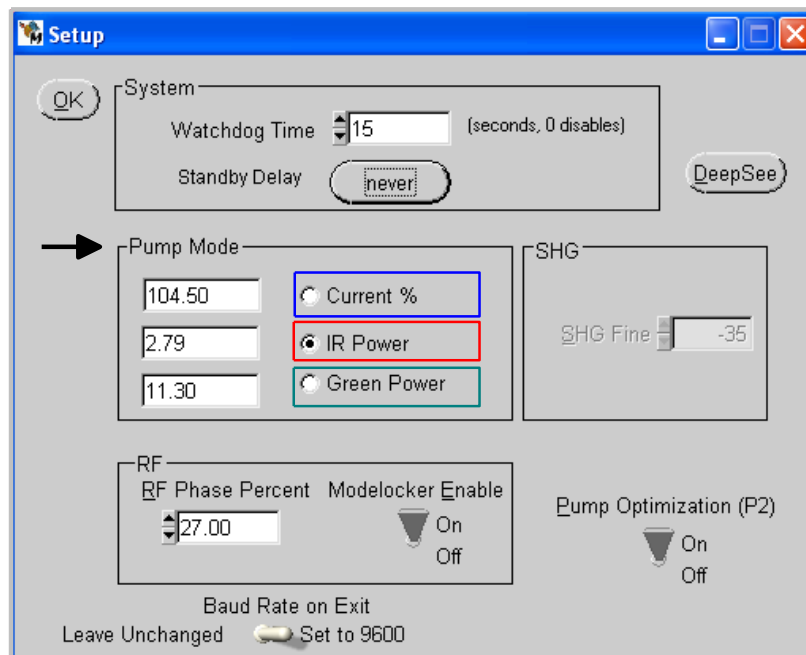


Figure II.13. The setup menu. The OK button is used to return back to the main menu. The three pump modes; i.e. current %, IR power, green power, of the Fs laser system are shown in the menu [125].

For caution, the setup menu parameters are set at the factory for optimum system performance. Not that this menu doesn't use to modify any parameters; *e.g.* watchdog time. In particular, it wasn't used to change the pump power setting. Increasing pump power may actually decrease output performance. These controls are for diagnostic purposes only and are to be used only by someone trained by spectra-physics. They are three pump modes, (i) current %, (ii) IR power, and (iii) green power. During 3D nanoprinting, the pump is fixed at the IR power mode [123,125].

II.3.2.1.2. The Info Menu

The info menu shown in Fig.II.14 provides information's on several important parameters of the laser system and it is for informational purposes only. Pump power indicator shows internal pump laser output power; *i.e.* in watts ($1W = 10^3mW$). Different wavelengths require different power settings and this value is dependent on the selected wavelength. This menu gives a general idea about different critical conditions of the pulsed laser during the emission process. See the Fs laser manual for more detail [125].

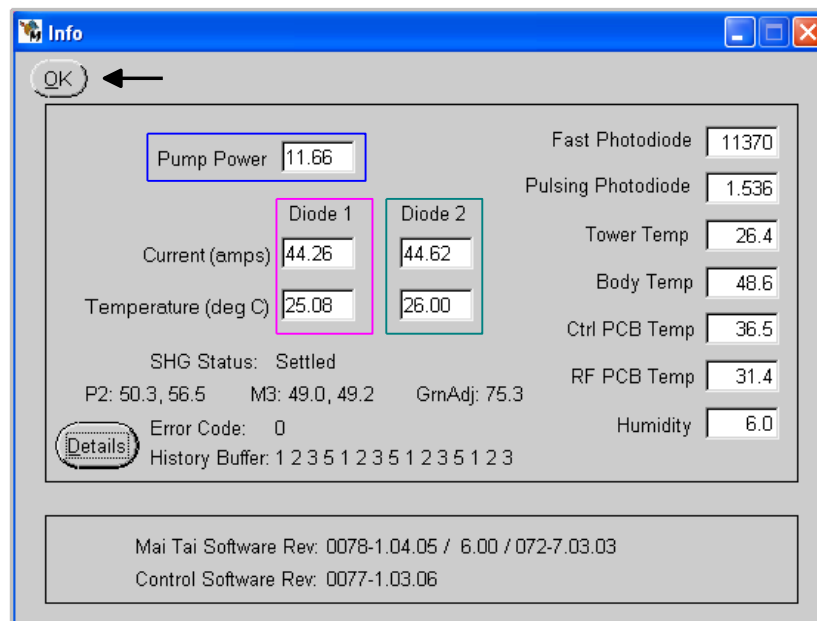


Figure II.14. The info menu, OK button means returns to the main menu. The settings affiche in this menu of the pump power depend on the wavelength; *i.e.* obtained by selecting $\lambda = 780 \text{ nm}$; 780 nm represents the wavelength used for TPP-based 3D nanoprinting (in this thesis).

II.3.2.1.3. The Scan Menu

The scan menu shown in Fig.II.15 provides a means to scan from a beginning to an end wavelength in pre-settable steps, to stop at each step for a preset period of time, and to turn the scan function on/off [125].

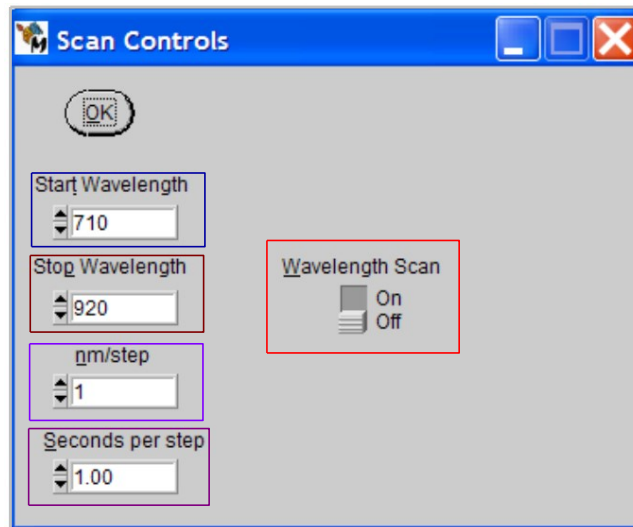


Figure II.15. The scan menu, OK button: returns to the main menu regardless of the wavelength scan switch setting. The change of the wavelength is controlled by 1 nm step.

II.3.2.2. Femtosecond (Fs) Laser Specification

Table II.1 lists the optical performance specifications for the Mai Tai HP laser system. Table II.2 lists the mechanical specifications. Table II.3 lists the environmental specifications [125].

Output Characteristics ¹	690 nm	700 nm	800 nm	920 nm	1020 nm
█ Average Power ²	>500 mW	>1 W	>2.5 W	>1.35 W	>400 mW
█ Peak Power ²	>60 kW	>120 kW	>310 kW	>165 kW	>50 kW
█ Pulse Width ³			100 fs		
█ Tuning Range ⁴			690 – 1020 nm		
█ Repetition Rate ⁵			80 MHz		
█ Noise ⁶			< 0.15%		
█ Stability ⁷			< ±1%		
█ Pointing Stability			< 50 μrad/100 nm		
█ Spatial Mode			TEM ₀₀		
█ Beam Roundness			0.9 – 1.1		
█ Astigmatism			<10%		
█ Beam Diameter at 1/e ² points			< 1.2 mm		
█ Beam Divergence, full angle			< 1 mrad		
█ Polarization			> 500:1 horizontal		

Table II.1. Mai Tai HP optical specifications. At $\lambda \sim 800$ nm, the laser system delivered a maximum output power; i.e. ~ 2.5 W that is corresponding to a peak power of ~ 310 kW [125].

Table Key:

¹Due to our continuous product improvement program, specifications may change without notice.

²Specifications apply to operation at the wavelength noted.

³A sech^2 pulse shape (0.65 deconvolution factor) is used to determine the pulse width as measured with a Spectra-Physics Pulse Scout autocorrelator.

⁴The Mai Tai HP is also available with a fixed factory preset wavelength within the wavelength ranges noted.

⁵Laser operation is specified at a nominal repetition rate of 80 MHz.

⁶Specification represents rms measured in a 10 Hz to 10 MHz bandwidth.

⁷Percent power drift in any 2-hour period with less than $\pm 1^\circ\text{C}$ temperature change after a 1-hour warm-up [125].

■ Size (L x W x H)		
Laser Head, Scientific	23.4 × 13.8 × 5.8 in.	59,5 × 35,0 × 14,7 cm
Laser Head, OEM	19.50 × 13.25 × 5.48 in.	49,5 × 33,7 × 13,9 cm
Model J80 Power Supply	17.9 × 19.0 × 6.9 in.	45,5 × 48,3 × 17,5 cm
Umbilical Length	10 ft	3 m
■ Weight		
Laser Head, Scientific	70 lb	32 kg
Laser Head, OEM	65 lb	29,5 kg
Model J80 Power Supply	49.5 lb	22,5 kg
■ Power Requirements		
Model J80 Power Supply	110 Vac $\pm 10\%$, <10 A, 60 Hz / 220 Vac $\pm 10\%$, <6 A, 50 Hz	

Table II.2. Mai Tai HP mechanical specifications.

For Indoor Use Only	
■ Altitude	Up to 2000 m
■ Ambient temperature	10 – 40°C
■ Maximum relative humidity	80% non-condensing for temperature up to 31°C
■ Mains supply voltage	See Specification Table on preceding page
■ Insulation category	II
■ Pollution degree	2

Table II.3. Environmental specifications [125].

II.3.2.3. Typical Tuning Curve

Shown in Fig.II.16 is the typical tuning curve of the Fs laser system (in our laboratory) which presents the emitted output power as a function of laser wavelength. The inset of Fig.II.16 shows the Fs laser system parameters employed for our TPP-based 3D nanoprinting. It is observed from the curve shown in Fig.II.16 that the maximum of the output laser-power of our Fs laser system is delivered when the wavelength is located near $\sim 780\text{ nm}$; thus, in our experiment of TPP-based 3D nanoprinting, we employed 780 nm as light source of TPA excitation (to induce stable and efficient TPP reaction). Not that the change of the laser wavelength can influence on the stability of the Fs-laser system; *e.g.* cavity mirror, (even by 1 nm step).

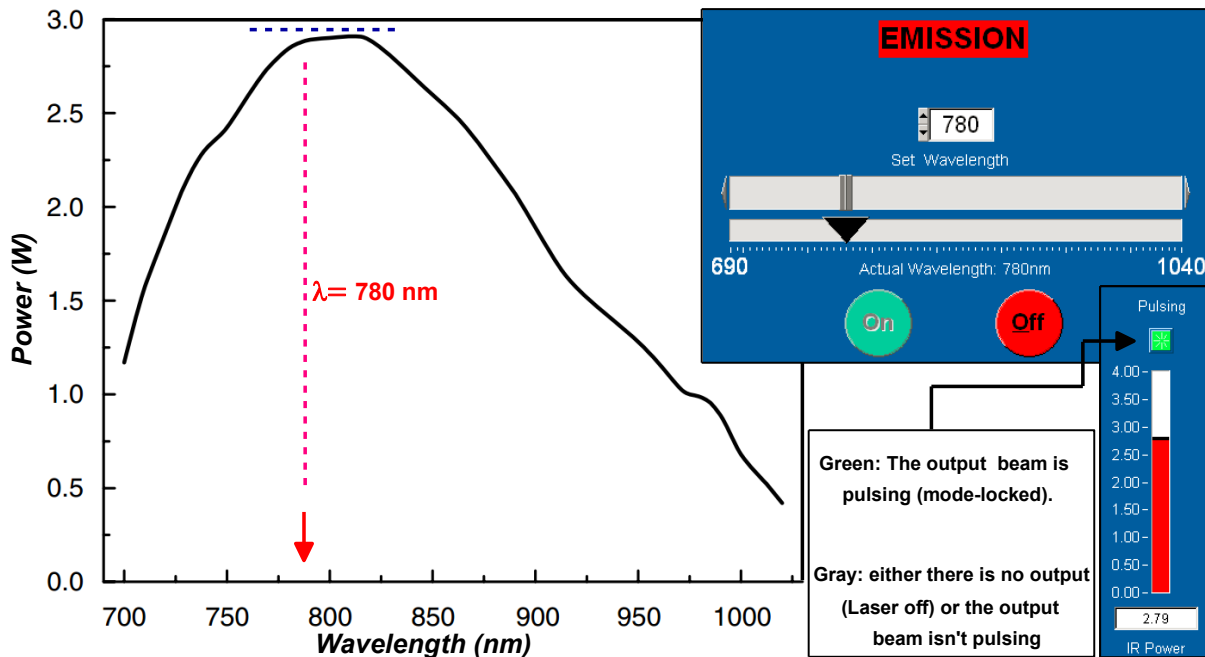


Figure II.16. Mai Tai HP tuning curve. The irradiation wavelength is indicated on the curve by a red arrow [125]. The pulsing mode and the main menu are shown as an inset. The maximum output of laser power is localized near ~ 800 nm.

II.3.3. Tight Light Focusing: Focusing Lens

The high laser intensity required to induce TPP; meaning that short and intense pulses lead to a local solidification of the resin, necessitates a tightly LFS delivered from an OL of high NA [42]. Also, to achieve high spatial-resolution of 3D printing, it is most favorable to use high focusing NA (~ 1.4); where $NA = n \sin\alpha$, and $n = 1.51$ is the refractive index of the immersion oil, and α denotes the half opening angle [20,126,127]. From the literature [9,28], it is well noted that all the OLs which focuses light within 3D nanoprinting are $1.4 \sim NA$, 100 x; corresponding to a half opening angle of $\alpha \sim 70^\circ$, 100 x is the OL magnification needed for monitoring (imaging) [128,129]. In our TPP optical system, we developed a costume-made inverted microscope; *i.e.* tight light focusing, as shown in Fig.II.17(a).

In our lab, we use a fully homebuilt inverted microscopic set-up for providing better mechanical stability and accuracy of 3D nanoprinting (Fig.II.17(a-b)). As presented in Fig.II.17(a), we focus the laser beam pulses by using an oil immersion OL of ~ 1.4 NA; yielding an intensity on the sample in the order of $\sim 10^9$ $mW\ cm^{-2}$ (inset of Fig.II.17(b)) [29]. This is the typical laser intensity needed to trigger TPE (TPP). Thanks to the NLO effect, TPP occurred only in the vicinity of the LFS and the size of the printed voxels was reduced to be much smaller than λ^3 ; $\lambda \sim 780$ nm [12].

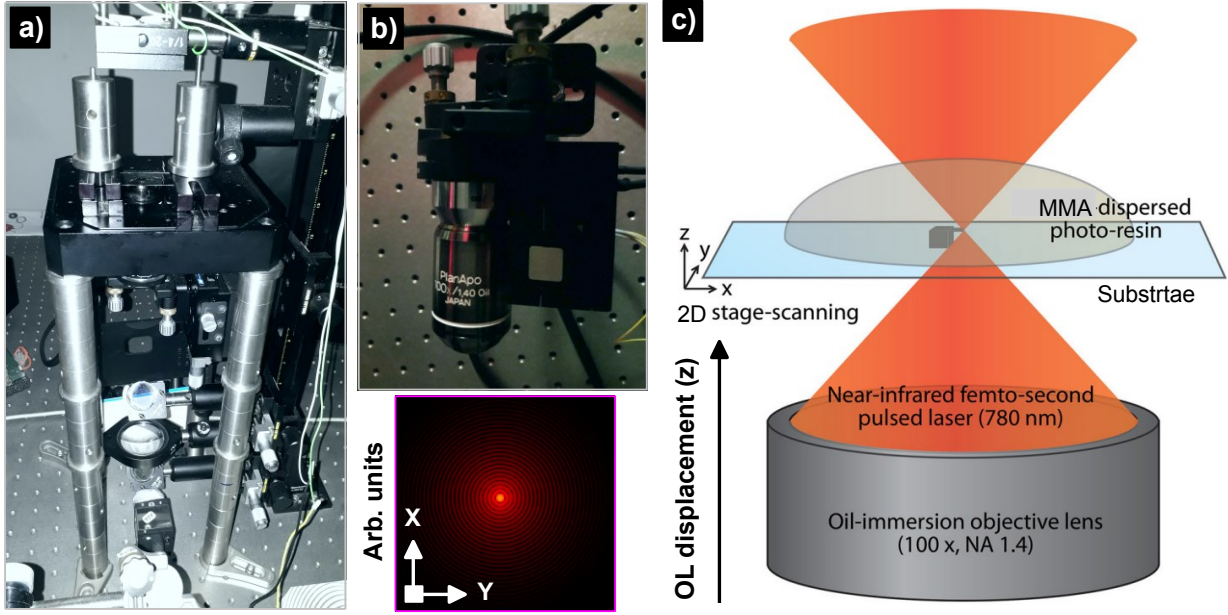


Figure II.17. Tight light focusing; *i.e.* OL. (a) Inverted microscope system used for 3D nanofabrication; *i.e.* based on a 1D piezostage for controlling the laser focus in the z -direction, dichroic mirror, lens for magnification, and a CCD camera for monitoring. (b) The immersion oil OL ($NA = 1.4, 100\times$) which is used to focus light. The inset is the diffraction pattern at the focal plane. (c) Experimental layout in cross-section for TPP-based 3D nanostructuring [129].

Shown in Fig.II.17(c) is the presentation of the tight focusing system that is based on an OL of 1.4 NA. Close matching of indices allows avoiding spherical aberration, and laser intensity is delivered to the focal volume without strong distortions [129]. Shown in the inset of Fig.II.17(b) is the focal diffraction pattern. Because of the tight focusing, polarization effects become pronounced; *e.g.* the LFS becomes slightly elongated along the direction of linear polarization [128]. The calculations of linearly polarized (E -field) beam at the LFS was done via the scalar Debye theory; see the ref. [128] for more detail. Vectorial Debye's theory predicts that a high focusing NA; *i.e.* $NA > 0.7$, breaks the cylindrical symmetry of the focal electric field distribution in 3D (xy, z) and a corresponding elongation takes place with alteration of E_x or E_y (axial) and E_z (longitudinal distribution) components [130].

Generally, in 3D nanoprinting, TPP only triggered around the LFS (voxel) (Fig.II.17(b)). The focal electric field is expressed as denoted in Eq.II.1 [130]:

$$E(r, \Psi, z) = \left(\frac{\pi i}{\lambda}\right) \{ [I_0 + \cos(2\Psi) I_2] i + \sin(2\Psi) I_2 j + 2i \cos(\Psi) I_1 k \}, \quad (\text{II.1})$$

Where i, j and k are the unit vectors in the x, y , and z directions, respectively, and the variables r, ψ , and z are the cylindrical coordinates of an observation point [128]. The integrals I_0, I_1 , and

I_2 are cumbersome to handle but can be straightforwardly calculated by integration over the focusing angle θ for a chosen apodization function [128]. Therefore, the irradiation light is depolarized at the focal region with a preferentially elongated LFS along the linear polarization direction of light; *e.g.* in the z -direction. A numerical simulation for the sin-apodization function $P(\theta)=\sqrt{\cos(\theta)}$, where θ is the focusing cone covering $0-\alpha$ with $NA = n \sin\alpha$. On the other hand, for a circularly polarized beam, scalar focusing is used to calculate the submicrometric focal volume; *i.e.* 3D voxel (Eq.II.2) [128,131].

$$E_{sc}(r, \Psi, z) = \frac{2\pi i}{\lambda} \int_0^\alpha P(\theta) \sin(\theta) J_0(kr \sin(\theta)) e^{-ikz \cos(\theta)} d\theta, \quad (II.2)$$

Analysis of light delivery at the tight focusing presented here shows the importance of the use of high NA as a focusing optic in TPP-based 3D nanoprinting by the use of high-repetition-rate pulses [20,128]. By precisely adjusting the focusing intensity in combination with low exposure time, 3D architectures with near-diffraction-limit features have been produced. TPP resolution is governed by NA focusing and the used excitation wavelength; *e.g.* $\sim 780 \text{ nm}$ in our case [12,108].

II.3.4. Nano-Positioning Translation System: Piezostage (PZT)

To accurately nano- translate the sample; *i.e.* the dropped resin on the cover glass, during 3D nanoprinting relative to the las, a high-resolution piezo-based translation system is needed. In our 3D microfabrication set-up (in our lab), a high-precision nanopositioning system (P-517.2CL, SN110024792, Multi-Axis Piezo Scanner) with two directions (x, y), possesses a resolution step of 1 nm was used (Fig.II.18(a-b)) [110]. Our PZT system offers a nano- writing/scanning travel that ranges of $100 \times 100 \mu\text{m}^2$; *i.e.* TPP-processing zone. While the LFS scans the sample in the z -direction using the motorized microscope OL (Fig.II.17(b)). The longitudinal dimension (in the z -direction) of the structures that need to be printed is restricted by the working distance (WD) of the OL; *i.e.* $WD \sim 200 \mu\text{m}$ in general for a 1.4-NA immersion oil OL [20].

To realize TPP stereolithography with a near-diffraction-limit resolution, the accuracy and stability of the positioning system need to be precisely controlled. Fig.II.18 displays the motorized piezo stage (in Fig.II.18 (a)) and their controller (in Fig.II.18 (b)) used in our 3D nanoprinting set-up. Shown in Fig.II.18(d) is a voxel-by-voxel (point-by-point); *i.e.* voxels accumulation, followed by layer-by-layer nanostructuring that were involved in the process of TPP nanoprinting in-order-to fabricate freestanding 3D micro-nano- objects from a pre-programmed CAD model [6,40]. Thus,

designed structures are solidified (polymerized) by moving x - y with-respect to the z -position of the laser's focal spot. Each layer is individually cured on the top of the previous one by lowering the stage after every layer; *i.e.* along the z -direction (z -pitch), as shown in Fig.II.18(c) [20].

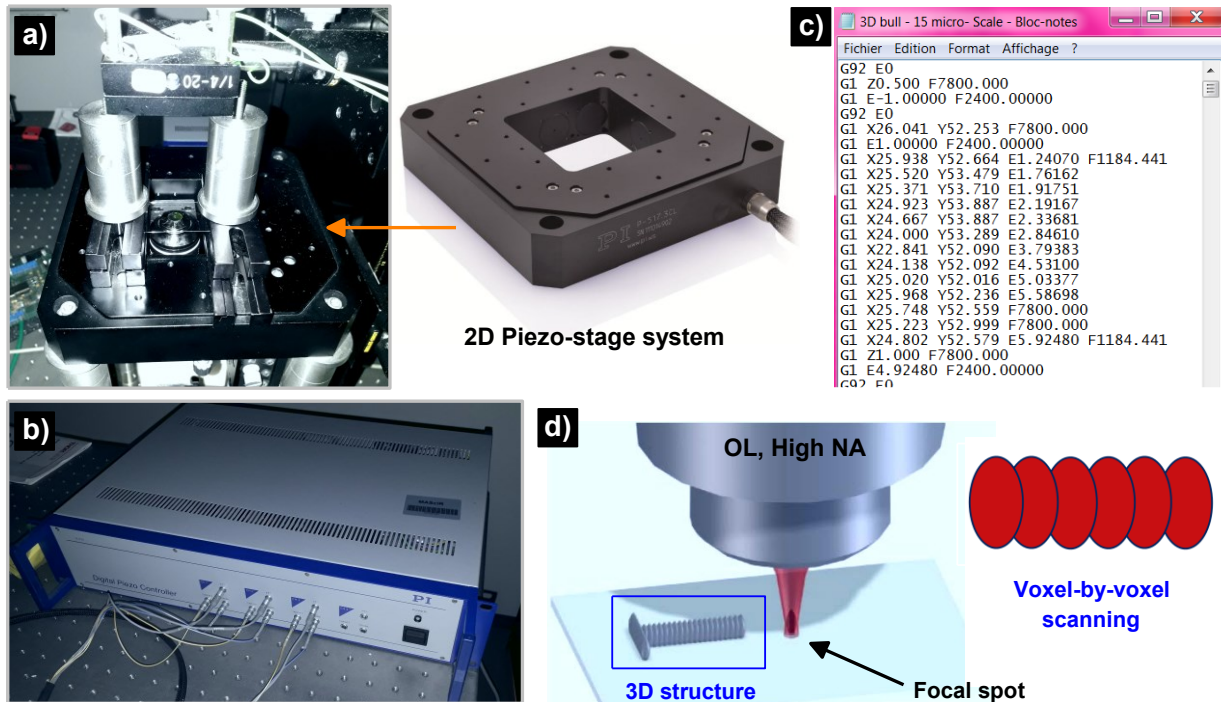


Figure II.18. Nano-positioning translation system. **(a)** 2D PZT used for TPP-based 3D nanoprinting; our PZT translation speeds range from 1 to 100 $\mu\text{m/s}$. **(b)** Piezostage controller; the positioning system was controlled using a homemade software. **(c)** G-code data used to control the PZT during TPP nanoprocessing. By moving the stage in x , and y -direction, arbitrary 3D features can be constructed. **(d)** Voxel-by-voxel micro-nano-structuring; *i.e.* each volumetric pixel is separately exposed [110].

It is important to know how the PZT-system displaced in the x - and y - directions during the process of TPP printing. Some basic controllers do not support the coordinated motion; which means that each axis of the PZT travels/move at a different speed to the commanded position without taking into consideration the position and speed of the other axes. In particular, it is not even guaranteed that the movement is strictly monotonic, as some controllers use iterative algorithms to approach the set position [128,129]. In our TPP set-up, we use a scanning PZT system based on voxel-by-voxel accumulation induced by one-shot of exposure per voxel (Fig.II.18(d)), which executes a sequence that commands the axes at the set position and waits until the set positions are reached and the axes are settled. Thus, the LFS is triggered to expose the resin for a defined time (Fig.II.18(d)). The advantage of this approach is that each voxel can be polymerized at well-controlled focusing parameters and it can be realized with nearly any type of PZT system [110].

To 3D print micro-nano-objects, 3D CAD models of these 3D objects were first extracted into a series of 2D slices corresponding to the profiles at different height levels (Fig.II.18(c)); *e.g.* z-position [115]. Starting from the first layer which is polymerized in contact with the cover glass, the lateral dimension of the printed structures is controlled by scanning the LFS over the surface of the dropped resin at a rate sufficiently low to form a gelled layer of polymer with desired and fixed depth. After the formation of the first layer; *i.e.* attached to the cover glass, a new layer was successively created on the first layer; *i.e.* layer-accumulation. Thus, the TPP scan starts from the glass and it gradually penetrates; *e.g.* step-by-step, in the z-direction inside the resin [20].

II.4. 3D Micro- Nanofabrication Software: CAD model

II.4.1. Influence of TPP-Scanning Mode

TPP-based 3D nanoprinting induced by TPP is performed by scanning a tightly focused pulses beam; *i.e.* accumulated photon density at the LFS, according to pre-designed patterns; *i.e.* CAD models, from the bottom slice to the upside slice until the entire 3D polymeric structure is produced [39]. They are two basic modes of 3D printing by TPP; that are; raster- and surface profile- scanning mode [3], of which their concepts are illustrated in Fig.II.19(a) and Fig.II.19(c), respectively.

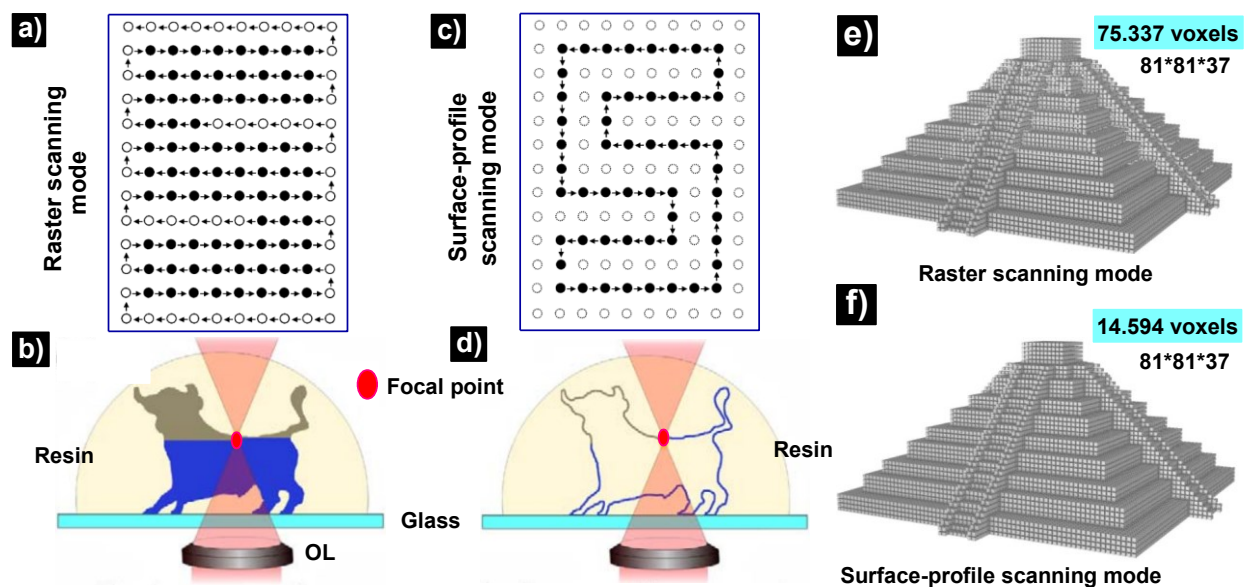


Figure II.19. Conceptive illustration of how the two scan modes could be applied for TPP-printing a character “S” and a 3D micro-sized bull. (a-b) Raster scanning; here, all of the volume that contains the microstructure was scanned by the LFS. (c-d) Surface profile scanning; only the crust is scanned; the solid and open circles denote exposed and unexposed parts of the resin, respectively [9]. CAD model of a 3D pyramid that can be fabricated by using (e) raster scanning and (f) surface-profile scanning mode.

In raster scanning mode (Fig.II.19(b)), all voxels (black-dots in Fig.) in a cubic volume that contains the structure are scanned; *i.e.* TPP-irradiated, by the actual/virtual LFS, depending on having the shutter (on (actual))/(off (virtual)). This process, thereby taking up a lot of printing time. Oppositely, in surface-profile-scanning mode (Fig.II.19(d)), the laser focus selectively traces the contour profile of the structure's design, which means that only the crust of structure is defined by the TPP process (Fig.II.19(d)), and the inside is solidified just after washing phase by the use of an UV light (maximum optical-absorption of the used resin). A TPP fabrication of a 3D bull was used as a demonstration of these two strategies, as shown in Fig.II.19(b) and Fig.II.19(d) [9,40].

3D microstructures printed through the process of surface profile scanning are too thin, almost $\sim 150\text{-}200\text{ nm}$; so maybe easily deformed; due to variations in the liquid flow and surface tensions of the rinse solvent; *i.e.* washing step. S. Kawata at al. [9] proved that the scanning time was reduced by $\sim 90\%$ due to the use of surface profile scanning (Fig.II.19(a-d)). The nanoprinted 3D bull by the use of surface profile scanning mode took $\sim 13\text{ min}$. Oppositely, the other printed by raster scanning mode took $\sim 180\text{ min}$. As an advantage of the profile scanning mode, this method of TPP scanning requires less processing time and significantly increases the fabrication efficiency. In our work, we use a raster scanning strategy in-order-to get better stability of 3D structures [20].

II.4.2. Creation of 3D Microstructures Design Model

Stereolithography (STL); *i.e.* a rapid prototyping technique, was introduced in 1981 by various research groups, and it has developed into a high potential 3D manufacturing process that is based on photopolymerization [132,133]. In the case of TPP-based stereolithography, the achieved spatial resolution and stability of the printed structures is improved by controlling the dimensions, shape, voxels number, z-position of the LFS, and layers number of the structures that need to be produced [12,40].

As shown in Fig.II.20, we use SolidWorks as a CAD software to create and design different models of 3D structures; *e.g.* micrologo of MAScIR. By using this 3D-software, we are succeeded to control the parameters needed to create the 3D design model of any kind of desired 3D structures (Fig.II.20). The CAD file is 'sliced' and each slice is exported as an *.stl* file; *i.e.* STereoLithography format (Fig.II.21). Shown in Fig.II.21 is a 3D CAD model; *e.g.* MAScIR pattern, in the *.stl* format [20]. The nano-STL process begins with the generation of a CAD model of the desired 3D micro-sized object. The 3D model of the object is sliced into several series of

horizontal planes representing 2D of the 3D model with slightly different z-coordinate values; *i.e.* layer-by-layer accumulation, following the z-direction [20].

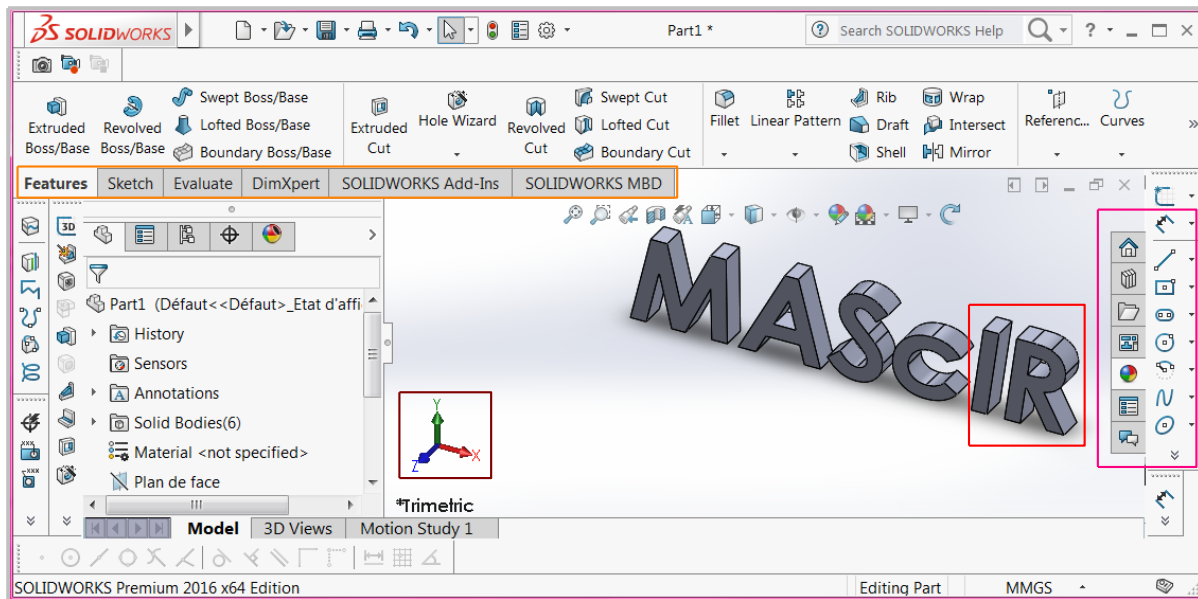


Figure II.20. Creation of structures design using SolidWorks software; this structure model is built as a layer by layer processing. The lateral dimension of 3D patterns was controlled before the export of stl. file.

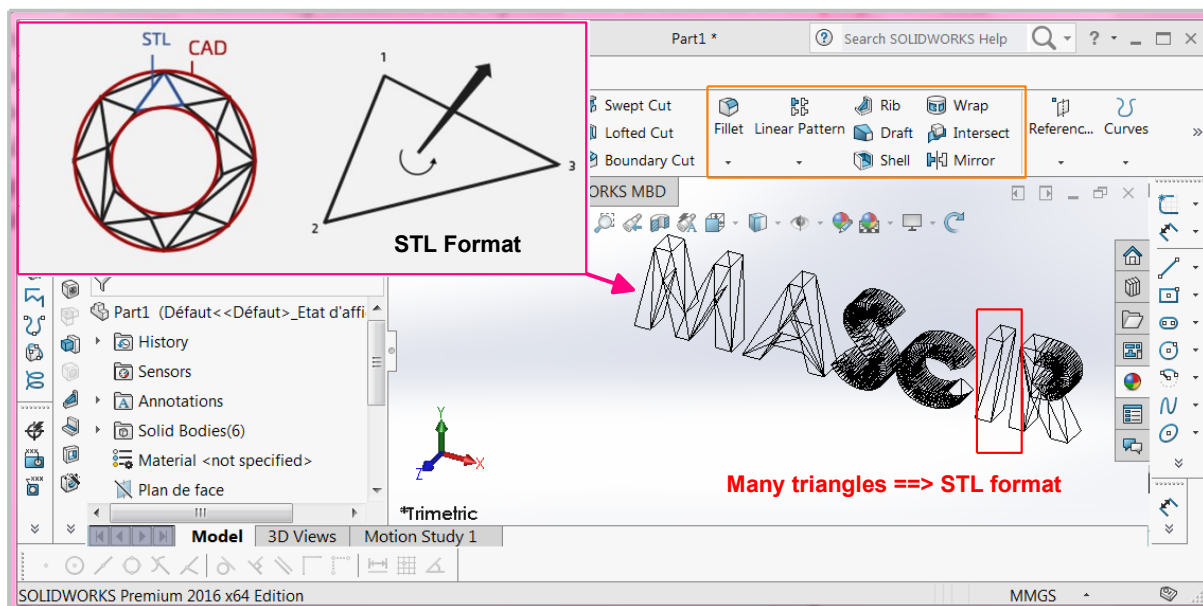


Figure II.21. 3D microstructure design in stl. format. Slicing procedure of 'MASCIR' for the generation of 3D scanning data. Each triangular patch in stl. format consists of three-line segments as shown as an inset. The stl. file stores information about 3D models and describes only their surface geometry in space.

Recently, the stereolithography (STL) technique is widely applied in various industrial fields; especially for 3D laser nanoprinting. STL is used from the inception of the basic design (Fig.II.20)

even before the fabrication of actual mechanical parts; thereby making the whole process more economical, it employs engineering materials such as photopolymers, hybrid materials, and metals. In the work described in this thesis, we use the TPA mechanism; *i.e.* TPP, coupled with micro-STL as a nanoprocessing tool to 3D print complex structures with near-diffraction-limit features [12].

II.4.3. Generation of G-Code Data Using .stl File

STL-based 3D nanoprinting involves voxel-by-voxel following by layer-by-layer polymerization process. Thus, the first layer of sliced data; *i.e.* g-code data, involving the 3D micro-sized structure is polymerized according to the scanning paths of the laser focus; then, the next layer is produced by translating the LFS-location along the z-direction; *i.e.* z-position [20]. The 3D *stl*. data is sliced vertically into many layers to generate the 2D scanning paths data of the LFS. The *stl*. data of 3D structures consist of many triangular patches of which the size generally stands for the resolution of the designed CAD model (Fig.II.22(a)) [134].

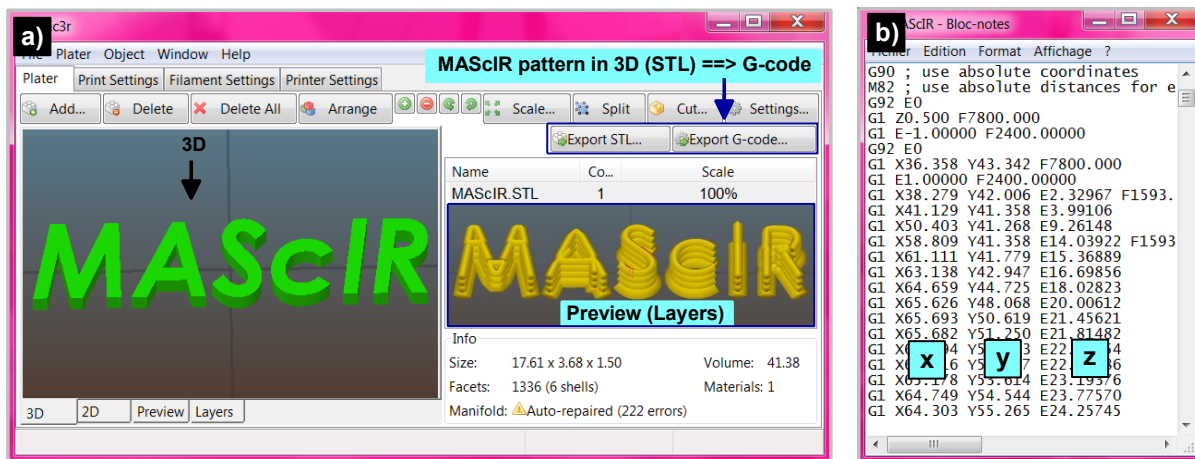


Figure II.22. (a) 3D software used to generate the g-code data for MAScIR.stl format. (b) G-code data of MAScIR.stl format. Data files in stereolithography format; *i.e.* .stl file, and g-code data, insures TPP micro- and nanofabrication of arbitrary 3D structures.

We use 3D software to generate g-code data which is needed to control the positioning system used for TPP-based 3D nanoprinting, as shown in Fig.II.22. In our TPP set-up, the positioning of PZT (x and y) was separately controlled compared to the motorized OL; *i.e.* following the z-direction. Thus, the PZT system was displaced in x and y directions; *i.e.* in the 2D. On the contrary, the OL which focuses light ensures the TPP scanning in the z-direction; *i.e.* in the 3D [20]. Shown in Fig.II.22(a) is the software that we employ to generate the g-code data of the nanoprinted structures presented in this thesis. The g-code of MAScIR pattern (as an example) is shown in Fig.II.22(b).

Also, we use this software to control the number of layers which can be polymerized for each printed structure. By accurately controlling the design parameters of the 3D model of structures; *e.g.* dimensions, overall size, number of layers, and 3D shape, stable and accurate 3D laser nanoprinting process with SDL resolution can be achieved, as we will show in the last sections of this chapter.

II.5. Laser Beam and Intensity Control

During the process of TPP-based 3D nanoprinting, the control of the laser beam; *i.e.* on/off, was realized by using a fast-mechanical shutter as shown in Fig.II.23(a-b). To control the laser intensity needed to trigger TPP (near TPP-threshold) and to realize different systematic studies of TPP nanofabrication that are discussed in this thesis, we use several neutral density filters; or variable attenuator; or a combination of a polarizer and a half-waveplate (Fig.II.23(c)) [108].

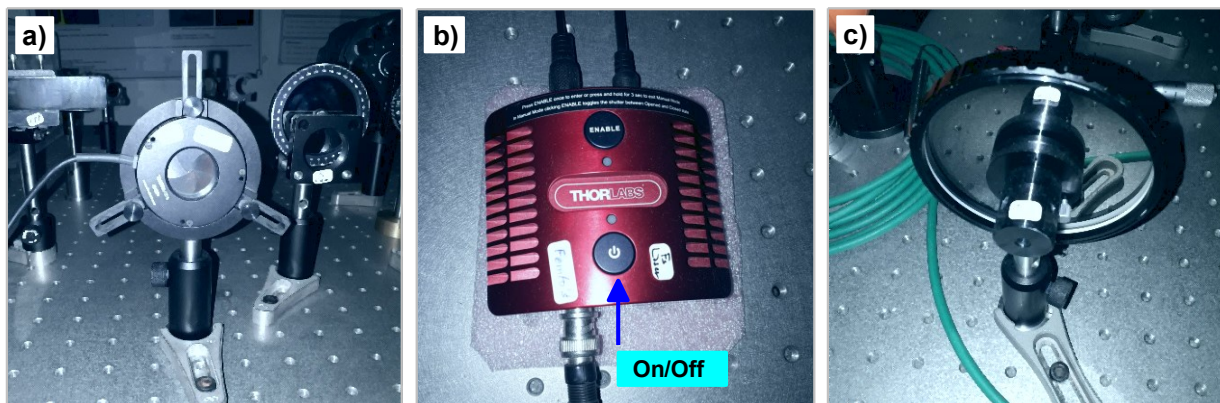


Figure II.23. Laser beam and intensity control. (a) High-speed shutter used in our TPP set-up for controlling the exposure time. (b) Fast mechanical shutter controller; the on/off button is indicated by a blue arrow. (c) Variable attenuator; *i.e.* ND filter.

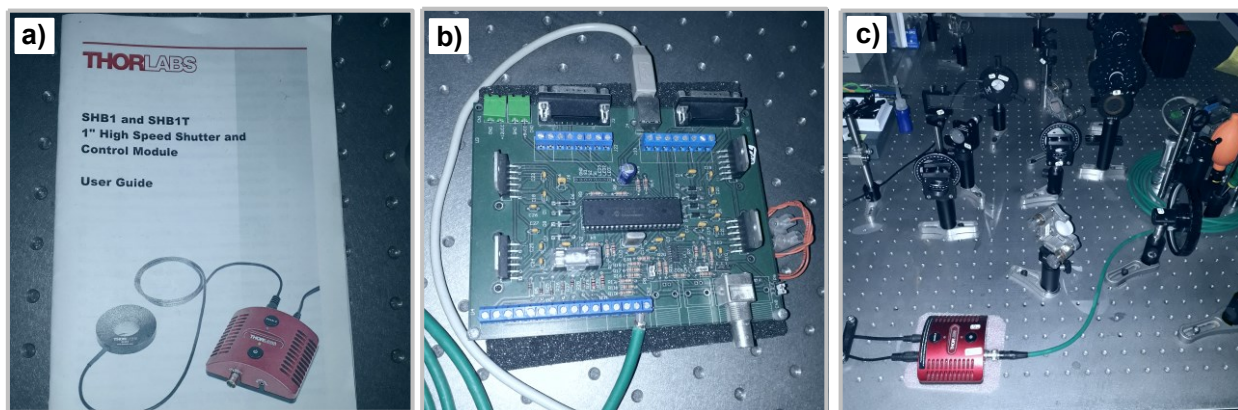


Figure II.24. (a) Manual of shutter. (b) Controller-card coupled with the shutter and a preprogrammed pattern. (c) Optical devices for controlling the laser beam; *e.g.* mirror for the setup alignment.

In order to get better stability of TPP nanoprinting, the optical and mechanical components used for our TPP optical set-up described above need to be centrally controlled and synchronized (Fig.II.24(c)). This can be performed using commercially available software, or by integrating laser scanning software or by home-made software [110]. It should be noted that nowadays there are several companies providing the optical devices that are needed for 3D micro- and nanofabrication systems; *e.g.* various laser sources, focusing lens, and scanning configurations [134].

II.6. 3D Nanoprinting by TPP

In the previous sections, we have discussed the TPA materials, TPP optical setup, and also the creation of CAD model of the printed 3D structures, that are necessarily needed for the realization of TPP nanofabrication in 3D [12]. Here, we investigate the realization of structures/objects with nanoscale features; *e.g.* near-diffraction limit resolution, by the use of a pulsed laser; *i.e.* emitted at $\lambda = 780 \text{ nm}$. The implementation of TPP-based 3D nanoprinting is achieved by scanning the sample with respect to the LFS (focus). Shown in Fig.II.25 is the achievement of SDL resolution using the TPP process; *e.g.* 3D pyramid in Fig.II.25(b) [20].

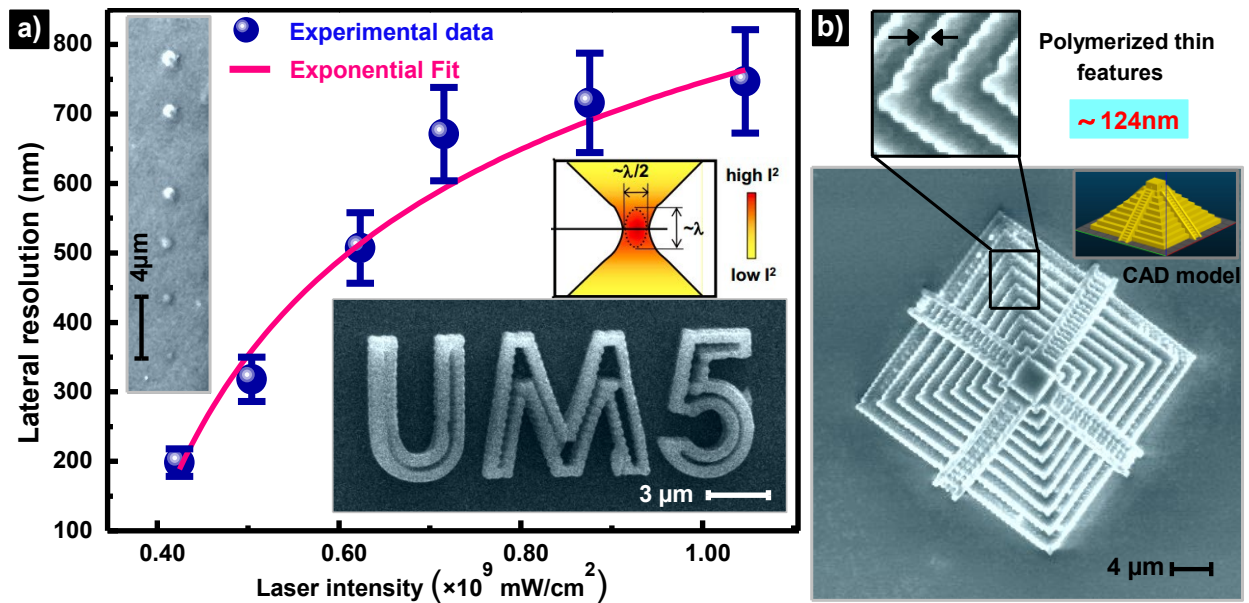


Figure II.25. 3D laser nanoprinting at SDL resolution. (a) Voxel-lateral-size (Δ_{xy}) dependency on laser intensity; TPE leads to strong confinement of the absorption probability to around the LFS (inset); an UM5 pattern is shown as an inset. (b) SEM image of a 3D micropyramid produced by raster scanning mode using the TPP process, the two-photon process took 120 min, and the structure was printed using voxel-by-voxel accumulation. The CAD design of the pyramid is shown as an inset.

After the optimization of all the TPP manufacturing parameters, we fabricated simple to complex microsized structures; which includes a set of voxels, microlines, lattices codes, logo of the institute

(*e.g.* MAScIR pattern), and 3D structures, etc. (Fig.II.25(a-b)) [12]. To depict the tiny features of the nanoprinted structures, a near-diffraction-limit resolution is needed, which is achieved via the NLO effect (Fig.II.25(a)). Fig.II.25(a) shows the lateral resolution (lateral size of the printed voxel Δ_{xy}) dependency on the laser intensities at a fixed exposure time of ~ 1 ms. Here, we demonstrate that a spatial resolution far smaller than the diffraction limit was achieved [21]. From Fig.II.25(a), Δ_{xy} follows an exponential dependency on the irradiation laser dose; meaning that the lateral size of the printed voxels (SEM image in Fig.II.25(a)) can be saturated at a certainly applied intensity used for TPP fabrication.

Compared with other fabrication techniques; *e.g.* electron-beam lithography (EBL), the virtue of TPP stereolithography as a tool for nanoprinting microdevices lies to its 3D fabrication capability with nanoscale features close to the diffraction limit (Fig.II.25(b)). Here we show that the diffraction limit is exceeded by the NLO effects; *e.g.* $\sim \lambda/6.24$ resolution (Fig.II.25(a)). Due to the SDL resolution of TPP, the achieved applications from this technique encompass photonic crystals, metamaterials, and biocompatible scaffolds for tissue engineering [45].

II.7. Conclusion

This work confirmed the feasibility of TPP to 3D print micro-objects at near-diffraction limit resolution. The proof-of-principle 3D nanoprinting is accomplished by building a TPP-stereolithography set-up by the use of a Ti: Sapphire Fs laser system as an excitation source. Here, a negative methacrylate-based resin was used as a recording medium to 3D print micro-nano-structures/objects. Nanofabricated structures may be shrunk in TPA lithography, an effect that can be precompensated in the computer design of the structure, or used to advantage to reduce the size of the printed structures. The two-photon process remains a very active field of research, and recently with the advent of the pulsed lasers, multiphoton excitation can find applications in fluorescence imaging of biological molecules [65,135], and power limiting [136], and micro-nano-fabrication including micro-optical components [75] and photonic crystals [22].

CHAPTER III

Systematic $\lambda/21$ Sub-wavelength Resolution by Two-Photon Absorption Induced Polymerization

Abstract

Stereolithography based on two-photon polymerization; *i.e.* 3D laser nanoprinting, in resins, has been recognized as one of the enabling technologies to fabricate functional 3D microdevices with near-diffraction-limit feature; *e.g.* up to ~ 100 nm resolution. This work focuses on improving the spatial resolution of two-photon nanofabrication using a femtosecond laser; *i.e.* emitted at $\lambda = 780$ nm, with a systematic nanofabrication process which we developed. In this study, we discuss the factors influencing the resolution; including the laser intensity, and exposure time, and scanning speed by fabricating polymerized-voxels, nanolines, and nanofibers suspended between two voxels. By introducing a novel approach to two-photon nanoprinting, we show that a resolution of ~ 36 nm; *i.e.* corresponds to $\sim \lambda/21$ of the irradiation laser wavelength (λ), is achieved. Finally, we show that stable 3D micro-nano-structures can be fabricated by using our custom-made optical setup.

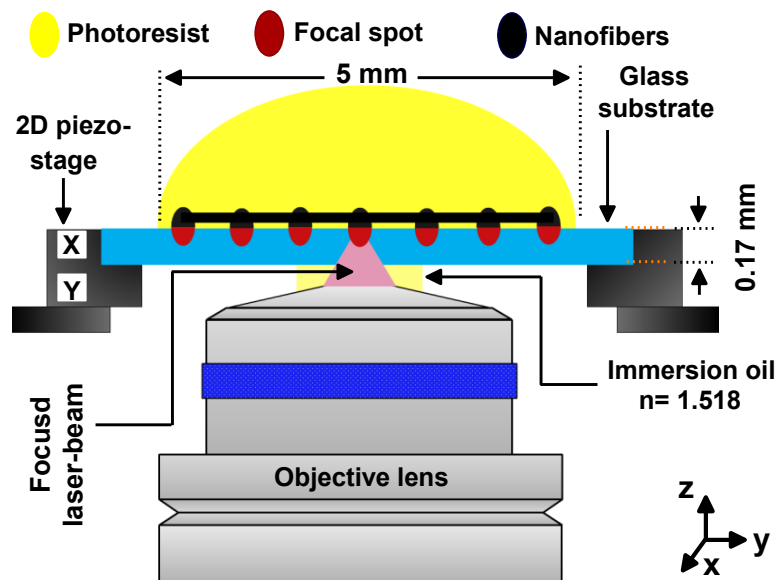


Fig.II.0. Schematic presentation of the resin exposure configuration in our two-photon polymerization 3D-nanoprinting system; *e.g.* 3D nanoprinting of suspended polymerized nanofibers (SPnF) [*].

[*] Y. Bougdid et al., *J. Micromech. Microeng.* 29, no. 3, pp. 1-7, 2019

III.1. Introduction

Two-photon polymerization (TPP) induced by femtosecond (Fs) lasers is one of the promising technologies for 3D nanoprinting that has a resolution beyond the diffraction limit [9,52]. A critical aspect of TPP printing is the resolution of the process. The most accurate measurement of TPP resolution is the size of the printed voxels; *i.e.* the 3D equivalent of 2D pixels. A voxel is well-defined as the smallest unit of a pattern polymerized by one shot of exposure [12,21]. The printed voxel through the TPP process can be much smaller than the cube of the laser wavelength; *i.e.* λ^3 [18,28]. Generally, a 780 nm Fs laser source was used to 3D-print voxels with a lateral size of $\Delta_{xy} \sim 120$ nm; *i.e.* $\sim \lambda/6.5$ resolution [9], and 800 nm laser was used to create voxels with $\Delta_{xy} \sim 80$ nm; *i.e.* $\sim \lambda/10$ resolution [137]. Recent reviews summarize the progress in this rapidly growing field [3,6,11]. To induce TPP, the photo-resin was excited by simultaneous absorption of two photons; *i.e.* TPA, within a time range of few femtoseconds; *e.g.* $1\text{fs} = 10^{-15}\text{sec}$ [40,99]. During TPP 3D-printing, the Fs laser beam was tightly focused on the resin through a high numerical aperture ($\text{NA} \sim 1.4$) of an objective lens (OL), initiating TPP reaction within the laser focal spot (LFS) volume; *i.e.* voxel. Thus, TPA polymerization shows a quadratic dependence; *i.e.* nonlinear optical effect (NLO), on the incident laser intensity. Based on the NLO effect, the LFS is used as a nano-pencil of light for 3D nanoprinting; *i.e.* Fs-laser-direct-writing (FsLDW) [19,30].

The main manufacturing parameters that defining the TPP-resolution are; the accuracy of the optical setup, focusing lens NA, LFS dimensions, focusing laser dose, and TPA material properties [39,108]. It is known from a long literature [45,52,60] that low laser intensity; near TPP threshold, is needed to achieve high TPP-resolution. In this work, by introducing a novel approach to TPP nanofabrication, we show that high resolution can still be achieved with high laser intensity when combined with fast laser-scanning speed. Thus, a nanofiber of ~ 36 nm lateral size; corresponding to $\sim \lambda/21$ of resolution, can be achieved by using our custom-made optical setup. In this systematic study, we two-photon printed single voxels, nanolines, and suspended nanofibers, in order to get fine features which can be smaller than the sub-diffraction limit (SDL) [12,110].

III.2. Realization of Sub-Diffraction-Limit Features

III.2.1. Voxel Dimensions in 3D Nanoprinting

In TPA-based 3D nanoprinting, the Fs laser beam can enter the resin without being absorbed and trigger TPP only in a submicron volume around the LFS (voxel); being the 3D analog of a 2D pixel (Fig.III.1(a)). The size of voxels produced by one-shot of TPP-exposure depends on the irradiation

power (; or intensity), exposure time, LFS z-position, and NA focusing-lens [11,20]. In the study described in this chapter [12], we investigate the effect of the laser intensity, exposure time and laser-scanning speed on the resolution of 3D nanoprinting; while the laser's threshold intensity (I_{th}), NA of the OL, z-position, and the resin refractive index are well known.

The limited NA of the OL which focuses light results in an ellipsoidal focal voxel with elongation along the propagation axis of the laser beam; *i.e.* in the z-direction (Fig.III.1(b)). TPP is activated by the use of a high density of photons; *i.e.* localized at the LFS, and result in an efficient and rapid crosslink (solidification) of the liquid resin [9,13]. The distributed light intensity at the LFS; where the two-photon excitation (TPE) is triggered, is assumed to be Gaussian (Fig.III.1(a)). A near-focus SLI distribution is shown in Fig.III.1(a) [18].

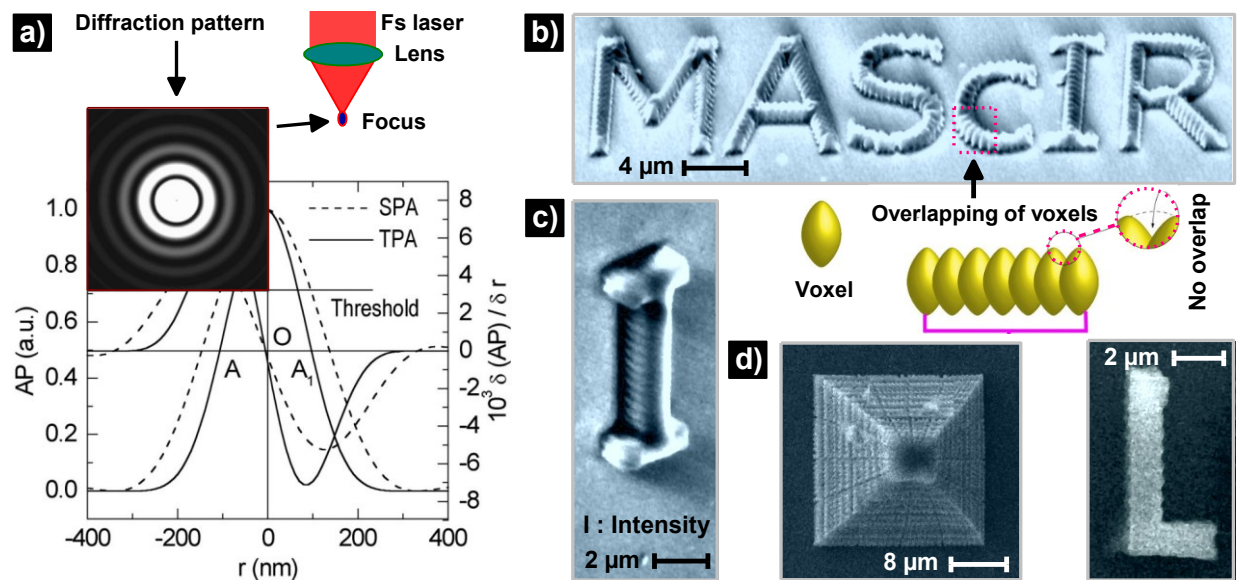


Figure III.1. Achievement of SDL resolution using TPP. (a) The absorption probability (AP) for single (SPA-IPA) and TPA are denoted by dashed and solid curves, respectively; the diffraction pattern from the focusing optics is shown as an inset [18]. (b) Top-view SEM image of 3D microstructures of MAScIR; the prolate spheroidal shape of voxels is shown as an inset. (c-d) SEM images of a 3D abbreviation of laser intensity 'T' and micro-sized pyramid and the abbreviation of light 'L'. The typical laser intensity used was $\sim 10^9 \text{ mW} \cdot \text{cm}^{-2}$, and the exposure time was kept at 1 ms.

By using a high NA-OL focusing, the light distribution at the focal volume of the LFS arises essentially from Fraunhofer diffraction (Fig.III.1(a)). Shown in the inset of Fig.III.1(a) is the diffraction pattern that was encountered in the current optics; *e.g.* focusing optics. Thus, the central peak exhibits a maximum intensity (Gaussian-profile), and the amplitude oscillates and gradually decreases away from the center. The amplitudes of the side peaks of the intensity distribution are

small compared to the central peak [12,18]. As shown in Fig.III.1(b-d), the SDL resolution of TPP printing was found possible in a threshold system, where the materials responded to light excitation with a pronounced threshold behavior. TPP threshold defines a level of the applied intensity above it the TPP-reactions become irreversible; *e.g.* modification of refractive index ($\Delta n \sim 0.08$) [110].

In 3D printing, the diffraction limit became just a measure of the LFS size; but did not put any actual restraint to the voxels size (thresholding effect). Experimentally, a lateral resolution down to $\sim 120 \text{ nm}$ was obtained by the use of high NA focusing optic [9,40]. Shown in Fig.III.1(b-d) are the scanning electron microscope (SEM) images of some examples of 3D structures that are produced at SDL resolution using TPP voxel-by-voxel accumulation (overlapping process) [12]. Also, 3D micro-nano-objects were accurately constructed by adjusting the position of the LFS (along the z-position) in the cover glass/resin interface. The free area between two overlapping voxels is filled over by diffusion assisted polymerization (inset of Fig.III.1(b)). The dimensions and extent of overlap between the voxels determine the resolution of nanofeatures that are presented in the printed 3D objects (Fig.III.1(b)). Shown in Fig.III.1(d) is a microsized pyramid which presents small finer features of about $\sim 100 \text{ nm}$; *i.e. resolution* $\sim \lambda/7.8$ [6,20].

The two-keys factors mentioned above; *i.e.* laser intensity and exposure time, were carefully investigated in this study. Accordingly, we printed voxels to confirm the laser intensity and exposure time dependencies on the 3D printing resolution; by the way, we investigate these dependencies by introducing two TPP explication; which we named LFS evolution and radical diffusion; respectively [12]. Also, we used a line TPP-scanning method in which we investigate the effect of the laser dose on the microline resolution. In the work done by J. F. Xing group's [137], theoretical calculations showed that Δ_{xy} can be dramatically decreased with reduced the applied laser dose (*exposure time * intensity*), which indicates that the resolution of TPP could be improved by using a more sensitive resin/initiator in the future.

III.2.2. Laser Intensity Dependency on Resolution

III.2.2.1. Voxel Diameter Dependency: Lateral Resolution

In this section, we report the effect of the irradiation intensity on the lateral size of the printed voxels (Δ_{xy}); thus, individual voxels were printed in a one-shot of exposure; *i.e.* 1 ms duration, under different intensities which are measured at the LFS; *i.e.* $I_{focus} = [0.61 \lambda/NA]/LFS_{surface}$ [108]. Experimentally, we optimizing Δ_{xy} by adjusting the focused laser dose; in-other-words, by

combining the intensity and exposure time. From the SEM images presented in this chapter, Δ_{xy} is measured from the top side in the x - y direction of the printed pattern; *i.e.* voxel diameter, and the resolution of TPP nanoprinting corresponds to the width of the printed voxel [20].

Shown in Fig.III.2(a) are the printed voxels under different irradiation intensities; *i.e.* in the order of $\sim 10^9$ mW/cm². We observe that when the intensity increases, Δ_{xy} linearly increases; this is explained by the LFS duplication following the increment of the laser density at the focal region [18]. Laser intensity of $0.71 * 10^9$ mW/cm², $0.87 * 10^9$ mW/cm² and $1.04 * 10^9$ mW/cm² lead to a voxel diameter of $\Delta_{xy} \sim 370$ nm, 584 nm, and 787 nm, respectively, and Δ_{xy} linearly grows within this intensity range (Fig.III.2(a)), and smaller voxels are realizable by reducing the intensity and exposure time; *i.e.* located near the TPP threshold [9]. Shown in Fig.III.2(b) is the presentation of the SLI distribution related to TPP threshold behavior. It well observed from Fig.III.2(b) that the maximum laser intensity of irradiation is localized at the LFS, as illustrated by the red color. The amount of local cross-linking; *i.e.* localization of TPA polymerization, depends on the accumulated absorbed dose (Fig.1(b)) [45].

Based on the achieved results (Fig.III.2(a)), the relationship between the voxel size; *i.e.* voxel width, and the irradiation SLI which is localized at the LFS is demonstrated (Fig.III.2(b)). The intensity distribution of the IR beam at the LFS is assumed to be gaussian (Fig.III.2(b)) [12,52]. The basis of the gaussian profile for a plane wave propagating in the z -direction which describes the intensity distribution at the LFS where TPP was triggered was detailed in Ref. [138]. In TPP-based 3D printing, the behavior of the laser beam in the neighborhood of the LFS is of utmost interest. From [95,138], the intensity profile in the radial direction; *i.e.* meaning x - and y -direction, of the gaussian beam at its waist, is expressed as follow:

$$I(r) = I_p \exp(-r^2/w_f^2) \quad (III. 1);$$

In the Eq.III.1, I_p symbolizes the peak intensity of irradiation, r is the radial coordinate direction and w_f is the beam radius at its waist. The peak intensity of the gaussian wave decreases with distance away from the center of the LFS as the beam expands, as shown in the inset of Fig.III.2(b) [30,52,138].

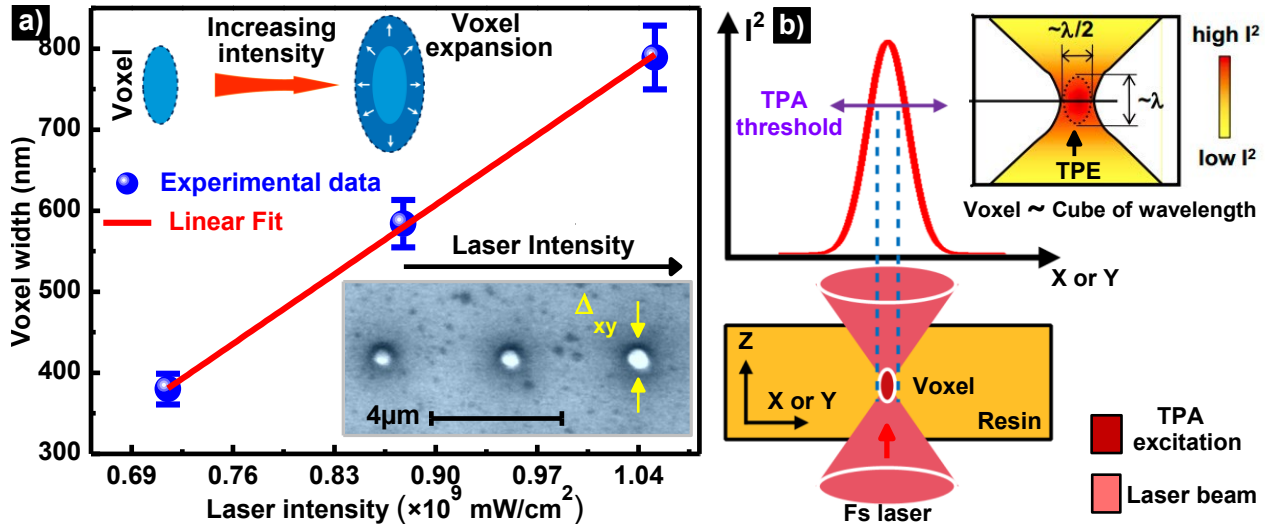


Figure III.2. Relationship between TPP lateral resolution and irradiation intensity. (a) Dependence of voxel width on the intensity at a fixed exposure time of $t_1 = 1$ ms. The blue scatters are experimental data and the full red-line is a linear theoretical fit guide to the eye. (b) Schematic illustration of the SLI distribution profile for the TPA process; the SLI distribution at the LFS is shown as an inset [110].

If we define the TPA intensity threshold (I_{th}) as the critical intensity needed to trigger TPP, then the beam radius over which the resin is expected to be polymerized at the LFS is obtained by setting the I_{th} equal to I ; i.e. $I_{th} = I$, in Eq. (III.1) and solving for the laser-beam radius $r_{th} = r$, as $I(r) = I_f \exp(-r_{th}^2/w_f^2)$ (III.2), where I_f denotes the peak intensity at the focal region. Thus, from Eq. (III.2) and refs. [138], the radius achieved at I_{th} is expressed as follow:

$$r_{th}(z) = w(z) \sqrt{\ln(I_P(z)) - \ln(I_{th}) + \ln(w_f/w(z))} \quad (III.3);$$

Following the TPA mechanism, TPP reaction most likely begins along the laser beam path before reaching the LFS, and thus the beam is attenuated starting at z_{max} , where $I_P = I_{th}$ for TPA polymerization (Fig.III.2(b)). The intensity distribution at the focal volume can then be expressed as follow [30,138]:

$$I(z, r) = \frac{P}{\pi w_f w(z)} \left(\frac{w_f}{w(z)} \right) \exp(-r^2/w(z)^2) \exp(-\alpha(z_{max} - z)) \quad (III.4)$$

Where, P , $w(z)$, and α denote the total beam power, the beam radius as a function of z -position, and the calculated maximum voxel dimension in the z direction. According to Fig.III.2(a), the smallest width of a printed voxel is about $\Delta_{xy} = 370$ nm. Besides, TPP resolution is controlled by the LFS size without any actual limitation, whereas for an usual optical FsLDW, the lateral size

d_{xy} of the optical laser-focus is limited by Rayleigh's criteria at 679.71 nm ($d_{xy} = 1.22 * \lambda/\text{NA}$, $\lambda = 780 \text{ nm}$, $\text{NA} = 1.4$) [12].

Here, we demonstrated that the SDL resolution was achieved by adjusting the intensity to $I_{th} \approx 0.71 * 10^9 \text{ mW/cm}^2$ (Fig.III.2(a-b)). Generally, in TPP printing, the voxel shape takes the form of the elliptical LFS which is defined by the SLI relative to the threshold level [11]. When $I_{irr} < I_{th}$, no polymerization; *i.e.* TPP, will take place (not shown), and oppositely when the LASER intensity is too high; *i.e.* when $I_{irr} > I_{th}$, the resin will boil as presented in Fig.III.3(a). A detailed investigation of voxel formation would be an immediate task for future research in 3D laser nanoprinting [20].

By three-dimensionally moving the LFS inside the resin, any desired structure can be TPP-printed (Fig.III.3) [27]. To confirm the SDL fabrication capability of TPP using voxel-by-voxel accumulation, we printed and designed various 3D structures; *e.g.* 'MAScIR' and 3D microbull (Fig.III.3), is shown, with near-diffraction-limit features. For this TPP processing, we used an intensity of $\sim 10^9 \text{ mW/cm}^2$, which gave rise to a resolution of approximately $\sim 100 \text{ nm}$ (not shown); *e.g.* according to Fig.III.3(d). By adjusting the intensity near the TPA threshold, stable structures were successfully printed (Fig.III.3(d)). Also, by using high irradiation intensity; *i.e.* $I_{irr} > I_{th}$, the printed structures can be damaged, as proved by 3D printing the microsized bull shown in Fig.III.3(b) [30]. In this case, the thin-parts of the printed structures can be damaged, due to the effect of out-focus TPP (Fig.III.3(c)). As shown in Fig.III.3(e), when $I_{irr} < I_{th}$, we observe that the printed structure is not stable; meaning that the efficiency of TPP can't reach $\sim 100\%$ [6].

Shown in Fig.III.3(a) is the voxels printed at $I_{irr} > I_{th}$ (and 1 ms exposure time), so, a low resolution (lateral size up the diffraction limit; *i.e.* $\Delta_{xy} \sim 1 \mu\text{m}$) is observed. As we can see in Fig.III.3(b-c) ($I_{irr} > I_{th}$), the thin parts presented in the structures are damaged; meaning that the overlapping process of voxel; *i.e.* the primitive building block of structures, wasn't proportional to the overall size of 3D structures [12]. Thus, in TPP printing, before we start fabricating the entire structure, it is necessary to establish the best-suited parameters that are met with this technique; *e.g.* laser intensity, since those factors will influence the whole nanofabrication procedure [30,40]. According to the thresholding effect, when the irradiation dose is quite high, the voxels will be burned and their width will be too large, as shown in Fig.III.3(a).

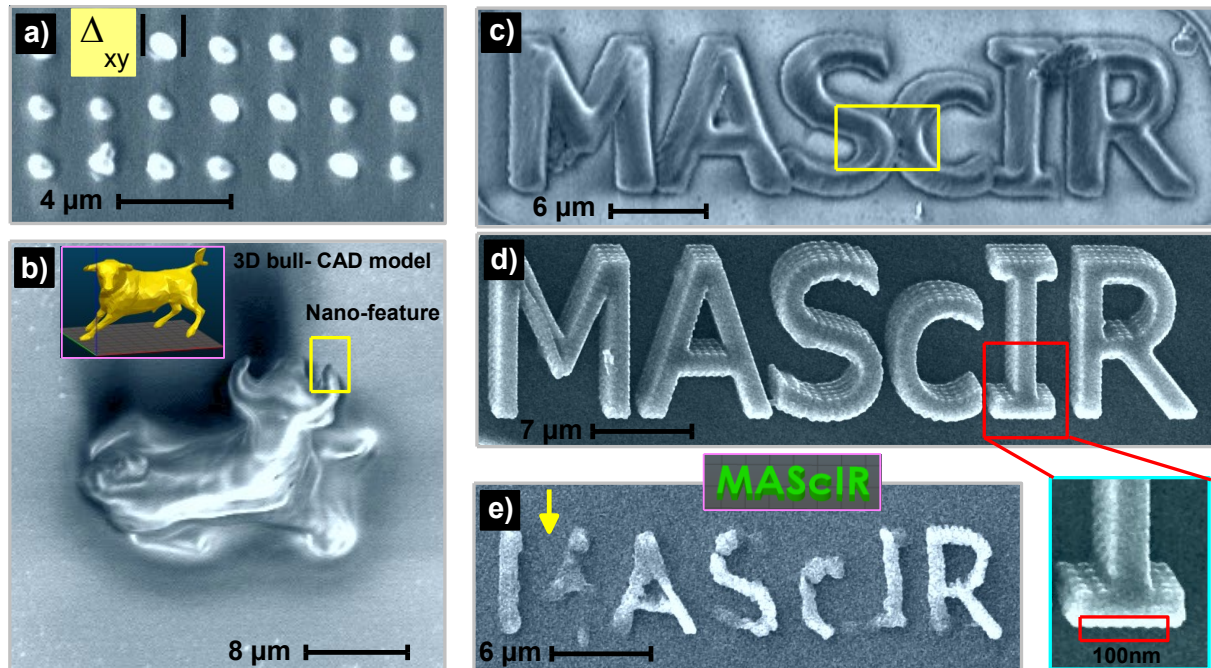


Figure III.3. Microstructures printed at, above, and less the TPP-threshold of intensity. (a) SEM image of voxel polymerized far above the threshold. (b-c) SEM images of a 3D microbull and “MAScIR” pattern printed far above the critical TPP-threshold. (d) SEM image of MAScIR pattern produced using exactly the laser dose needed to trigger TPP; *i.e.* $I_{th} = 1.14 \times 10^9 \text{ mW/cm}^2$. (e) SEM image of MAScIR pattern printed below the threshold of TPP. The exposure time was kept at 1 ms for (a), (b), (c) and (d).

The combinative action of the chemical, optical, and material nonlinearities make it possible to achieve reproducible TPP resolution of tens of nanometers; *i.e.* at a level of $\sim \lambda/10$ to $\lambda/50$, which is much smaller than the diffraction limit [6]. Theoretically, voxels may be further reduced in size only if the laser intensity is regulated closer to but still above the threshold level. However, it is tough to experimentally confirm since printed voxels resulted from low irradiation-exposure of irradiation are mechanically too weak to resist washing-solvent and to survive electron beam exposure during SEM observation (Fig.III.3(e)). The unique high precision; *i.e.* 3D prototyping capability, of 3D printing, has been fully approved [12].

III.2.2.2. Line-Width Dependency

To quantitatively investigate the effect of the laser intensity on the resolution of 3D nanoprinting, nanolines structures are designed in 1 ms exposure time by varying the irradiation intensity, as shown in Fig.III.4(a-b) [110]. Microlines structures are built from the polymerized voxels that can overlap with each other using TPP-based FsLDW. The nanolines are written by combining single-exposure shots of a continuous scan of voxels (inset of Fig.III.4(a)). Generally, the accuracy of TPP structuring is determined by the smallest achievable voxel that was polymerized for printing

microlines. According to the overlapping process, the desired center-to-center distance of voxels is readily chosen, meaning that the possibility of dimension definition to any value larger than the polymerized voxel itself with precision much beyond the restriction of the voxel size (Fig.III.4(a)). A much smoother surface of the nanoprinted line could be obtained after the developing phase; this is due to a self-smoothing process [6,110].

Shown in Fig.III.4(a) is the relationship between the nanolines width and the irradiation intensity levels; *e.g.* I_i where $i = 1-5$. From the SEM image shown in the inset of Fig.III.4(a), it is clearly seen that the nanoline-width decreased; *e.g.* from $\sim 1.074 \mu\text{m}$ to $\sim 429 \text{ nm}$, when the laser intensity decreases; *e.g.* from $\sim 1.48 \times 10^9 \text{ mW/cm}^2$ to $\sim 0.71 \times 10^9 \text{ mW/cm}^2$, respectively [12]. Also, as the laser intensity is reduced, the distance between two nanolines patterns became large, so there is a logarithmic increase in the nanoline-width, as presented in Fig.III.4(b). According to Fig.III.4(a), the nanoline width is expected to reach a plateau for intensities larger than $\sim 1.62 \times 10^9 \text{ mW/cm}^2$, as the concentrations of the initiator and MMA monomer existing inside the focal-volume are consumed during the TPP reaction; *i.e.* polymerization step [18,21,28].

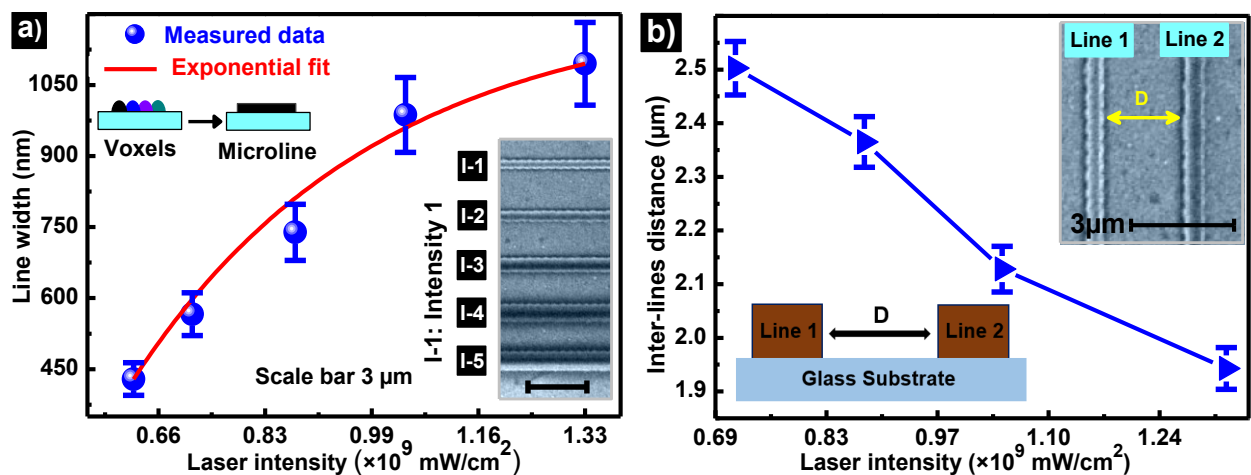


Figure III.4. TPP resolution of printed microline. (a) Line-width dependence on laser intensity; (inset) a top-view SEM image of the corresponding printed-microlines; scatters are experimental data and the solid line is an exponential fit guide to the eye. (b) Interline distance between two printed nanolines as a function of the irradiation intensity; at a fixed exposure time of 1 ms [110].

It is known from the literature [137] that the resolution of microlines can be determined; *e.g.* measured, both by the nanoline width or by measuring the distance between two adjacent nanolines (inset of Fig.III.4(b)). As an example, we investigate the distance between two printed nanoline, as shown in Fig.III.4(b). It is observed that the inter-line distance increases by decreasing the laser intensity. The increment of the linewidth follows the increases in the lateral size of voxels. As an

application that can be achieved via the laser printing of nanolines, it can be used as microchannels on the top of the glass substrate. The inset of Fig.III.4(b) illustrates a schematic presentation of the printed lines that are connected to the top of the cover glass.

Experimentally, to fabricate nanosized lines, the sample (resin on glass) was moved in x - and y -direction through the nanopositioning stage (PZT), but the OL which focuses light on the resin was still fixed. When the irradiation intensity increases and by using a multifunctional monomer; *i.e.* MMA monomer, polymerized chain propagation may occur by the interaction of a radical with already-reacted monomer molecules [6]. This kind of reaction leads to the formation of branched polymer structures, whose size significantly exceeds the average length of a single polymer chain [3]. Consequently, by carefully controlling the laser dose to match $\sim I_{th}$, the region where TPP induced can be easily reduced to a nanometric scale; this is explained by the NLO effect. Optically, high resolution of nanolines was obtained by using high NA focusing, as described elsewhere in the experimental section, which is detailed in chapter II; *i.e.* TPA material and optical system [12].

III.2.2.3. Focal Spot Evolution (Duplication)

According to the irradiation intensity dependency on the resolution of the nanoprinted patterns, we proposed a TPP explanation, as we will discuss in the present axis. The best resolution which is achieved in the near-threshold region corresponds to the lowest intensity needed to trigger the TPP reaction. The initially formed voxels; *i.e.* at I_{th} , take the elliptical form of the LFS which is defined by the SLI relative to the threshold level (Fig.III.5(a)). In this Fig. the threshold level is defined by the intensity I_1 ; corresponding to the LFS shown by the red color. This process is called laser focus duplication [28]. The schematic presentation in Fig.III.5(a) shows that the voxel duplication increases in both axial (Δ_{xy}) and longitudinal (Δ_z) dimension by the increase of the laser intensity. The inset schematic presentation in Fig.III.5(a) illustrates the localization of the LFS inside the resin (fully inside the resin) by using high NA focusing of ~ 1.4 [20].

Fig.III.5(a) schematically shows the near-LFS isophotes; *i.e.* the contour lines of the light intensity (SLI distribution). In TPP near-threshold, the voxel size scaling abides by different laws, especially the low related to irradiation intensity [12]. The expansion of voxel with the increase of intensity follows the growth of the LFS volume in all dimensions; *i.e.* in 3D directions, but becomes especially enlarged along the optical longitudinal axis; *i.e.* in the z -direction; this is due to the nature of diffraction [21]. A numerical simulation done by Kawata et al. [11] discusses the

evolution of the voxels size as a function of intensity; *i.e.* near-threshold. According to Fig.III.5(a), we examine the mechanism of TPP at the LFS-volume with different intensities levels I_1, I_2, I_3, I_4 and I_5 . Shown in Fig.III.5(b) is the 3D structures that were exactly printed at the TPA threshold level. It well observed from the SEM image shown in Fig.III.5(b) that the printed structures present high stability against the washing solvent; this is due to the thresholding effect of TPP [3]. Here, we demonstrate the capability of TPP to achieve high stability of the nanoprinted structures by using the critical I_{th} .

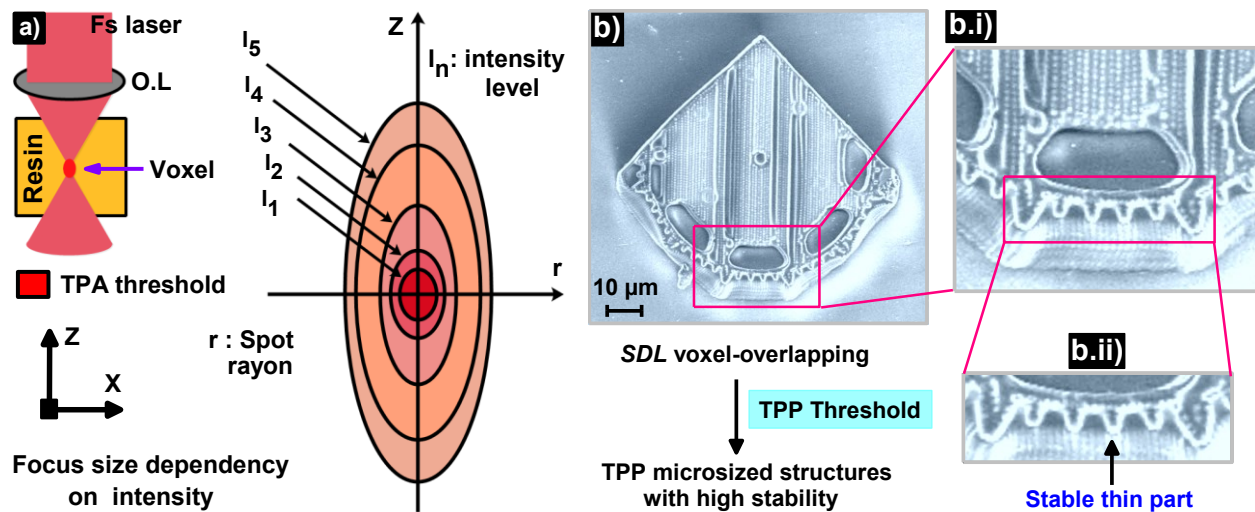


Figure III.5. Focal spot evolution dependence on laser intensity. (a) Schematic showing the mechanism of the formation of voxels under different intensities; *i.e.* LFS duplication. (b) SEM image of structures fabricated using the TPA threshold level; (b.i) zoom image of the portions of structures which presents smallest achieved patterns; *i.e.* TPP resolution; (b.ii) thin parts which present stable polymerized portion.

As demonstrated in Fig.III.5(b), we investigate the effect of I_{th} on the stability of the nanoprinted structures. By using I_{th} as irradiation intensity, fine and stable structures can be achieved, due to the high efficiency of TPP, which means that 100% of polymerization was reached (Fig.III.5(b)) [139]. On the other hand, if we use $I_{irr} < I_{th}$, the efficiency of TPP which is attained can't reach 100%, thus, the printed structures can be deformed by washing solvent. According to the TPA thresholding effect, by using the proposed LFS evolution model; a systematic TPP process of stable polymeric micro-nano-objects was demonstrated [12].

S. Kawata et al. [140] demonstrates that the use of high TPA cross-section of resin in conjunction with high NA focusing, lead to creating voxels of $\Delta_{xy} = 80 \text{ nm}$; *i.e.* $\lambda/10$ of resolution; $\lambda = 800 \text{ nm}$. Due to the shape of the nonlinear point spread function, the size of voxels along the direction of the laser propagation is generally a factor of 3-5 larger than the transverse size; *i.e.*

voxel aspect ratio. Thus, the elliptical geometry character of the LFS must be taken into account when fabricating 3D structures [20]. Based on the SLI spatial distribution at the focus; the degree of monomer conversion decreases from the inside to outside of voxel. This phenomenon has important ramifications for the chemical and physical properties of the printed structures. Besides, the NA-OL also has a dominant influence on the voxel's dimensions [11]. F. Burmeister et al. [141] reported the effect of high NA focusing on the resolution 3D nanoprinting.

III.2.3. Exposure Time Dependency

III.2.3.1. Dependence of Voxel Diameter

Here, we investigate TPP resolution by controlling the irradiation time. Figs.III.6(a-b) show SEM images of voxels that were printed by single spot irradiation under different times of exposition, at a fixed laser intensity of $\sim 0.71 * 10^9$ mW/cm² in Fig.III.6(a) and $1.32 * 10^9$ mW/cm² in Fig.III.6(b), respectively. We use two values of intensity to show the saturation of Δ_{xy} against the applied exposure time [12]. Δ_{xy} monotonically increases with the exposure time (*vide infra*), and reaches a saturation statut at a certain time of exposition. After the initial voxel formation, continuous irradiation causes the polymerized volume to expand in the 3-directions, as schematically shown in the inset of Fig.III6(a) [28].

Note that the solidified voxel and its surrounding is a clear-cut division of liquid; *i.e.* methyl methacrylate monomer, MMA-M, and solid; *i.e.* poly(methylmethacrylate) PMMA, phases. The inset of Fig.III.6(b) illustrates the solidified voxel (solid phase) and its surrounding phases; meaning solid-liquid phase which contains a mixture of PMMA-MMA (not stable phases), and liquid phase which only contains MMA monomers [110]. Thus, when the exposure time increases, voxel expands in all direction, this phenomenon can be explained by that the printed voxel is surrounded by the active MMA-M which able to be polymerized after TPE process [142,143].

Instantaneously, after 1 ms exposure time, a voxel of a certain size is formed around the maximum of the SLI; thus, the voxel consists of highly cross-liked-PMMA [110]. As shown in the inset of Fig.III.6(b), when the resin is subjected to prolonged exposure, three different regions of varied concentrations of cured resin are obtained, which means three phases; *e.g.* solid, liquid-solid, and liquid. The 1st phase is a high molecular weight densely polymerized region; *i.e.* solid and stable pattern. For the 2nd phase, it has a low weakly polymerized region and an external unpolymerized region; *e.g.* when the exposition was prolonged [28]. The 2nd phase; *i.e.* liquid-solid state, and the

3rd phase; *i.e.* liquid resin, are likely to be eliminated after washing. Consequently, the liquid-solid phase was considered as a result of an irradiation intensity below the TPA threshold; consequently, the mini-polymerized part is considered not stable to survive the washing process.

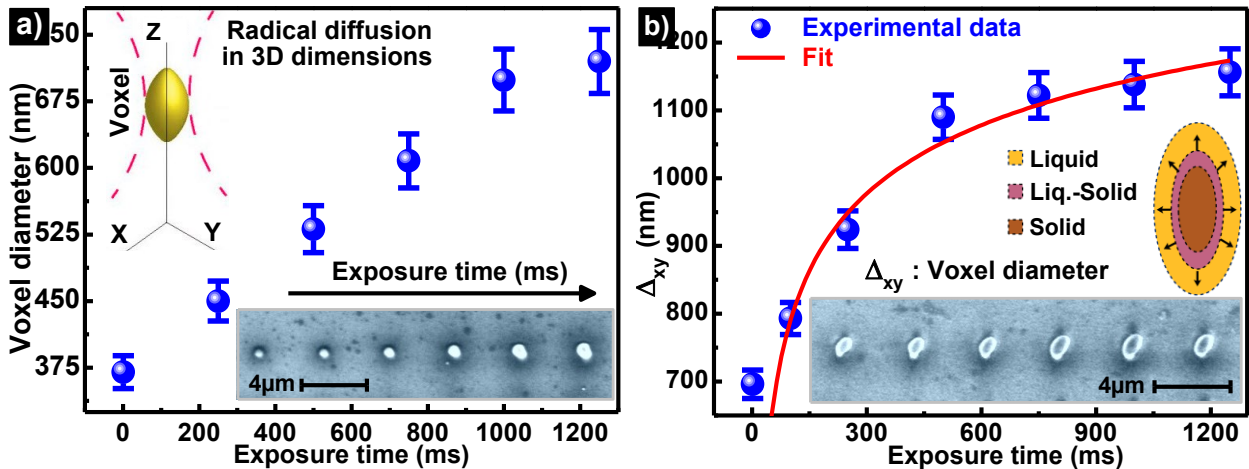


Figure III.6. Exposure time dependency. (a) Exposure time dependency on Δ_{xy} at a fixed intensity of $I_1 = 0.71 * 10^9 \text{ mW/cm}^2$; SEM image of the corresponding printed voxels and illustration of voxel expansion in 3D, are shown as an inset. (b) Δ_{xy} dependency on exposure time at $I_2 = 1.31 * 10^9 \text{ mW/cm}^2$; (inset) schematic presentation of different states of the resin as a function of exposure time; solid (polymerized state), liquid-solid (mixed state-weakly polymerized region), liquid (liquid resin: MMA-M); the full line is a logarithmic fit guide to the eye [12].

To get further insight into the dependence of Δ_{xy} on exposure time, we increased the intensity from $0.71 * 10^9 \text{ mW/cm}^2$ (Fig.III.6(a)) to $1.31 * 10^9 \text{ mW/cm}^2$ (Fig.III.6(b)) to note a saturation in the voxel size; this saturation means that the concentration of MMA monomer in the resin mixture is consumed around the focal voxel [40]. The SLI contour defines the voxel shape in their Δ_{xy} and Δ_z dimensions. Indeed, Fig.III.6(b) shows that the Δ_{xy} of voxel depends on the exposure duration, and follows a logarithmic behavior which corresponds to the exponential decay of the MMA monomers concentration upon TPE [12]. At longer time of irradiation, MMA monomers are consumed around the LFS; corresponding to the contour of SLI distribution; preventing the voxel growth. From the literature [18,21,28], we infer that Δ_{xy} is more sensitive to the laser intensity than to exposure time.

Following the SLI distribution at the focal region, and as described in [53], the voxel size dependency on exposure time can be explained by the threshold performance of TPP [54,55]. If the photopolymerizable resin has a threshold of laser dose $L_d(th)$; *i.e.* in energy E_n per unit area, for polymerization or solidification within an exposure time t , the LFS of an intensity profile $I(r)$

produces successful TPP reaction with the following condition $I(r)t \geq L_d(th)$ [56,57]. If t is so small that only the central part of the gaussian beam satisfies this condition; the printed voxel has a radius r_s smaller than the $1/e^2$ intensity beam radius w . As t increases, Δ_{xy} gradually grows; *e.g.* following the LFS expansion, as shown in Fig.III.6(a-b). This criterion for exposure size is independent of thresholding mechanisms; therefore, it holds for resin solidified by various mechanisms; including steps of polymerization; *i.e.* TPP [42].

III.2.3.2. Microline Diameter Dependency

Here, we investigate the resolution of the nanofabrication of nanoline by varying the exposure time (Fig.III.7(a)). Based on the inspired results of Δ_{xy} -dependent exposure time, we printed microlines using the TPP continuous scan of voxels [108]. D. Wu's group [144] proved that the fluctuation of the voxel size is the major factor that counteracts the self-smoothing effect even if the scanning step (pitch) is sufficiently small. The accuracy of 3D nanoprinting is determined by the voxel resolution, but higher precision has been achieved in practical model prototyping; *i.e.* CAD design. The higher precision of TPP-printed structures was technically guaranteed by; (i) high reproducibility of voxels with the respect of their size and shape, and (ii) high positioning accuracy of voxels due to the usage of PZT with resolution step better than $\sim 1 \text{ nm}$.

Shown in Fig.III.7(a) is the lateral size of nanoline evolution as a function of irradiation time (for one voxel). As we mentioned in the previous axis, the resolution dependency on exposure time is explained by the growth of polymerization inside the focal region [39]. In the high-precision of TPP, a small linewidth is from major importance. Hence, the influence of exposure time on the quality of the written voxels, and the size of nanoline was investigated. From Fig.III.7(a), at 1 ms of exposure and under an intensity of $I_{th} \sim 0.71 * 10^9 \text{ mW/cm}^2$, the average linewidth was $310 \pm 0.05 \text{ nm}$. By increasing the exposure time, the linewidth gradually increased. Thus, it well proved that the nanolines size strongly depends on the voxel dimensions; *e.g.* Δ_{xy} [12].

A further reduction of exposure time; *i.e.* increasing the scanning velocity, implicated improvement of the resolution of nanolines. The high quality of nanoline (smoothness of surface) was printed with a high velocity of TPP scanning; corresponding to a minimum exposure time; *e.g.* $t = 1 \text{ ms}$ in Fig.III.7(a). A further increase of exposure time; *e.g.* 2 sec , results in the damage of structures (Fig.III.7(b)); this damage may be due to micro- explosions phenomenon in the resin [110].

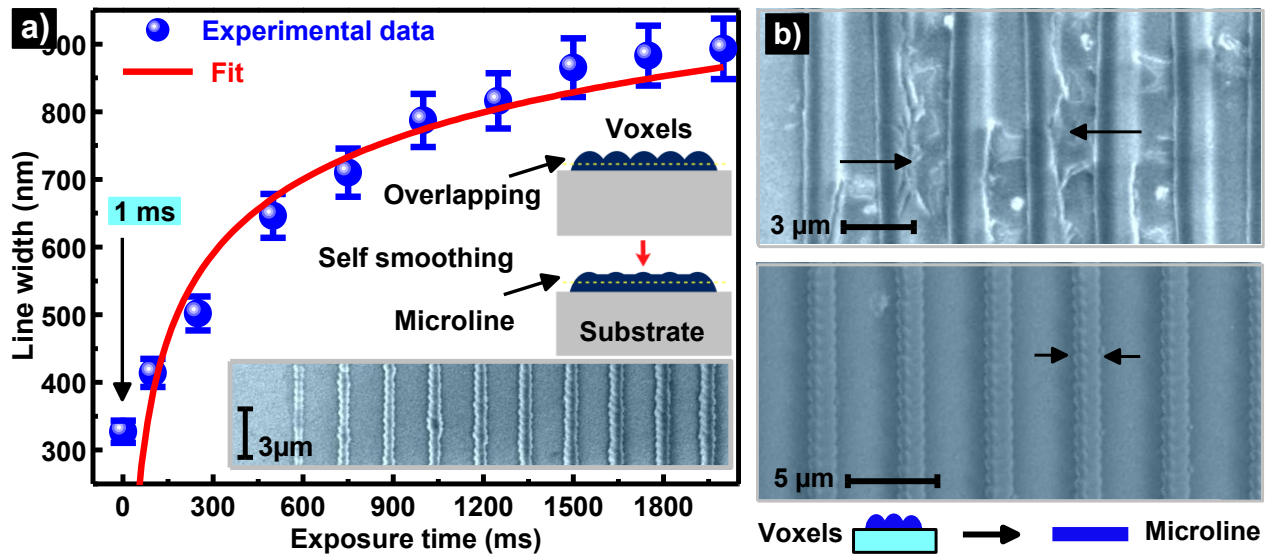


Figure III.7. Nanoline lateral-size dependency on exposure time. **(a)** Nanoline width dependency on exposure time at a fixed intensity of $0.71 \times 10^9 \text{ mW/cm}^2$; the SEM image of the corresponding nanolines was shown as an inset; the full line is a logarithmic fit guide to the eye; (inset) schematic which presents the voxels overlapping induced high-resolution. **(b)** SEM images of microlines printed using the same intensity, but at different exposure times, (top) $t = 2000 \text{ ms}$, (bottom) $t = 1 \text{ ms}$; respectively.

When the exposure time increases, the voxels; which are overlap to fabricate micro-nano-line, gradually grow at their active dangling ends as a result of their interaction with the new MMA monomer unit; *e.g.* mixed state-weakly polymerized region, wherein a chain reaction proceeds. The voxel growth is considered as a radical diffusion-dominated process; *i.e.* in all isotope direction. From the two scaling laws of voxels; *i.e.* the dependency on intensity and exposure time, a combination of low intensity and appropriate exposure time is advantageous to achieve high resolution of 3D printing [9,21]. Accordingly, we demonstrate that a long time of TPP-exposure (even at I_{th}) results in the damage of nanopatterns (bottom of Fig.III.7(b)).

III.2.3.3. Radical diffusion (R_e): Voxel Growth

According to resolution dependency on exposure time; we propose a TPP explanation, that involves radical diffusion (R_e) as schematically shown in Fig.III.8(a). When the exposure time increments after the initial voxel formation at $t_1 = 1 \text{ ms}$, the solidified volume of voxel expands by radical diffusion (R_e) in all dimensions; *i.e.* isotropically, following the process of formation of the first voxel (Fig.III.8(a)) [12]. The first printed voxel is considered as an active body, and the R_e is conceptualized as follow: polymer chains entangle inside the focal 3D volume which is defined by the LFS size, and their extensions; *i.e.* at their active dangling ends, accept new MMA-M radicals and become either long-chain or short-chain, and the polymerization reaction terminates; *i.e.* TPP

termination step [145]. Decreasing the exposure time; e.g. from 1500 ms to 1ms (Fig.III.7(a)), causes the size of the printed patterns to decrease, and at a certain point below TPP-threshold; there is no TPP reaction; e.g. the laser dose applied for TPP structuring is not enough to produce a stable solidification of resin.

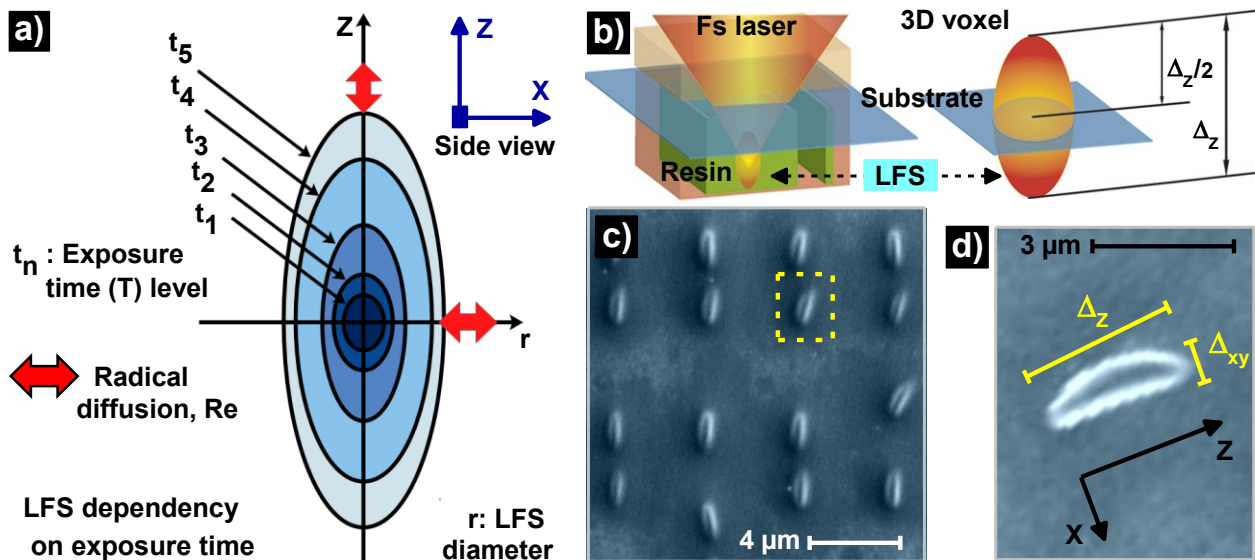


Figure III.8. Radical diffusion (Re). (a) Illustration of original voxels formation under different times of exposition; r and z are the lateral and axial directions of LFS; Re is indicated by a red arrow along the x - and z - directions; although the diffusion is isotropic. (b) Typical positions of LFS in the glass/resin interface. (c) SEM Image of complete 3D voxels; the used intensity is $0.503 \times 10^9 \text{ mW/cm}^2$, and exposure time is 1ms. (d) SEM image of a complete voxel; Δ_{xy} and Δ_z denote the lateral and longitudinal size of a voxel; respectively.

H. B. Sun et al. [28] demonstrate that after a threshold of exposure time, the voxel of a certain size is immediately formed around the maximum SLI distribution; consisting of highly solidified high-weight polymers, while its surrounding is abundant on monomer radicals and oligomer molecules with less molecular weight. This phenomenon is explained by three processes; that are [145]: (i) Brownian motion that is governed by the temperature that was triggered during TPE; (ii) diffusion with a thermal dynamic tendency from sites of high to low concentration of initiator and monomer, and (iii) remanent chemical reactions. Brownian motion is more obvious for smaller particles and is isotropic; therefore, it does not play a significant role in the anisotropic growth of printed voxels; i.e. TPP evolution. If exposure stops after the formation of the initial voxels, most of the surrounding species will diffuse; i.e. unstable polymerized resin, and finally dissolved and removed by washing.

To achieve a high resolution of 3D printing, the exposure time needs to be minimized in-order to reduce the voxel growth via the R_e process. This radical diffusion-dominated process is called voxel growth. Experimentally, we printed voxel in 1 ms exposure time to confirm the SLI distribution profile (elliptical geometric character) of the LFS. The voxel size evaluated from dot voxel which is only characterized by Δ_{xy} , to an elliptic form of a complete voxel (Δ_{xy}, Δ_z) as shown by the SEM image shown in Fig.III.8(d). According to different forms of voxels printed using TPP, the voxel arrays are influenced by the z-position of LFS; *e.g.* $\sim 1.4 \mu m$, relative to the glass/resin interface (Fig.III.8(b)). The correlation between the voxel size and exposure time possessed a non-linear behavior and it is investigated, as discussed in [110].

III.2.4. Focal Spots Related to TPE

The TPA process was theoretically analyzed within the semiclassical formalism of light-matter interaction [146]. In 3D nanoprining, the Fs laser beam is tightly focused on the resin through a high NA-OL. Thus, a TPP reaction can be initiated by TPE (NLO effect); *i.e.* localized around the LFS. Thanks to NLO effect, the laser beam can be focused (LFS) inside of the resin; not just on the surface of it. The LFS was originally defined in ray optics as a geometrical point at which parallel light ray's incident from a focusing lens; *e.g.* OL, are focused after refracting or reflecting [40]. Further treatment involved optical-diffractions at an aperture, on which primary imaging theories were established [18]. 3D photolithography; including TPP is pursuing SDL accuracy, and a spatial resolution 20% of the diffraction limit has been achieved. Therefore, it is desired to systematically study the properties of the LFS related to TPE; not only its lateral dimensions; but also, their longitudinal one. Shown in Fig.III.9 is the LFS field distributions related to TPE. An OL lens of $NA = 0.1$ was used as focusing optic; note that this low NA mentioned here, it is just used to characterize the TPE behavior at the focal region (LFS) [46].

Optical focusing; *e.g.* OL, can be understood as the interference of propagation components of the optical field emanating from different locations of the pupil plane of the lens; *e.g.* Huygens-Fresnel principle. In typical Fourier optics treatment, low-NA OL; *e.g.* $NA = 0.1$, is considered as a thin focusing lens and its function is a pure phase modulation to the incident field [46]. The highest angle between two propagating waves from the diametrically opposing parts from the aperture gives rise to the highest spatial frequency fringes and consequently determines the resolution of OL, as shown by $NA_1 > NA_2$ in Fig.III.9(a) [18,21,28]. Hence, the NA is defined as follow $NA = n \sin \Theta_{max}$, where n denotes the refractive index in the image space, and Θ_{max} is the opening

angle of the OL. This, provides a measure of the resolution power of the focusing optic. As an example of the application of the use of LFS related to multiphoton excitation, is 3D printing using Fs laser. In our work [12,20], that is discussed in this thesis, a Ti sapphire Fs laser operating in mode-lock emitting at 780 nm with 140-fs pulse width; was tightly focused through $\text{NA} \sim 1.4$; yielding a focused intensity on the sample in the order of $\sim 10^9 \text{ mW/cm}^2$.

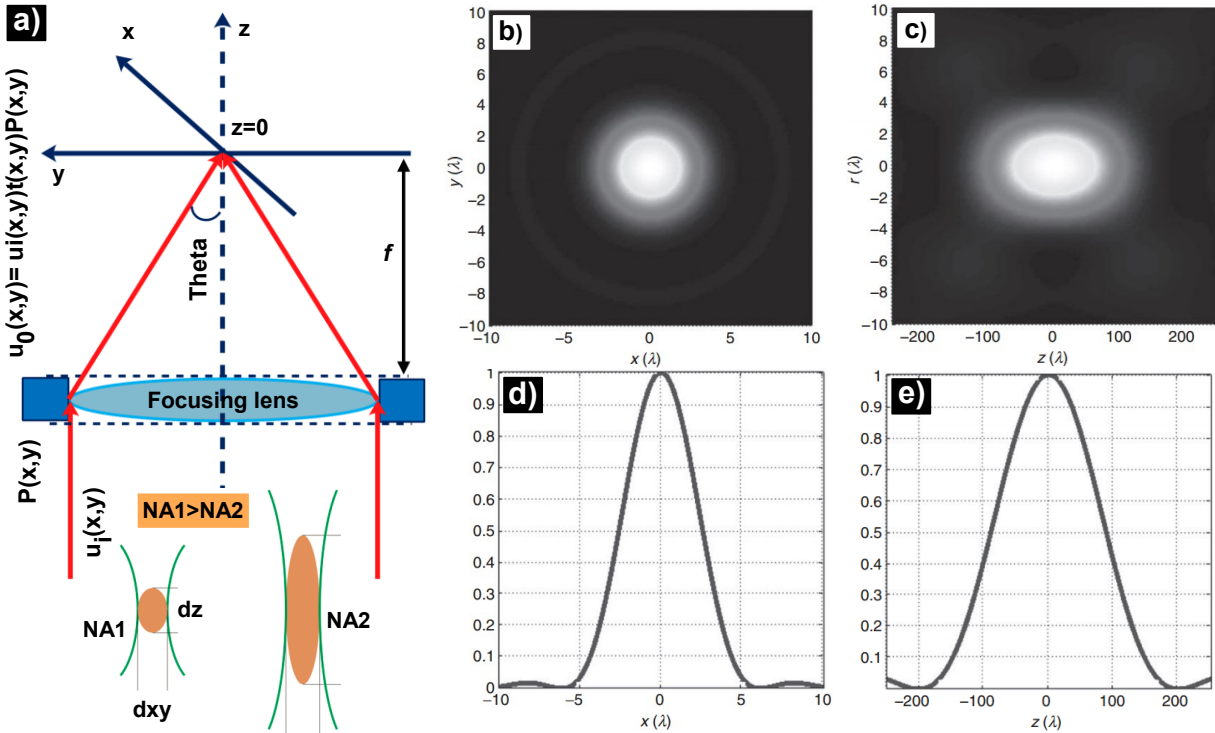


Figure III.9. Focal field distributions of an OL of an $\text{NA} = 0.1$. **(a)** Presentation of the diagram and coordinates for the focal field calculation of a thin OL; the LFS dimensions are influenced by NA ($\text{NA1} > \text{NA2}$) as shown as an inset. **(b)** Total intensity profile in the focal plane (xy). **(c)** Total intensity in the (xoz) plane showing a very elongated LFS. **(d)** Line scan of the distribution in the focal plane for **(b)**. **(e)** Line scan of the distribution along the optical axis for **(c)** [46].

Shown in Fig.III.9 is the spatial distribution of the laser beam at the focal plan of the OL; *i.e.* LFS. At a given laser wavelength of λ ; $\lambda = \lambda_0/n$, for a corrected focusing lens with a focal length of f , the transmission function of the lens which focuses light is given by [46]:

$$t(x,y) = e^{i(k/2f)(x^2+y^2)} \quad (\text{III. 5})$$

Multiplying this transmission function to the incident field $u_0u(x,y)$ and the lens pupil function $P(x,y)$, and applying the Fresnel propagation; the optical field near the geometrical focal plane can be expressed as follows:

$$\begin{aligned}
u(x, y, z) &= \frac{i u_0}{\lambda f} e^{-ikf} \int_{-\infty}^{+\infty} \int_{-\infty}^{+\infty} u_0 u(x', y') P(x', y') e^{-i(\frac{k}{2f})[(x-x')^2 + (y-y')^2]} dx' dy' \quad (III.6) \\
&= \frac{i u_0}{\lambda f} e^{-ikf} e^{-i(k/2f)(x^2 + y^2)} \int_{-\infty}^{+\infty} \int_{-\infty}^{+\infty} u(x', y') P(x', y') e^{i(k/f)[xx' + yy']} dx' dy'
\end{aligned}$$

For a circular focusing lens with a radius of a , the pupil function is described as follows:

$$P(x, y) = P(\rho) = \begin{cases} 1, & \rho \leq a \\ 0, & \text{otherwise } \rho = \sqrt{x^2 + y^2} \end{cases}$$

Under uniform illumination ($u(x, y) = 1$), the Eq. (III.6) can be recast in the polar coordinates as:

$$u(v, u) = 2iNe^{-ikf} e^{-i(v^2/4N)} \int_0^1 u_0 P(r') e^{i(uv'^2/2)} J_0(vr') r' dr' \quad (III.7)$$

Where $N = \pi a^2 / \lambda f$ is the Fresnel number, $r' = r/a$ is the radial distance normalized to the lens radius, and $J_0(\cdot)$ is the zeroth-order Bessel function of the first kind; the parameters v and u are the normalized radial and axial coordinates; which is defined as follows [46]:

$$v = \frac{2\pi}{\lambda} r \sin\theta_{max} = k_0 r (NA) \quad (III.8)$$

$$u = \frac{2\pi}{\lambda} z \frac{a^2}{f^2} \approx \frac{k_0 z}{n} (NA)^2 \quad (III.9)$$

It can be seen that the higher lens-NA, a smaller of the real coordinate r will be; which leads to smaller LFS size, as denoted in Eq.III.7. It is worth pointing out that the focal field is calculated from the transmitted field on a planar reference surface right after the OL (Fig.III.9(a)); *e.g.* Huygens-Fresnel principle. This is very different from the high NA case. The inset of Fig.III.9(a) shows the difference in the focusing behavior between low and large NA [46,52]. One example of the focal field calculated with Eq.III.7 for $NA = 0.1$ is shown in Fig.III.9(b-e). It can be seen from Eq.III.6 that the focal field is a Fourier transform of the illumination within the pupil aperture of the focusing lens. In an optical focusing system; *e.g.* OL, higher NA gives rise to higher spatial resolution; *e.g.* as in the case of TPP nanoprining [95].

To investigate the TPE-related LFS; one is interested in the SLI distribution at the focal volume. To experimentally investigate TPE which is proceed at the LFS, one needs; (*i*) a recording media

(resin), that quadratically responds to IR-light excitation. Also, (ii) a technique that is capable of revealing the 3D size of LFS; *i.e.* TPP [20]. X-Z. Dong et al. [57] investigate the profile of the intensity at the near-LFS region; thus, a complicated SLI distribution was found. At near-LFS region; *i.e.* diffraction-pattern center, a tubular structure of high intensity exists (Fig.III.10(a)). Experimentally, the LFS-volume can be several times larger than the diffraction limit, and theoretically could be as small as ~ 10 nm order, limited by the molecular size of the polymerizable media [40]. Since diffraction occurs at circular apertures imposed by the focusing OL. In the neighborhood of the LFS, the SLI distribution is rotationally symmetrical about the optical axis (u -axis in Fig.III.10(a)), and mirror-symmetrical about the geometrical focal plane [57].

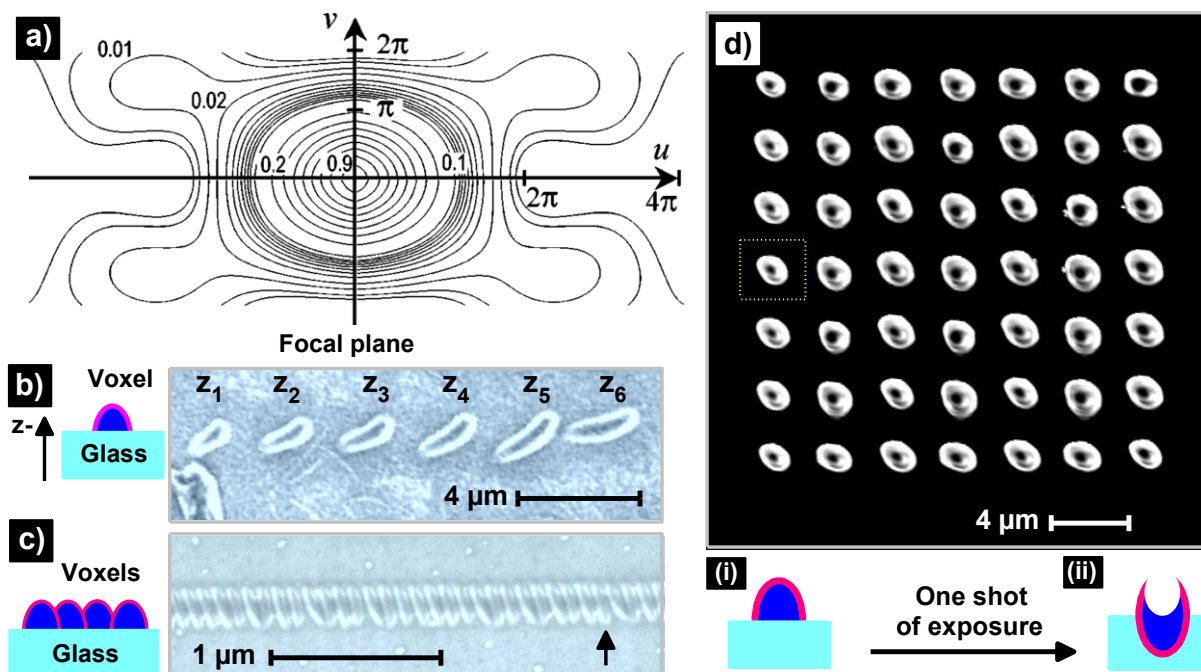


Figure III.10. LFS related to TPE. (a) The SLI isophotes of focus; unitless parameters, u , and v are normalized axial (z) and lateral (r) coordinates [40]. (b) SEM image of voxels that were printed by controlling the z -position of the LFS ($z \sim 100$ nm step) at $I_{th} \sim 820$ kW/cm²; this test demonstrates the elliptical geometry character of the LFS. (c) SEM image of nanoline printed by SDL overlapping of the LFS. (d) SEM image shows the recording of the LFS on a polymerized pattern; *i.e.* PMMA; where (i) TPP process and (ii) Fs laser ablation; we use one shot of exposure as shown as an inset.

As an application of the use of the LFS; it is used to remove the matter from the polymerized pattern (by increasing the power of excitation). The recording of the LFS on the polymerized phase of the resin is shown in Fig.III.10(d). From this SEM image, we conclude that the focal spot influence on the printed voxel, by fabricating nanohole; *e.g.* Fs laser ablation, which can be taken the elliptical geometry of the LFS (Fig.III.10(d)).

The pre-polymers resin used for 3D nanoprinting serves such a recording media for characterizing and optimizing the TPE-related LFS; as experimentally proved by the nanoprinted voxel and their laser-ablation shown in Fig.III.10(b-c). The number of photons absorbed per molecule per unit time; by means of TPE; is proportional to the (i) SLI distribution and (ii) TPA cross-section of the initiator involved in the resin preparation [11,28]. Also, the total number of photons absorbed per unit time is proportioned to the initiator concentration (C_{PI}), and the excited submicron volume of voxel (V_{voxel}). In the absence of saturation and photobleaching effect, the number of radicals generated per unit time N is given by [3,40]:

$$N = C_{PI} \delta \phi I_0^2 \int_V S^2(r, \theta, z) dV_{voxel},$$

Where I_0 symbolizes the exposure intensity at the geometrical focal voxel V_{voxel} , $S(r, \theta, z)$ is a unitless function used to describe the incident light distribution, and ϕ is the quantum efficiency of radical yield. The shape of the two-photon excited-LFS is determined by $S^2(r, \theta, z)$ [11]. To practically realize the idea which is formulated above, a 780 nm, 140 fs, mode-locked Ti: sapphire Fs laser, operating at 80 MHz, was used as a light source. The laser was focused using a 1.4 NA oil-immersion OL [20]. Accurate information on the LFS related to TPE is essential for not only in TPP 3D-nanoprinting; but also, for diversified fields such as; optical integrated circuits, optical memory, and holographic recording in various materials [11].

III.3. Realization of $\lambda/21$ Sub-Wavelength Resolution

III.3.1. SDL Resolution in 3D Nanoprinting

In this axis, we review the effect of manufacturing parameters which influence the resolution of 3D nanoprinting; e.g. laser intensity and scanning speed. The accuracy of 3D nanoprinting is always a trade-off with the writing/scanning time; meaning the velocity of the continuous scan presented in the structures need to be printed [12,110]. The increase of the intensity and/or decrease of the writing speed; there is a decrease in TPP resolution [144]. However, increased irradiation intensity and time lead to a micro-explosion phenomenon (photoionization) in the resin, as shown in the SEM image in Fig.III.11(e); which is believed to occur as a result of a rapid increase of temperature occurred during TPP reaction. Experimentally, the micro-explosion phenomenon is manifested by intense white light emission parents; i.e. collected by the CCD camera, to the laser breakdown phenomenon [12]. The damage of the printed nanoline is explained by the micro-explosion phenomenon (Fig.III.11(e)). It is known from the literature [18,21,28] that low laser

intensity is needed to achieve a high TPP-resolution. The high writing speed greatly decreased the exposure time; resulting in very thin nanolines; *e.g.* ~ 36 nm resolution. Thus, a resolution below the diffraction limit was achieved using our custom-made optical setup.

Kawata's group [9] demonstrated that a lateral resolution down to ~ 120 nm (Fig.III.11(a)) has been achieved; which is considered much better than that obtained by conventional lithography-based polymerization, and by laser-rapid-prototyping [6]. As shown in Fig.III.11(b), a logarithmic dependence of voxel size; *i.e.* Δ_{xy} and Δ_z , on laser intensity was obtained, which is considered as a natural result of the exponential decay of the monomer concentration versus the irradiation dose; this phenomenon was explained by the duplication of the LFS.

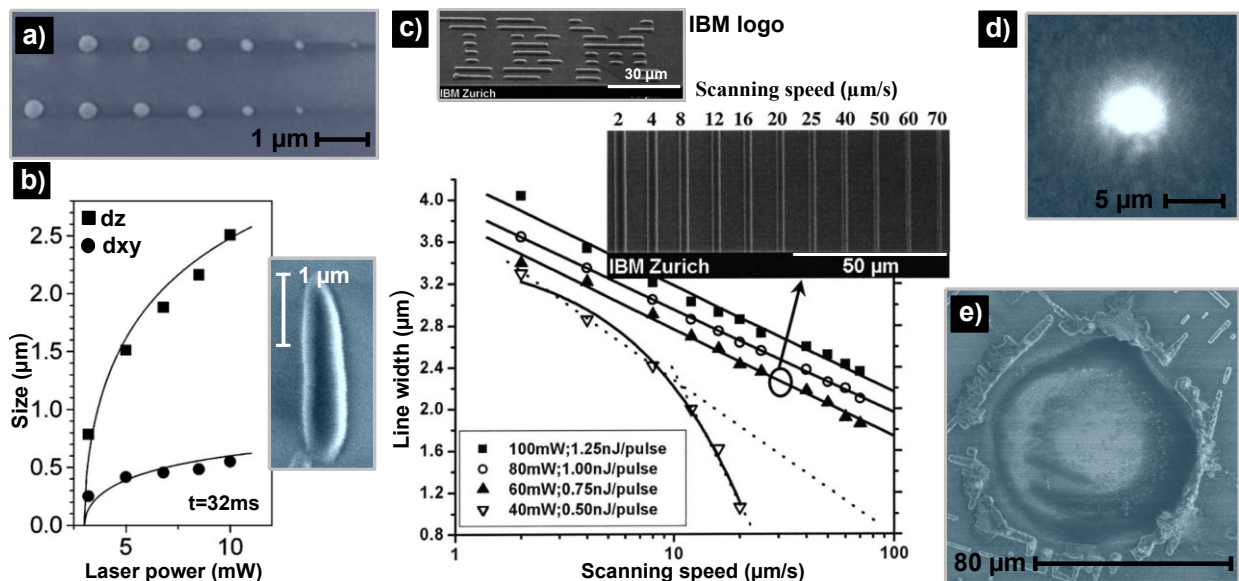


Figure III.11. Realization of SDL resolution. (a) A SEM micrograph of voxels polymerized under different exposure conditions; *e.g.* laser intensity. (b) The laser power-dependent Δ_{xy} and Δ_z under an exposure time of 32 ms; a complete voxel is shown as an inset. (c) Linewidth as a function of scanning speed for different laser energies; the inset presents a SEM micrograph of microlines fabricated at different scanning speeds (laser energy is 0.75 nJ/pulse), and an IBM pattern produced by continuous scan mode of microline. (d) Microexplosion phenomenon collected by the CCD camera. (e) TPA material; *i.e.* resin, damaged after the explosion phenomenon.

Shown in Fig.III.11(c) is the linewidth versus the scanning speed applied during TPP nanostructuring [147]. It is observed (Fig.III.11(c)) that the linewidth was reduced when the scanning speed increases; meaning a reduction of irradiation time for each exposure shot; *i.e.* for each TPP irradiation step. According to these results which are considered as literature review, we printed short SDL nanoline (~ 2 μm in length) between two adjacent voxels but with a high TPP resolution; *e.g.* $\sim \lambda/21$ nm. In TPP-based 3D nanoprinting, both NLO absorption and thresholding

effects (*vide infra*), contribute to high resolution. The size of printed voxels (Fig.III.11(a)), which defines the TPP resolution, can be tuned to be much smaller than that defined by the diffraction limit. This effect is called the material nonlinearity [12].

III.3.2. Achievement of $\lambda/21$ Sub-Wavelength Resolution

In conventional photolithography, the resolution attains one-over-quarter wavelength; *i.e.* $\lambda/4$, of the light source used for 3D nanostructuring process [3,6]. In the work discussed in this section, we initiate a new approach to TPP nanoprinting that obtains a resolution of $\lambda/21$; corresponding to ~ 36 nm of the smallest printed pattern. Thus, we succeeded to TPP-fabricate many periodic series of SDL nanofibers; *i.e.* called suspended polymerized nanofibers (SPnF(s)), connecting two adjacent polymerized-voxels [12].

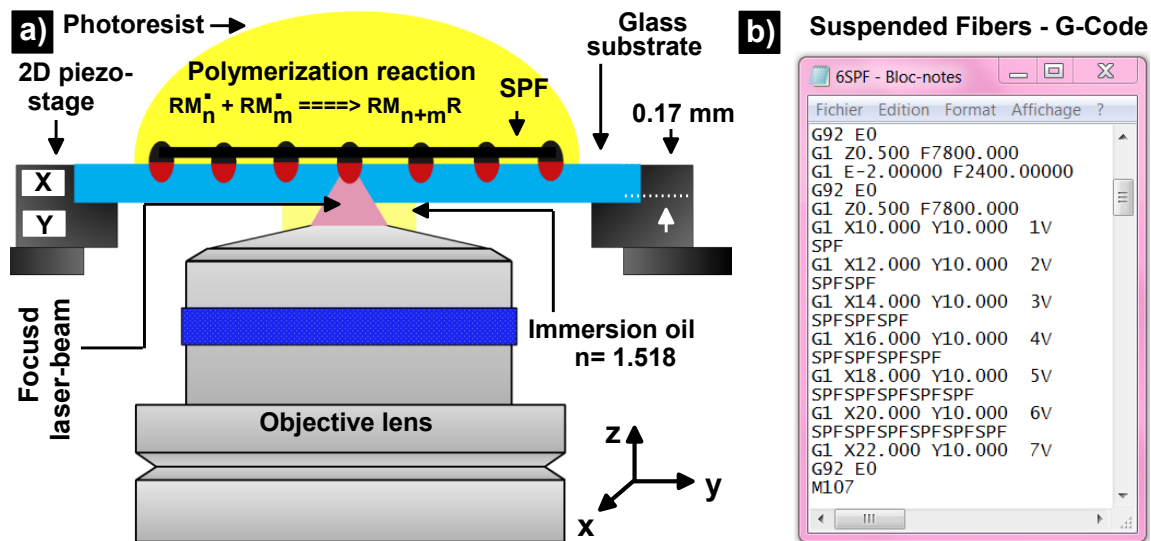


Figure III.12. Achievement of SDL resolution of suspended polymerized nanofibers (SPnF(s)). **(a)** Schematic illustration of the developed 3D micro/nanofabrication set-up used for the FsLDW of SPnFs(s) connecting two voxels. **(b)** G-Code data of the nano-SPF connecting two voxels; the z-position in this nanofabrication process was fixed at ~ 500 nm from the substrate/resin interface.

To TPP-print SPnF(s), we applied as manufacturing conditions a high laser intensity combined with fast scanning speed; *i.e.* $V(A-B) = dx/dt$. Where $V(A-B) = 100$ mm s^{-1} refers to the speed of the PZT/sample when moving from the first voxel (A) to the next voxel (B); $x = A-B$, and t denotes the scanning time; *i.e.* exposure time, when the sample moves from voxel A to B (Fig.III.12(a)). More details concerning the experimental set-up were discussed in chapter II. Shown in Fig.III.12(a) is a schematic of the developed TPP-based FsLDW set-up employed for the nanoprinting of SPnF(s). Fig.III.12(b) presents the G-Code data applied to displace the positioning PZT system during the TPP-fabrication of SPnF(s) [110].

As shown in Fig.III.13(a), SPnF(s) were successfully printed when the z-position of the LFS is set around $1/2$; *i.e.* $z\text{-position} \sim 500 \text{ nm}$, into the interface between the cover glass and resin (along the z-direction). Fig.13(a) presents the SPnF(s) printed under different z-positions of the LFS; as demonstrated by the levels 1-4 (level of the LFS in the interface). Therefore, when the LFS is positioned less than $1/2$ of their longitudinal size inside the resin, no stable nanofibers can be polymerized; *e.g.* levels 1-2 in Fig.III.13(a). Consequently, the form of the printed SPnF(s) is shaped following the elliptical geometry character of the LFS [12]. Thus, the longitudinal size (or resolution) of SPnF(s); *i.e.* corresponds to Δ_z of a voxel, is always larger than their polymerized width. High-resolution nanofiber with a width of $\sim 36 \text{ nm}$; about $\approx \lambda/21$ of resolution, is achieved by introducing this novel TPP-approach.

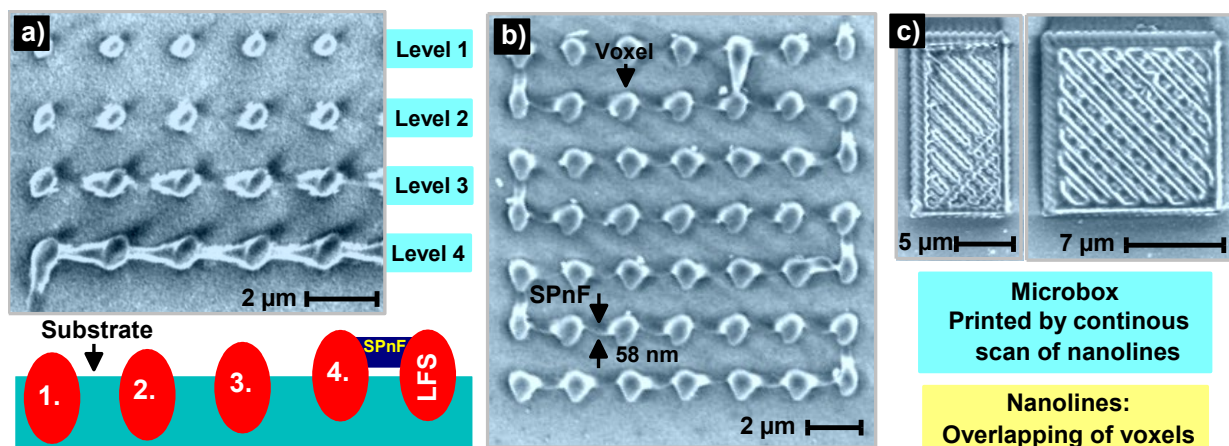


Figure III.13. Achievement of SDL resolution of SPnF(s). (a) TPP printing of SPnF(s) using different LFS-z-positions ($\sim 100 \text{ nm}$); stable SPnF(s) can be printed only when $1/2$ of the LFS was submerged inside the resin. (b) SEM image of SPnF(s) printed at a high scanning speed of 100 mm/sec . (c) SEM images of 3D microcubes printed with different sizes using a continuous-scan mode of nanoline; a serie of nanolines is observed as a building-block of the 3D cubes.

Fig.III.13(b) shows an example of the SPnF(s) produced using this TPP-approach [25]. Thus, a resolution of $\sim 58 \text{ nm}$; *i.e.* $\lambda/13$, is achieved. T. T. Chung's group [139] demonstrated that the nanofeature sizes of the printed structures were determined by the irradiation intensity and writing speed. At a certain laser intensity of irradiation, SPnF(s) thinned down when the scan speed was increased until a limit; *e.g.* too thin to survive washing. The scan speed was accelerated along the direction of the writing direction. Due to the weak intensity of the outer part of the LFS; there was a lower-degree polymerized zone at the outer portion of voxels; *i.e.* no stable SPFs can be printed. In this case, when we use an intensity below the TPP threshold, SPnF(s) were always disappeared during the development phase [12].

The SEM micrographs shown in Fig.III.14 depicts the experimental evidence of SPnF with a polymerized SDL-width of 151 nm ($\lambda/5$) in (a), 121 nm $\lambda/6$ in (b), 51 nm $\lambda/15$ in (c), 44 nm $\lambda/17$ in (d), 36 nm $\lambda/21$ in (e), and no SPnF in (f) by using irradiation intensities of $2.24 * 10^9\text{ mW/cm}^2$, $1.80 * 10^9\text{ mW/cm}^2$, $1.48 * 10^9\text{ mW/cm}^2$, $1.31 * 10^9\text{ mW/cm}^2$, $0.98 * 10^9\text{ mW/cm}^2$, and $0.91 * 10^9\text{ mW/cm}^2$; respectively. These intensities values were calculated at the vicinity of the LFS, and the dimensions of the SPnF(s) in their axial and longitudinal resolution depend on the photon fluence density of the laser dose; *i.e. intensity * exposure time*. Thus, the diffraction limit of light is broken by using a nonlinear absorption process; *i.e.* TPA mechanism. TPP-based stereolithography at SDL resolution using MMM-resin as a matrix material was verified by printing SPnF(s).

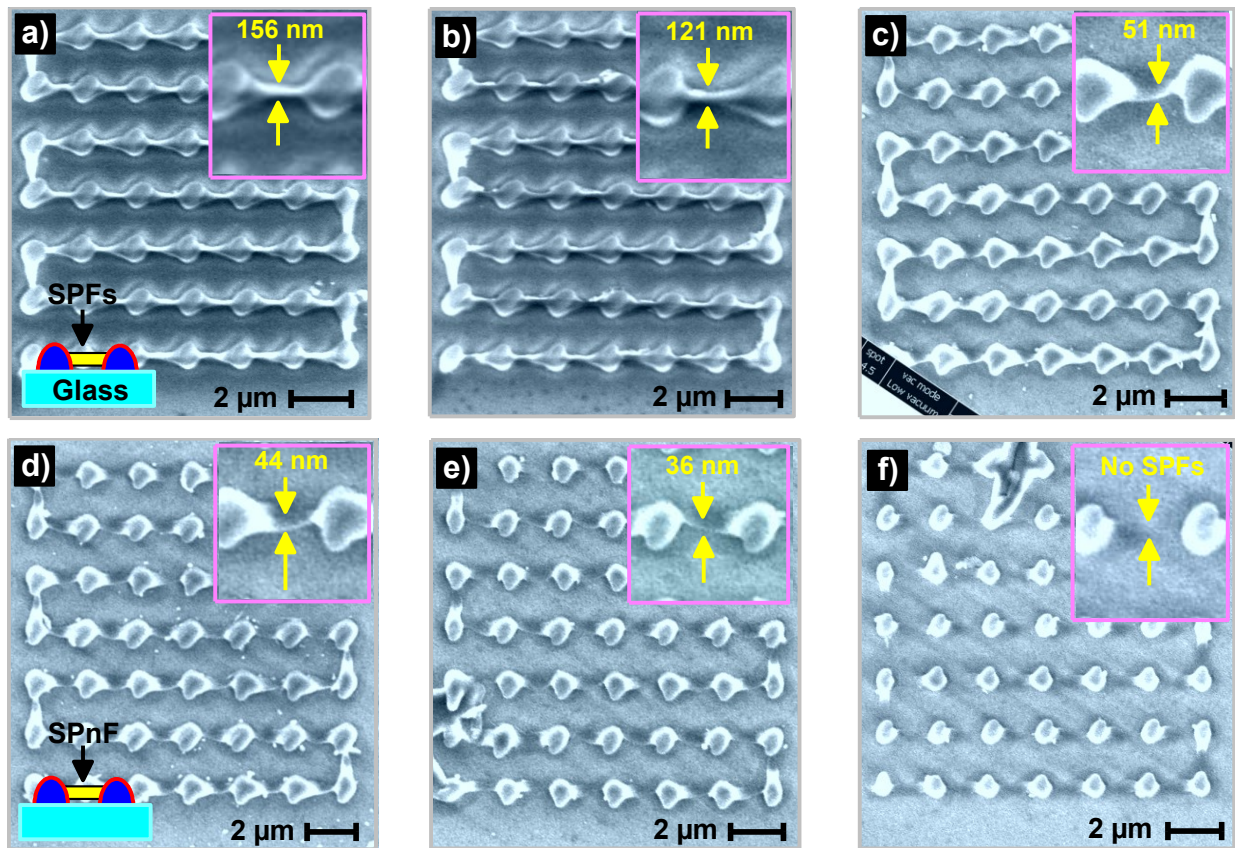


Figure III.14. SEM images of submicrometer SPnF(s) fabricated by TPP nano-stereolithography between two voxels at a laser intensity of (a) $2.24 * 10^9\text{ mW/cm}^2$, (b) $1.80 * 10^9\text{ mW/cm}^2$, (c) $1.48 * 10^9\text{ mW/cm}^2$, (d) $1.31 * 10^9\text{ mW/cm}^2$, (e) $0.98 * 10^9\text{ mW/cm}^2$, and (f) $0.91 * 10^9\text{ mW/cm}^2$, and a fixed scanning speed of 100 mm/sec .

We observe that the printed SPnF(s) disappear when the intensity decreases under to $\sim 0.98 * 10^9\text{ mW cm}^{-2}$, even at the same scanning speed (Fig.III.14(f)). In this case, SPnF(s) are not

completely polymerized; so, it is not stable; by the reason that the irradiation laser dose is not enough to trigger the TPP reaction; *e.g.* $I_{irr} < I_{th}$. In general, fast scanning speed greatly reduces the exposure time; resulting in very thin SPnF(s). From these results, we confirm that the patterns printed at $I_{irr} < I_{th}$ are not stable to survive washing. As well, we can say that the SPnF(s) may be ablated by the electronic beam during SEM observation; meaning that the printed patterns are too thin than $\sim 36 \text{ nm}$ of width. Also, we experimentally demonstrate that when the distance between two adjacent voxels is larger than $\sim 2 \mu\text{m}$, no SPnF(s) can be formed; because these printed SPnF(s) are too thin, and also long to survive the developing step [25].

In this work; *i.e.* corresponds to Fig.III.12-14, a Ti sapphire Fs-laser operating in mode-lock at 80 MHz and $\lambda = 780 \text{ nm}$ with a pulse width less than 140-fs was used as a light source and it was focused using an OL of $\sim 1.4 \text{ NA}$; yielding a focused laser intensity on the resin in order of $\sim 10^9 \text{ mW/cm}^2$. Here, the smallest feature size which we achieved; *e.g.* about $\sim \lambda/21$ resolution, is appreciably smaller than that reported in the literature [145]. Finally, we can say that we are succeed to introduce a novel approach to TPP-based 3D nanoprinting. These results demonstrate that the process of TPP exhibits the ability of 3D printing at the nanometric scale, as we will discuss in the last axis of this chapter.

III.4. Achievement of SDL 3D Microstructures

In the present segment, we will investigate the resolutions of 3D micro-nano-structures made by 3D printing using our home-made TPP-optical set-up. The basic building unit that characterizes the resolution of 3D laser nanoprinting is usually represented by the smallest polymerized pattern (voxel) as shown in Fig.III.15(a-b) [12]. The measurement results of the printed voxels indicated that the minimum resolution is about $\sim 94 \text{ nm}$; *e.g.* Δ_{xy} , which was quite good for 3D printing by using MMA-resin without supplementary additive; *i.e.* quencher radical [148]. Commercially available MMA-resin; *i.e.* consisting of benzil-initiator, is transparent to the IR Fs laser; *e.g.* 780 nm wavelength, and allows it to penetrate deeply; meaning that TPA can only be triggered around the LFS (Fig.III.15(b)).

The used OL which focuses light provides a small size of LFS which is required for fine feature detail in 3D, and allows the use of low laser power of high repetition rate; while still providing adequate intensity at the focal region; *i.e.* $\sim 10^9 \text{ mW/cm}^2$. Because that the nonlinear probability of TPA quadratically depends on the intensity I with a TPA rate of $R = \delta I^2$, where δ denotes TPA

cross-section of the pre-polymer resin; this allows a narrower excitation in 3D space; *i.e.* in volume pixel, and thus, true 3D microsized structures can be printed by 3D-scanning the LFS inside the resin, according to a pre-programmed pattern; *i.e.* CAD model (Fig.III.15(c)) [21,20].

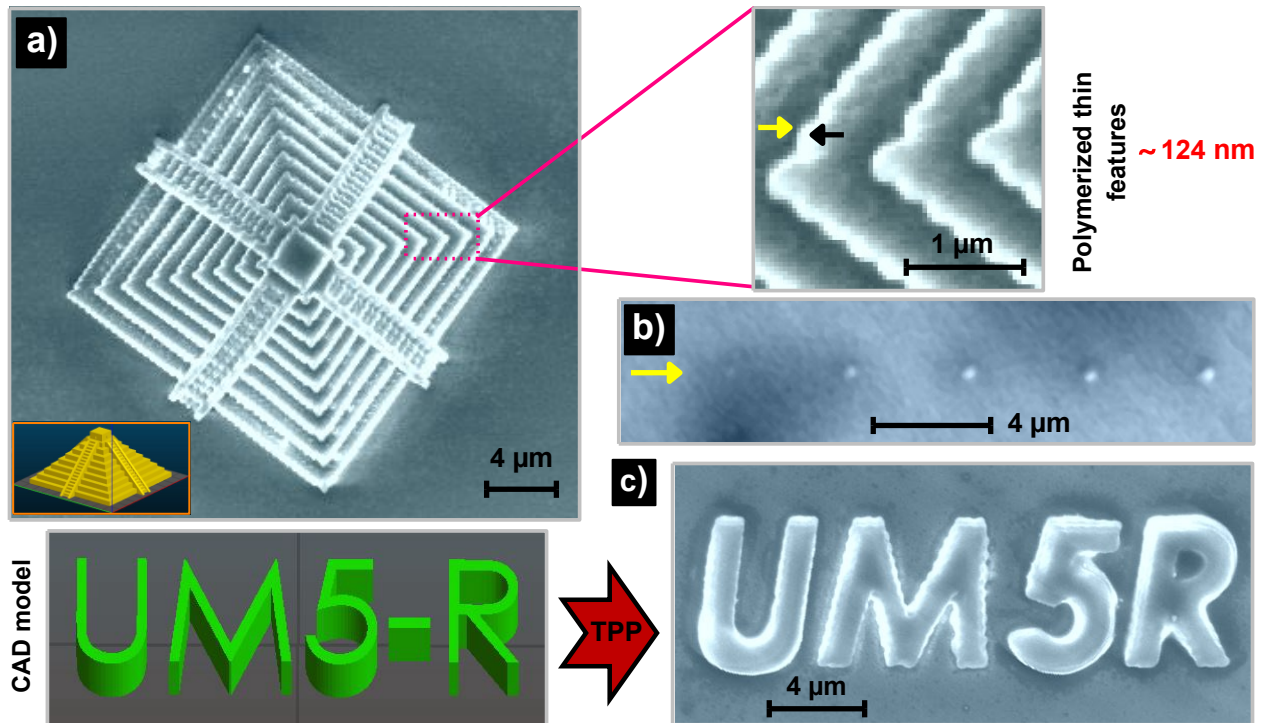


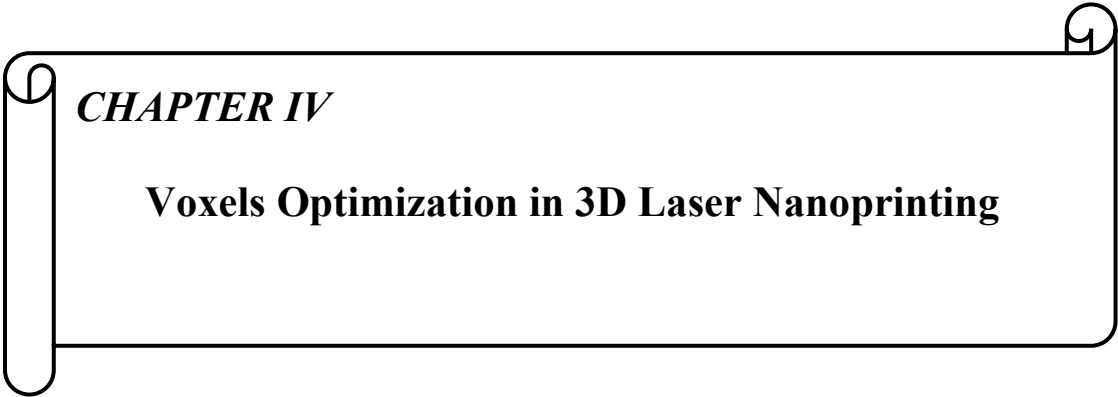
Figure III.15. Experimental evidence of SDL resolution. (a) SEM image of a 3D pyramid produced by using TPP printing; the thin features of the pyramid which demonstrates the resolution (~ 124 nm) is shown as an inset. (b) SEM image of voxels printed in different z-positions of the LFS (~ 50 nm); a resolution of ~ 94 nm is achieved. (c) SEM image of 'UM5R' pattern; UM5R denotes Mohammed 5 University in Rabat; every character scale is ~ 5 μm, about the half-size of a red human blood-cell; (inset) 3D model of UM5R pattern; *i.e.* CAD model.

In 3D nanoprinting, the 3D microsized architectures were produced by using TPP process; which combines the concepts of TPA with polymerization of a free radical (Fig.III.15(a)). By pinpoint scanning the LFS according to a programmed pattern; *i.e.* assured in our TPP set-up by a g-code data, 3D structures were successfully fabricated (Fig.III.15(c)) [128]. The SEM images of some of these structures are shown in Fig.III.15. In particular, the SEM image of the pyramid of sub-micrometric features; *e.g.* ~ 124 nm resolution, are clearly observable on the pyramid, as shown in Fig.III.15(a). The typical laser intensity used for this TPP fabrication is $\sim 1.14 \times 10^9$ mW/cm², and the exposure time is 1 ms. Thus, the fabrication of 3D microsized structures using our custom-made TPP-setup and the programmed pattern is demonstrated [108]. Based on the inspired results

that are achieved in this study, and for our future work, we think that we can achieve a microdevice via TPP technology, which can be used for future applications.

III.5. Conclusion

To sum up, we developed a TPP optical setup for 3D nanoprinting by utilizing a pulsed Fs-laser. The Fs laser is used for its capability to provide a high intensity of irradiation that is needed to induce TPP. In this study, we investigated the effect of different manufacturing parameters; *e.g.* laser intensity and exposure time, on TPP resolution. This work provides an analysis of TPP process and also explication models that are related to dependency of the resolution on laser intensity and exposure time. We also developed a novel approach for TPP-printing of stable SPnF(s) connecting two voxels by combining high intensity and fast scanning speeds. SPnF(s) were successfully printed when $\sim 1/2$ of the longitudinal size of the LFS; *i.e.* $z\text{-position} \sim 506 \text{ nm}$, is positioned in the resin which is dropped on a cover-glass. Thus, high resolution of $\sim 36 \text{ nm}$; *i.e.* one over twenty-one wavelength $\lambda/21$, is achieved. 3D laser nanoprinting with a resolution three times smaller than the diffraction limit has been demonstrated. The goal of this research is to investigate the potential for mass-producing 3D microdevices using TPP-based 3D nanoprinting.

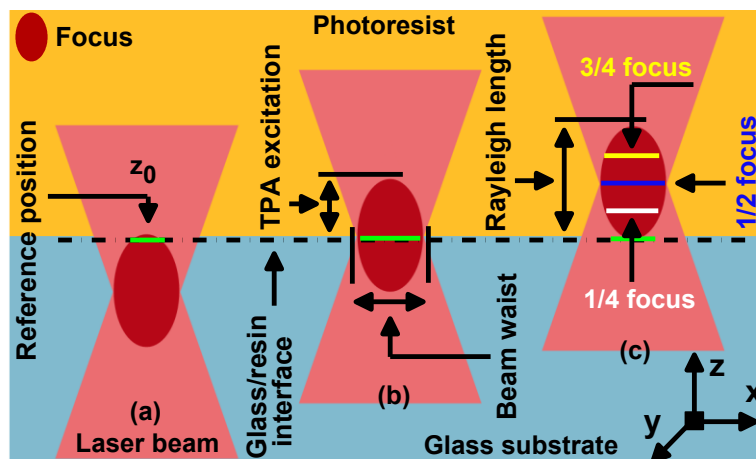


CHAPTER IV

Voxels Optimization in 3D Laser Nanoprinting

Abstract

In this chapter, we aim at studying the low-limit size of voxels fabrication by two-photon absorption in photopolymerizable resins by varying the position of the laser's focal spot, with respect to the cover glass/resin interface; *i.e.* in the longitudinal z -direction. The printed voxels are ellipsoidal owing to the shape of the focused laser beam, and we show that their dimensions; *e.g.* lateral and longitudinal, can be optimized when the laser focus is moved in the z -direction. We systematically printed voxels starting from the glass/resin interface, whereby the tip of the laser focus is positioned at the interface prior to scanning, and we studied the effect of the z -position of the focus on the width (Δ_{xy}), height (Δ_z) and aspect ratio ($AR = \Delta_z/\Delta_{xy}$) of the printed voxels. We found that the minimum Δ_{xy} of complete voxels is diffraction-limited, and the Δ_z depends on the extent of penetration of the laser focus inside the resin. Truncated voxels, which are fabricated by a partial overlap of the resin and the laser focus, allow for the fabrication of nano-features that are not diffraction-limited, and we achieved near ~ 100 nm feature sizes in our 3D fabricated objects. This study gives detailed information and quantitative analysis of the effect of the z -position of the laser focus on the size of the nanoprinted voxels as well as the resolution of 3D laser nanoprining.



Scheme. 0. Illustration of the variation of the position of the laser focus along the z -direction; (a) reference position of the focus; (b) half of the focus inside the resin (focus-waist); (c) full focal spot in contact with the resin (Rayleigh length). TPA denotes the two-photon absorption process [*].

[*] Y. Bougdid, and Z. Sekkat, Scientific Reports 10, no. 10409, 2020.

IV.1. Introduction

The “magic” of two-photon absorption (TPA), as opposed to one-photon absorption (OPA), lies in the tails of the tight laser’s focal spot (LFS) [28,52]. In TPA-based 3D nanoprinting, the amount of local cross-linking; *i.e.* TPA polymerization (TPP), depends on the accumulated (absorbed) laser dose at the focus; *i.e.* voxel. TPP is based on the nonlinear optical (NLO) interaction of a near-infrared (NIR) light; *i.e.* femtosecond (Fs) laser, with a transparent resin [137]. Due to the NLO effect of TPA, when a Fs laser beam is tightly focused into the resin through an objective lens (OL) of high numerical aperture ($NA \sim 1.4$), photo- physical and chemical events can be localized within the LFS. At the focal region, TPA results from the squared light intensity (SLI) distribution, which is spatially and temporally narrower than that of linear absorption. The tail of the LFS reduces the interaction volume of light with matter and induces a negligible solidification of the resin by TPA; thereby improving the TPP resolution [42]. Material’s nonlinearity; the so-called thresholding effect, can further reduce the size of printed voxels, and finer features much smaller than the cube of the laser wavelength (λ^3) can be fabricated [9,21].

Stimulated-emission depletion (STED) techniques can add up to optical nonlinearity and thresholding to further reduce the resolution of TPP beyond the diffraction limit [149,150]. Technical tricks can also reduce the resolution of 3D printing. For example, increasing the scanning speed reduces the exposure time, and improves resolution, as we have demonstrated in a recent work where a $\sim \lambda/21$ resolution; *e.g.* $\lambda = 780 \text{ nm}$, was achieved [12]. With such a resolution, only fibers could be achieved, and stable 3D structures were obtained with a $\sim \lambda/8.3$; *e.g.* $\sim 94 \text{ nm}$, resolution [110]. In this chapter, we will discuss another technical, albeit, an important trick to further control the size of the printed voxels. That is, the dependence of the voxel size on the z-position of focus. Our study complements those of H. B. Sun et al. [11,28] and L. Zheng et al. [151], in the sense that it gives a detailed information of the effect of the LFS z-position on the size of the printed voxels as well as the TPP resolution. In our study [20], we report what is believed the first detailed study of the voxel size dependence on the z-position of the LFS in 3D nanoprinting. That is, we study the evolution and the low-limit size (diameter (Δ_{xy}) and length (Δ_z)) of voxels fabricated in the vicinity of the substrate/resin interface. Our work is of central interest to 3D nanoprinting, since it addresses the spatial resolution of 3D printing technology, and might have potential impact for industry.

IV.2. TPA Recording Medium and Developed Optical Set-up

In order to optimize and manipulate the spatial arrangement; *e.g.* orientation, of voxels by varying the *z*-position of the LFS; *i.e.* used as a pen of light for 3D nanoprinting, one needs: (i) a pre-polymer media; *i.e.* photoresin (Fig.IV.1(a-b)), that is quadratically responds to light excitation; meaning two-photon excitation (TPE), and a technique; *i.e.* TPP lithography, that is capable of revealing the dimensions of the laser focus in 3D, as shown in Fig.VI.2(a-b) [11]. In this study of voxels optimization, we have chosen to 3D print voxels on an acrylate negative-resin. The chemical structure of the compounds involved in the preparation of our resin are shown in Fig.IV.1(a). The first component is (i) methyl methacrylate monomer (MMA) (49wt%), that acts as the main skeleton of the printed voxels; *i.e.* poly-(MMA). The second component is (ii) benzil photoinitiator (PI) (1wt%), that is used to produce an active specie upon light excitation [20].

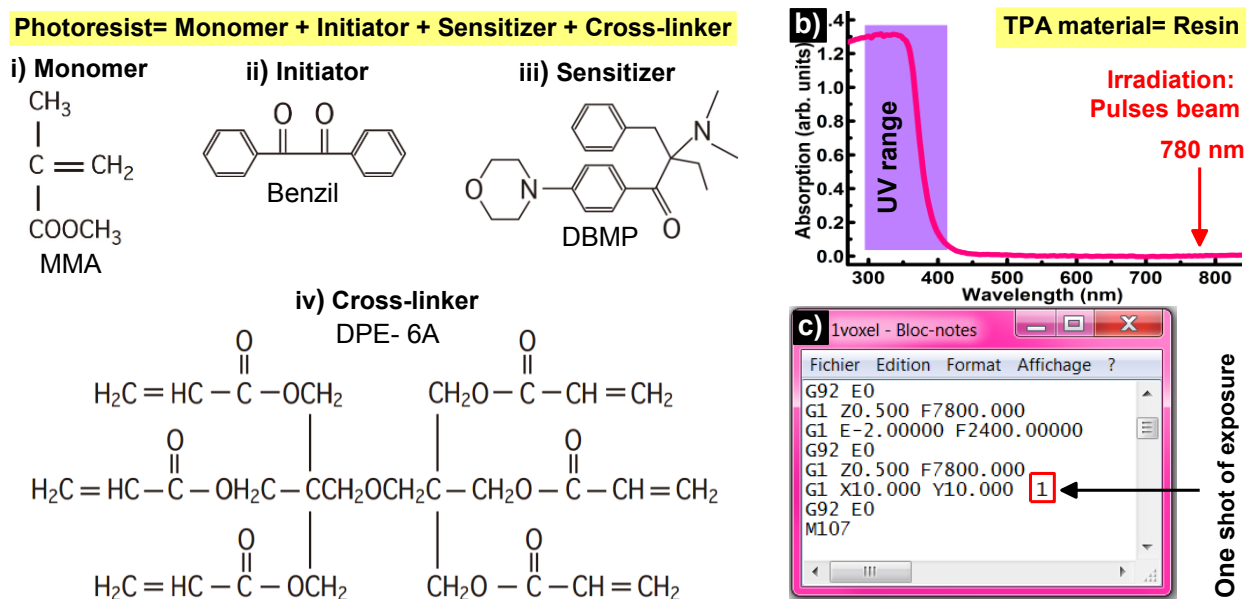


Figure IV.1. TPA material and g-code data. (a) Chemical structures of the compounds involved in the preparation of our resin. (b) The absorption spectrum of our resin. (c) G-code data applied for TPP nanoprinting of a single voxel (coordinates in g-code: $x \sim 10$, $y \sim 10$, $z \sim 0$ μm).

The third component is (iii) 2-benzyl-2-(dimethylamino)-4'-morpholino-butyrophenone 97% photosensitizer (PS) (1wt%), that is capable of absorbing light and transferring the excitation energy; *i.e.* TPE, to the PI system. From literature [3], the PI is considered as an indispensable specie needed to trigger the reaction of TPP. The last component is (iv) DPE-6A cross-linker (49wt%), which is responsible to promote the hardness of the polymerized voxels [108]. To get a complete mixing of this prepared resin, we let the viscous mixture steer overnight with a magnetic stirrer.

The absorption spectrum of our resin was measured by using an UV-Vis spectrophotometer (Perkin Elmer-Lambda 1050). It's clearly observed (Fig.IV.1(b)) that this resin shows a strong optical absorption in the UV range, which is due to π - π bond of benzil PI, as well as the absorption by the PS. Oppositely, no absorption can be observed in the NIR region; *i.e.* $\sim 100\%$ of transmittance [12]. Therefore, to efficiently induce the TPP reaction, we used a Fs laser with an irradiation wavelength of 780 nm . Hence, the rate of TPA is proportionally related to SLI distribution; *i.e.* I^2 , where I symbolizes the light intensity of irradiation, and 2 denotes the number of photons that are simultaneously absorbed in the duration of the TPP process [45].

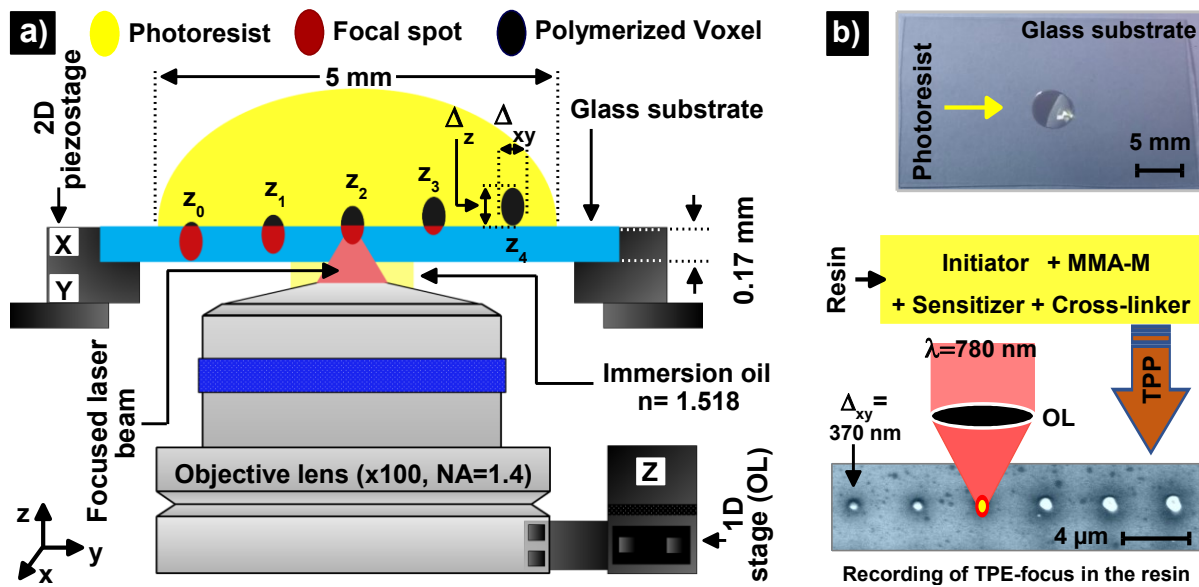


Figure IV.2. 3D laser nanoprinting of voxels. (a) Schematic presentation of the variation of z -position of the LFS; *i.e.* z -scan process; z_0, z_1, z_2, z_3, z_4 show the different z -positions of the LFS inside the resin; *e.g.* $z_0 \sim 20\text{ nm}$, $z_1 \sim 250\text{ nm}$, $z_2 \sim 500\text{ nm}$, $z_3 \sim 750\text{ nm}$ and $z_4 \sim 1000\text{ nm}$. (b) Recording of the LFS in the resin by TPP (*i.e.* polymerized voxels) under different exposure times of 1, 250, 500, 750, 100, and 1250 ms, at $I_{irr} = 0.71 \times 10^9\text{ mW}\cdot\text{cm}^{-2}$.

In order to characterize, manipulate, and optimize the spatial arrangement of printed voxels by TPP, we developed a custom-made optical system. A mode-locked Ti: sapphire laser system operating at 780 nm and 80 MHz repetition rate generates a NIR light pulse; *i.e.* 140-fs as pulse width, was used as a light source. To 3D print voxels, Fs laser pulses were tightly focused by a high-NA OL ($100\times$, $NA = 1.4$) onto the sample. The precision of the z -position of LFS was accurately controlled by the motorized OL which is coupled with a home-made software (Fig.IV.1(a)). TPP of the resin; *e.g.* voxels shown in Fig.IV.2(b), results in a change of the refractive index; *i.e.* $\Delta n \sim 0.08$, compared to liquid resin; where $n_{MMA} = 1.41$, and $n_{Poly(MMA)} = 1.49$. This allows

monitoring *in-situ* fabrication by a CCD camera [20]. The effect of z-positions of the LFS on the voxels shape and size will be discussed with detail in the next sections.

IV.3. Laser Nanofabrication of Voxels Using TPP

IV.3.1. Scaling Laws of Voxels in 3D Nanoprinting

In 3D laser nanoprinting, the voxel; *i.e.* the 3D equivalent of 2D pixel, is considered as a 3D image of the LFS in the resin. Understanding the performance of voxels obtained by one exposure-shot is critical to establish TPP lithography as a nanoprocessing tool to fabricate 3D architectures with nanoscale features; *e.g.* $\sim 100\text{ nm}$ (Fig.IV.3(e)) [151]. In this section, we report that at near-threshold exposure of TPP; *i.e.* laser's intensity threshold (I_{th}), the shape and size of the printed voxels scaling follow different laws in the courses of varying different focusing parameters, as shown in Fig.IV.3(d) [12]. We experimentally observed that Δ_{xy} of the printed voxel increase when the LFS gradually penetrates inside the resin (Fig.IV.3(a)). This figure shows a SEM image of voxels obtained in different LFS level (z-position), at a fixed exposure time of 1 ms, and at a laser power of 1.536 mW. A Δ_{xy} of $\sim 94\text{ nm}$ is achieved when the LFS is shifted just in the area which connects the resin and cover glass. Also, we demonstrate that when the LFS gradually penetrates inside the resin along the z-direction (Fig.IV.3(c)), Δ_z of voxels linearly increases (not shown) and reaches a saturation status that corresponds to full and stable voxels (Δ_{xy}, Δ_z) (Fig.IV.3(b)) [28].

Accurate optimization of focusing parameters; *e.g.* I_{th} , is needed to achieve stable 3D structures; thus, a deep understanding of single voxels; *i.e.* the primitive building block of 3D structures, is needed, as proved by printing the 3D micro- pyramid shown in Fig.IV.3(e). Recently, many studies [38-40] have been done along this line. As examples, some of the current authors [11] and DeVoeet et al. [19] proposed a z-scan and a suspending bridge method; respectively, in order to analyze and optimize the spatial resolution of 3D nanoprinting. In our study [20], we report the use of the z-scan strategy to introduce several nanoscale features of voxels that have not been fully noticed before. According to the analysis of the achieved results, it is shown that the accuracy of voxel dimensions; *e.g.* Δ_{xy} and Δ_z , play a significant role in the commercialization of 3D micro-nanofabrication technology. Low aspect ratio of the printed voxels; *i.e.* Δ_z/Δ_{xy} , are preferable for TPP nanoprinting; since they allow for maximum resolution in all three dimensions (TPP fabrication in 3D).

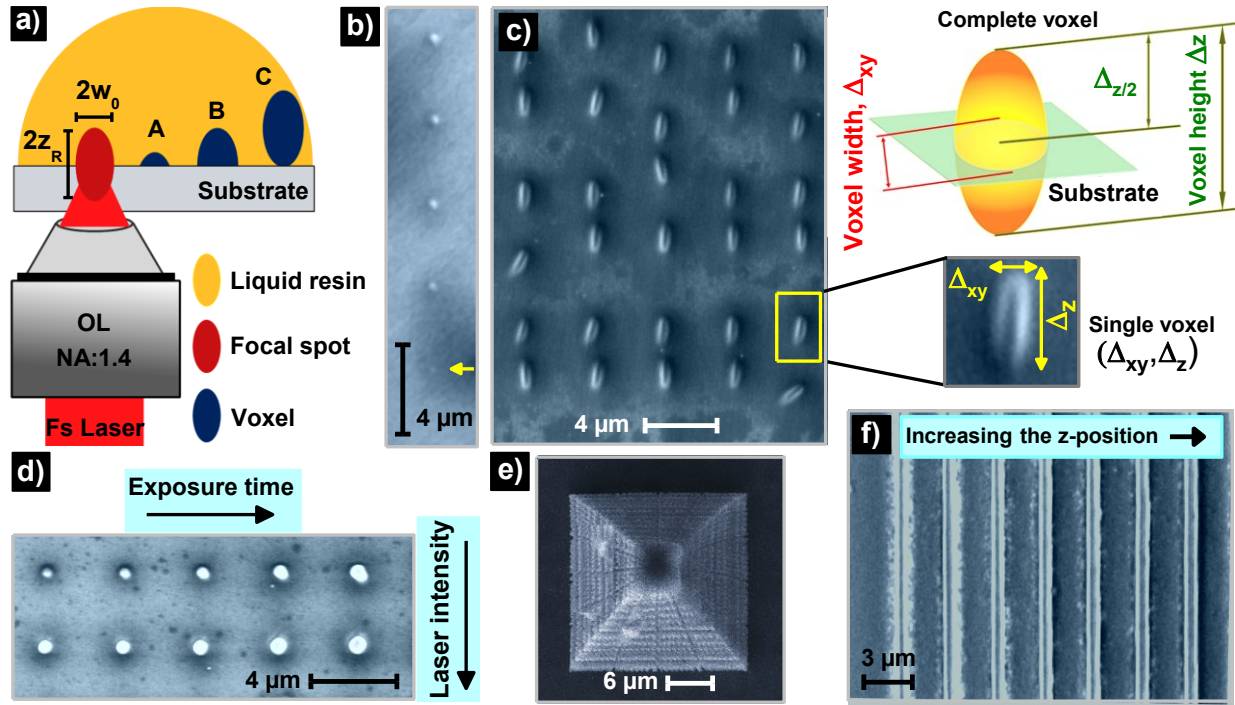


Figure IV.3. Scaling law of voxels in TPP nanoprinting. **(a)** Schematic presentation of the z-scan method (z -step = 45 nm). **(b)** Achievement of SDL resolution; e.g. ~ 94 nm. **(c)** SEM image of complete voxels obtained via z-scan process; experimental investigation of voxel dimensions in 3D. **(d)** Achievement of SDL voxels under different intensities as a function of exposure time. **(e)** SEM image of a 3D pyramid with nanoscale features; e.g. ~ 100 nm resolution. **(f)** SEM image of microlines that are polymerized by varying the z -position of the LFS; i.e. ~ 80 nm as z -step.

Shown in Fig.IV.3(a) is the presentation of the z -process used to characterize the spatial arrangement of voxels in 3D. Thus, we show that the dimensions of the voxels scale with different z -position of the LFS (Fig.IV.3(b-c)). It is clearly observed in the SEM image shown in Fig.IV.3(b) that a resolution of $\Delta_{xy} \sim 94$ nm is achieved by optimizing the LFS z -position (i.e. ~ 95 nm) in the interface glass/resin. Also, we found that the complete voxels can be polymerized when the LFS is fully located inside the resin, as shown in Fig.IV.3(c). From Fig.IV.3(c), it is well proved that the dimensions of the printed 3D voxels follow the elliptical geometry character of the LFS which is related to the SLI distribution at the focal region [28].

Following the scaling laws of voxels, we achieve SDL resolution by printing voxels at I_{th} under different exposure times (Fig.IV.3(d)). Thus, the smallest Δ_{xy} of a voxel is ~ 370 nm; i.e. $< \lambda/2$. Due to the NLO effect and thresholding effect of TPA, TPP resolution is controlled by the size of the LFS without any actual limitation [20]. Here, $\Delta_{xy} \sim 370$ nm resolution is attained by adjusting the focusing intensity to I_{th} ; i.e. $I_{th} \sim 0.71 * 10^9$ mWcm $^{-2}$. The top of the SEM image shown in

Fig.IV.3(d) shows the printed voxels by using I_{th} but under different times of exposition; *e.g.* $t = 1, 250, 500, 750 \text{ ms}$ and 1 sec . Δ_{xy} monotonically increases with the increment of the time of irradiation. After the formation of the first voxel; *i.e.* at I_{th} and $t = 1 \text{ ms}$, continuous irradiation causes the polymerized volume to expand in all directions.

We conclude from Fig.IV.3(f) that the nano- linewidth increases when the LFS was gradually penetrated inside the resin; *i.e.* by $\sim 80 \text{ nm}$ step in the z -direction. Here, we show that the microline size follows the increment of Δ_{xy} . TPP resolution was conventionally characterized by the interaction between the resin and the LFS; meaning where TPE was proceeded (Fig.IV.3(a)). By using SEM measurement, Δ_{xy} and Δ_z of the interaction between the LFS and the resin were considered as the lateral and longitudinal resolution of TPP nanoprinting (Fig.IV.3(c)). By using the z -scan, it's possible to print minimum patterns in a nonmetric range; *e.g.* $\sim 94 \text{ nm}$ of Δ_{xy} , which would be needed to produce 3D suspended structures [20,151]. An important issue for achieving stable and accurate 3D nanoprinting is the truncation amount effect, which caused a lot of observation errors as we will discuss in the following sections [99].

IV.3.2. Achievement of SDL Resolution

Shown in Fig.IV.4(a) is the achievement of SDL resolution of 3D nanoprinting obtained by adjusting the laser dose at near TPA threshold; *i.e.* $\text{laser dose} = I_{th} * (t = 1 \text{ ms})$. Here, this limit of resolution is achieved when almost $\sim 1/2$ of the LFS reaches the resin along the z -direction; *e.g.* beam waist ($2w_0$). The SEM image of the corresponding voxels that were polymerized by varying the intensity (at $t = 1 \text{ ms}$) is shown as an inset of Fig.IV.4(a) [40]. As a result, a $\Delta_{xy} \sim 228 \text{ nm}$; *i.e.* $\sim 1/4$ laser wavelength, is achieved; which is not considered as the limit of the accuracy/resolution of TPP printing that can be achieved using our costume made optical setup; *i.e.* TPP system. We show that when the intensity increases, a growth of voxel size is clearly observed, this is due to LFS duplication (Fig.IV.4(b)) [12]. Laser intensity of $\sim 560 \text{ kW/cm}^2$ and $\sim 1180 \text{ kW/cm}^2$ lead to a voxel width of $\Delta_{xy} \sim 228 \text{ nm}$ and $\Delta_{xy} \sim 747 \text{ nm}$; respectively, and the size of the voxel grows within these intensities range as shown by the SEM image in Fig.IV.4(a). Based on the inspired results, a Δ_{xy} three-time smaller than the diffraction limit is achieved (thanks to the NLO effect) [3,30,45,137].

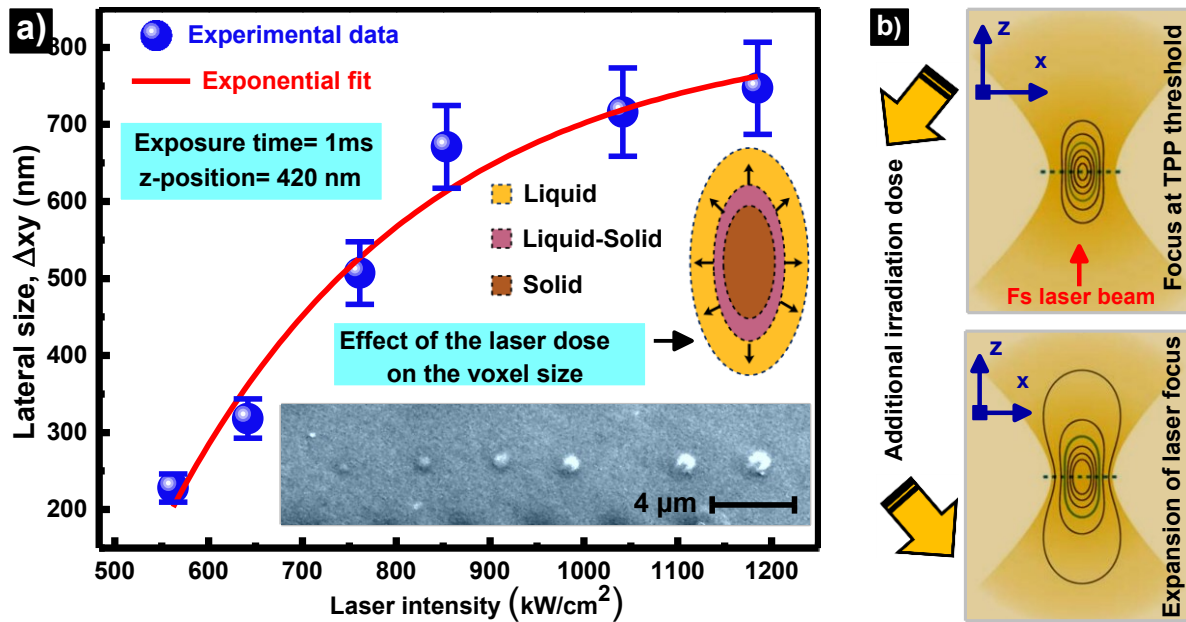


Figure IV.4. Experimental evidence of SDL spatial resolution. **(a)** Laser intensity dependent Δ_{xy} ; a SEM image of the corresponding voxels is shown as an inset; scale bar is 4 μm . **(b)** Effect of the increase of the laser intensity (or laser dose) on the LFS expansion; the expansion of the printed voxel follows the SLI distribution at the 3D volume of the LFS; e.g. volume pixel [20].

The inset of Fig. IV.4(b) schematically displays the near-focus isophotes (illustrated by the contour of lines) that represent the SLI distribution. We experimentally found that the printed voxels take the elliptical shape of the LFS relative to the threshold level of the SLI (not shown). Here, the threshold level is schematically defined by the smallest contour of the LFS. We call this process; LFS duplication model, for more detail, see refs. [11,12,18]. As explication of this expected phenomenon, the voxel expansion with the increase of intensity follows the growth of the LFS in 3D. The LFS duplication indicates that a low irradiation intensity in combination with low exposure time; *i.e.* 1 ms per voxel, is advantageous to achieve high resolution of 3D nanoprinting.

The results of this study are compared with the usual optical-resolution achieved by the use of a 780 nm excitation wavelength and 1.4 NA focusing optic; with $d_{xy} = 1.22\lambda/NA \sim 679.71 \text{ nm}$, showing that the TPP resolution is much smaller than the usual diffraction limit [30]. According to the dependency of TPP resolution on the laser intensity and exposure time, we proposed two explications; meaning LFS duplication; *i.e.* P-dependency, and radical diffusion (R_e); *i.e.* T-dependency. These two proposed explications are needed for tuning voxel size according to the requirements of 3D nanoprinting. Consequently, at the beginning of every 3D nanoprinting process, it is essential to make sure what is the size and shape of the printed voxels [110].

IV.4. Analysis of Voxel Dimensions

IV.4.1. Experimental Results: Evolution of Δ_{xy} and Δ_z

Here, in this section, we examine the manufacturing factors that influence the formation of voxels in order to optimize the accuracy and resolution of TPP-based 3D nanoprinting. While the TPP process, the dimensions of the printed voxels depend on the laser intensity, exposure time, z-position of the LFS, and lens NA [12,40]. In our case, and with more precision, the polymerized width; *i.e.* Δ_{xy} (Fig.IV.5(b)), and length; *i.e.* Δ_z (Fig.IV.5(c)), of voxels are influenced by the laser intensity, exposure time, and z-position, while the laser's threshold dose, lens NA, resin refractive index, and refractive index of the immersion oil are well known.

Thanks to the thresholding effect, TPP occurs only in a small volume that corresponds to the LFS; *e.g.* focal voxel, where the focusing density of light is considered high enough to induce TPE, as shown in Fig.IV.5(a). However, the shape of the point-spread function of the LFS leads to an axial size of voxels; *i.e.* Δ_z , larger than Δ_{xy} (inset of Fig.IV.5(a)). Thus, voxels typically have the shape of an ellipsoid with an elongation factor; *i.e.* $\sim \Delta_z/\Delta_{xy}$, in the range of 3 to 5 (Fig.IV.5(c)) [20,99].

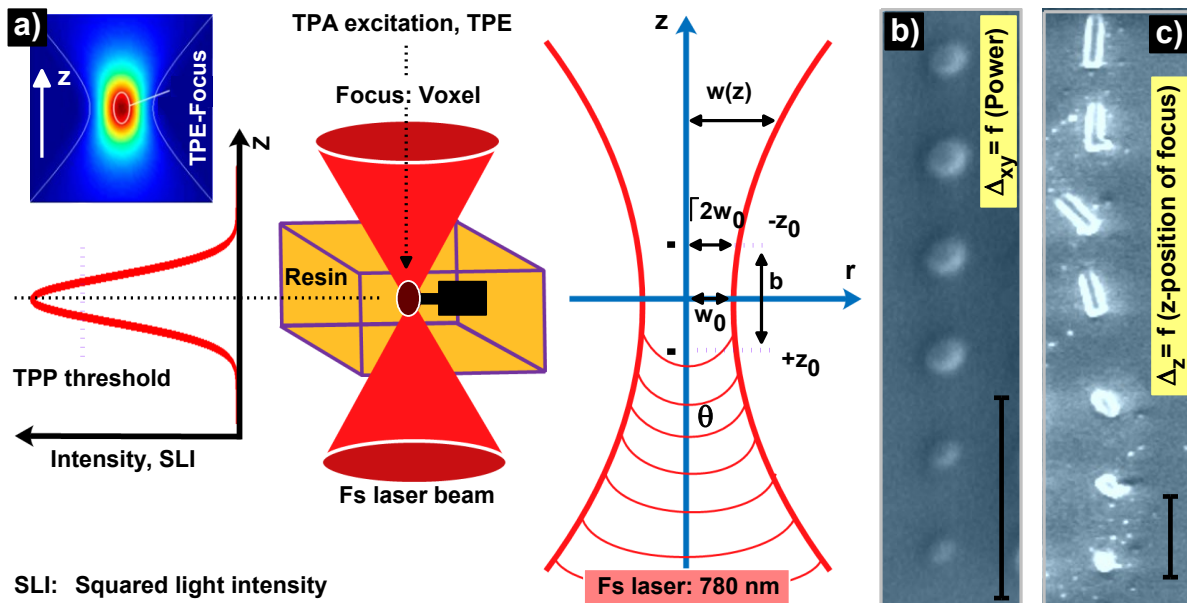


Figure IV.5. Analysis of voxel dimensions in TPP printing. (a) Schematic presentation of the Gaussian SLI distribution profile for TPA; (inset) the laser intensity at the focus is assumed by a Gaussian profile. (b) SEM image of voxels obtained under different laser intensities; $T = 1 \text{ ms}$. (c) SEM micrograph of voxels that were printed by varying the z-position of the LFS ($\sim 100 \text{ nm}$ step) at a fixed laser dose; $\sim I = 950 \text{ kW/cm}^2$ and $T = 1 \text{ ms}$. Scale bar in (b) and (c) denotes $4 \mu\text{m}$ [30].

Therefore, the TPA rate and the profile of the laser intensity in the micromachining focal volume (Fig.IV.5(a)) need to be systematically discussed. However, the equations which describe the

dimensions of a printed voxel; *i.e.* Δ_{xy} and Δ_z , as a function of the laser intensity and exposure time are originally introduced by J. Serbin et al. [22]. At the focal region, where the TPP reaction proceeded, we approximate the intensity distribution of the incident IR light; *i.e.* Fs laser, by a Gaussian profile, as shown in FigIV.5(a). In our TPP set-up, exposure to cause TPA induced polymerization; *i.e.* TPP, was carried out using a 780 nm Ti-sapphire Fs laser operating at 75-140 fs pulse width, 80 MHz repetition rate. As focusing optic, we use an OL (NA~1.4) to focus light (to induce the TPA process) [4].

IV.4.2. Gaussian Profile of the SLI Distribution

The spatial distribution of the focused laser intensity; *i.e.* needed to trigger TPP at the focal voxel, is assumed by a Gaussian profile; thus, the geometric optical properties of the LFS are needed to study the effect of different focusing parameters on the dimensions of the printed voxels. At a certain z-position along the laser beam; *i.e.* measured from $z = 0$, the lateral size of focus $\omega(z)$ is given by Eq.IV.1. $\omega(z)$ denotes the distance from the beam axis; *i.e.* $z = 0$, where the intensity drops to $1/e^2$ (~13.5%) of their maximum value. The relation which relating the evolution of $\omega(z)$ versus ω_0 is depressed as the following Eqs.; where w_0 symbolizes the beam waist [19,30].

$$\omega(z - \text{position}) = \omega_0 (z = 0) [1 + (z/z_R)^2]^{1/2} \quad (IV. 1)$$

$\omega(z)$ varies along the propagation direction according to Eq.IV.1, as demonstrated in Fig.IV.6. The full width at half maximum (FWHM) of the intensity profile is ≈ 1.18 times the Gaussian beam radius $w(z)$. Here, z_R symbolizes the Rayleigh length; meaning the length over which the beam can propagate without diverging significantly, which is defined in the following Eq. [152]:

$$z_R = \frac{\pi\omega_0^2}{\lambda} \quad (IV. 2)$$

The Rayleigh range is the distance from the beam waist (in the z-direction) where ω_0 is increased by a factor of $\sqrt{2}$. $\omega(z)$ is hyperbole, we could write the relation in Eq.IV.3 and Eq.IV.4.

$$\frac{r_0^2}{w_0^2} - \frac{z^2}{(b/2)^2} = 1 \quad (IV. 3)$$

$$\omega_0 = \lambda f / \pi d \quad \text{and} \quad b = (2\pi\omega_0^2 / \lambda) \quad (IV. 4)$$

Where f , ω_0 , d , b , and λ are the focal length, focal width, beam radius, Rayleigh range, and laser wavelength; *e.g.* 780 nm as we used for 3D printing set-up, respectively. For a Gaussian beam, the Rayleigh length is determined by ω_0 and λ [11,30,152]. Shown in Fig.IV.6(a) is the variation of the lateral size of the LFS versus the z -position.

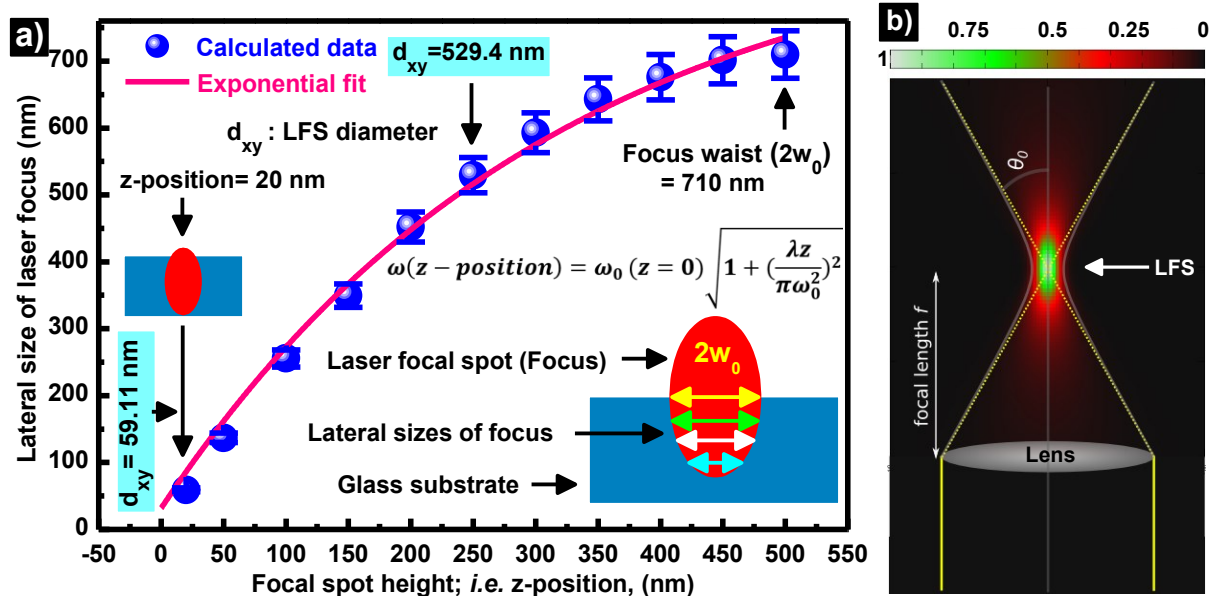


Figure IV.6. Theoretical analysis. (a) Lateral size of focus as a function of z -position. $w(z\text{-position})$ is the beam radius in the plane with the distance of z . (b) Schematic presentation shows the intensity distribution (arb. unit) of a Gaussian beam behind a lens; the yellow lines show the rays of geometric optics.

As we can see in Fig.IV.6(b), the coming laser intensity has a maximum with a certain width in the focused laser spot (green color). Laterally the beam shows a 2D Gaussian profile. The intensity distribution in the whole beam can be described as a Gaussian function with position-dependent width $w(z)$. The hyperbolic green short-dot in the schematic which illustrates the Gaussian beam (Fig.IV.6(b)) represents the evolution of the Gaussian width when the beam propagates through the beam waist position.

IV.4.3. Theoretical Analysis

IV.4.3.1. Voxel Dimensions Dependency on Laser Dose

Because of the threshold behavior of TPP, a resolution beyond the diffraction limit can be achieved; *e.g.* 100 nm . To predict the size of the printed voxels one needs to define the TPP threshold; *i.e.* thresholding effect [153]. We assume that the pre-polymer resin is two-photon polymerized as soon as a particle density of radicals; *i.e.* $\rho = \rho(r, z, t)$, exceeds a certain minimum concentration; *i.e.* concentration's threshold of radical ρ_{th} . It is known from the literature [22,30] that the spatial

distribution of the laser's intensity at the focal region is rotationally symmetrical; *e.g.* diffraction pattern. Hence, ρ can be expressed as a function of z, r and t ; here z denotes the distance from the focal plane in cylindrical coordinates along the z -direction, r is the distance from the optical axis in the xy -directions, and t is the total processing irradiation time; *i.e.* exposure time [20].

Based on the analysis of the optical geometric character of the LFS that is used as a pen of light for 3D nanoprinting of structures, Δ_{xy} and Δ_z can be determined starting from the Eq.IV.5 [22]. In the course of the TPP process, the radical density $\rho(r, z, t)$ resulted from the TPE of the resin can be calculated by solving the rate equation (Eq.IV.5.), and the solution can be expressed as Eq.IV.6. Eq.IV.5 describes the formation of active radicals by the PI system; *e.g.* benzil in our resin mixture.

$$\partial\rho/\partial t = (\rho_0 - \rho)\sigma_2 I^2 \quad (IV.5);$$

$$\rho = \rho_0 (1 - e^{-\sigma_2 t I^2}), \quad (IV.6);$$

Where $\sigma_2 = \sigma_2^a \eta$.

Here, ρ is the density of radicals, ρ_0 is the primary initiator particle; *i.e.* PI molecules, density, σ_2 symbolizes the effective two-photon cross-section for the generation of polymerizable radicals, I is the photon flux intensity, η is the efficiency of the initiation process, and σ_2^a is the ordinary TPA cross-section.

The approximation of the distribution of photon flux intensity $I(r, z)$; *i.e.* at distances r along the cross-section and of z in the propagation direction from the center (z -position of the LFS), is done with the aid of the following Gaussian distribution formula denoted by Eq.IV.7 [5,31].

$$I(r, t) = I_0 (w_0^2/w(z)^2) \exp(-2r^2/w(z)^2) \quad (IV.7);$$

Here, I_0 denotes the photon flux of the laser intensity at the beam center; *i.e.* $r = 0$ and $z = 0$. From refs. [22,30], the average photon flux intensity at the focal plane; *i.e.* I_{focus} , is expressed as follows:

$$I_{\text{focus}} = P/\pi w_0^2 \tau f h \nu \quad (IV.8);$$

Where P, τ, f, h and ν symbolizes the laser power, pulse width, repetition frequency, Planck constant, and light frequency, respectively. The relationship between the focal intensity I_{focus} and I_0 (photon flux intensity) can be written as follows:

$$I_0 = \frac{2e^2}{e^2 - 1} I_{\text{focus}} \approx 2.3 I_{\text{focus}} \quad (\text{IV.9});$$

Then, the viscous resin solidifies; *i.e.* TPP reaction, when the density of radical $\rho(r, z)$ is higher than ρ_{th} ; *i.e.* $\rho(r, z) \geq \rho_{\text{th}}$. The photon flux intensity at $z = 0$; *i.e.* at the LFS center, reaches their maximum, where $I(r, z = 0) = I_0 \exp(-2r^2/w_0^2)$. Neglecting the losses of the polymerizable radicals between the applied laser pulses for 3D nanoprinting, Δ_{xy} of printed voxels can be estimated as follow:

$$\Delta_{xy}(P, t) = w_0 \left[\frac{\sigma_2 I_0^2 n \tau}{C} \right]^{1/2} \quad (\text{IV.10});$$

Where $n = f * t$ symbolizes the number of pulses, t is the irradiation (exposure) time that is used to print one voxel, and C is a constant; *i.e.* $C = \ln[\rho_0 / (\rho_0 - \rho_{\text{th}})]$ [30].

Therefore, the voxel length $\Delta_z(P, t)$ at $r = 0$ is obtained by the use of the similar way as Δ_{xy} (voxel diameter). The photon flux intensity along the z -direction; *i.e.* in the axial direction, can be expressed as the following equation:

$$I(z) = \left[\frac{I_0 w_0^2}{w(z)^2} \right] \quad (\text{IV.11});$$

As a result, the calculated Δ_z of a printed voxel is defined in Eq.IV.9.

$$\Delta_z(P, t) = 2z_R \left[\left\{ \frac{\sigma_2 I_0^2 n \tau}{C} \right\}^{1/2} - 1 \right]^{1/2} \quad (\text{IV.12});$$

We conclude from the Eq.IV.12 that the longitudinal size of the printed voxels strongly depends on the laser intensity (or laser dose). We found experimentally when the intensity increases (above I_{th}), the printed voxels gradually grow at their active dangling ends as a result of their interaction with new monomers; *i.e.* MMA-M, wherein a chain reaction proceeds [3,12].

IV.4.3.1. Voxel Dimensions Dependency on z-Position

❖ Lateral Size of Voxels (Δ_{xy})

From X. Zhou et al. [30], the calculated lateral size of the printed voxels is expressed by Eq.IV.10. From this Eq. and refs. [22,30], Δ_{xy} was calculated by the use of the beam waist (w_0); which means that in this case the half of the LFS (in the z -direction) was penetrated inside the resin (along the z -

direction). Therefore, in order to calculate Δ_{xy} as a function of z-position, we use $w(z)$ for each z-position (Fig.IV.6(a)). Hence, the variation of voxel diameter against the z-position of the LFS is depressed as the following Eq.:

$$\Delta_{xy}(P, t) = \omega_0 \left[1 + \left(\frac{z}{z_R} \right)^2 \right]^{1/2} \left[\frac{\sigma_2 I_0^2 n \tau}{C} \right]^{1/2} \quad (IV. 13);$$

The voxel diameter is defined as the region where $\rho(r, z) \geq \rho_{th}$ is fulfilled; where $\omega(z)$ is the beam radius in the plane with a distance of z , and z means the distance from $z = 0$ (along the longitudinal direction).

❖ Longitudinal Size of Voxel (Δ_z)

To determine Δ_z as a function of z-position of the LFS, we starting from Eq.IV.12; thus, the variation of Δ_z versus the z-position is defined as the following equation;

$$\Delta_z(P, t) = z_{\text{position}} \left[\left\{ \frac{\sigma_2 I_0^2 n \tau}{C} \right\}^{1/2} - 1 \right]^{1/2} \quad (IV. 14);$$

Where z_{position} symbolizes the position of the LFS in the interface between the glass substrate and resin along the z-direction.

In the special case, the overall longitudinal size of the printed voxels (full polymerized voxel) is determined by the Rayleigh length of the LFS. Here, $\Delta_z(P, t)$ is expressed as follow;

$$\Delta_z(P, t) = 2z_R \left[\left\{ \frac{\sigma_2 I_0^2 n \tau}{C} \right\}^{1/2} - 1 \right]^{1/2} \quad (IV. 15);$$

Where $\sim 2z_R$ represents the longitudinal size of the focused laser-spot [30].

According to the Eqs.IV.1-15 discussed above and following the z-scan strategy used to study the voxels size in 3D laser nanoprinting; both Δ_{xy} and Δ_z are strongly dependent on the focusing laser dose and z-position of the LFS. Due to the nature of diffraction (at the focus), the shape of voxel coincides with the grain of rice [11]. So, to achieve an optimal resolution of 3D nanoprinting, Δ_{xy} and Δ_z need to be accurately and systematically controlled. From ref. [18,110], we conclude that Δ_{xy} strongly depend on the laser dose. On the other hand, by optimizing the z-position, we

demonstrate that the tail of voxels ranges from a polymerized dot to a spinning ellipsoid (complete voxel).

IV.5. Truncation Issue in TPP NanoPrinting

An issue that must always be considered during the 3D nanoprinting by TPP is the truncation issue [99]. Generally, in 3D nanoprinting, after developing step by the use of a solvent; *e.g.* ethanol or acetone, which is used to remove the nonirradiated; *i.e.* unscanned liquid resin (Fig.IV.7(a)), the nanoprinted patterns remain and physically attached on the cover glass (Fig.IV.7(b-d)); where the resin was initially dropped. After that, a SEM imaging was used to observe and characterize the dimensions and shapes of the nanoprinted structures, as demonstrated by 3D printing an ‘UM5R’ pattern (Fig.IV.7(d) [20].

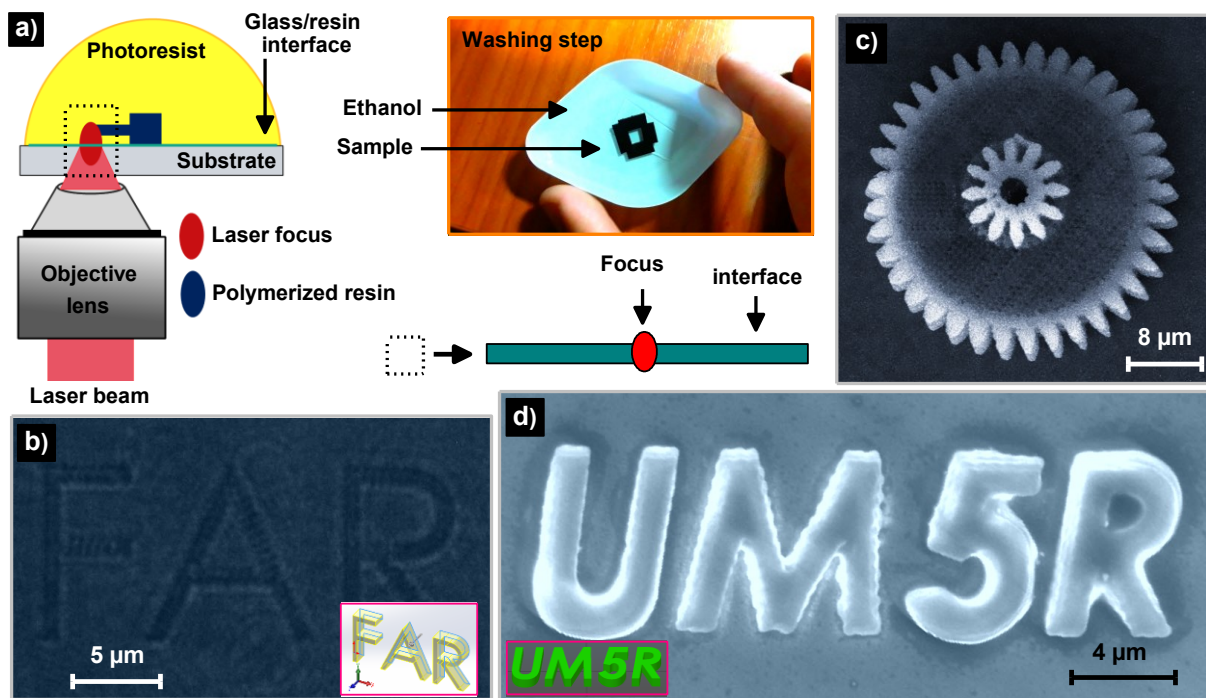


Figure IV.7. Truncation issue in TPP printing. (a) Schematic illustration shows the location of the LFS in the interface glass/resin; *i.e.* used to print stable micro-structures/patterns. (b) Bright-field image of ‘FAR’ pattern that was printed above the interface; FAR abbreviation symbolizes forces armée royal. (c) SEM image of a micro-gear fabricated in the interface. (d) SEM image of ‘UM5R’ microstructure; UM5R denotes université mohammed 5 à Rabat.

Experimentally, we found that the structures which are fully printed in the resin above the interface are washed away during the development (not shown); *e.g.* this kind of structures were completely disappear. This issue can be explained by the reason that the bottom-layer of the printed structures wasn’t attached to the glass substrate. This expected phenomenon is called the truncation amount

issue [11]. To investigate the truncation issue that can be appeared during the 3D nanoprinting, we fabricated different structures by using the TPP process, as shown in Fig.IV.7(b-c).

Shown in Fig.IV.7(b) is a bright-field image of 'FAR' pattern imaged through the CCD camera; *i.e.* used to monitor 3D printing in real-time. It well observed during our TPP experiments that the taken images of structures using the CCD camera can't give enough information if the polymeric structure is attached to the cover glass; or it is just positioned above it. Due to the effect of the rinsing step (Fig.IV.7(a)), we confirm this truncation outcome. Oppositely, the SEM image shown in Fig.IV.7(c-d) demonstrates that these microstructures are well connected to the substrate. Here, for this TPP process, we use a laser intensity fixed at $\sim 0.82 - 1 \text{ kW/cm}^2$ and an exposure time of 1 ms [20,108]. The corresponding CAD model is shown as an inset in Fig.IV.7(b and d).

For a nanoprinted structure or an individual voxel, to remain after rinsing, it must be polymerized in contact with the cover glass (Fig.IV.7(a)) [139,144]. We experimentally confirmed that the truncation issue becomes more complex when the printed patterns cannot be viewed by the CCD camera. Direct observation by the camera of the TPE induced fluorescence around the LFS volume tends to give distorted optical image; *i.e.* less accurate view; this is due to the saturation; *i.e.* white intense fluorescence, and sometimes to the camera insufficient resolving power [11,18].

The truncation issue is generally considered as the first factor that must always be examined during the TPP-based 3D printing to achieve high accuracy and stability; meaning where the LFS needs to be positioned for printing stable structures that can survive the developing step? [99]. Before starting 3D printing, such contact of the LFS with the substrate is needed, which means that the LFS needs to be partially submerged in the glass in order to ensure a physical adhesion between the printed structure and glass; thus, the structure will remain after washing [12]. The truncation issue is exacerbated by the fact that the smallest printed voxels cannot be viewed during processing, but rather must be imaged later by the SEM observation.

IV.6. Effect of z-Position on 3D Nanofabrication

In the present section, we will mainly focus on the stability of the fabricated structure as a function of the accuracy of the LFS; *i.e.* in the longitudinal direction. By using the z-scan method, we investigate the impact of the accuracy of z-position; *i.e.* relative to the interface between the cover glass and resin, on the stability of the nanoprinted structures; *e.g.* voxels and 3D architectures (Fig.IV.8) [20].

TPE induced by the NLO effect; *i.e.* TPA process, occurs only in a sub-micrometric volume of the LFS; *i.e.* focal voxel, in which the focused laser intensity is high enough to induce TPP, as shown in the inset of Fig.IV.8(a). Apparently, it is more appropriate to consider the LFS as a nanometric pencil of light [45]. The printed voxel is considered as a 3D image of the LFS in the pre-polymer resin, which is considered as a TPA recording media (Fig.IV.8(a)). The effect of the z-position on the formation of 3D microstructures that are polymerized by TPA is shown in Fig.IV.8(a-f) [20].

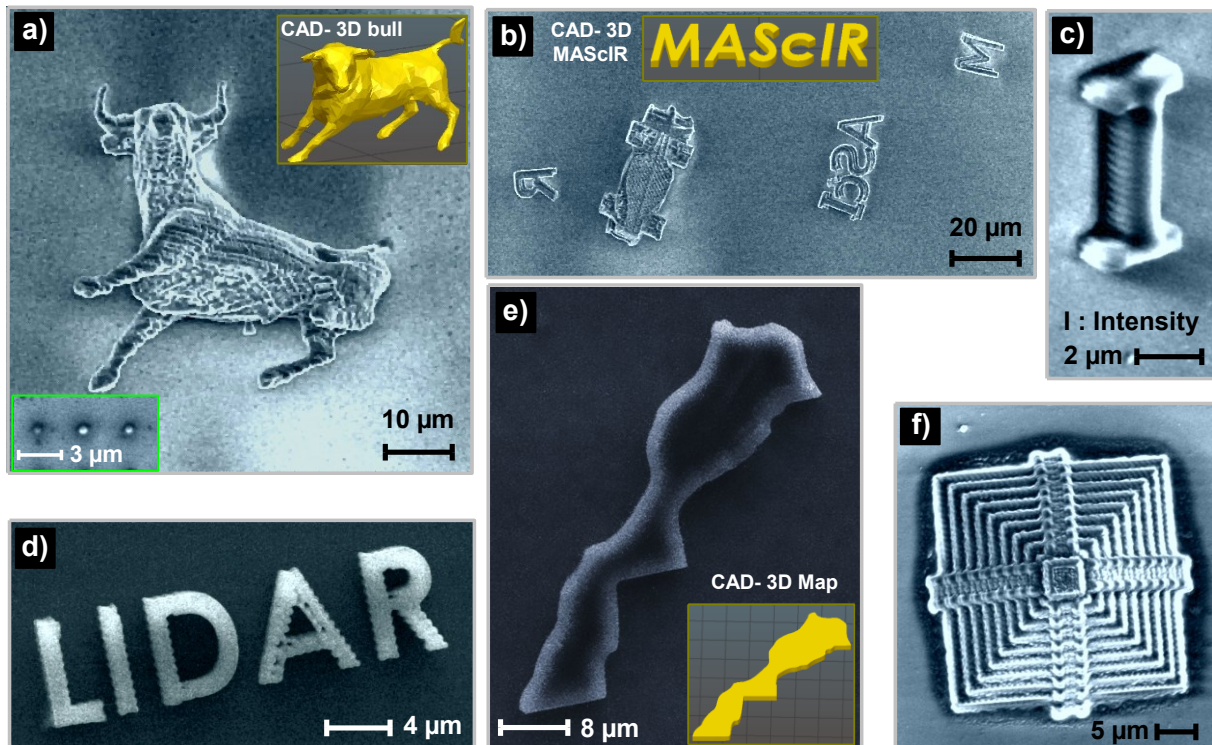


Figure IV.8. Study of the effect of the z-position on 3D nanoprinting. (a) SEM image of a 3D microscale bull sculpture fabricated above the glass/resin interface; the CAD design of this bull is shown as an inset. (b) SEM micrograph of a micro- car and logo of MAScIR printed above the interface. Top-view SEM image of (c) an abbreviation of intensity 'I', (d) a LIDAR pattern which is exactly polymerized in the interface; LIDAR symbolizes -light detection and ranging- project. (e) 3D design of the true moroccan map, and (f) 3D pyramid printed with SDL accuracy; *i.e.* ~ 100 nm. The typical intensity used is $\sim 0.82 \times 10^9$ mW/cm² and the exposure time is kept at 1 ms [12,20].

Fig.IV.8(a) presents a top-view SEM image of a 3D microbull with fine 3D features that was polymerized; *i.e.* by using TPP raster scanning mode [3,12], far above the contact with the cover glass. We observe that this printed bull was toppled over after the washing step by the reason that its printed bottom layer was not physically attached to the glass. This issue of truncation amount is explained as follows: TPP scanning by the LFS starts the polymerization scanning of the liquid

resin above the interface. The expected format (CAD design) of the printed bull; *i.e.* can be obtained after washing, is shown as an inset in Fig.IV.8(a).

The same problem (truncation) is experimentally demonstrated by fabricating a 3D microcar and a 3D micro logo of MAScIR above the interface between the glass and resin, as proved by the SEM image in Fig.IV.8(b). The 3D computer-aided design (CAD) model of the printed micro logo of MAScIR is shown as an inset in the same figure. Conversely and as demonstrated in Fig.IV.8(c-f), once the tip of the LFS starts the TPP scanning from the glass/resin interface, the nanoprinted structures were well linked and adhered to the glass and they remain at their location after developing step [11,99]. Shown in Fig.IV.8(f) is a stable 3D pyramid that was polymerized by accurately positioning the tip of the LFS in the interface where the dropped resin has contact with the glass. Here, for this 3D printing process, a resolution of about $\sim 100\text{ nm}$ is achieved.

Based on the inspired results, a solution to overcome the truncation issue (Fig.IV.8(a-b)) of the obtained structures made by the TPP process is urgently needed. To overcome the truncation issue, a z-scan strategy was developed by starting TPP scan from the interface prior to scanning. The obtained results may provide an efficient reference to optimize the manufacturing parameters in the duration of 3D nanoprinting in order to attain high accuracy of TPP and also to overcome the truncation issue. This finding is important to understand and further develop TPP lithography as a nanoprocessing tool for producing stable 3D-functional-microdevices [20].

IV.7. Spatial Arrangement of Voxel in 3D Nanofabrication

In order to characterize and manipulate the spatial arrangement of voxels, we proposed a systematic study of voxels nanofabrication by using a z-scan of the LFS. Thus, we investigate the effect of the accurate z-position of the focus; *i.e.* the height z-position of the LFS inside the glass/resin interface, on the spatial arrangement, dimensions, shape, and stability of the printed voxels via TPP lithography [22].

In this axis, we performed a first experiment (Fig.IV.9(a)) to study the shape of the voxel as a function of the z-position. Here, we fabricated individual voxels at different z-positions of LFS with a 1 ms laser exposure time and an average intensity of *e.g.* $I \sim 1110\text{ kW/cm}^2$. The step of the z-position was varied by $\sim 50\text{ nm}$. To experimentally performed this study, the LFS starts the

TPP scanning from the glass at ($z_{\text{position}} \sim (-)50 \text{ nm}$) from the reference position z_0 ; *e.g.* the LFS is fully positioned below the resin in the cover glass (Fig.IV.9(a)).

Fig.IV.9(b) shows a SEM image of the voxels fabricated for different z -positions of the LFS at 5 different in-plane locations of z_0 which are separated by $4 \mu\text{m}$. The formation of isolated voxels; *i.e.* complete voxels, is observed for large z -positions; *i.e.* larger than $1 \mu\text{m}$ where the LFS is nearly fully located inside the resin, as schematically shown in Fig.IV.9(c-d).

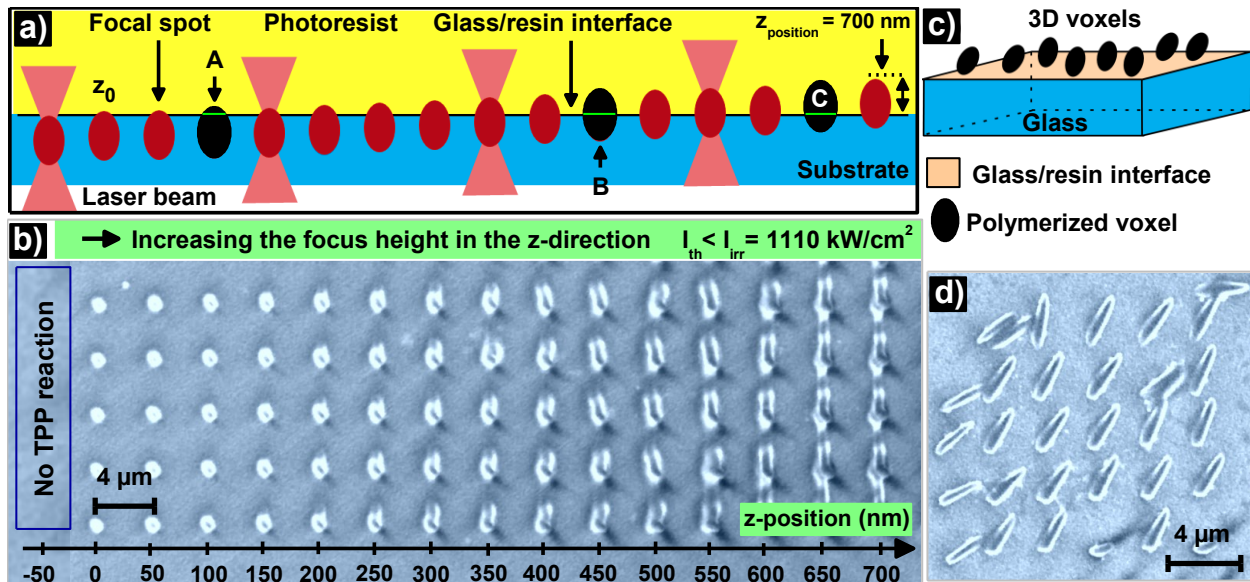


Figure IV.9. Analysis of voxel dimensions via the z -scan method. (a) Schematic illustration of the variation of the LFS position along the z -direction; *i.e.* by a step of $\sim 50 \text{ nm}$. (b) Top-view SEM image of printed voxels presented in (a). (c) Illustration of complete voxels that are two-photon polymerized on the top surface of the glass substrate. (d) SEM image of voxels illustrated in (c); the LFS z -position is positioned at $\sim 1.4 \mu\text{m}$ away from the glass. The typical intensity used in (b) and (d) is $\sim 1110 \text{ kW/cm}^2$ [20].

When the LFS is not too far away; *i.e.* z larger than $1.4 \mu\text{m}$, from the interface, the full voxels are physically attached to the cover glass, as schematically depicted on Fig.IV.9(c) and shown on Fig.IV.9(d), and they remain on the top of the glass substrate, with different spatial arrangements, after the development phase. Fig.IV.9(b) also shows that the longitudinal size of the printed voxel increases with the increasing z -position, and, in particular, truncated voxels are observed for small z -positions; *e.g.* $\sim 700 \text{ nm}$. No fabricated structures were observed when z is smaller than z_0 . The truncated voxels stick to and erect from the top of the glass, revealing their lateral size information; *i.e.* Δ_{xy} . By printing complete voxels (Fig.IV.9(d)), both Δ_{xy} and Δ_z sizes can be measured.

Also, we experimentally proved that the rightest voxels; *i.e.* polymerized up $z = 1.4 \mu\text{m}$, are flushed away (not shown) by the solvent employed for washing. This systematic z -scan study of

voxels described in Fig.IV.9(a-b) demonstrates their capability as an efficient nanoprocessing tool for characterizing and optimizing and controlling the dimensions of the printed voxels [12]. Through Fig.IV.9(a), the laser focus is positioned at different focusing z-levels in order to polymerize different voxel sizes and shapes; e.g. below half (voxel A), half (B), and over half (C).

Fig.IV.10(a) is a schematic presentation of the z-scan strategy [151]. Different feature sizes can be printed by placing the LFS at different z-positions (Fig.IV.10(b)). At certain z-position of the focus relative to glass/resin interface; e.g. up $z \sim 1.4 \mu\text{m}$, the printed voxels will be toppled down during washing, and they will barely adhere to the top surface of the cover glass; e.g. voxel B_2 in Fig.IV.10(a). Ensuing the nature of diffraction [11,18], the shape of the printed voxels follows the elliptical geometry character of the SLI distribution at the focal region. To prove this expected phenomenon, we fabricated 3D complete voxels (voxel B_1) by completely positioning the LFS inside the resin, with an end at the interface (to ensure adhesion). Note that these printed voxels weren't removed by the rinsing process (Fig.IV.10(b)).

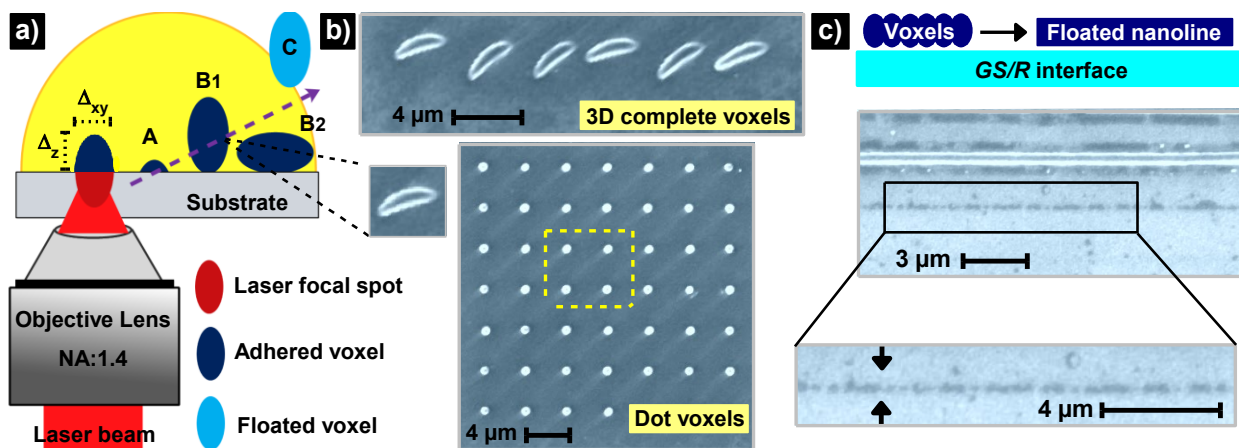


Figure IV.10. TPP z-scan scan process. (a) Schematic principle of the z-scan method which is for achieving the dot and complete voxels. (b) (top) SEM image of 3D complete voxels; i.e. voxel B_1 in (a). (Bottom) SEM image of voxels dot; i.e. voxel A in (a). (c) SEM image of microline polymerized by scanning the LFS from the inside to above of the interface; the magnified nanoline was flushed away during washing (flushed nanoline not shown). The intensity used is $\sim 1100 \text{ kW/cm}^2$ in (b) and $\sim 1040 \text{ kW/cm}^2$ in (c).

We experimentally proved that: to place nanoprinted structures on the cover glass, a part of the LFS is needed to be submerged in the interface, as shown by the voxel A and B_1 in Fig.IV.10(a). Therefore, only the submerged part of the LFS inside the photoresin is able to initiate TPP with an appropriate laser dose; i.e. $I_{th} * 1\text{ms}$. The other part of the focus located in the glass is able to ensure the adhesion of the printed structures on it. By gradually z-moving the LFS inside the resin,

we are succeeded to achieve complete voxels (Δ_{xy}, Δ_z). As shown in Fig.IV.10(b) (top), the complete voxels were printed by positioning the end-tip of the LFS near the glass, this allows that a finer feature of these voxels has adhered with the glass. By printing complete voxels, both Δ_{xy} and Δ_z can be obtained; thus, the lateral and longitudinal resolution of 3D printing can be measured [40]. The variation of the cross-section size of voxels; *i.e.* Δ_x , Δ_y and Δ_z , exists along with all directions and they affect the nanofeatures size of the structure; *e.g.* 3D microscale objects [20].

In a special case of voxel nanofabrication (Fig.IV.11(a)); *i.e.* corresponds to the complete voxels, a thinner portion of the printed voxels is needed to be positioned in the glass end (Fig.IV.11(b)). In this case, the voxels maybe tilt and attach to the glass; this phenomenon can be explained by the effect of the force applied by the washing solvent [99]. An intact voxel can be achieved by using this technical approach (Fig.IV.11(b)). Shown in Fig.IV.11(c) are some of the nanostructures that were produced by accurately positioning the LFS in the interface resin/glass; *i.e.* $z \sim 400 \text{ nm}$. It's well-observed from the SEM images (Fig.IV.11(c)) that the printed structures are were linked to the glass, which gives high stability of 3D printing. A SDL accuracy of about $\sim 100 \text{ nm}$; *i.e.* $\sim \lambda/7.8$ resolution, was reached by using our costume-made optical set-up [20,110].

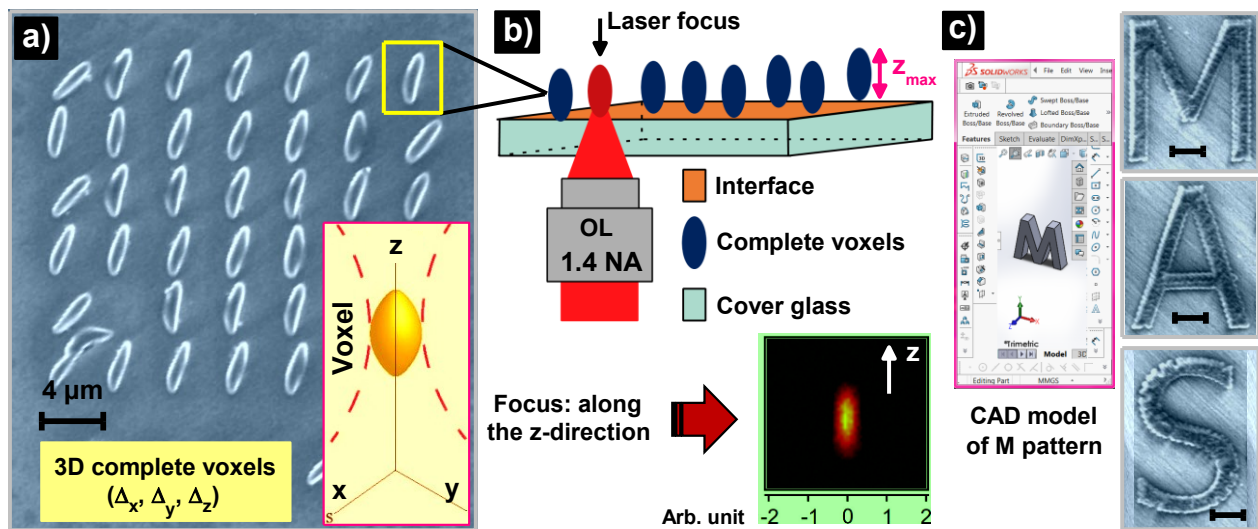


Figure. IV.11. Accuracy of z-scan process. (a) SEM image of single complete voxels. (b) Experimental set-up for achieving complete voxel at $z_{max} \sim 1.4 \mu\text{m}$; the SLI distribution of the LFS along the z-direction is shown as an inset. (c) SEM image of the patterns, M, A, and S, printed by accurately positioning the LFS in the interface; all scale bar in (c) denotes $1 \mu\text{m}$; the CAD model of M pattern is shown as an inset. The used laser intensity and exposure time used are $\sim 1100 \text{ kW/cm}^2$ and 1 ms , respectively.

By adjusting the LFS z-position, Δ_{xy} and Δ_z of the printed voxels was systematically controlled with SDL accuracy in order to fabricate stable 3D microstructures (Fig.IV.11(c)). We demonstrated

that the control of the z-position of the LFS is considered as an effective strategy for optimizing and positioning the first polymerized layer of structures that need to be printed. We conclude from the Fig.IV.11(c) that the nanoprinted pattern; *e.g.* M , A and S , were survived after the washing step, this is explained by the reason that the first printed layer of these patterns was well physically attached to the glass.

In TPP printing, the LFS is sometimes not truly reflected by the printed voxels (3D image of the LFS); meaning where the I^2 was distributed (inset of Fig.IV.11(b)). *E.g.*, when the laser dose (used for 3D printing) is so high as to induce breakdown ($\gg I_{th} * t$). In particular, in the case of micro-explosion phenomena [12], the voxel shape was significantly different from that of LFS, so, the printed pattern doesn't follow the scaling laws of voxel in TPP. Thus, it is necessary to establish the best-suited manufacturing parameters; *e.g.* I and t , that are met with this 3D nanofabrication, since those factors will influence the whole TPP process [45,128]. One of the most important factors which play a quite significant role in the stability of 3D printing is the LFS z-position.

IV.8. Voxel Dimensions Dependence on Z-position of LFS

To study the effect of the z-position of the LFS on the voxel dimensions; *i.e.* Δ_{xy} and Δ_z , we used a z-scan strategy whereby we first position the upper tip of the LFS near the glass/resin interface; *i.e.* reference position, then we move it gradually by steps of $\sim 50 \text{ nm}$ followed by $\sim 100 \text{ nm}$ into the resin with a precision of $\sim 20 \text{ nm}$. The LFS, after passing through the OL, is elliptically shaped with a diameter ($2w_0 \sim 1.22\lambda/NA \sim 680 \text{ nm}$), and a longitudinal dimension; *i.e.* the depth of focus, which is twice the Rayleigh length, $2z_R = 1013 \text{ nm}$; with ($z_R = \pi w_0^2/\lambda = 506.5 \text{ nm}$) imposed by the laser wavelength; *e.g.* 780 nm , and the OL used; *e.g.* $NA = 1.4$ [22,52].

IV.8.1. Lateral Size Dependency

One factor that has successfully and substantially influence the stability and resolution of TPP-based 3D printing is the accuracy of the z-position of the LFS [151]. In 3D nanoprinting, the control of z-position allows very precise control of the size and shape of voxels (Fig.IV.12(a)) and also of 3D structures (Fig.IV.12(b)). In this section, we will examine the effect of the z-position on the lateral size of voxels; *i.e.* Δ_{xy} . In this experiment, we studied the evolution of Δ_{xy} with the increment of the position of the LFS inside the resin; *i.e.* along the z-direction. For this experiment, we set the laser's average intensity to $I_{th} \sim 820 \text{ kW.cm}^{-2}$, and we used 1 ms exposure time for each point exposure event, and we varied z by steps of $\sim 50 \text{ nm}$, starting from z_0 up to $z \sim 700 \text{ nm}$

(Fig.IV.12(a)). We chose 1 ms, as the minimum time of irradiation, at I_{th} to keep the printed voxels to minimum sizes, for better precision. Exposure at near I_{th} ensures full TPA polymerization. In fact, large exposure times and intensities lead to larger TPP fabricated voxels; e.g. slim voxels, and may damage the printed structures [35,154].

Figure IV.12(a) shows the evolution of Δ_{xy} with the z-position of focus; and it follows an exponential law for z up to ~ 700 nm owing to the SLI distribution, within the Rayleigh range, required for TPA. The closer the center of the LFS to the resin, the stronger the TPP reaction. As shown in Fig.IV.12(a), a lateral size of $\Delta_{xy} \sim 220$ nm can be achieved at z_0 when only a small portion of the LFS reaches the resin (see also the SEM image in the inset). The achieved $\Delta_{xy} \sim 220$ nm feature size is better than predicted by Abbe's diffraction limit, or lateral resolution, $\lambda/2NA \sim 279$ nm, and it is due to the fact that only the tip of the LFS reaches the resin; i.e. smaller than $2w_0$, and to the optical nonlinearity nature of TPP; e.g. to the SLI law of TPA [18,20,30,35].

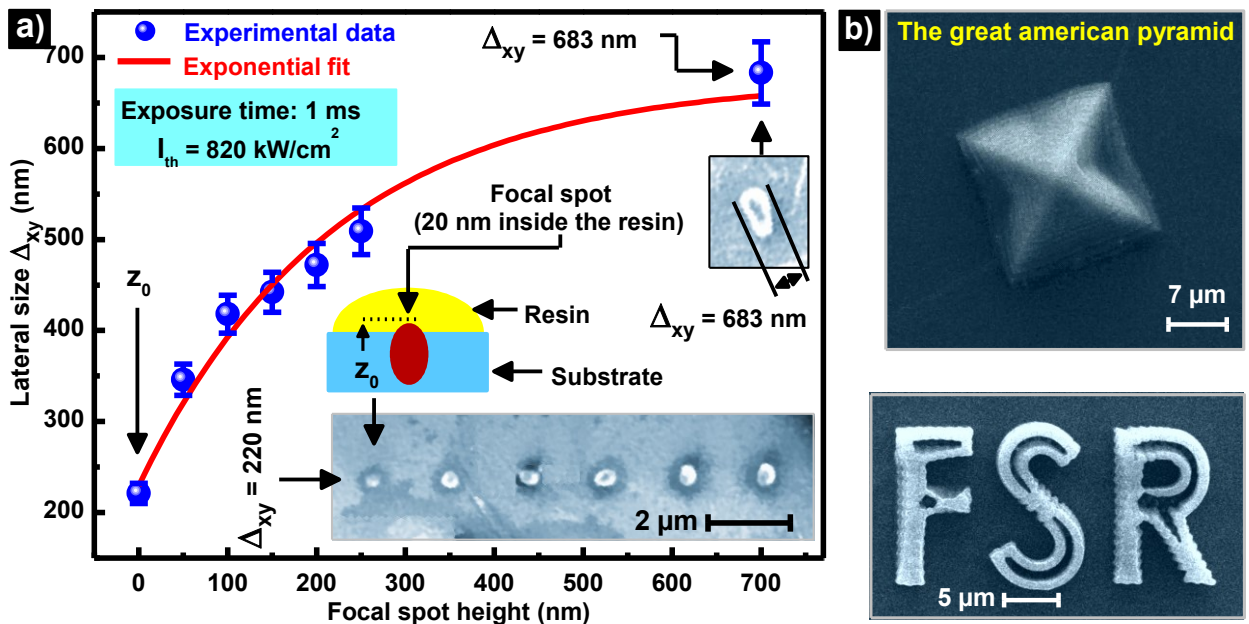


Figure. IV.12. Effect of z-position on 3D nanoprinting. (a) LFS z-position-dependent Δ_{xy} . Blue scatters are experimental data and the solid red line is an exponential theoretical fit; the SEM micrograph of SDL voxels that are produced under different z-position is shown as an inset. (b) Achievement of SDL resolution; e.g. ~ 200 nm, by using the z-scan process; a 3D laser nanofabrication capability of the z-scan strategy is shown.

Our study clearly shows that the minuteness of the feature size that can be fabricated by TPP depends on how small is the interaction volume of the LFS and the resin much like in STED lithography [20,155]. It is experimentally proved that Δ_{xy} saturates; i.e. $\Delta_{xy} = 683$ nm, at z-

position of 700 nm ; a lateral size which is close to the theoretical diameter of the LFS; *i.e.* $\sim 680\text{ nm}$ (vide infra). Indeed, at such a z-distance, more than $2/3^{\text{rd}}$, and consequently, the diameter of the LFS is fully located into the resin. Although we have no clear explanation as to why the experimentally observed lateral dimension of full voxels, obtained by near-threshold irradiation, are close to the theoretical size of LFS; it is very much plausible that it can be due to the nature of the photoresist used which favors efficient cross-linking at low irradiation doses close to the threshold, given that Δ_{xy} depend on the irradiation dose and the type of photoresist used. Indeed, we measured the evolution of Δ_{xy} with the energy dose by varying the laser intensity around I_{th} for a fixed exposure time (1 ms) and z-position ($\sim 420\text{ nm}$), and we found that Δ_{xy} increases exponentially with the laser dose in agreement with the literature [11,28,151].

To achieve finer feature of the printed voxel via z-scan process, we set the top-tip of focus in the resin; *e.g.* by 20 nm , this allows that only this part of the LFS that was submerged in the resin will be solidified; *i.e.* TPE induced polymerization, as shown by the schematic presentation in the inset of Fig.12(a) [20]. It is clearly observed from this Fig. that a voxel lateral size of $\Delta_{xy} \sim 220\text{ nm}$; *i.e.* corresponds to $\lambda/5.54$, can still be achieved. In this study of voxel nanofabrication, we also achieve a resolution of $\lambda/8.29$, *i.e.* 94 nm (not shown) [12,110]. The size of laser fabricated nanostructures (Fig.IV.12(b)) depends on the laser's intensity, and the above nanofabrication findings are observed with a threshold intensity ($I_{th} \sim 820\text{ kW.cm}^{-2}$).

In most cases involving 3D printing by TPP, a high NA (~ 1.4) is needed to achieve high resolution [3,6,156]. As it can be seen in Fig.IV.12(b), 3D printing using the z-scan is based on layer-by-layer accumulation. Therefore, we found that the z-scan method used in this study can be employed as a functional optical technique for measuring, controlling, and optimizing the accuracy of TPP.

IV.8.2. Longitudinal Size Dependency

Here, we investigate the effect of the LFS z-positions on Δ_z of voxels. To investigate this relationship, a systematic study of voxel nanofabrication (by TPP) was done. In this study, by varying the z-position of focus, *i.e.* in the longitudinal direction, but at the same fixed laser dose (for all voxels), different Δ_z of voxels can be obtained. The SEM image shown in the inset of Fig.IV.13(a) shows the voxels that were printed under different z-positions. By varying the position of focus along the z-direction; *i.e.* $z \sim 0.7, 0.8, 0.9, 1.0, 1.1, 1.2, 1.3, \text{ and } 1.4\ \mu\text{m}$ relative to the

reference position; *i.e.* $z \sim 20 \text{ nm}$ inside the resin; as a result, different Δ_z of voxel; *i.e.* $\sim 1.587, 1.733, 1.914, 2.152, 2.332, 2.561, 2.758,$ and $2.913 \mu\text{m}$ are achieved; respectively.

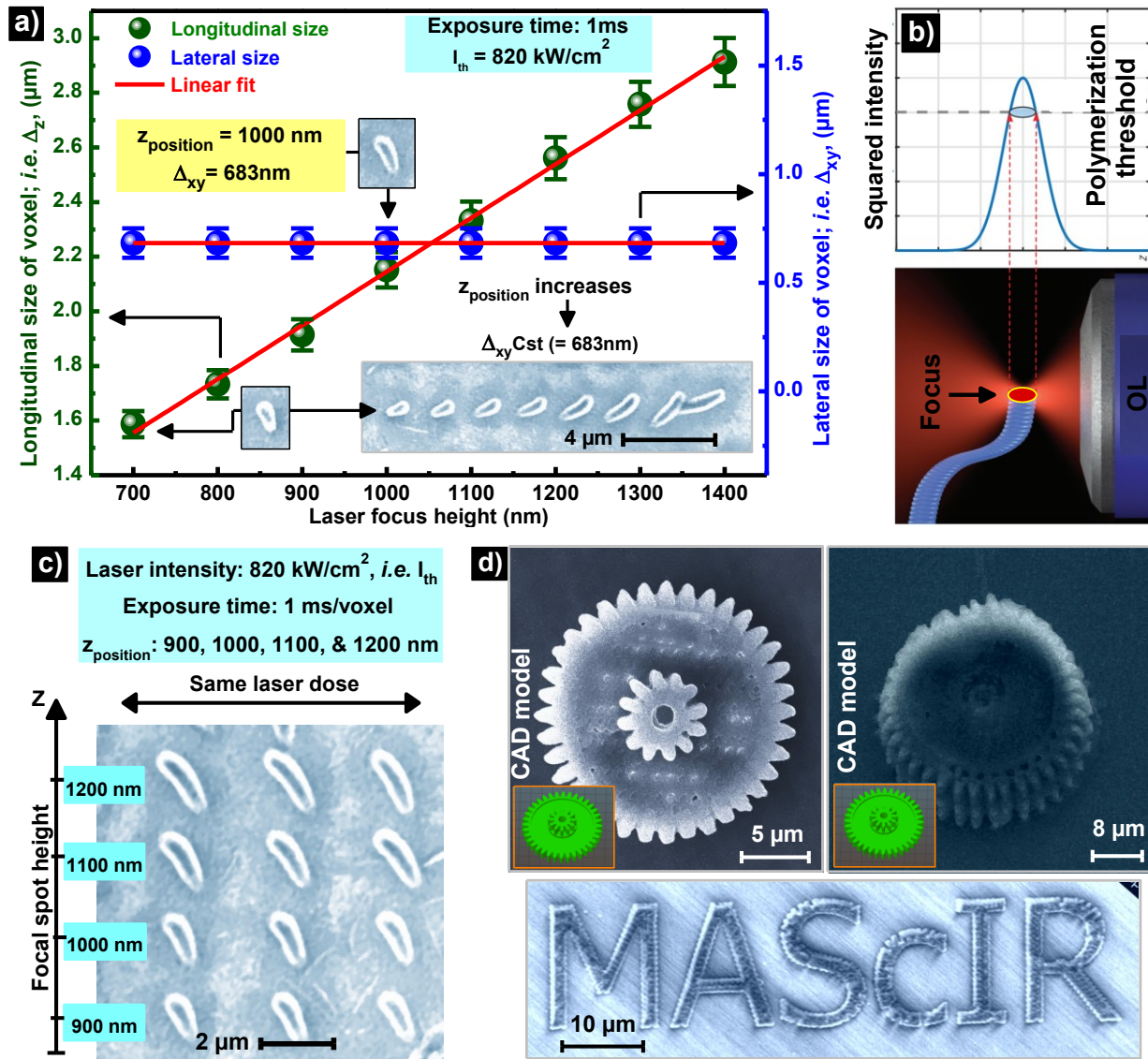


Figure IV.13. Δ_z of voxel versus the LFS z -position. (a) Longitudinal (green solid sphere) and lateral (blue solid sphere) size of voxels dependency on z -position; scatters are experimental data and solid red lines are linear theoretical fits. (b) Polymerization threshold vs. LFS. (c) SEM image of voxels polymerized in different z -positions of the LFS; every three horizontal voxels were polymerized at the same focusing conditions; *e.g.* the laser dose and z -position. (d) Effect of the accuracy of the LFS on 3D nanofabrication. The irradiation intensity used for this nanofabrication process is $\sim 0.82 \cdot 10^9 \text{ mW/cm}^2$.

For z -positions larger than 700 nm , Δ_{xy} remains unchanged, as intuitively expected for a given exposure dose, and Δ_z changes appreciably; *e.g.* linearly up to $1.4 \mu\text{m}$, as shown in Fig.IV.13(a). We explain the linear dependence of Δ_z versus the z -position by the reason that the shape of the elementary LFS; *i.e.* responsible for solidifying the resin, is considered as a revolution of an

ellipsoid ($\Delta_{xy} < \Delta_z$) [11]. The longitudinal size of the voxel at $z = 1.4 \mu\text{m}$, is $\Delta_z \sim 2.913 \mu\text{m}$, and for z much larger than $\sim 1.4 \mu\text{m}$, the voxels are washed away during the development phase (not shown). When the LFS is fully located inside the resin, the longitudinal size of the voxel exceeds $2z_R$; *e.g.* exceeds $\sim 1,013 \mu\text{m}$, indicating that the resin in the close proximity of the LFS is also polymerized in the longitudinal; *e.g.* the propagation direction of the laser beam; a feature which could be explained by a chain, or seed, photo-polymerization and/or self-guiding the laser light propagation caused by the solidified resin (Fig.IV.13(b)) [42].

To confirm the linear dependence of Δ_z versus the z -position, we systematically printed three voxels for four z -positions; *i.e.* $z = 0.9, 1.0, 1.1, \text{ and } 1.2 \mu\text{m}$. As a result, Δ_z of $\sim 1.914, 2.152, 2.332, \text{ and } 2.561 \mu\text{m}$ are achieved; respectively. Shown in Fig.IV.13(c) is the voxel obtained for the same z -position at different in-plane; *e.g.* lateral, positions. With the increase of the height of the LFS, a greater number of thick voxels in the z -direction are solidified due to the elliptical geometry character of the LFS. Thus, the dependency of Δ_z on the LFS z -position follows the growth of the SLI distribution of the 3D-LFS along the z -direction [28]. The obtained results show that the shape of the printed voxels is more sensitive to the change of the z -position than to change of other factors; *e.g.* laser intensity and exposure time. Shown in Fig.IV.13(b,d) is the effect of the accuracy of the LFS on the stability of the nanofabrication in 3D by TPP.

IV.9. Effect of TPA-Threshold and z -Position on 3D Printing

In this axis, we will discuss the effect of the TPP threshold and z -position on the voxels size; *e.g.* Δ_z . Generally, polymerization induced by TPA begins when the concentration of the polymerizable radicals exceeds a certain threshold; this is explained by the presence of a quencher effect [3]. However, any chemical species that tends to prohibit the generation of TPP reaction; even in a small concentration, is called quencher; *e.g.* the dissolved O_2 in the resin. This property defines the threshold of TPP; *i.e.* defined by a critical laser dose, and thus further reduced the TPP resolution [9,39]. However, due to the existence of a chemical quencher effect, radicals survive and initiate TPP only at the LFS center, and thus the TPP threshold effect is formed. Both the optical nonlinearity; *i.e.* TPA, and threshold peculiarity contribute to the TPP resolution. From previous work realized by K. Takada et al. [140], the highest TPP resolution; *i.e.* $\sim 100 \text{ nm}$, has been determined for a specific resin doped with an anti- quencher effect.

T. Baldacchini et al. [42] demonstrated that the threshold of TPP; *e.g.* laser dose $(P, t)_{threshold}$, is reached when the radical attains a given concentration; *i.e.* C_{th} , and that a constant repetition rate and pulse duration are employed, then;

$$P_{th, fab}^2(w) \sigma_2(w) \phi_2(w) = k \quad (IV. 16);$$

Here, P is the laser power, $\sigma_2(w)$ denotes the TPA cross-section, $\phi_2(w)$ is the radical quantum yield, and k is a constant. The action spectrum of polymerization; *i.e.* $A(w)$, is determined by rearranging the following Eq.:

$$A(w) \propto \frac{1}{P_{th, fab}^2(w)} = \frac{\sigma_2(w) \phi_2(w)}{k} \quad (IV. 17);$$

The two-photon $\phi_2(w)$ at a frequency w can be estimated by the measure of the single-photon fluorescence (SPF) quantum yield at frequency $2w$ [42]. The quantum yield at $2w$ was determined to be ~ 0.006 at 400 nm wavelength; *i.e.* $\sim \lambda/2$ irradiation wavelength, by comparison of the integrated fluorescence to that of a molecule with a known yield at the same laser wavelength. See more detail in Ref. [42]. To determine $A(w)$, the $P_{th, fab}(w)$ was measured as a function of the wavelength of excitation.

Fig.IV.14(a) shows the results of the printed voxels; *i.e.* size and shape, as a function of the z -position of LFS; but in this study, we use an irradiation laser intensity of $I_{irr} \sim 1104 \text{ kW/cm}^2$ that is considered above the I_{th} [20]. According to the previous results (voxel size vs. z -position) and from the SEM image shown in the inset of Fig.IV.14(a), we demonstrate that the overall size of voxels increases when the laser dose of irradiation increases for different z -position of the LFS. This is explained by the LFS duplication versus I_{irr} . For more detail, see ref. [12]. By using $I_{irr} > I_{th}$; *i.e.* above $I_{th} \sim 820 \text{ kW/cm}^2$, we observe a fast saturation of Δ_{xy} . Also, we detect a strong linear increment of Δ_z of the printed voxels following the variation of z -position; *i.e.* by 100 nm step.

It is shown (Fig.IV.14(a)) that Δz ; *i.e.* from $\Delta z \sim 800 \text{ nm}$ to $\sim 1800 \text{ nm}$, was obtained for z -positions that are only ranged following a short step of $z \sim 0.1 \mu\text{m}$, *i.e.* from $z \sim 0.0 \mu\text{m}$ to $0.4 \mu\text{m}$ from the z_0 . Thus, we can explain this fast increment of Δz by the reason that the resin solidified ensuing the SLI distribution at the 3D-LFS; *e.g.* LFS duplication [110]. According to the results discussed in the previous segments, we confirmed that Δ_{xy} and Δ_z are strongly influenced by the

irradiation laser dose (Fig.IV.14(b)). To confirm the dependency of voxels size on the laser intensity in 3D nanoprinting, we printed a 3D pyramid by using an intensity above the TPA threshold; e.g. $I_{irr} \sim 1104 \text{ kW/cm}^2$ (Fig.IV.14(b)).

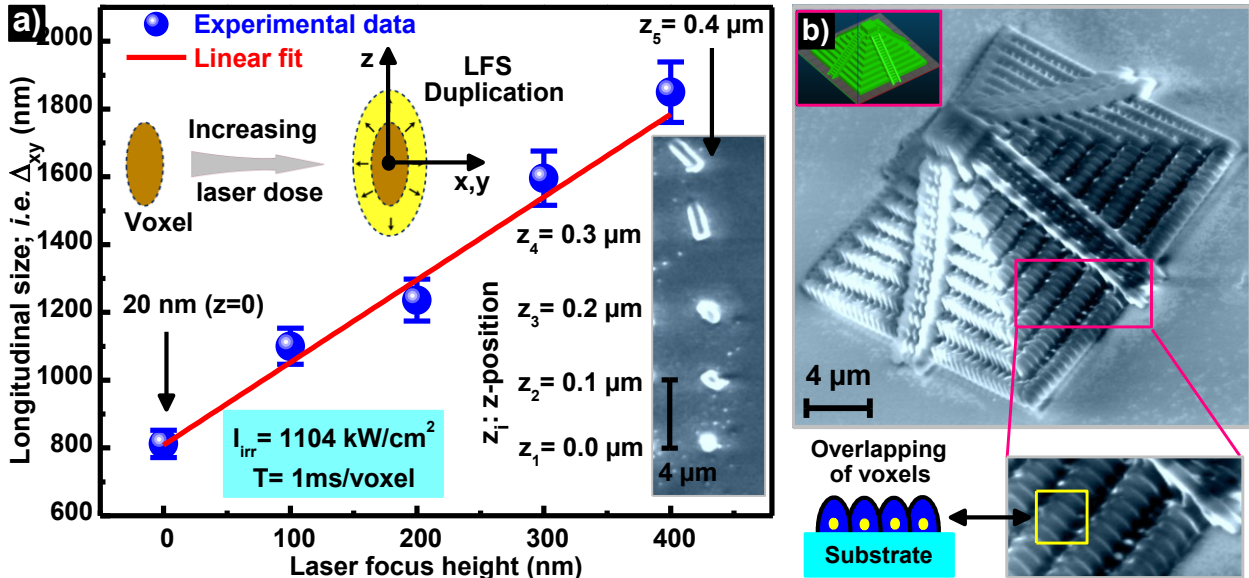


Figure IV.14. TPP thresholding effect vs. z -position of focus. (a) Δ_z evolution versus the z -position of the LFS using an intensity above the TPA threshold, the inset sketch presents the LFS duplication following the effect of the increase of the intensity. (b) SEM micrograph of a 3D micro-pyramid fabricated using a low overlapping mode of voxels; the voxels-overlapping presented in the pyramid is shown as an inset.

Shown in Fig.IV.14(b) is a 3D pyramid produced by using an overlapping accumulation of voxels. Here, we use a large overlapping-pitch of the LFS in order to well observe the true dimensions of the voxels; i.e. used to build the 3D pyramid. As shown by the SEM image in Fig.IV.14(b), the presence of the complete voxels in the 3D pyramid is well demonstrated. Due to the low resolution achieved from the pyramid, we conclude that a large dose near the TPP threshold is needed to improve the TPP-resolution [40]. The delicate control to voxel size involves three factors: (i) absorbed photon number, (ii) their spatial distribution; i.e. governed by the exposure time and NA , respectively, and (iii) the concentrations of the initiator and quencher in the resin [39,118,139].

IV.10. Effect of Z-position on the Aspect Ratio (AR)

Here, we study the effect of the z -position of the LFS on the AR of the printed voxels (Fig.IV.15). The AR; i.e. the elongation factor, is defined as the ratio of Δ_z of a single voxel on Δ_{xy} ; i.e. $AR = \Delta_z / \Delta_{xy}$. It is known that a high NA -OL, e.g. ~ 1.4 , is needed to achieve high TPP resolution [57,75,156]. Oppositely, lower NA tends to give larger Δ_z of voxels; this expected phenomenon could be interpreted by the threshold effect, meaning that the SLI is vertically distributed in the 3D

volume of LFS; *i.e.* along the z -direction [11]. H-B. Sun et al. [28] studied the effect of the exposure time on the AR and they found that the AR strongly depend on the laser dose. The same group [28] also found that a low-NA focusing does not necessarily give rise to Δ_{xy} worse than high-NA because of the thresholding effect.

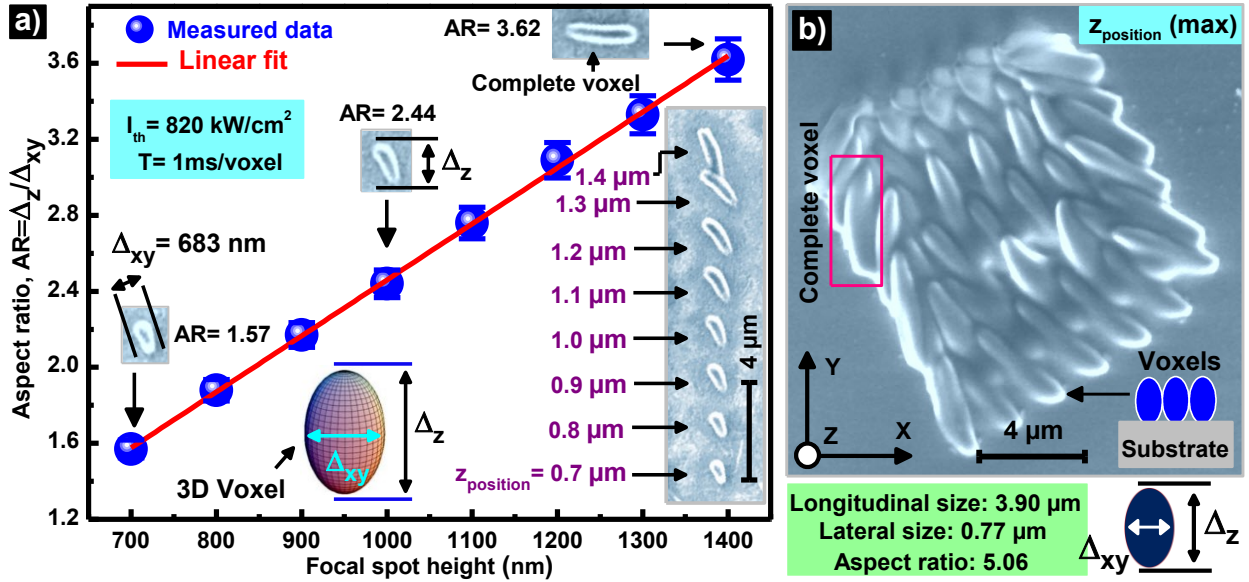


Figure IV.15. Elongation factor; *i.e.* $AR = \Delta_z / \Delta_{xy}$, of voxels versus the z -position of the LFS; blue scatter are the measured AR of the nanoprinted voxels shown in the SEM image (inset); the full red line is a linear theoretical fits guide to the eye. **(b)** SEM micrograph of complete voxels that are polymerized far above the laser's threshold intensity; *i.e.* $I_{irr} \sim 1650 \text{ kW/cm}^2 > I_{th} \sim 820 \text{ kW/cm}^2$.

The dependence of the AR on the z -position is shown in Fig.IV.15(a). The experimental data points of this figure are adapted from Δ_{xy} and Δ_z in Fig.IV.13(a), and they show that the AR increases linearly with the increased z -position of LFS, ranging from $AR \sim 1.57$, for a truncated voxel at $z \sim 700 \text{ nm}$, to $AR \sim 3.62$ for fully developed voxel at $z \sim 1.4 \mu\text{m}$. For our set up, Abbe's axial resolution is $2\lambda/NA^2 \sim 796 \text{ nm}$; a resolution which is not as fine as the lateral one. For Gaussian beams, Abbe's lateral resolutions may be corrected for the SLI associated with TPA, and a $\sqrt{2}$ factor should be introduced as $d_{xy} = \lambda/2\sqrt{2} NA \sim 197 \text{ nm}$, while the axial resolution d_z is at least 2.5 times worse than d_z ($d_z = 2.5d_{xy} \sim 394 \text{ nm}$) [20,52].

Voxels that are produced with large z -positions; *e.g.* $z > 1.4 \mu\text{m}$, are washed away during the rinsing phase (*vide infra*). When the laser intensity is increased above I_{th} , voxels are much larger; *i.e.* all Δ_{xy} and Δ_z and AR increase with the increased intensity, or irradiation dose. Indeed, Fig.IV.15(b) shows that voxels fabricated with a 1 ms exposure at $I_{irr} \sim 1650 \text{ kW/cm}^2$; *e.g.* nearly

double of I_{th} , exhibit $\Delta_{xy} = 770 \text{ nm}$, and $\Delta_z = 3.9 \mu\text{m}$, and $AR = 5.06$ larger than those observed with I_{th} exposure for the same time and the same z-position. We chose $z = 1.4 \mu\text{m}$ for Fig.IV.15(b) to compare with the largest voxel observed in Fig.IV.15(a). Clearly, Δ_z is more sensitive to exposure dose than Δ_{xy} , and lower laser intensity at near-threshold exposure is advantageous to achieve voxels with lower AR and high spatial resolution.

In this study of voxel nanofabrication, we found that Δ_z is considered as a good factor to reach a high resolution of 3D printing, and it is more realistic to expect an AR between 3 to 6; $AR = 3.62$ in our case [20]. By increasing the irradiation intensity; meaning $I_{irr} > I_{th} \sim 820 \text{ kW/cm}^2$, we found that the focal voxel was laterally shrunken and vertically expanded, this led to slim voxels and provides worse AR; *e.g.* $AR \sim 5.06$. The voxel expansion with the increase of intensity follows the growth of the LFS in 3D. In our previous work [12], we have proposed an explanation of voxel formation as a function of intensity; *i.e.* we called LFS evolution.

IV.11. Linewidth Dependence Z-position of LFS

In this section, we investigate the influence of the z-position on the linewidth. The microscale lines were polymerized using a continuous scan mode of voxels; *i.e.* overlapping process, as shown as an inset in Fig.IV.16(a), and each microline was scanned once with a constant scanning speed [110]. As previously discussed, a voxel is considered as an elementary component of the printed patterns; *e.g.* microlines [108]. In the previous sections, a z-scan scan of the LFS was proposed to characterize and manipulate the spatial arrangement of voxels in 3D, from which accurate forms of TPE at the LFS was obtained. Thus, we found that the distribution of the laser intensity in the focal region is of quasi ellipsoid shape with a major axis in the z-direction.

Shown in Fig.IV.16(a) is the linewidth; *i.e.* microlines resolution, dependency on the LFS z-position; *i.e.* by $\sim 50 \text{ nm}$ step. The SEM image (top view) of the corresponding microlines is shown as an inset in the Fig.IV.16(a). It can be seen from this Fig. that when only a small part of the LFS (tip of an iceberg) reaches the resin; *e.g.* $\sim 30 \text{ nm}$ away from the glass-end, fine patterns of microline are created with $\sim 178 \text{ nm}$ width; corresponding to $\lambda/4.38$ resolution; *i.e.* below the $SDL \sim \lambda/2NA = 278 \text{ nm}$ [20]. With the increase in height of the LFS (in the z-direction), a greater number of thick nanolines are printed, this is due to the shape of the focal voxels. Fig.IV.16(b) shows a serie of microlines truncated by cover glass under different z-positions; *i.e.* by 15 nm z-

step. In this experiment, we positioned more than the tip of the focus inside the resin; *e.g.* $z \sim 350 \text{ nm}$, for the first step; here, we labeled this position by $z = 0 \text{ nm}$.

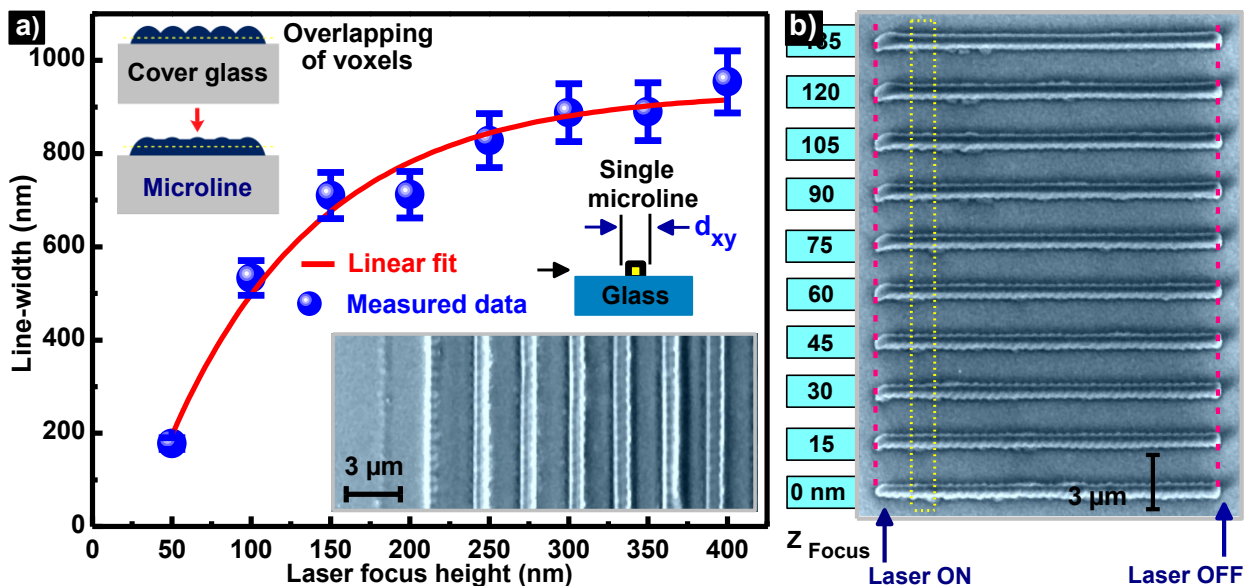


Figure IV.16. TPP fabrication of microline through the z -scan method. (a) The variation of linewidth according to z -position of the LFS; the schematic presentation of the overlapping process of the voxel is shown as an inset; the typical laser intensity applied is $\sim 800 \text{ kW/cm}^2$. (b) Microline lateral-size dependency on z -position using $\sim 15 \text{ nm}$ for each z -step; *i.e.* $\sim 15 \text{ nm}$ of height between two lines; the used intensity is $\sim 0.71 \times 10^9 \text{ mW/cm}^2$.

From Fig.IV.16(b), almost no difference detected of width can be observed between diverse printed lines under different z -positions, this is due that the voxels which are responsible for printing the microlines reach their saturation status; *i.e.* Δ_{xy} saturates. Thus, we conclude that d_{xy} isn't depends on the z -position when Δ_{xy} of voxels saturates. We demonstrate that there is a limit to how much the d_{xy} can be increased with respect to the z -scan method. It can be seen from Fig.IV.16(a) that the nanofeature size; *e.g.* d_{xy} , go up with the increase of the z -position of the LFS. The systematic investigation of the resolution of the microlines was realized just to confirm the efficacy of the z -scan method at the submicrometric scale; *i.e.* $\sim 15 \text{ nm}$ step (Fig.IV.16(b)) [20].

IV.12. Achievement of SDL Resolution of Voxels

In TPP-based 3D printing, the voxel; *i.e.* the reflection of the fabrication resolution, is considered as the image of the LFS in the pre-polymer resin (Fig.IV.17(a)). At the focus, the incident photons are absorbed in a nonlinear manner and confined in a volume much smaller than λ^3 ; *e.g.* $\lambda = 780 \text{ nm}$. Thanks to the nonlinear effect of TPA, the Fs laser beam penetrates in the resin without

being absorbed (Fig.IV.17(b)); *i.e.* along the path of the beam, and triggers TPP only in a small volume around the LFS; thus, a SDL resolution can be achieved [95,115].

By systematically adjusting the z-position of the LFS, SDL voxel of $\Delta_{xy} \sim 94 \text{ nm}$ is attained, *i.e.* corresponding to $\sim \lambda/8.20$ resolution (Fig.IV.17(a)). Δ_{xy} shows an exponential dependency versus the penetration of the LFS inside the resin; *i.e.* by 45 nm step of z-position. Also, it well demonstrated that after a certain z-position; *i.e.* $z \sim 400 \text{ nm}$, Δ_{xy} become saturated. According to z-position of focus-dependent Δ_{xy} , we further observe that the printed voxels up $\sim 100 \text{ nm}$ away from the glass-end present almost a horizontal slop; this is explained by the elliptical geometry character of the distributed SLI at the tip-end of the LFS. In high-resolution of TPP, the variation of voxel cross-section size in the glass/resin contact is of much concern in affecting the formation of precise 3D structures as well as its nanofeature size [11,20].

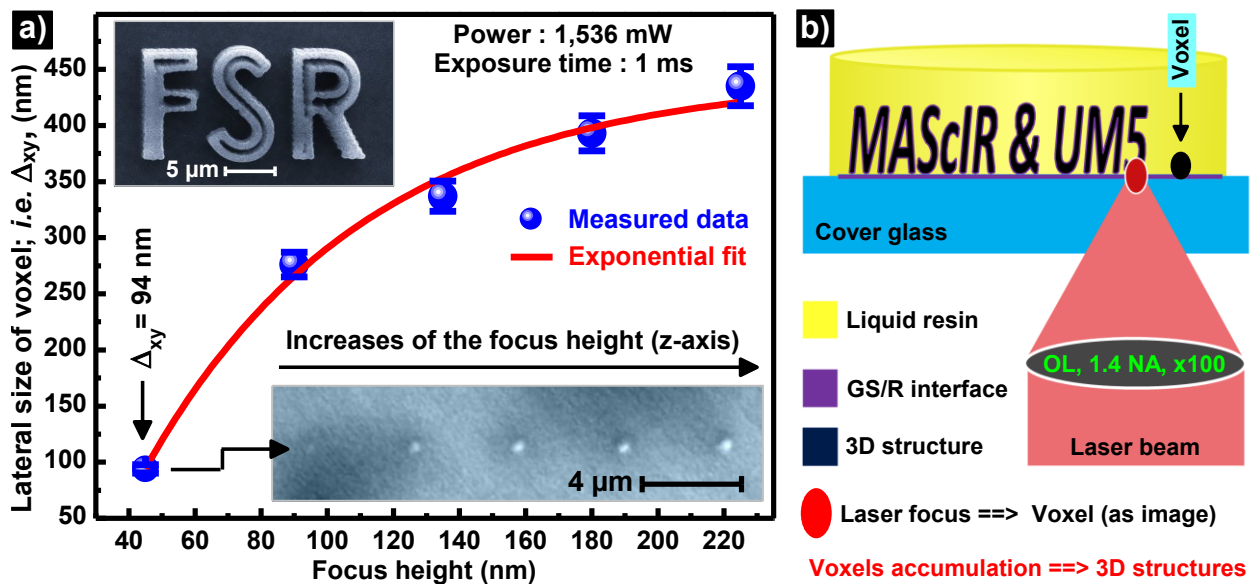


Figure IV.17. Achievement of SDL voxels via z-scan strategy. **(a)** LFS height dependent Δ_{xy} under a fixed laser dose; the SEM image of the corresponding printed voxels is shown as an inset. **(b)** Schematic showing the principle of the use of the TPP z-scan strategy for achieving stable 3D nanofabrication; here, the LFS is positioned in the glass/resin interface.

According to the study of voxel's optimization in 3D nanoprining discussed in many researches, we believed that most of the reported measurements of the TPP resolution were performed without properly considering the truncation amount effect. Therefore, the measured values of resolution are more (+) or less (-) small than the actual ones. The truncation amount causes the measurement error of the resolution of 3D printing, and sometimes leading to confusing conclusions. Accurate

information on 3D-LFS related to TPE is essential for not only in 3D nanoprinting, but also for diversified fields such as optical integrated circuits, optical memory, and holographic recording [11,28].

IV.13. 3D Laser Nanoprinting at SDL Resolution

The results achieved through the study of voxels-optimization in 3D nanoprinting are essential for properly designing stable and precise 3D polymeric-objects with near-diffraction-limit features; *e.g.* SDL resolution (see Fig.IV.18) [20]. By controlling and optimizing the z -position of the LFS, we have demonstrated the spatial arrangement of voxels; *i.e.* the 3D resolution, in 3D nanoprinting. In our work, TPP microstructures are produced by continuously bonding voxel to voxel like blocks along the scanning paths of the LFS; *i.e.* a nano-pencil of light. To fabricate stable 3D objects with the finest possible resolution with our setup, we position the LFS at $z \sim 100 \text{ nm}$ above z_0 (see Fig.IV.18(a)). At this position, we obtain a truncated voxel with a lateral size of $\sim 400 \text{ nm}$, and a nano-fiber of $\sim 420 \text{ nm}$ diameter with a $\sim 100 \text{ nm}$ feature size; *i.e.* the smallest printed feature.

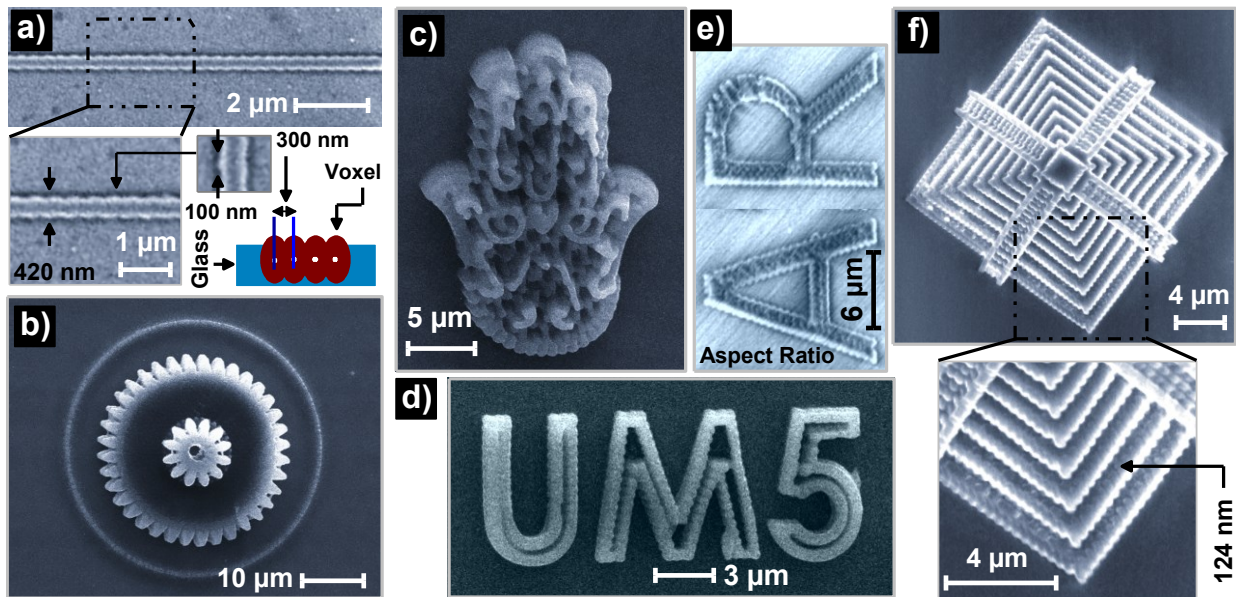


Figure IV.18. SEM images of 3D micro objects/patterns fabricated by using TPP-based 3D nanoprinting. (a) Nano-fiber of a $\sim 420 \text{ nm}$ diameter; (inset) the overlapping of voxels; *i.e.* the scanning pitch in the x - and y - directions, was fixed to $\sim 300 \text{ nm}$. (b) Top-view of a 3D micro-gear. (c) A 3D micro human-hand (*khmissa*). (d) Microsized UM5 pattern. (e) SEM image of the “Aspect Ratio, AR” structure. (f) A 3D pyramid fabricated at SDL accuracy; *e.g.* $\sim 124 \text{ nm}$ resolution. The typical intensity and the focus z -position used in (a-f) are $I_{th} \sim 820 \text{ kW} \cdot \text{cm}^{-2}$ and $z_{\text{position}} = 120 \text{ nm}$ away from z_0 ; respectively [20].

The exposure time was 1 ms at I_{th} , and the lateral scanning pitch was $\sim 300 \text{ nm}$; so that voxels overlap laterally by $\sim 100 \text{ nm}$. Thus, the nanofiber that was printed through the mentioned focusing

configuration is stable; meaning it remains; *e.g.* physically attached, on the substrate after the rinsing step (Fig.IV.18(a)). With this configuration, we also fabricated stable 3D nano-micro-objects by raster scanning layer-by-layer, with a pitch between layers in the z-direction of $\sim 500\text{ nm}$, to ensure a strong overlap between the voxels in the z-direction; *e.g.* overlap by the Rayleigh length of the LFS. The smallest feature size of our 3D micro-nano-objects varied between $\sim 100\text{ nm}$ and $\sim 124\text{ nm}$ (Fig.IV.18(a-f)); a feature's size which is far below the TPA modified Abbe diffraction limit.

A comment must be made about the resolution of TPP-based 3D nanofabrication. Clearly, besides, the nonlinearity of TPA; *i.e.* NLO effect, and materials thresholding and nanofabrication parameters; including the exposure dose and scanning speed, as previously reported in a long literature. Our experimental results show that the resolution of 3D nanofabrication is strongly dependent on the spatial overlap of the LFS and the pre-polymer resin, and the scanning pitch for voxels connection which make up 3D structures. That is fabrication parameters play a major role in defining the resolution of 3D nanoprinting (Fig.IV.18(a-f) [156]).

IV.14. Conclusion

In summary, we investigated the influence of the LFS z-position on the resolution of TPP-based 3D nanoprinting. Using a systematic nanofabrication of voxels by varying the z-position of the LFS, we have experimentally examined their spatial dimensions; *e.g.* both lateral and longitudinal. We found that, while the voxel size depends on the laser's exposure dose, its size is dictated by the extent of overlap between the LFS and the resin. By using truncated voxels having small aspect ratios, we could fabricate stable 3D micro-nano-objects, with feature sizes, near $\sim 100\text{ nm}$, away below Abbe's diffraction limit. TPP fabrication parameters play a major role in defining the resolution of 3D printed stable-structures, and this study clearly demonstrates the impact of the z-position of the LFS on the precision and the resolution of TPP nanofabrication; a feature which is of primary importance in 3D laser nanoprinting. Indeed, in most of the published literature, attention is not paid to the z-position and the overlap of the LFS and the resin, and our study, at the substrate/resin interface, demonstrates how important is the z-position in 3D nanoprinting. Perhaps, more studies should focus on this interface, by for example chemical treatment of the substrates for better adhesion of the resin, with the aim of using lower irradiation doses for better resolution. The resin itself is extremely important, from the points of view of materials nonlinearity

and polarization sensitivity. Indeed, using polarization-sensitive resins would allow for the fabrication of polarization-sensitive structures for; *e.g.* applications in diffractive, polarization-sensitive, nano-optical devices.

General Conclusions

Since the report of the first experiments by Kawata's group in 1997 on 3D microfabrication by TPA induced solidification; *i.e.* photopolymerization, of photoresists, a tremendous amount of research works have been carried out in TPP-based 3D nanoprinting owing to the potential of such a technology in enabling manufacturing at extremely small scales; *e.g.* nanoscales (near-diffraction limit resolution), with enhanced speed and flexibility. The most important application of 3D laser nanoprinting is the realization of complex 3D micro-nano-structures with the combinations of different materials to realize minute objects with multiple functionalities, and mesoscale printing is also of importance; and applications of printed 3D micro-nano-sized objects range from scaffolds for cell culture and tissue engineering, and photonics crystals, and micro-optics, and micro-lens-array systems, and movable microsized machines.

The objective of this research was to analyze and optimize the spatial resolution of TPP-based 3D nanoprinting; also, to understand how the focusing parameters; *e.g.* laser power, exposure time, scanning speed, and z-position of the laser's focal spot, influence on the resolution and accuracy (voxel formation) in 3D laser nanoprinting. In this work, we have developed a Fs laser-writing 3D micro-nano-fabrication system based on TPP lithography to fabricate arbitrary 3D SDL structures, in which the resolution can be systematically controlled. We investigated the effect of different laser writing parameters on the spatial resolution of the TPP laser writing fabrication. The size of laser fabricated nanostructures depends on the laser's intensity, and the above nanofabrication findings are observed with a laser's threshold intensity; and for laser intensities exceeding the TPP threshold, the printed voxels are large; *i.e.* with AR values larger than ~ 3.62 , leading to larger resolution of 3D nanoprinting. Finally, we fabricated 3D microsized structures by TPP stereolithography based on a custom-made programmed pattern, *e.g.* CAD 3D model. This systematic 3D micro/nanofabrication confirmed our capability for fabricating microdevices which can be applied for the future applications.

Areas of Future Research

There are a variety of potential areas of future research in the field of TPP-based 3D-laser nanoprinting, and adapting the process to more commercial fabrication applications (future applications). The achieved result by using our custom-made TPP-optical set-up during the period of the preparation of this thesis is not an end of work on TPP nanoprinting; but this achievement is part of the dynamics of a broader research project. Thus, and in view of the presented results, the perspectives of our work are summarized in two ideas; first, and taking into account as Pr. Z. Sekkat discussed with the TPA-nanofabrication team; we think that we can focus our future research on the field of the nanofabrication of tissue engineering by using a special photoresin (the work on the software and 3D design of complex structures is in progress). As the second perspective of our work is to try to fabricate medical functional-microdevices (also the work concerning the CAD model-design is in progress). Last but not least, we think that many works can be realized in the future by using our Fs laser system.

References List

- [1] M. Carloti and V. Mattoli, "Functional materials for two-photon polymerization in microfabrication," *Small*, vol. 15, no. 40, pp. 1-22, 2019.
- [2] H. B. Sun and S. Kawata, "Two-photon laser precision microfabrication and its applications to micro-nanodevices and systems," *J. J. of Lightwave Technology*, vol. 21, no. 3, pp. 624-633, 2003.
- [3] Z. Sekkat and S. Kawata, "Laser nanofabrication in photoresists and azopolymers," *Laser and photonics reviews*, vol. 8, pp. 1-26, 2014.
- [4] J. Li, L. O'Faolain, I. H. Rey, and T. F. Krauss, "Four-wave mixing in photonic crystal waveguides: slow light enhancement and limitations," *Opt. Express*, vol. 19, no. 5, pp. 4458, 2011.
- [5] H. Zhang et al., "A novel optical lithography implement utilizing third-harmonic generation via metallic tip-enhanced near field," *Opt. Commun.*, vol. 383, pp. 418-422, 2017.
- [6] Y. Zhang, Q. Chen, H. Xia, and H. B. Sun, "Designable 3D-nanofabrication by femtosecond laser direct writing," *Nano Today*, vol. 5, no. 5, pp. 435-448, 2010.
- [7] C. Liao, W. Anderson, F. Antaw, and M. Trau, "Two-photon nanolithography of tailored hollow three-dimensional microdevices for biosystems," *ACS Omega*, vol. 4, no. 1, pp. 1401-1409, 2019.
- [8] H. Ceylan et al., "3D-Printed biodegradable microswimmer for theranostic cargo delivery and release," *ACS Nano*, vol. 13, no. 3, pp. 3353-3362, 2019.
- [9] S. Kawata et al., "Finer features for functional microdevices," *Nature*, vol 412, pp. 697-698, 2001.
- [10] S. Maruo, O. Nakamura, and S. Kawata, "Three-dimensional microfabrication with two-photon-absorbed photopolymerization.," *Opt. Lett.*, vol. 22, no. 2, pp. 132-134, 1997.
- [11] H. Sun, T. Tanaka, S. Kawata, H. Sun, T. Tanaka, and S. Kawata, "Three-dimensional focal spots related to two-photon excitation," *Appl. Phys. Lett.*, vol. 80, no. 2002, pp. 2011-2014, 2013.
- [12] Y. Bougdid et al., "Systematic $\lambda/21$ resolution achieved in nanofabrication by two-photon-absorption induced polymerization," *J. Micromechanics Microengineering*, vol. 29, no. 3, pp. 1-7, 2019.
- [13] L. Li and J. T. Fourkas, "Multiphoton polymerization," *MaterlasToday*, vol. 10, no. 6, pp. 30-37, 2007.
- [14] J. W. Perry et al., "Two-photon polymerization initiators for three-dimensional optical data storage and microfabrication" *Nature*, vol 398, pp. 51-54, 1999.
- [15] J. Li et al., "Two-photon polymerization 3D printed freeform micro-optics for optical coherence tomography fiber probes," *Sci. Rep.*, vol. 8, no. 1, pp. 1-9, 2018.
- [16] M. T. Raimondi, S. M. Eaton, M. M. Nava, M. Laganà, G. Cerullo, and R. Osellame, "Two-photon laser polymerization: from fundamentals to biomedical application in tissue engineering and regenerative medicine," *J. Appl. Biomater. Biomech.*, vol 10, pp. 55-65, 2012.
- [17] A. Ovsianikov et al., "Two-photon polymerization of hybrid sol-gel materials for photonics applications," *Laser Chem.*, vol. 2008, pp. 1-7, 2008.
- [18] T. Tanaka, H. B. Sun, and S. Kawata, "Rapid sub-diffraction-limit laser micro/nanoprocessing in a threshold material system," *Appl. Phys. Lett.*, vol. 80, no. 2, pp. 312-314, 2002.
- [19] Robert J. DeVoe, H. W. Kalweit, C. A. Leatherdale, T. R. Williams,, "Voxel shapes in two-photon microfabrication," *Proceedings of SPIE*, vol. 4797, pp. 310-316, 2003.

- [20] Y. Bougdid, and Z. Sekkat, "Voxels optimization in 3D laser nanoprinting," *Sci. Rep.*, vol. 10, no. 1, pp. 1-8, 2020.
- [21] H. B. Sun, S. Matsuo, and H. Misawa, "Three-dimensional photonic crystal structures achieved with two-photon-absorption photopolymerization of resin," *Appl. Phys. Lett.*, vol. 74, no. 6, pp. 786-788, 1999.
- [22] J. Serbin et al., "Femtosecond laser-induced two-photon polymerization of inorganic-organic hybrid materials for applications in photonics," *Opt. Lett.*, vol. 28, no. 5, pp. 301, 2003.
- [23] M. Malinauskas, H. Gilbergs, A. Ukauskas, V. Purlys, D. Paipulas, and R. Gadonas, "A femtosecond laser-induced two-photon photopolymerization technique for structuring microlenses," *J. Opt.*, vol. 12, no. 3, 2010.
- [24] T. Chung, Y. Tu, Y. Hsueh, S. Chen, and W. Li, "Micro-lens array fabrication by two photon polymerization technology," *auSMT*, vol. 3, no. 2, pp. 131-135, 2013.
- [25] A. Seidel, C. Ohrt, S. Passinger, C. Reinhardt, R. Kiyon, and B. N. Chichkov, "Nanoimprinting of dielectric loaded surface-plasmon-polariton waveguides using masters fabricated by 2-photon polymerization technique," *J. Opt. Soc. Am. B*, vol. 26, no. 4, p. 810, 2009.
- [26] S. D. Gittard et al., "Fabrication of microscale medical devices by two-photon polymerization with multiple foci via a spatial light modulator," *Biomed. Opt. Express*, vol. 2, no. 11, p. 3167, 2011.
- [27] S. Ushiba, K. Masui, N. Taguchi, T. Hamano, S. Kawata, and S. Shoji, "Size dependent nanomechanics of coil spring shaped polymer nanowires," *Sci. Rep.*, vol. 5, no. February, 2015.
- [28] H. Sun, K. Takada, M. Kim, K. Lee, and S. Kawata, "Scaling laws of voxels in two-photon photopolymerization nanofabrication," *App. Phys. Lett.*, vol. 83, no. 1104, pp. 1-4, 2003.
- [29] S. Ushiba, S. Shoji, K. Masui, P. Kuray, J. Kono, and S. Kawata, "3D microfabrication of single-wall carbon nanotube/polymer composites by two-photon polymerization lithography," *Carbon*, vol. 59, pp. 283-288, 2013.
- [30] X. Zhou, Y. Hou, and J. Lin, "A review on the processing accuracy of two-photon polymerization," *AIP Adv.*, vol. 5, no. 3, pp. 1-22, 2015.
- [31] J. G.- Mayer, "Über Elementarakte mit zwei Quantensprüngen," *Annalen der physik*, vol. 401, pp. 273-294, 1931.
- [32] W. Kaiser and C. G. B. Garrett, "Two-photon excitation in $\text{CaF}_2: \text{Eu}^{2+}$," *Phys. Rev. Lett.*, vol. 7, no. 6, pp. 229-231, 1961.
- [33] Q. Cui, Y. Li, J. Chang, H. Zhao, and C. Xu, "Temporally resolving synchronous degenerate and nondegenerate two-photon absorption in 2D semiconducting monolayers," *Laser Photonics Rev.*, vol. 13, no. 2, pp. 1-10, 2019.
- [34] M. Rumi and J. W. Perry, "Two-photon absorption : an overview of measurements and principles," *Advances in Optics and Photonics*, vol. 2, pp. 451-518, 2010.
- [35] S. Kawata and H. B. Sun, "Two-photon photopolymerization as a tool for making micro-devices," *Appl. Surf. Sci.*, vol. 208-209, no. 1, pp. 153-158, 2003.
- [36] A. S. Dvornikov, E. P. Walker, and P. M. Rentzepis, "Two-photon three-dimensional optical storage memory," *J. Phys. Chem. A*, vol. 113, no. 49, pp. 13633-13644, 2009.
- [37] M. B. Ericson, C. Simonsson, S. Guldbrand, C. Ljungblad, J. Paoli, and M. Smedh, "Two-photon

- laser-scanning fluorescence microscopy applied for studies of human skin,” *J. Biophotonics*, vol. 1, no. 4, pp. 320–330, 2008.
- [38] S. Wu, J. Serbin, and M. Gu, “Two-photon polymerisation for three-dimensional micro-fabrication,” *J. Photochem. Photobiol. A Chem.*, vol. 181, no. 1, pp. 1–11, 2006.
- [39] K. S. Lee, R. H. Kim, D. Y. Yang, and S. H. Park, “Advances in 3D nano/microfabrication using two-photon initiated polymerization,” *Prog. Polym. Sci.*, vol. 33, no. 6, pp. 631–681, 2008.
- [40] H. B. Sun and S. Kawata, “Two-photon photopolymerization and 3D lithographic microfabrication,” *Adv. Polym. Sci.*, vol. 170, pp. 169–273, 2004.
- [41] A. Selimis, V. Mironov, and M. Farsari, “Direct laser writing : Principles and materials for scaffold 3D printing,” *Microelectron. Eng.*, vol. 132, no. 25, pp. 1–7, 2015.
- [42] T. Baldacchini et al., “Acrylic-based resin with favorable properties for three-dimensional two-photon polymerization,” *Journal of Applied Physics*, vol. 95, no. 11, pp. 6072-6076, 2004.
- [43] E. Andrzejewska, “Photopolymerization kinetics of multifunctional monomers,” *Prog. Polym. Sci.*, vol. 26, no. 4, pp. 605–665, 2001.
- [44] L. J. Jiang et al., “Two-photon polymerization: investigation of chemical and mechanical properties of resins using Raman microspectroscopy,” *Opt. Lett.*, vol. 39, no. 10, pp. 3034-3037, 2014.
- [45] V. Hahn, F. Mayer, M. Tiel, and M. Wegener, "3D laser nanoprinting", *Opt. Photon. News*, vol 30, pp. 28-35, 2019.
- [46] T. Baldacchini, "Three-dimensional microfabrication using two-photon polymerization fundamentals, technology, and applications", Hardcover ISBN: 9780323353212, eBook ISBN: 9780323354059, (2016)
- [47] E. Andrzejewska et al., “Variations of rate coefficients and termination mechanism during the after-effects of a light-induced polymerization of a dimethacrylate monomer,” *Macromol. Theory Simulations*, vol. 10, no. 9, pp. 842–849, 2001.
- [48] E. Andrzejewska, M. B. Bogacki, M. Andrzejewski, and M. Janaszczyk, “Termination mechanism during the photo-induced radical cross-linking polymerization in the presence and absence of oxygen,” *Phys. Chem. Chem. Phys.*, vol. 5, no. 12, pp. 2635–2642, 2003.
- [49] M. Malinauskas, M. Farsari, A. Piskarskas, and S. Juodkazis, “Ultrafast laser nanostructuring of photopolymers: A decade of advances,” *Phys. Rep.*, vol. 533, no. 1, pp. 1–31, 2013.
- [50] D. A. Bolon and K. K. Webb, “Barrier coats versus inert atmospheres: The elimination of oxygen inhibition in free-radical polymerizations,” *J. Appl. Polym. Sci.*, vol. 22, no. 9, pp. 2543–2551, 1978.
- [51] M. Farsari, M. Vamvakaki, and B. N. Chichkov, “Multiphoton polymerization of hybrid materials,” *J. Opt.*, vol. 12, no. 12, 2010.
- [52] J. Fischer and M. Wegener, “Three-dimensional optical laser lithography beyond the diffraction limit,” *Laser Photonics Rev.*, vol. 23, pp. 1–23, 2012.
- [53] M. Kavaldzhiev et al., “Biocompatible 3D printed magnetic micro needles,” *Biomed. Phys. Eng. Express*, vol. 3, pp. 1–14, 2017.
- [54] Y. Lin and J. Xu, “Microstructures fabricated by two-photon polymerization and their remote manipulation techniques: Toward 3D printing of micromachines,” *Adv. Opt. Mater.*, vol. 6, no. 8, pp. 1–11, 2018.

- [55] C. H. Lee, T. W. Chang, K. L. Lee, J. Y. Lin, and J. Wang, "Fabricating high-aspect-ratio sub-diffraction-limit structures on silicon with two-photon photopolymerization and reactive ion etching," *Appl. Phys. A*, vol. 79, no. 8, pp. 2027–2031, 2004.
- [56] J. Fischer, G. Von Freymann, and M. Wegener, "The materials challenge in diffraction-unlimited direct-laser-writing optical lithography," *Adv. Mater.*, vol. 22, no. 32, pp. 3578–3582, 2010.
- [57] X. Dong, Z. Zhao, and X. Duan, "Improving spatial resolution and reducing aspect ratio in multiphoton polymerization nanofabrication," *App. Phys. Lett.*, vol. 92, pp. 90–93, 2008.
- [58] P. Prabhakaran, Y. Son, C. W. Ha, J. J. Park, S. Jeon, and K. S. Lee, "Optical materials forming tightly polymerized voxels during laser direct writing," *Adv. Eng. Mater.*, vol. 20, no. 10, pp. 1–13, 2018.
- [59] K. Takada et al., "Size-dependent behaviors of femtosecond laser-prototyped polymer micronanowires," *Opt. Lett.*, vol. 34, No. 5, pp. 566–568, 2009.
- [60] D. Tan et al., "Reduction in feature size of two-photon polymerization using SCR500," *Appl. Phys. Lett.*, vol. 90, pp. 1–4, 2007.
- [61] D. Wu et al., "High numerical aperture microlens arrays of close packing," *Appl. Phys. Lett.*, vol. 97, no. 3, pp. 1–4, 2010.
- [62] E. Wolf, "IX The diffraction theory of aberrations," *Rep. Prog. Phys.*, vol. 14, no. 95, 1965.
- [63] K. Matsumoto, "STM/AFM nano-oxidation process to room-temperature-operated single-electron transistor and other devices," *Proc. IEEE*, vol. 85, no. 4, pp. 612–628, 1997.
- [64] A. Tarun, M. R. H. Daza, N. Hayazawa, Y. Inouye, and S. Kawata, "Apertureless optical near-field fabrication using an atomic force microscope on photoresists," *Appl. Phys. Lett.*, vol. 80, no. 18, pp. 3400–3402, 2002.
- [65] S. W. Hell, "Far-field optical nanoscopy," *Science*, vol. 316, no. 1153, 2007.
- [66] L. Liu, D. Yang, W. Wan, H. Yang, Q. Gong, and Y. Li, "Fast fabrication of silver helical metamaterial with single-exposure femtosecond laser photoreduction," *Nanophotonics*, vol. 8, no. 6, pp. 1087–1093, 2019.
- [67] X. Q. Liu et al., "Optical nanofabrication of concave microlens arrays," *Laser Photonics Rev.*, vol. 13, no. 5, pp. 1–5, 2019.
- [68] G. J. Lee, Y. J. Yoo, and Y. M. Song, "Recent advances in imaging systems and photonic nanostructures inspired by insect eye geometry," *Appl. Spectrosc. Rev.*, vol. 53, no. 2–4, pp. 112–128, 2018.
- [69] S. Petsch, S. Schuhladen, L. Dreesen, and H. Zappe, "The engineered eyeball, a tunable imaging system using soft-matter micro-optics," *Light Sci. Appl.*, vol. 5, no. 7, pp. 1–7, 2016.
- [70] Y. H. Kim et al., "Optically selective microlens photomasks using self-assembled smectic liquid crystal defect arrays," *Adv. Mater.*, vol. 22, no. 22, pp. 2416–2420, 2010.
- [71] Y. Qu, J. Kim, C. Coburn, and S. R. Forrest, "Efficient, nonintrusive outcoupling in organic light emitting devices using embedded microlens arrays," *ACS Photonics*, vol. 5, no. 6, pp. 2453–2458, 2018.
- [72] B. Hao et al., "Versatile route to gapless microlens arrays using laser-tunable wet-etched curved surfaces," *Opt. Express*, vol. 20, no. 12, pp. 12939, 2012.

- [73] Q. Xu et al., “Fabrication of polymer microlens array with controllable focal length by modifying surface wettability,” *Opt. Express*, vol. 26, no. 4, p. 4172, 2018.
- [74] C. de Marco et al., “Indirect 3D and 4D printing of soft robotic microstructures,” *Adv. Mater. Technol.*, vol. 4, no. 9, pp. 1–7, 2019.
- [75] W. Xiong et al., “Laser-directed assembly of aligned carbon nanotubes in three dimensions for multifunctional device fabrication,” *Adv. Mat.*, vol. 9, no. 10, pp. 2002–2009, 2016.
- [76] K. Masui et al., “Laser fabrication of Au nanorod aggregates microstructures assisted by two-photon polymerization,” *Opt. Express*, vol. 19, no. 23, pp. 22786, 2011.
- [77] H. Ishitobi, S. Shoji, T. Hiramatsu, H.-B. Sun, Z. Sekkat, and S. Kawata, “Two-photon induced polymer nanomovement,” *Opt. Express*, vol. 16, no. 18, p. 14106, 2008.
- [78] T. Fujigaya, S. Haraguchi, T. Fukumaru, and N. Nakashima, “Development of novel carbon nanotube/photopolymer nanocomposites with high conductivity and their application to nanoimprint photolithography,” *Adv. Mater.*, vol. 20, no. 11, pp. 2151–2155, 2008.
- [79] D. Baskaran, J. W. Mays, and M. S. Bratcher, “Polymer-grafted multiwalled carbon nanotubes through surface-initiated polymerization,” *Angew. Chemie - Int. Ed.*, vol. 43, no. 16, pp. 2138–2142, 2004.
- [80] S. Kim, S. Lee, J. Lee, B. J. Nelson, L. Zhang, and H. Choi, “Fabrication and manipulation of ciliary microrobots with non-reciprocal magnetic actuation,” *Sci. Rep.*, vol. 6, no. 30713, pp. 1–9, 2016.
- [81] S. Tottori, L. Zhang, F. Qiu, K. K. Krawczyk, A. Franco-Obregón, and B. J. Nelson, “Magnetic helical micromachines: Fabrication, controlled swimming, and cargo transport,” *Adv. Mater.*, vol. 24, no. 6, pp. 811–816, 2012.
- [82] X. Wang et al., “3D printed enzymatically biodegradable soft helical microswimmers,” *Adv. Funct. Mater.*, vol. 28, no. 45, pp. 1–8, 2018.
- [83] F. Soto and R. Chrostowski, “Frontiers of medical micro/nanorobotics: In vivo applications and commercialization perspectives toward clinical uses,” *Front. Bioeng. Biotechnol.*, vol. 6, no. 170, pp. 1–12, 2018.
- [84] S. Guo, Q. Pan, and M. B. Khamesee, “Development of a novel type of microrobot for biomedical application,” *Microsyst. Technol.*, vol. 14, no. 3, pp. 307–314, 2008.
- [85] A. Chałupniak, E. Morales-Narváez, and A. Merkoçi, “Micro and nanomotors in diagnostics,” *Adv. Drug Deliv. Rev.*, vol. 95, pp. 104–116, 2015.
- [86] F. Qiu, R. Mhanna, L. Zhang, Y. Ding, S. Fujita, and B. J. Nelson, “Artificial bacterial flagella functionalized with temperature-sensitive liposomes for controlled release,” *Sensors Actuators B*, vol. 196, pp. 676–681, 2014.
- [87] X. Wang et al., “Surface-Chemistry-Mediated Control of Individual Magnetic Helical Microswimmers in a Swarm,” *ACS Nano*, vol. 12, no. 6, pp. 6210–6217, 2018.
- [88] F. Paquin, J. Rivnay, A. Salleo, N. Stingelin, and C. Silva, “Multi-phase semicrystalline microstructures drive exciton dissociation in neat plastic semiconductors,” *J. Mater. Chem. C*, vol. 3, no. 207890, pp. 10715–10722, 2015.
- [89] H. W. Huang, M. S. Sakar, A. J. Petruska, S. Pané, and B. J. Nelson, “Soft micromachines with programmable motility and morphology,” *Nat. Commun.*, vol. 7, pp. 1–10, 2016.

- [90] B. Gaihre, M. S. Khil, D. R. Lee, and H. Y. Kim, "Gelatin-coated magnetic iron oxide nanoparticles as carrier system: Drug loading and in vitro drug release study," *Int. J. Pharm.*, vol. 365, no. 1–2, pp. 180–189, 2009.
- [91] T. H. C. Salles, C. B. Lombello, and M. A. D'Ávila, "Electrospinning of gelatin/poly (vinyl pyrrolidone) blends from water/acetic acid solutions," *Mater. Res.*, vol. 18, no. 3, pp. 509–518, 2015.
- [92] Y. Tu, F. Peng, P. B. White, and D. A. Wilson, "Redox-sensitive stomatocyte nanomotors: destruction and drug release in the presence of glutathione," *Angew. Chemie - Int. Ed.*, vol. 56, no. 26, pp. 7620–7624, 2017.
- [93] C. Heller et al., "Vinylcarbonates and vinylcarbamates: Biocompatible monomers for radical photopolymerization," *J. Polym. Sci. Part A Polym. Chem.*, vol. 49, no. 3, pp. 650–661, 2011.
- [94] A. Hartschuh, N. Anderson, and L. Novotny, "Near-field Raman spectroscopy using a sharp metal tip," *J. Microsc.*, vol. 210, no. 3, pp. 234–240, 2003.
- [95] S. H. Park, D. Y. Yang, and K. S. Lee, "Two-photon stereolithography for realizing ultraprecise three-dimensional nano/microdevices," *Laser Photonics Rev.*, vol. 3, no. 1–2, pp. 1–11, 2009.
- [96] T. Asavei et al., "Fabrication of microstructures for optically driven micromachines using two-photon photopolymerization of UV curing resins," *J. Opt. A: Pure Appl. Opt.*, vol. 11, no. 034001, 2009.
- [97] J. Serbin, A. Ovsianikov, B. Chichkov, and L. Zentrum, "Fabrication of woodpile structures by two-photon polymerization and investigation of their optical properties," vol. 12, no. 21, pp. 5221–5228, 2004.
- [98] Q. Geng, D. Wang, P. Chen, and S. C. Chen, "Ultrafast multi-focus 3-D nano-fabrication based on two-photon polymerization," *Nat. Commun.*, vol. 10, no. 1, pp. 1–7, 2019.
- [99] C. N. Lafratta, J. T. Fourkas, T. Baldacchini, and R. A. Farrer, "Multiphoton fabrication," *Angew. Chem. Int. Ed.*, vol. 46, pp. 6238–6258, 2007.
- [100] I. Coto Hernández et al., "Two-photon excitation STED microscopy with time-gated detection," *Sci. Rep.*, vol. 6, no. 19419, pp. 1–9, 2016.
- [101] R. Wollhofen, J. Katzmann, C. Hrelescu, J. Jacak, and T. A. Klar, "120 nm resolution and 55 nm structure size in STED-lithography," *Opt. Express*, vol. 21, no. 9, pp. 10831, 2013.
- [102] D. G. Grier, "A revolution in optical manipulation," *Nature*, vol. 424, pp. 810–816, 2003.
- [103] R. J. Narayan, A. Doraiswamy, D. B. Chrisey, and B. N. Chichkov, "Medical prototyping using two photon polymerization," *Mater. Today*, vol. 13, no. 12, pp. 42–48, 2010.
- [104] H. Cao, M. Zheng, X. Dong, F. Jin, Z. Zhao, and X. Duan, "Two-photon nanolithography of positive photoresist thin film with ultrafast laser direct writing," vol. 201108, no. 2013, 2014.
- [105] K. Ohlinger et al., "Undistorted 3D microstructures in SU8 formed through two-photon polymerization," *AIP Advances*, vol. 1, no. 032163, 2011.
- [106] A. L. Pénard, T. Gacoin, and J. P. Boilot, "Functionalized sol-gel coatings for optical applications," *Acc. Chem. Res.*, vol. 40, no. 9, pp. 895–902, 2007.
- [107] R. Houbertz et al., "Investigations on the generation of photonic crystals using two-photon polymerization (2PP) of inorganic-organic hybrid polymers with ultra-short laser pulses," *Phys. Stat. Sol. Appl. Mater. Sci.*, vol. 204, no. 11, pp. 3662–3675, 2007.

- [108] Y. Bougdid, Z. Sekkat, A. Rahmouni, I. Maouli, K. Mochizuki, and M. Halim, "Laser nanofabrication in photoresists by two-photon absorption," Proc. of SPIE Vol. 10740 107400G-1, 2018.
- [109] C. N. LaFratta and T. Baldacchini, "Two-photon polymerization metrology: Characterization methods of mechanisms and microstructures," Micromachines, vol. 8, no. 4, pp.1-25, 2017.
- [110] Y. Bougdid, Y. El Idrissi, I. Maouli, and Z. Sekkat, "Direct laser writing of submicrometric voxels in two-photon photopolymerization," Proc. of SPIE Vol. 11098 110980G-1, 2019.
- [111] M. Malinauskas, V. Purlys, M. Rutkauskas, and R. Gadonas, "Two-photon polymerization for fabrication of three-dimensional micro- and nanostructures over a large area," Proc. of SPIE Vol. 7204 72040C-1, 2009.
- [112] J. P. Fouassier, "Photoinitiation, photopolymerization and photocuring," Polymer International, vol. 40, no. 4, pp.315-316, 1996.
- [113] S. Turunen et al., "Pico- and femtosecond laser-induced crosslinking of protein microstructures: Evaluation of processability and bioactivity," Biofabrication, vol. 3, no. 4, pp. 1-14, 2011.
- [114] Y. L. Sun et al., "Dynamically tunable protein microlenses," Angew. Chemie - Int. Ed., vol. 51, no. 7, pp. 1558–1562, 2012.
- [115] X. Zheng et al., "A method for positioning the focal spot location of two photon polymerization," AIP Advances, vol. 7, no. 095318, 2017.
- [116] H. A. Willis, V. J. I. Zichy, and P. J. Hendra, "The laser-Raman and infra-red spectra of poly(methyl methacrylate)," Polymer, vol. 10, pp. 737–746, 1969.
- [117] T. Baldacchini and R. Zadoyan, "In situ and real time monitoring of two-photon polymerization using broadband coherent anti-Stokes Raman scattering microscopy," Opt. Express, vol. 18, no. 18, p. 19219, 2010.
- [118] A. Taguchi, A. Nakayama, R. Oketani, S. Kawata, and K. Fujita, "Multiphoton-excited DUV photolithography for 3D nanofabrication," arXiv e-prints, 2019.
- [119] T. P. Callou, R. Garcia, A. Mukai, N. T. Giacomini, R. G. de Souza, and S. J. Bechara, "Advances in femtosecond laser technology," Clin. Ophthalmol., vol. 10, pp. 697–703, 2016.
- [120] J. B. Geddes, W. J. Firth, and K. Black, "Pulse dynamics in an actively mode-locked laser," SIAM J. Appl. Dyn. Syst., vol. 2, no. 4, pp. 647–671, 2003.
- [121] A. Bartels, D. Heinecke, and S. A. Diddams, "Passively mode-locked 10 GHz femtosecond Ti:Sapphire laser," Opt. Lett., vol. 33, no. 16, pp. 1905–1907, 2008.
- [122] A. Abou Khalil et al., "Direct laser writing of a new type of waveguides in silver containing glasses," Sci. Rep., vol. 7, no. 1124, pp. 1–9, 2017.
- [123] "Mode-locked femtosecond titanium : Sapphire laser," Version Trestles, Del Mar Photonics, Inc 4119 Twilight Ridge, San Diego, CA 92130.
- [124] C. Rulli, "Femtosecond laser pulses; Principale and experiments," Second Edition, Photonics Spectra, vol. 35, no. 10, p. 20, 2001.
- [125] User Manual, "Mai Tai HP, high-performance, mode-locked, Ti:sapphire laser," Part Number 0000-349A, Rev. A, January 2006.

- [126] L. Jonusauskas et al., “Augmentation of direct laser writing fabrication throughput for three-dimensional structures by varying focusing conditions,” *Optical Engineering*, vol. 53, no. 12, pp. 125102, 2015.
- [127] F. Burmeister, U. D. Zeitner, S. Nolte, and A. Tünnermann, “High numerical aperture hybrid optics for two-photon polymerization,” *Opt. Express*, vol. 20, no. 7, p. 7994, 2012.
- [128] J. Stampfl, R. Liska, A. Ovsianikov, “Multiphoton lithography techniques, materials and applications,” wiley online library, DOI: 10.1002/9783527682676, 2016.
- [129] J. B. Müller, “Exploring the mechanisms of 3D direct laser writing by multi-photon polymerization,” DOI: 10.5445/IR/1000047792, 2015.
- [130] J. W. M. Chon, X. Gan, and M. Gu, “Splitting of the focal spot of a high numerical-aperture objective in free space,” *Appl. Phys. Lett.*, vol. 81, no. 9, pp. 1576–1578, 2002.
- [131] E. G. Gamaly et al., “Laser-matter interaction in the bulk of a transparent solid: Confined microexplosion and void formation,” *Phys. Rev. B*, vol. 73, no. 214101, pp. 1-16, 2006.
- [132] H. Kodama, “Automatic method for fabricating a three-dimensional plastic model with photo-hardening polymer,” *Rev. of Sci. Instrum.*, vol. 52, no. 11, pp. 1770–1773, 1981.
- [133] E. Skliutas et al., “A Bio-based resin for a multi-scale optical 3D printing,” *Sci. Rep.*, vol. 10, no. 1, pp. 1-10, 2020.
- [134] C. Liao and M. Bouriau, “Two-dimensional slicing method to speed up the fabrication of micro-objects based on two-photon polymerization,” *App. Phys. Lett.*, vol. 91, no. 033108, pp. 1–4, 2007.
- [135] R. K. P. Benninger and D. W. Piston, “Two-photon excitation microscopy for the study of living cells and tissues,” *Current Protocols in Cell Biology*, DOI: 10.1002/0471143030.cb0411s59, pp. 1–24, 2013.
- [136] T. C. Lin, Y. F. Chen, C. L. Hu, and C. S. Hsu, “Two-photon absorption and optical power limiting properties in femtosecond regime of novel multi-branched chromophores based on tri-substituted olefinic scaffolds,” *J. Mater. Chem.*, vol. 19, no. 38, pp. 7075–7080, 2009.
- [137] J. Xing, X. Dong, W. Chen, X. Duan, N. Takeyasu, and J. Xing, “Improving spatial resolution of two-photon microfabrication by using photoinitiator with high initiating efficiency,” vol. 90, no. 131106, pp. 8–11, 2007.
- [138] S. L. H. F. Gregory et al., “Analysis of voxels size during two-photon polymerization,” *Proceedings of the ASME 2012 International Manufacturing Science and Engineering Conference MSEC2012*, pp. 1–8, 2012.
- [139] I. B. Sohn et al., “Direct femtosecond laser lithography for photoresist patterning,” *Opt. Eng.*, vol. 48, no. 2, p. 024301, 2009.
- [140] K. Takada, H. Sun, S. Kawata, and K. Takada, “Improved spatial resolution and surface roughness in photopolymerization- based laser nanowriting,” *App. Phys. Lett.*, vol. 86, no. 071122, pp. 1–4, 2005.
- [141] F. Burmeister, U. D. Zeitner, S. Nolte, and A. Tünnermann, “High numerical aperture hybrid optics for two-photon polymerization,” *Opt. Express*, vol. 20, no. 7, p. 7994, 2012.
- [142] S. Kawata et al., “Two-photon laser micro-nano fabrication; understanding from single-voxel level,” *Mat. Res. Soc. Syrup. Proc.*, vol. 758, DOI: 10.1557/PROC-758-LL4.6, 2011.

- [143] D. Peyrade, "Visible microlaser two-photon polymerization in a microfluidic cell : A resist study," *Microelectron. Eng.*, vol. 88, no. 8, pp. 2725–2728, 2017.
- [144] D. Wu et al., "High numerical aperture microlens arrays of close packing," *Appl. Phys. Lett.*, vol. 97, no. 3, 2010.
- [145] K. Lee, R. H. Kim, and D. Y. Yang, "Two-photon stereolithography," *J. of Nonlinear Optical Physics & Materials*, vol. 16, no. 1, pp. 59–73, 2007.
- [146] M. G. Kuzyk, "Fundamental limits on two-photon absorption cross sections," *J. Chem. Phys.*, vol. 119, no. 16, pp. 8327–8334, 2003.
- [147] C. G. Smith et al., "Effect of low numerical-aperture femtosecond two-photon absorption on (SU-8) resist for ultrahigh-aspect-ratio microstereolithography," *J. of App. Phys.*, vol. 97, no. 054907, 2015.
- [148] S. H. Park, T. W. Lim, D. Yang, R. H. Kim, and K. Lee, "Improvement of spatial resolution in nano-stereolithography using radical quencher," *Macromol. Res.*, vol. 14, no. 5, pp. 559–564, 2006.
- [149] T. F. Scott et al., "Two-color single-photon photoinitiation and photoinhibition for subdiffraction photolithography," *Science*, vol. 324, no. 5929, pp. 913–917, 2009.
- [150] L. Li et al., "Achieving $\lambda/20$ resolution by one-color initiation and deactivation of polymerization," *Science*, vol. 324, no. 5929, pp. 910–913, 2009.
- [151] L. Zheng et al., "Nanofabrication of high-resolution periodic structures with a gap size below 100 nm by two-photon polymerization," *Nanoscale Res. Lett.*, vol. 14, no. 134, 2019.
- [152] J. Alda, "Laser and gaussian beam propagation and transformation," *Encycl. Opt. Eng.*, 2003.
- [153] H. B. Sun, M. Maeda, K. Takada, J. W. M. Chon, M. Gu, and S. Kawata, "Experimental investigation of single voxels for laser nanofabrication via two-photon photopolymerization," *Appl. Phys. Lett.*, vol. 83, no. 5, pp. 819–821, 2003.
- [154] K. S. Lee, D. Y. Yang, S. H. Park, and R. H. Kim, "Recent developments in the use of two-photon polymerization in precise 2D and 3D microfabrications," *Polym. Adv. Technol.*, vol. 17, no. 2, pp. 72–82, 2006.
- [155] X. He, T. Li, J. Zhang, and Z. Wang, "STED direct laser writing of 45 nm width nanowire," *Micromachines*, vol. 10, no. 11, pp. 1–9, 2019.
- [156] Y. Lin and J. Xu, "Microstructures fabricated by two-photon polymerization and their remote manipulation techniques: Toward 3D printing of micromachines," *Adv. Opt. Mater.*, vol. 6, no. 8, pp. 1–11, 2018.

Scientific Production

1. Publications & Conference Proceedings

1.1. Peer-Reviewed Publications

1. **Y. Bougdid** and Z. Sekkat, “Voxels Optimization in 3D Laser Nanoprinting”, *Scientific Reports* **10**, Jun 2020.
2. **Y. Bougdid**, I. Maouli, A. Rahmouni, K. Mochizuki, I. Bennani, M. Halim, and Z. Sekkat, “Systematic $\lambda/21$ Resolution Achieved in Nanofabrication by Two-Photon-Absorption Induced Polymerization”, *J. Micromech. Microeng.* **29**, Feb 3, 2019.
3. A. Rahmouni, **Y. Bougdid**, S. Moujdi, D. V. Nesterenko, and Z. Sekkat, “Photo-assisted Holography in Azo Dye Doped Polymer Films”, *J. Phys. Chem. B* **120**, Nov 3, 2016.

1.2. Conference Proceedings

4. **Y. Bougdid**, I. Maouli, Y. El-idrissi, and Z. Sekkat, “Direct Laser Writing of Submicrometric Voxels in Two-Photon Photopolymerization”, Proc. of SPIE, vol. 11098, 110980G, Molecular Nano Machines II (2019), Edited by Z. Sekkat and T. Omatsu.
5. S. Moujdi, **Y. Bougdid**, A. Rahmouni, T. Mahfoud, D. Nesterenko, M. Halim, and Z. Sekkat, “Azo-polymers for Holographic Recording: Photo-assisted Holography and Surface Relief Gratings”, Proc. of SPIE, Vol. 10944, 05 Mar, 2019.
6. **Y. Bougdid**, I. Maouli, A. Rahmouni, K. Mochizuki, M. Halim, and Z. Sekkat, “Laser Nanofabrication in Photoresists by Two-Photon Absorption”, Proc. of SPIE vol.10740, 107400G, Molecular Machines (2018), Edited by Z. Sekkat.

1.3. Upcoming Publications:

7. **Y. Bougdid**, and Z. Sekkat, “Analysis of Voxel Dimensions in 3D Laser Nanofabrication”, to be submitted (SPIE Conference).
8. **Y. Bougdid**, and Z. Sekkat, “3D Nanoprinting by Two-Photon Absorption”, (Review paper).

2. Oral & Poster Presentation:

2.1. Oral & Presentation:

August 01.2016 The First OSCIM Meeting, OSA Student Chapter in Morocco; **Topic:** “Light Polarization Dependence of Holographic Storage in Azo-polymers”.

March 28 to 30.2017 The International Conference on Advance Materials for Photonics, Sensing and Energy Applications (AMPSECA' 2017); **Topic:** “Light Polarization Dependence of Holographic Storage in Azo-polymers”.

June 16 to 21.2019 Summer school “1st North American Summer School on Photonic Materials (NASSPM)” in Centre for Optics, Photonics, and Lasers (COPL), Laval University, Quebec,

Canada; **Topic:** “Optical Sensors Based on Photo-inscribed Glass Waveguides fabricated by Femtosecond (Fs) Laser”.

Oct 30 to Nov 1.2019 The International Conference on Advanced Materials for Photonics, Sensing and Energy Applications (AMPSECA' 2019); **Topic:** “Laser Nanofabrication in Photoresists by Two-Photon Absorption Induced Photopolymerization”.

2.2. Poster Presentation

March 09 to 11.2016 The 5th Edition of Doctoral, Faculty of Sciences, Rabat, Morocco;
Topic: “Holographic Recording in Azo Dye Doped Polymer Films”.

August 24 - 26.2019 SPIE Conference; Molecular Nano Machines II (2019), Edited by Z. Sekkat and T. Omatsu. **Topic:** “3D Laser Nanofabrication by Two-Photon Absorption”.

April 13 - 14.2017 DEMESYS Conference (2017), Edited by N. B. CE3M G. Manager.
Topic: “Light Polarization Dependence of Holographic Storage in Azopolymers”.

3. Participation: Summer School - Laval University, Canada

The 1st North American summer school on Photonics Materials has been held in Centre for Optics, Photonics and Lasers -(COPL), Laval University, Quebec, Canada on June 16-21, 2019. It gathered graduate and senior undergraduate students and postdocs in Physics, Chemistry, and Engineering Departments.



Research Topic: “Optical Sensors Based on Photo-inscribed Glass Waveguides fabricated by Fs Laser”.

Presentation of the team:

Milos Krbal, University of Pardubice, CZ

Yahya Bougdid, MAsCIR & Mohammed V University, Rabat, Morocco

Cord Beck, Austin Peay State University, USA

Chuyu Zhong, Zhejiang University, China

Thomas Meyneng, COPL- Laval University, Canada, Quebec



4. Research Training - Osaka University, Japan

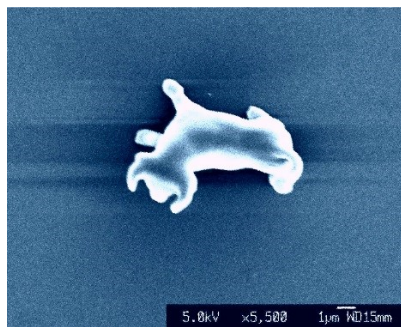
Period: From 1st to May 31st, 2018.

At the Laboratory of Scientific Instrumentation and Engineering, Osaka University, Japan.

The Program name: Nano-Functional Photonics: study of new nano optical/photonic functions originating from the interaction of photon and nanostructured materials.

Purpose of invitation: Sharing/exchanging the research and promoting the joint research between MAScIR and Photonics Center (Osaka University).

Research Topic: Multiphoton-Excited Deep-Ultraviolet Photolithography for 3D Nanofabrication.



SEM images of 3D micro-sized bull printed by using TPA-based Deep-UV; a resolution of 100 nm was achieved in this nanofabrication process.

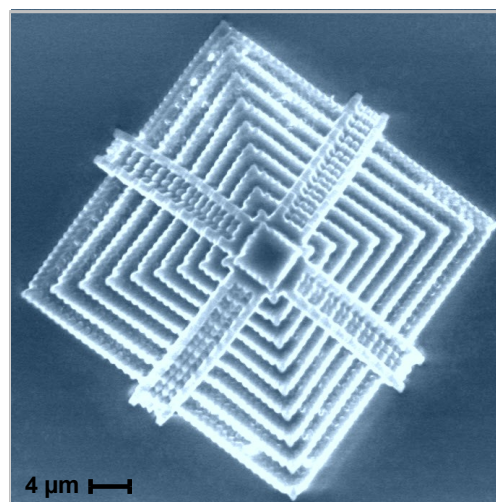
Link: <https://pubs.acs.org/doi/10.1021/acsnm.0c02519>

5. Awards

Due to the achieved results which are presented in this thesis, I am selected for participating in the 71th Lindau Nobel Laureate Meetings (2021).

The Lindau Nobel Laureate Meetings are triennial scientific conferences held in Lindau, Bavaria, Germany; from **27 Jun - 2 July, 2021**. Their aim is to bring together Nobel laureates and young scientists to foster scientific exchange between different generations and cultures. In this event, more than 50 Nobel laureates in the fields of medicine/physiology, physics, and chemistry will be spending a week at Lake Constance engaging in an exchange of ideas and opinions.

Link: <https://www.lindau-nobel.org/>



3D micro-sized pyramid fabricated by TPP.